2019

The Effects Of Cationic Charges In Metal-Ligand Cooperativity

Samuel Mccollom
University of Pennsylvania

The Effects Of Cationic Charges In Metal-Ligand Cooperativity

Abstract

The utility of metal ligand cooperativity has demonstrated great promise in the ability to activate strong bonds under mild conditions. The work described below endeavors to contribute to this field through two thrusts: 1. Exploiting a chelating phosphinimine ligand designed to take advantage of the electron density at the phosphinimine nitrogens, caused by zwitterionic character of the phosphinimine, to aid in catalytic applications. 2. The development of ligands that can pre-form heterobimetallic clusters for combined action toward strong-bond activation chemistry. To this end, two ligand designs were studied. The first is a set of novel tren-based tris(phosphinimine) ligands (P3tren; tren = tri(2 aminoethyl)amine). The P3tren ligands were designed to maintain the primary coordination sphere observed in other tetradentate ligands such as tren and tmpa, while providing a convenient means for varying the donor strength of the terminal nitrogens. Poor π-overlap between nitrogen and phosphorous results in significant ylidic character, thereby enhancing the basicity of the nitrogen donor atom while maintaining an overall neutral charge. The second was through a collaboration with the Walsh group, where Chen Wu experimentally found that DavePhos(Pd) can activate aryl fluorides in similar yields and rates as aryl chlorides for the coupling with phenyl Grignard. DFT calculations were performed to probe the possible reaction mechanism, suggesting the key factor was the coordination of a magnesium cation by the biphenyl system of DavePhos. The magnesium ion was proposed to aid aryl halide activation through a heterobimetallic pathway.

Degree Type

Dissertation

Degree Name

Doctor of Philosophy (PhD)

Graduate Group

Chemistry

First Advisor

Neil . Tomson

Subject Categories

Inorganic Chemistry

THE EFFECTS OF CATIONIC CHARGES IN METAL-LIGAND COOPERATIVITY

Samuel P. McCollom

A DISSERTATION

in

Chemistry

Presented to the Faculties of the University of Pennsylvania

in

Partial Fulfillment of the Requirements for the

Degree of Doctor of Philosophy

2019

Supervisor of Dissertation

_____

Dr. Neil C. Tomson

Assistant Professor of Chemistry

Graduate Group Chairperson

_____

Dr. David W. Christianson

Roy and Diana Vagelos Professor in Chemistry and Chemical Biology

Dissertation Committee

Dr. Eric J. Schelter, Professor of Chemistry

Dr. Daniel J. Mindiola, Brush Family Professor of Chemistry

Dr. Donald H. Berry, Professor of Chemistry

Acknowledgment

First, I would like to express my sincere graditude to my advisor, Dr. Neil Tomson. Your enthusiasm for research and support along the way, in everything from setting up the lab together, to guiding me how to properly conduct and write about science, was immensely helpful. I would not be the scientist I am today without you.

I would also like to thank other faculty and staff at Penn. First, I want to sincerely thank my committee: Dr. Eric Schelter, Dr. Dan Mindiola, and Dr. Don Berry for their support, guidance, insightful comments, and often difficult questions on research. Next, I would like to thank Dr. Pat Carrol and Dr. Mike Gau for running and maintining a top notch X-ray crystallography center. They have been immensely helpful in my many failed crystallization attempts. I also want to thank Dr. Simon Berrit for extremely helpful discussions and allowing me to use all of the equipment in the HTE center. Finally, I want to deeply thank Dr. Jun Gu and the late Dr. George Furst. For reasons unkown to me, they chose me as the NMR TA in 2016. I learned a tremendous amount from them both and am truly so thankful that I was chosen for that opportunity.

I also want to thank all of my friends and collegues at Penn, especially everyone in the Tomson lab. You all made my days easier to get through and the scientific discussions we had helped me grow immensely as a scientist.

Lastly, but certainly not least, I want to thank my family. For my Mom, Dad, and sister for shaping me into the person I am today. I cannot thank you enough for raising me the way you did. Finally, I want to thank my wife, Nora. I could not have done any of this without your love and support over the years.

ABSTRACT

THE EFFECTS OF CATIONIC CHARGES ON METAL-LIGAND COOPERATIVITY

Samuel P. McCollom

Dr. Neil C. Tomson

The utility of metal ligand cooperativity has demonstrated great promise in the ability to activate strong bonds under mild conditions. The work described below endeavors to contribute to this field through two thrusts: 1. Exploiting a chelating phosphinimine ligand designed to take advantage of the electron density at the phosphinimine nitrogens, caused by zwitterionic character of the phosphinimine, to aid in catalytic applications. 2. The development of ligands that can pre-form heterobimetallic clusters for combined action toward strong-bond activation chemistry. To this end, two ligand designs were studied. The first is a set of novel tren-based tris(phosphinimine) ligands (P_3tren; tren = tri(2-aminoethyl)amine). The P_3tren ligands were designed to maintain the primary coordination sphere observed in other tetradentate ligands such as tren and tmpa, while providing a convenient means for varying the donor strength of the terminal nitrogens. Poor π-overlap between nitrogen and phosphorous results in significant ylidic character, thereby enhancing the basicity of the nitrogen donor atom while maintaining an overall neutral charge. The second was through a collaboration with the Walsh group, where Chen Wu experimentally found that DavePhos(Pd) can activate aryl fluorides in similar yields and rates as aryl chlorides for the coupling with phenyl Grignard. DFT calculations were performed to probe the possible reaction mechanism, suggesting the key factor was the coordination of a magnesium cation by the biphenyl

system of DavePhos. The magnesium ion was proposed to aid aryl halide activation through a heterobimetallic pathway.

Table of Contents

Acknowledgements ..... **ii**

Abstract ..... **iii**

List of Figures ..... **vii**

List of Schemes ..... **ix**

List of Tables ..... **x**

Chapter 1: Archetypes of Metal-Ligand Cooperativity **1**
1.1 Introduction 1
1.2 Cooperative Bond Activation Across a Metal-Ligand Bond 3
1.3 Cooperative Bond Activation With Redox-Active Ligands 6
1.4 Coordination of Alkali Metals by Ligand 7
1.5 Dissertation Overview 10
1.6 References 14

Chapter 2: Synthesis of Highly Reduced Copper Centers through Tripodal Phosphinimine Frameworks and Subsequent Studies of Novel End-On Copper(II) Superoxides **19**
2.1 Introduction 19
2.2 Results and Discussion 23
2.2.1 Synthesis of Novel tren-based tris(phosphiniminato) ligands and Cu(I) Complexes 23
2.2.2 Cyclic Voltammetry 26
2.2.3 Formation of End-On Superoxide Complexes 28
2.2.4 DFT Calculations 30
2.2.5 Proton-Coupled Electron Transfer (PCET) Reactivity of 2 33
2.2.6 Formation of heteroleptic di(cupric)peroxide (5) 36
2.2.7 Comments on Thermal Decomposition of 2 38
2.3 Conclusion 41
2.4 References 43
2.5 Experimental 47

Chapter 3: Mechanism for the Catalytic Dehydrogenation of Indoline to Indole by Tripodal Phosphinimine Copper Complexes and O_2 with Metal-Ligand Cooperativity **89**
3.1 Introduction 89
3.2 Results and Discussion 91
3.2.1 Results from Catalysis 91
3.2.2 Mechanistic Studies 94
3.2.2.1 Background 94
3.2.2.2 Kinetics 95
3.2.2.3 Stoichiometry Determination 96
3.2.2.4 Synthetic Observations and Deuterium Labeling 98
3.2.2.5 Hammett Analysis 101

3.2.2.6 Stoichiometric Indoline Reactivity with P_3tren-Cupric Superoxide 103
3.2.2.7 Reaction Mechanism 105
3.3 Conclusion 106
3.4 References 107
3.5 Experimental 110

Chapter 4: Additive Free Catalytic Oxidation of Alcohols by Tripodal Phosphinimine Copper Complexes and O_2 with Metal-Ligand Cooperativity 139
4.1 Introduction 139
4.2 Results and Discussion 142
4.2.1 Synthesis of Copper(I) Precursors 142
4.2.2 Optimization of Benzyl Alcohol Oxidation 143
4.2.3 Reaction Scope 145
4.2.4 Byproduct Analysis for Mechanistic Interpretation 147
4.3 Conclusion 153
4.4 References 153
4.5 Experimental 156

Chapter 5: Aryl Fluoride Activation Through Palladium Magnesium Bimetallic Cooperation: A Synthetic and Computational Study 164
5.1 Introduction 164
5.2 Results and Discussion 168
5.2.1 Catalyst Identification and Optimization 168
5.2.2 Reaction Scope 170
5.2.3 Mechanistic Insights 172
5.2.4 Computational Study 175
5.2.5 Experimental Support for Heterobimetallic Mechanism 185
5.3 Conclusion 189
5.4 References 190
5.5 Experimental 193

List of Figures

Figure 1.1 Relationship of energy consumption to population over time. 2

Figure 2.1 Literature examples of biomimetic copper complexes demonstrating tunable redox potentials through functional group substitution in the secondary coordination sphere. 20

Figure 2.2 Proposed kinetic scheme (Karlin[15], Schindler[16]) for biomimetic Cu/O_2 reactions. 22

Figure 2.3 Zwitterionic character of phosphinimies and pentamethylguanidine shown through natural population analysis charge (blue/purple), and pK_a values in MeCN (red). 24

Figure 2.4 Molecular structure of 1-PMe_3 with thermal ellipsoids set to 50%. Hydrogen atoms and $B(C_6F_5)_4^-$ counteranion omitted for clarity Crystals grown from Et_2O at -35 °C. 25

Figure 2.5 CV traces of 1-PMe_3 (black, $E_{1/2}$ = -780 mV; ΔE_p = 68 mV), 1-PMe_2Ph (red, $E_{1/2}$ = -740 mV; ΔE_p = 116 mV), 1-$PMePh_2$ (blue, $E_{1/2}$ = -630 mV; ΔE_p = 187 mV), and 1-PPh_3 (green, $E_{1/2}$ = -370 mV; ΔE_p = 66 mV) Conditions: 200 mV/s, 100 mM of NBu_4PF_6, 1 mM analyte, MeCN, Pt electrode. 27

Figure 2.6 UV/vis spectrum of compounds 1-PMe_3 (-100 °C, 0.5 mM, THF, black), 2-PMe_3 (-100 °C, 0.5 mM, THF, green), and 4-PMe_3 (20 °C, 0.25 mM, MeCN, red). Absorbances normalized for differing concentrations. 28

Figure 2.7 DFT calculated β (spin down) MO diagram for Cu(I) complexes. HOMO is highest shown orbital for each complex. 30

Figure 2.8 DFT calculated β (spin down) MO diagram for CuO_2 complexes. HOMO for 1-PMe_3 and ^{NME2}tmpa is the $d_{x^2-y^2}$. HOMO for tmpa is π^*_σ. 31

Figure 2.9 DFT calculated β (spin down) MO diagram for 1-PMe_3. 33

Figure 2.10 (a) Pseudo-first-order plot obtained by monitoring the treatment of 2-PMe_2Ph (0.52 mM) with 1.5 equiv of 2,6-di-*tert*-butyl-4-methoxyphenol in THF at 173 K. (b) Plot of k_{obs} vs. concentration of substrate to determine second-order rate constant and KIE; proteo (circles), deutero (squares). 35

Figure 2.11 UV/vis spectra of compounds 1 (black), 2 (green), and 3 (purple). 38

Figure 2.12 (A) UV/vis spectra of 2PMe_3 (0.5 mM) showing decay at -40 °C. 40

Figure 3.1 Scope of indolines for oxidation to indole. 94

Figure 3.2 Dependence of the reaction rate on (a) copper concentration and (b) indoline concentration. 97

Figure 3.3 Hammett correlation plot for the catalytic dehydrogenation of indoline by (P_3tren)Cu(I) under O_2. 101

Figure 3.4 Plot of (k_BT/e) ln(k) versus E_{ox} for the catalytic dehydrogenation of indoline by 1 under O_2. 102

Figure 3.5 Hammett correlation plot for the catalytic dehydrogenation of indoline by cupric superoxide, 4, at -100 °C in THF. 104

Figure 4.1 Scope of benzyl alcohols for oxidation to benzaldehydes. 146

Figure 4.2 Scope of saturated alcohols for oxidation to aldehydes and ketones. 147

Figure 4.3 Byproducts observed in catalytic alcohol oxidations. 151

Figure 5.1 Literature examples of Pd-catalyzed cross-coupling reactions with aryl fluorides. 166

Figure 5.2 Key transitions states for heterobimetallic cooperativity. 167

Figure 5.3 Scope of aryl fluorides with aryl Grignard reagents.[a,b] 171

Figure 5.4 Non-competition Time Course Experiments at Mg:ArX Ratios of 1:1 and 2.5:1. 174

Figure 5.5 Kumada coupling pathway. 177

Figure 5.6 Potential energy diagram for the Kumada cycle. 178

Figure 5.7 Heterobimetallic cycle. 180

Figure 5.8 Nakamura group proposed Mg/Ni cooperative activation of ArX. 181

Figure 5.10 Potential energy diagram for the heterobimetallic pathway. 185

Figure 5.11 Non-competition Experiments at Mg:ArX Ratios of 0.25:1, 1:1 and, 2.5:1 using 2,6-dimethyl-1-fluorobenzene or 2,6-dimethyl-1-chlorobenzene 186

Figure 5.12 DFT optimized structure of TS4F-OB; all hydrogen atoms were removed for clarity. Important bond lengths (Å) and angles (deg): Pd-C1 2.158, Pd-C2 2.061, Pd-C3 2.405, Pd-Mg 2.662, Pd-P 2.386, F-C2 1.690, Mg-C1 2.294, Mg-C4 2.776, Mg-C5 3.062, F-Mg-Br 105.9, Pd-Mg-C1 51.1 C2-F-Mg 95.0. 188

Figure 5.13 Reactions with modified phosphines. 189

List of Schemes

Scheme 1.1 General scheme for cooperative bond activation across a metal-ligand bond.3

Scheme 1.2 Proposed cooperative activation of H_2 in [FeFe] hydrogenase..... 4

Scheme 1.3 Bullock pendant amine demonstrating metal-ligand cooperativity. 5

Scheme 1.4 Examples of metal ligand cooperativity in the primary coordination sphere. 6

Scheme 1.5 Proposed mechanism of alcohol reduction by galactose oxidase. 7

Scheme 1.6 Non-systematically controlled alkali metal placement for activation of small molecules. 9

Scheme 1.7 Systematically controlled alkali metal placement for activation of small molecules. 10

Scheme 2.1 Synthesis of Cu(I) and CuO_2 compounds. 23

Scheme 2.2 Synthesis of heteroleptic trans-1,2-dicupricperoxide species. 36

Scheme 3.1 Proposed reaction mechanism. 107

Scheme 4.1 Mecahanism paradigms for Cu/O_2 alcohol oxidation. 140

Scheme 4.2 Synthesis of P_3tren by the Staudinger reaction and [(P_3tren)Cu][$BArF_{20}$]. 142

Scheme 4.3 Synthesis of P_3tren(KI) through three step synthesis..... 143

List of Tables

Table 2.1 TDDFT calculated transitions of CuO_2 complexes. 32

Table 3.1 Selected optimization of indoline oxidation.[a] 92

Table 3.2 Selected controls of indoline oxidation.[a] 93

Table 3.3 Selected controls of indoline oxidation using H_2O_2 as the oxidant.[a] 98

Table 4.1 Selected optimization of benzyl alcohol oxidation.[a] 144

Table 4.2 Substrate scope for catechol and hydroquinones. 148

Table 4.3 Substrate scope for phenols..... 150

Table 5.1 Selected optimization of coupling between 1a and 2a.[a] 169

Table 5.2 Competitive experiments between aryl fluorides and aryl chlorides. 173

Chapter 1: Archetypes of Metal-Ligand Cooperativity

1.1 Introduction

Climate change is a modern problem requiring innovative solutions. While many fields, from engineering to politics, are focusing on solving this multi-generational problem, chemists will also play an important role in developing solutions. Great strides have been made by chemists in recent decades toward synthesizing fuels from renewable sources,[1] harnessing renewable feedstocks,[2] and lowering energy consumption.[3] Despite these gains, 85 % of the world's energy still comes from fossil fuels.[4] Human energy consumption has skyrocketed in the post-World War II era, coinciding with a population boom (Figure 1.1).[5] The continuation of these trends, while still deriving a majority of our energy needs from fossil fuels, is unsustainable and has the potential to create a catastrophic problem in the years ahead. While many solutions will be needed to resolve this pending crisis, one area where chemists have the tools to make an immediate impact to curtail growing energy needs is by lowering energy consumption in chemical processes.

The development of improved catalysts is the primary means by which chemists decrease the amount of energy needed for producing a given product. Catalysts operate by providing an alternative reaction pathway to a chemical transformation that is lower in energy than the uncatalyzed reaction pathway.[6] In homogenous catalysis, the ability to impart control on a metal center comes from the choice of ligands bound to the transition metal. These ligands play a pivotal role in tuning the properties of the metal center, but they typically do not participate in bond making or breaking processes. However, it has

been found that nature has evolved enzymes with ligand environments that cooperatively aid in bond activation for a wide variety of substrates.[7] The development of new transition metal catalysts bearing ligands that cooperate with the metal, similar to ways in which enzymes operate, may lead to new types of catalysis, especially in applications requiring activation of strong bonds that have historically needed large energy inputs.[8]

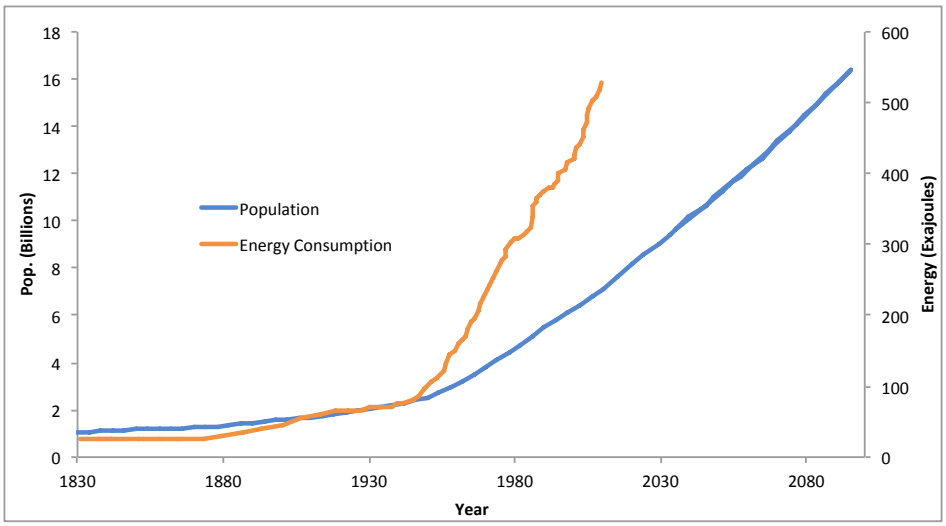

Figure 1.1 Relationship of energy consumption to population over time.

Over the past several decades, metal-ligand cooperativity has been studied in great detail in enzymes and those lessons are being applied to synthetic systems. Applications of these principals has led to less energy-intensive reaction pathways for important catalytic reactions.[9] To follow will be a brief synopsis on common archetypes of metal ligand cooperativity, both in nature and in synthetic systems, that directly relate to the topics in this dissertation. These include bond activation across a metal-ligand bond, the use of redox active ligands in conjunction with metals, and the coordination of alkali metals to aid in strong-bond activation. The examples to follow are intended to

give background on metal ligand cooperativity, to show the inspiration for this work and to place the chemistry in this dissertation within the broader field. Many areas of metal ligand cooperativity are outside of the scope of this work but have led to positive impacts in the field, most notably the strategy of using ligand-based dearomatization/aromatization to activate alcohols, amines, and H_2, as pioneered by Milstein and co-workers.[10]

Finally, the research in this dissertation will be introduced; this work involves study into the effects of positively charged moieties in the secondary coordination sphere on metal-ligand cooperativity. Two different ligand design principles were used in this context: 1. A chelating phosphinimine ligand was designed to take advantage of the electron density at the phosphinimine nitrogens to aid in catalytic applications, including the aerobic oxidation of alcohols and heterocycles. 2. Cation-π interactions were used to bind an alkaline earth metal near a redox-active transition metal to aid in strong-bond activation and functionalization.

1.2 Cooperative Bond Activation Across a Metal-Ligand Bond

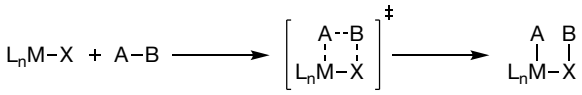

Scheme 1.1 General scheme for cooperative bond activation across a metal-ligand bond.

Cooperative bond activation across a metal-ligand bond has been showcased by many different metal systems with a variety of substrates (Scheme 1.1).[8] The most relevant examples to this dissertation contain pendant, nitrogenous bases that act

cooperatively with the metal center. Inspiration for this motif comes from [FeFe]- and [NiFe]-hydrogenases, which are able to catalyze the heterolytic splitting of H_2. The [NiFe]- hydrogenases accomplish this task through addition across a metal-sulfur bond, where a bridging thiolate acts both as a ligand for the metals and as a base for H_2 activation. The [FeFe]-hydrogenases use a pendant amine in close proximity to an H_2-binding site on one of the metal centers.[11] The mechanism for the [FeFe]-hydrogenase is proposed to proceed via H_2 binding to the iron center that is distal to the Fe_4S_4 cluster, where the H_2 is then deprotonated by the nearby amine to form an iron hydrido species and an ammonium ion (Scheme 1.2).

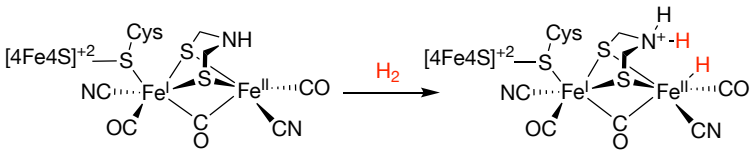

Scheme 1.2 Proposed cooperative activation of H_2 in [FeFe] hydrogenase.

Synthetic systems mimicking the [FeFe]-hydrogenase strategy of a pendant amine in the secondary coordination sphere have been successfully developed by the Bullock and Mock groups.[12] In one example from the Bullock group, they were able to observe the activation of H_2 across a Mn complex with a pendant amine (Scheme 1.3).[12d] Using labeling studies they discovered that the hydride and proton are in rapid exchange, even at -95 °C, which they hypothesize is representative of a close energy match between the heterolytically cleaved product and the η^2-H_2 adduct.

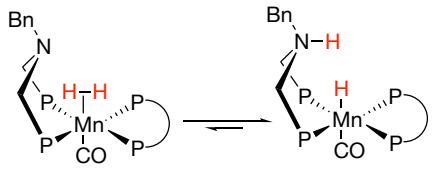

Scheme 1.3 Bullock pendant amine demonstrating metal-ligand cooperativity.

Similarly, mimics of the [NiFe]-hydogenases have been synthesized that make use of bases bound to the metal for the cooperative activation of small molecules (Scheme 1.4). Among the numerous examples that can activate H_2 in a manner similar to the metalloenzymes is the Guan group's (PNP)Fe^{II} complex, FeH(PNP)CO, where PNP = bis[(2-(diisopropylphosphino)ethyl]amine, which reversibly adds H_2 across the Fe-N bond to yield a second iron hydride and a neutral amine ligand. The resulting iron dihydride species is proposed to catalyze the acceptorless dehydrogenation of alcohols under base-free conditions.[13] In addition to amines, other 2p-element-based donors can perform cooperative small molecule activation across a metal-ligand bond. During the investigation of the catalytic cycle for the reduction of N_2 to NH_3, the Peters group found that the resting state of their cycle was in an iron-borohydride-hydride complex.[14] This occurs via H_2 cooperative addition to an Fe–B species; the reversibility of this addition can be observed through the loss of H_2 when the complex is placed under vacuum. Overall, cooperative bond activation across a metal-ligand bond can proceed with a variety of ligands and while not highlighted here, a number of substrates, including alcohols and silanes, can be used.[15] Predominate among this archetype are the numerous examples of nitrogen-based ligands acting as proton acceptors.

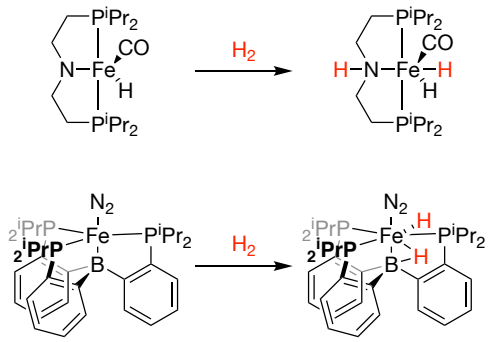

Scheme 1.4 Examples of metal ligand cooperativity in the primary coordination sphere.

1.3 Cooperative Bond Activation With Redox-Active Ligands

Redox-active ligands are emerging in relevance towards the field of metal ligand cooperativity. This stems from the general applicability of redox non-innocence, where low-lying π* ligand orbitals have similar energies to transition metal centers such that facile shuttling of electrons between the metal and ligand can occur. While many ligands have been found to behave in this manner and even to aid in the activation of numerous substrates by several transition metals,[16] detailed examples will not be discussed because it is not directly applicable to further chemistry in this dissertation.

The features of metal ligand cooperativity involving redox-active ligands that do have direct relevance to the work described below are instances in which the ligand directly makes or breaks bonds due to its altered redox state. A prime example of this can be seen in the biological system galactose oxidase (Scheme 1.5).[17] Galactose oxidase contains redox active tyrosyl ligands coordinated to copper. During catalytic turnover, alcohols are deprotonated by the phenoxide moiety of one tyrosyl ligand, while a second, oxidized tyrosyl ligand performs a hydrogen atom abstraction. This cycle can then be

turned over by oxygen, which reforms the phenoxide and phenoxyl moieties and produces hydrogen peroxide as a byproduct. This same reactivity pattern with copper has been exploited in several synthetic systems, including the first example of aerobic benzylic alcohol oxidation that was performed without additives, like bases or hydrogen atom acceptors (*e.g.* TEMPO).[18]

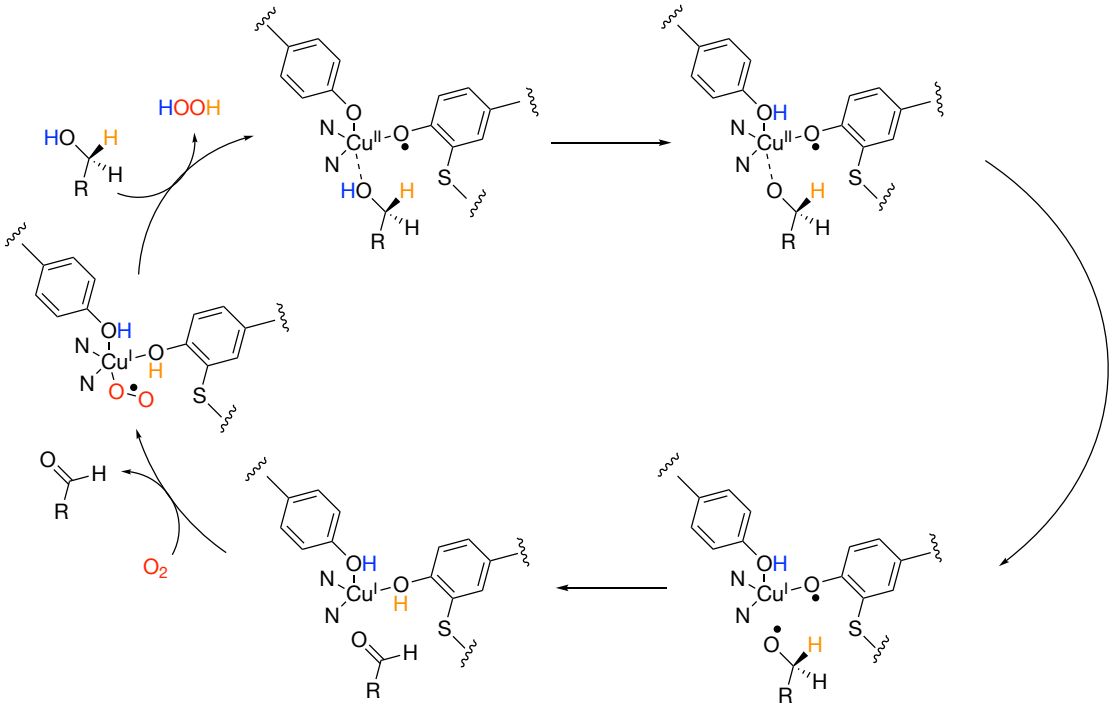

Scheme 1.5 Proposed mechanism of alcohol reduction by galactose oxidase.

1.4 Coordination of Alkali Metals by Ligand

Studies into coordination of alkali metals are emerging as a versatile tool in coordination chemistry. In the literature, there are two types of studies into this field: 1. the serendipitous binding of alkali metals to influence ground state electronic structures and 2. the systematic binding of alkali metals to harness the combined action of both

metals for organometallic applications. Focusing on the former point first, for example, the Holland group found upon reduction of iron-bound μ-N_2 complexes with KC_8, the resulting potassium counterions become bound in a cation-π interaction with the aryl groups of the ligand.[19] This bound potassium cation in the secondary coordination sphere is proposed to help stabilize the reduced μ-N_2 bound between two iron centers (Scheme 1.6). Similar results have been obtained by Limberg using a nickel β-diketiminate complex in which the resulting potassium ions are bound in a cation-π interaction in the secondary coordination sphere of the ligand. These cations are observed to activate CO as measured by a decrease in the CO stretching frequency compared to a lithium analog that is proposed to lack a cation-π interaction (Scheme 1.6).[20] Finally, some early work from the Nakamura group has extensively studied the role of lithium cations in organic reactions using organocuprates. Kinetic and DFT studies have shown that lithium cations play a pivotal role in substrate activation.[21]

However, all of the examples described above lacked predesigned control over placement of the alkali metal. Recent work from both the Nakamura and Walsh groups have created a coordination space for alkali metals through the use of ligands with a deprotonatable site near the active metal center. Upon treatment of these complexes with an alkali metal-containing base, the ligand deprotonates and binds the alkali metal for use in further reactivity. The Nakamura group used a hydroxyphosphine ligand in which an alkoxy-bridged Ni–Mg heterobimetallic complex forms upon addition of Grignard. This intermediate was proposed as key to several Ar–X activation reactions, even leading to the cleavage of Ar–F bonds, one of the strongest carbon based bonds (Scheme 1.7).[22]

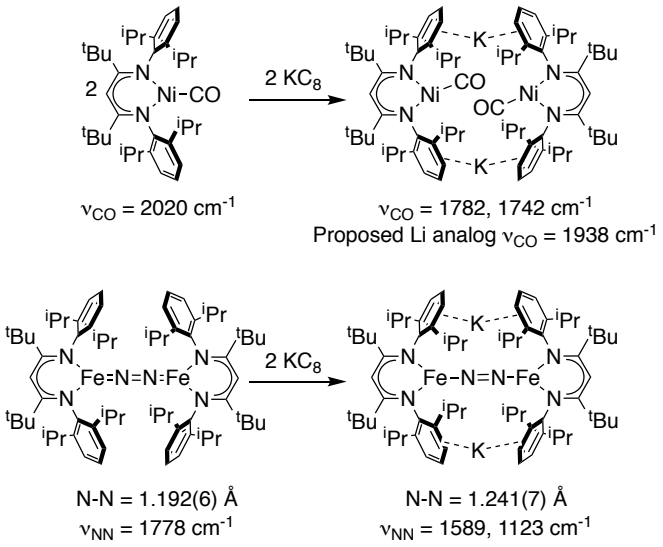

Scheme 1.6 Non-systematically controlled alkali metal placement for activation of small molecules.

The Walsh group has had previous success repurposing Brønsted acidic (NIXANTPHOS)Pd complexes (Scheme 1.7) designed by van Lewuuen and coworkers.[23] Under the basic reaction conditions used for the coupling of diarylmethanes with aryl chlorides, the NIXANTPHOS N–H bond (pK_a ~21 in DMSO) was found to be deprotonated, generating an anionic ligand that binds potassium to both the nitrogen on the ligand and the aromatic π-system of the substrate. This catalyst is able to oxidatively add unactivated aryl chlorides at room temperature, indicating a substantial decrease in activation energy compared to other palladium catalysts bearing bidentate ligands, which normally require the elevated reaction temperatures.[24a] Further support for cooperativity between the main group metal and Pd in the M(NIXANTPHOS)Pd-based system (M = Li, Na, or K) was elucidated by the chemoselective functionalization of 2-benzylfuran[22b] and the arylationof toluene.[24c] The use of coordinating alkali metals for cooperative

activation of small molecules has shown utility, but the tools to control the placement of alkali metals in the coordination environment remains underdeveloped.

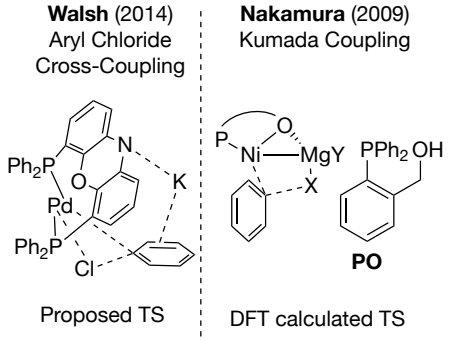

Scheme 1.7 Systematically controlled alkali metal placement for activation of small molecules.

1.5 Dissertation Overview

The utility of metal ligand cooperativity has demonstrated great promise in the ability to activate strong bonds under mild conditions. The work described below endeavors to contribute to this field through two thrusts: 1. Exploiting a chelating phosphinimine ligand designed to take advantage of the electron density at the phosphinimine nitrogens, caused by zwitterionic character of the phosphinimine, to aid in catalytic applications. 2. The development of ligands that can pre-form heterobimetallic clusters for combined action toward strong-bond activation chemistry. To this end, two ligand designs were studied. The first is a set of novel tren-based tris(phosphinimine) ligands (P_3tren; tren = tri(2-aminoethyl)amine). The P_3tren ligands were designed to maintain the primary coordination sphere observed in other tetradentate ligands such as tren and tmpa, while providing a convenient means for varying the donor strength of the

terminal nitrogens. Poor π-overlap between nitrogen and phosphorous results in significant ylidic character, thereby enhancing the basicity of the nitrogen donor atom while maintaining an overall neutral charge. The second was through a collaboration with the Walsh group, where Chen Wu experimentally found that DavePhos(Pd) can activate aryl fluorides in similar yields and rates as aryl chlorides for the coupling with phenyl Grignard. DFT calculations were performed to probe the possible reaction mechanism, suggesting the key factor was the coordination of a magnesium cation by the biphenyl system of DavePhos. The magnesium ion was proposed to aid aryl halide activation through a heterobimetallic pathway.

In Chapter 2, a novel class of highly reducing Cu(I) complexes bound by tren-based, tris(phosphinimine) ligands is reported. These complexes display *quasi*-reversible Cu(I/II) redox potentials as far negative as -780 mV vs. Fc/Fc^+ in isobutyronitrile (IBN). Treatment of the Cu(I) species with dry O_2 at low temperatures yields end-on cupric superoxide complexes, as determined via UV/vis spectroscopy and reactivity studies. The cupric superoxides were found to be remarkably stable toward thermal decomposition, with one member of the series persisting for an appreciable amount of time at temperatures as high as -40 °C ($t_{1/2}$ = 1.4 h). Hydrogen atom transfer (HAT) reactivity typical of end-on cupric superoxide complexes was demonstrated by their ability to abstract hydrogen atoms from 2,6-di-*tert*-butyl-4-methoxyphenol to form the corresponding phenoxyl radical, with a measured kinetic isotope effect (KIE) value of 4.6. Further supporting the end-on coordination of O_2, upon treatment of the superoxide complex with [(tmpa)Cu(I)]$BArF_{20}$ ($BArF_{20}$ = $[B(C_6F_5)_4]^-$), a heteroleptic di(cupric)-1,2-

peroxide species is observed, despite the fact that these superoxides fail to form the analogous homoleptic form of this complex when treated with their P_3tren copper(I) precursor complex.

With an understanding of the properties of the P_3tren ligand and its effects on copper-dioxygen chemistry, we next attempted to use the phosphinimine arms to aid in the aerobic oxidation of C–H bonds. In Chapter 3, the catalytic dehydrogenation of indolines to indoles is described, along with kinetic studies and a proposed reaction mechanism. From these studies, we hypothesize that one of the phosphinimine arms binds indoline through a hydrogen-bonding interaction with the N-H bond of the substrate. Subsequent O_2 binding leads to a cupric superoxide that undergoes rate-limiting activation of the α-C-H bond of indoline. In addition to the kinetic studies, experimental evidence is provided for the hydrogen-bonding interaction between indoline and a phosphinimine arm of the ligand, and it was found that the end-on superoxide described in Chapter 2 is capable of dehydrogenating indoline with similar kinetic parameters to room temperature indoline dehydrogenation.

With evidence for the importance of metal ligand cooperativity to the dehydrogenation of indoline by the (P_3tren)Cu/O_2 system, we pursued the aerobic oxidation of alcohols. In Chapter 4, the oxidation of benzyl alcohols, saturated alcohols, and phenol by the (P_3tren)Cu/O_2 system is described. It was found that the (P_3tren)Cu/O_2 system is one of only three copper systems reported thus far that can perform benzyl alcohol oxidation without the addition of bases or reagents that perform hydrogen atom

abstraction. This highlights the utility of the P_3tren ligand toward reactions involving metal-ligand cooperativity.

Finally, Chapter 5 describes a series of palladium complexes that catalyze the cross-coupling of aryl Grignard reagents with a wide array of electronically and structurally diverse fluoroarenes, including unactivated aryl fluorides. The experimental work described in this chapter was performed in the laboratories of Prof. Patrick Walsh (Univ. of Penn.). The Walsh team used high-throughput screening of various phosphine donors to identify a class of monodentate phosphine ligands with two cyclohexyl groups and one biphenyl-type group that was able to provide high catalyst activity. Experimental (Walsh) and computational (Tomson) investigations into the mechanism support the view that while a standard Kumada-type cross-coupling pathway is preferred for the activation of Ar–Cl electrophiles by this system at low Grignard to electrophile ratios ($\leq$ 1:1), a heterobimetallic mechanism predominates during Ar–F and Ar–Cl activation at higher Grignard to electrophile ratios (i.e. 2.5:1). The transition state for heterobimetallic activation of Ar–X bonds was proposed to involve simultaneous Pd backbonding to the arene and Lewis acid activation of the halide by Mg to create a low-energy transition state for oxidative addition. The insights gained from this computational study led to the development of a new phosphine ligand design that was shown to be similarly competent for Ar–F bond activation.

1.6 References

1. (a) Wang, W.; Li, N.; Li, G.; Li, S.; Wang, W.; Wang, A.; Cong, Y.; Wang, X.; Zhang, T. *ACS Sustainable Chem. Eng.* **2017**, 52, 1812. (b) Lanzafame, P.; Abate, S.; Ampelli, C.; Genovese, C.; Ampelli, C., Genovese, C.; Passalacqua, R.; Centi, G.; Perathoner *Chem. Sus. Chem* **2017**, *10*, 4409. (c) Zhoe, F.; Azofra, L. M.; Ali, M.; Kar, M.; Simonov, A. N.; McDonnell-Worth, C.; Sun, C.; Zhang, X.; MacFarlane, D. *Energy Environ. Sci.* **2017**, 10, 2516. (d). Andersen, S. Z.; Colic, V.; Yang, S.; Schwalbe, J. A.; Nielander, A. C.; McEnaney, J. M.; Enemark-Rasmuseen, K.; Baker, J. G.; Singh, A. R.; Rohr, B. A.; Statt, M. J.; Blair, S. J.; Mezzavilla, S.; Kibsgaard, J.; Vesborg, P. C.; Cargnello, M.; Bent, S. F.; Jaramillo, T. F.; Stephens, I. E. L.; Norskov, J. K.; Chorkendorff, I. *Nature* **2019**, 570, 504.

2. (a) Besson, M.; Gallezot, P.; Pinel, C. *Chem. Rev.* **2014**, 114, 3, 1827 (b) Straathof, A. J. J. *Chem. Rev.* **2014**, 114, 3, 1871. (c) Khoo, H. H.; Wong, L. L.; Tan, J.; Isoni, V.; Sharratt, P. *Resour. Conserv. Recy.* **2015**, *95*, 174.

3. (a) Liu, L.; Corma, A. *Chem. Rev.* **2018**, 118, 10, 4981. (b) Higashi, T.; Kusumoto, S.; Nozaki, K. *Chem. Rev.* **2019**, *in press*.

4. BP Statistical Review of World Energy **2019**

5. Smil, V. *Energy Transitions: History, Requirements, Prospects*; Praeger, **2010**.

6. "Catalyst". *IUPAC Compendium of Chemical Terminology*. **2009**.

7. Wodrich, M. D.; Hu, X. *Nature Reviews Chemistry* **2017**, 2, 0099, 1.

8. Khusnutdinova, J. R.; Milstein, D. Angew. Chem. Int. Ed. **2015**, 54, 12236.

9. (a) Rauchfuss, T. B. *Acc. Chem. Res.* 2015, 48, 7, 2107. (b) Chang, M.; Jesse, K. A.; Filatov, A. S.; Anderson, J. S. *Chem. Sci.* 2019, 10, 1360. (c) Alig, L.; Fritz, M.; Schneider, S. Chem. Rev. 2019, 119, 2681. (d) Verhoeven, D. G. A.; Moret, M. *Dalton Trans.* **2016** 45, 15762.

10. Gunanathan, C.; Milstein, D. *Acc. Chem. Res.* **2011**, 44, 8, 588.

11. (a)Peters, J. W.; Schut, G. J.; Boyd, E. S., Mulder, D. W.; Shepard, E. M.; Broderick, J. B.; King, P. W.; Adams, M. W. W. Biochimica et Biophysica Acta **2015**, 1853, 1350. (b) Winkler, M.; Senger, M.; Duan, J.; Esselborn, J.; Wittkamp, F.; Hofmann, E.; Apfel, U. Stripp, S. T.; Happe, T. *Nature Communications* **2017**, 8, 16115, 1. (c) Mulder, D. W.; Shepard, E. M.; Meuser, J. E.; Joshi, N.; King, P. W.; Posewitz, M. C.; Broderick, J. B.; Peters, J. W. *Structure* **2011**, 19, 8, 1038.

12. (a) Kendall, A. J.; Johnson, S. I.; Bullock, R. M.; Mock, M. T. *J. Am. Chem. Soc.* **2018**, 140, 7, 2528. (b) Kumar, N.; Darmon, J. M.; Weiss, C. J.; Helm, M. L.; Raugei, S.; Bullock, R. M. *Organometallics* **2019**, 38, 6, 1391. (c) Prokopchuk, D. E.; Chambers, G. M.; Walter, E. D.; Mock, M. T.; Bullock, R. M. *J. Am. Chem. Soc.* **2019**, 141, 1871 (d) Hulley, E. B.; Welch, K. D.; Appel, A. M.; DuBois, D. L.; Bullock, R. M. *J. Am. Chem. Soc.* **2013**, 135, 11736

13. Chakraborty, S.; Dai, H.; Bhattacharya, P.; Fairweather, N. T.; Gibson, M. S.; Krause, J. A.; Guan, H. *J. Am. Chem. Soc.* **2014**, 136, 7869.

14. (a) Del Castillo, T. J.; Thompson, N. B.; Peters, J. C. *J. Am. Chem. Soc.* **2016**, 138, 5341. (b) Fong, H.; Moret, M.; Lee, Y.; Peters, J. C. *Organometallics* **2013**, 32, 3053.

15. (a) Noyori, R.; Ohkuma, T. *Angew. Chem., Int. Ed.* **2001**, 40, 40. (b) Doucet, H.; Ohkuma, T.; Murata, K.; Yokozawa, T.; Kozawa, M.; Katayama, E.; England, A. F.; Ikariya, T.; Noyori, R. *Angew. Chem., Int. Ed.* **1998**, 37, 1703. (c) Hashiguchi, S.; Fujii, A.; Takehara, J.; Ikariya, T.; Noyori, R. *J. Am. Chem. Soc.* **1995**, 117, 7562. 20 (d) Casey, C. P.; Singer, S. W.; Powell, D. R.; Hayashi, R. K.; Kavana, M. *J. Am. Chem. Soc.* **2001**, 123, 1090; (e) Casey, C. P.; Johnson, J. B.; Singer, S. W.; Cui, Q. *J. Am. Chem. Soc.* **2005**, 127, 3100. (f) Wilson, R.; Chu, W.-Y.; Rauchfuss, T. B. *Inorg. Chem.* **2015**, 54, 5596.

16. (a) Bouwkamp, M. W.; Lobkovsky, E.; Chirik, P. J. *J. Am. Chem. Soc.* **2005**, 127, 9660; (b) Trovitch, R. J.; Lobkovsky, E.; Chirik, P. J. *Inorg. Chem.* **2006**, 45, 7252; (c) Russell, S. K.; Milsmann, C.; Lobkovsky, E.; Weyhermuller, T.; Chirik, P. J. *Inorg. Chem.* **2011**, 50, 3159; (d) Hoyt, J. M.; Sylvester, K. T.; Semproni, S. P.; Chirik, P. J. *J. Am. Chem. Soc.* **2013**, 135, 4862; (e) Hoyt, J. M.; Schmidt, V. A.; Tondreau, A. M.; Chirik, P. J. *Science* **2015**, 349, 960; (f) Bart, S. C.; Chłopek, K.; Bill, E.; Bouwkamp, M. W.; Lobkovsky, E.; Neese, F.; Wieghardt, K.; Chirik, P. J. *J. Am. Chem. Soc.* **2006**, 128, 13901; (g) Darmon, J. M.; Stieber, S. C. E.; Sylvester, K. T.; Fernández, I.; Lobkovsky, E.; Semproni, S. P.; Bill, E.; Wieghardt, K.; DeBeer, S.; Chirik, P. J. *J. Am. Chem. Soc.* **2012**, 134, 17125. (h) Monfette, S.; Turner, Z. R.; Semproni, S. P.; Chirik, P. J. *J. Am. Chem. Soc.* **2012**, 134, 4561. (i) Obligacion, J. V.; Chirik, P. J. *Org. Lett.* **2013**, 15, 2680; (j) Palmer, W. N.; Diao, T.; Pappas, I.; Chirik, P. J. *ACS Catal.* **2015**, 5, 622. (k)

Schaefer, B. A.; Margulieux, G. W.; Small, B. L.; Chirik, P. J. *Organometallics* **2015**, 34, 1307. (l) Kaim, W. *Inorg. Chem.* **2011**, 50, 9752.

17. (a) Himo, F.; Siegbahn, P. E. M. *Chem. Rev*. **2003**, 103, 2421. (b) Parrikka, K.; Master, E.; Tenkanen, M. *J. Mol. Catal. B Enzym.* **2015**, 120, 47. (c) Whittaker,J. W. *Arch Biochem Biophys.* **2005**, 433(1), 227. (d) Himo, F.; Eriksson, L. A.; Maseras, F.; Siegbahn, P. E. M. *J. Am. Chem. Soc.* **2000**, 122, 33, 8031. (e) Firbank, S. J.; Rogers, M. S.; Wilmot, C. M.; Dooley, D. M.; Halcrow, M. A.; Knowles, P. F.; McPherson, M. J.; Phillips, S. E. V. *P. Natl. Acad. Sci. USA* **2001**, 98 (23), 12932.

18. (a) Chaudhuri, P.; Hess, M.; Flörke, U.; Wieghardt, K. *Angew. Chem., Int. Ed.* **1998**, 37, 2217. (b) Chaudhuri, P.; Hess, M.; Weyhermuller, T.; Wieghardt, K. *Angew. Chem. Int. Ed.* **1999**, 38 (8), 1095. (c) Chaudhuri, P.; Hess, M.; Muller, J.; Hildenbrand, K.; Bill, E.; Weyhermuller, T.; Wieghardt, K. *J. Am. Chem. Soc.* **1999**, 121 (41), 9599

19. (a) Rodriguez, M. M.; Eckhard, B.; Brennessel, W. W.; Holland, P. L. *Science* **2011**, 334, 780. (b) McWilliams, S. F.; Holland, P. L. *Acc. Chem. Res.* **2015**, 48, 2059.

20. Horn, B.; Pfirrmann, S.; Limberg, C.; Herwig, C.; Braun, B.; Mebs, S.; Metzinger, R. *Z. Anorg. Allg. Chem.* **2011**, 637, 1169.

21. (a) Yoshikai, N.; Iida, R.; Nakamura, E. *Adv. Synth. Catal*. **2008**, 350, 1063. (b) Nakamura, E.; Mori, S. *Angew. Chem., Int. Ed.* **2000**, 39, 3750–3771. (c) Yoshikai, N.; Nakamura, E. *J. Am. Chem. Soc.* **2004**, 126, 12264. (d) Rodriguez, M. M.; Bill, E.; Brennessel, W. W.; Holland, P. L. *Science* **2011**, 334, 780.

22. Yoshikai, N.; Matsuda, H.; Nakamura, E. *J. Am. Chem. Soc.* **2009**, 131, 9590.

27. van der Veen, L. A.; Keeven, P. H.; Schoemaker, G. C.; Reek, J. N. H.; Kamer, P. C. J.; van Leeuwen, P. W. N. M.; Lutz, M.; Spek, A. L. *Organometallics* **2000**, 19, 872.

24. (a) Zhang, J.; Bellomo, A.; Trongsiriwat, N.; Jia, T.; Carroll, P. J.; Dreher, S. D.; Tudge, M. T.; Yin, H.; Robinson, J. R.; Schelter, E. J.; Walsh, P. J. *J. Am. Chem. Soc.* **2014**, 136, 6276. (b) Zhang, J.; Sha, S.; Bellomo, A.; Trongsiriwat, N.; Gao, F.; Tomson, N. C.; Walsh, P. J.; *J. Am. Chem. Soc.* **2016**, 138, 4260. (c) Sha, S.-C.; Tcyrulnikov, S.; Li, M.; Fu, Y.; Kozlowski, M. C.; Walsh, P. J.; Hu, B. *J. Am. Chem. Soc.* **2018**, 140, 12415. (d) Jiang, H.; Sha, S.-C.; Jeong, S. A.; Manor, B. C.; Walsh, P. J. *Org. Lett.* **2019**, 21, 1735.

Chapter 2: Synthesis of Highly Reduced Copper Centers through Tripodal Phosphinimine Frameworks and Subsequent Studies of Novel End-On Copper(II) Superoxides*

2.1 Introduction

Tuning transition metal redox properties is of importance in areas as far-reaching as enzymatic activity and industrial catalysis. While a wide array of transition metals are used for redox-dependent processes, copper is responsible for several chemical transformations relevant to both nature and society.[1-4] In biology, copper sites within metalloenzymes are observed to participate in a wide variety of redox processes, including simple electron transfer events as well as NO_2^-, N_2O, and O_2 reduction chemistry.[5] Cupredoxins (blue copper proteins) are a well-studied subset of electron transfer reagents in biology. These enzymes have evolved to tune their redox potentials over a 700 mV range, from around 100 mv to 800 mv vs. NHE, through alteration of the number of hydrogen bonds in the secondary coordination sphere, thereby allowing the enzymes to match oxidizing power to specific organic substrates.[6] On the other hand, copper-based enzymes participating in the activation and reduction of O_2 rely on a proper arrangement of the primary coordination sphere in order for the redox potential to be "tuned down," such that O_2 can easily oxidize the copper center, and the resulting cupric superoxide ($Cu^{II}–O_2^{\bullet-}$) can be subsequently stabilized with respect to O_2 loss.[5]

* Portions of this chapter are reproduced from a soon to be submitted manuscript from authors: McCollom, S. P.; Weberg; A. W.; Gau, M. R.; Carrol, P. C.; Tomson, N. C.; please note kinetics studies and crystal structures of the PMe_3 ligand derivatives were conducted by Alex Weberg.

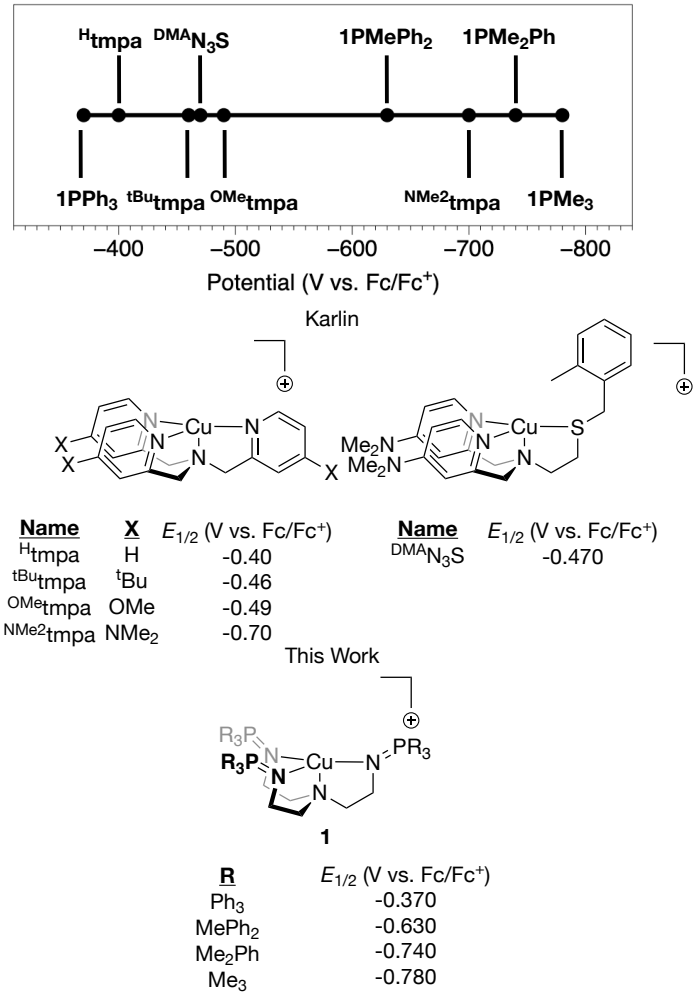

Figure 2.1 Literature examples of biomimetic copper complexes demonstrating tunable redox potentials through functional group substitution in the secondary coordination sphere.

Biomimetic studies have sought to similarly tune the redox properties of metal centers through alteration of the secondary coordination sphere,[7-9] although few studies have focused on copper.[10,11] Recently, the Tolman group reported cupric hydroxide compounds bound by NNN pincer-type bis(carboxamide)pyridine ligands, wherein charged residues were incorporated at the *para* position on the aryl ring of the

carboxamide arms.[10] Concordantly, a shift of 300 mV, in the formally Cu(II/III) redox couple, was observed upon switching between substitution of a cationic group ($-NMe_3^+$) and an anionic group ($-SO_3^-$). Earlier, Karlin and coworkers reported a series of copper(I)-tmpa complexes (tmpa = *tris*(2-pyridylmethyl)amine), wherein a systematic adjustment of the Cu(I/II) redox couple was attained through substitutions at the *para* position of the tmpa pyridyl rings[12] (Figure 2.1). Introducing electron-donating groups at these positions resulted in a shift of the Cu(I/II) couple to more negative potentials, ultimately attaining a remarkably reducing redox potential of -0.70 V (vs. Fc/Fc^+) for the dimethylamino-substituted tmpa derivative. In addition to the chemistry of this species with O_2, this copper complex is notable in that it was recently shown by Matyjaszewski and coworkers to be the most active atom transfer radical polymerization (ATRP) catalyst reported to date, as a direct consequence of its highly negative Cu(I/II) redox couple.[13,14]

A direct correlation has been shown between the reducing power of tmpa-copper(I) complexes and the thermal stability of the corresponding cupric superoxide complexes that form on addition of O_2.[15,16] Accordingly, the same dimethylamino-substituted tmpa-copper(I) complex was found to form the most thermally stable cupric superoxide ($t_{1/2}$ = ~4 h at -85 °C) among the series of tmpa derivatives. In-depth stopped-flow kinetic measurements in THF and EtCN showed that the decomposition mechanisms of these complexes proceed through loss of O_2 and formation of di(cupric)-μ-peroxide complexes (Figure 2.2). It has been proposed that the thermal stability of the cupric superoxides is related to the Cu(I/II) redox potential; *i.e.* a more negative potential shifts the equilibrium in equation 1 (Figure 2.2) to favor O_2 binding, thereby minimizing

the availability of Cu(I) in solution and slowing the rate of the reaction to form the di(cupric)peroxide complex (Figure 2.2, Equation 2).

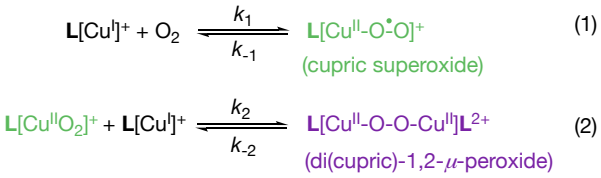

Figure 2.2 Proposed kinetic scheme (Karlin[15], Schindler[16]) for biomimetic Cu/O_2 reactions.

Herein, we report a new class of copper complexes bound by a series of novel tren-based tris(phosphinimine) ligands (P_3tren; tren = tri(2-aminoethyl)amine). The P_3tren ligands were designed to induce virtually identical geometries with those observed in TMG_3tren complexes, but with a greater degree of sigma donor ability of the phosphiniminato nitrogens, stemming from worse π overlap between nitrogen and phosphorous, resulting in enhanced anionic localization at the donor atom. The P_3tren ligands further offer a convenient means for varying the steric profile of the secondary coordination sphere of the ligated metal ion. As described below, a series of P_3tren ligands has been successfully bound to Cu(I) ions and used to dramatically alter the electrochemistry and O_2-binding reactivity of the metal ion. Spectroscopic and kinetic studies support the view that the P_3tren ligand offers unprecedented stability to end-on coordinated cupric superoxides.

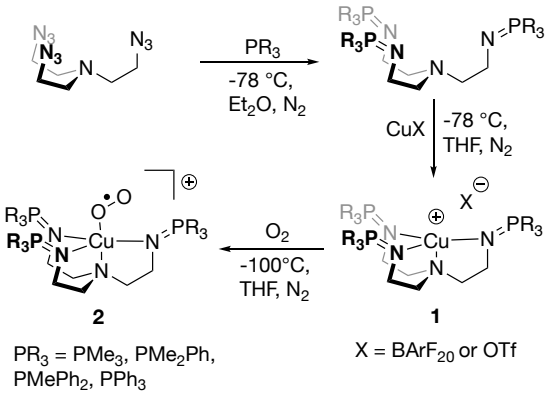

Scheme 2.1 Synthesis of Cu(I) and CuO_2 compounds.

2.2 Results and Discussion

2.2.1 Synthesis of Novel tren-based tris(phosphiniminato) ligands and Cu(I) Complexes

A series of novel tren-based tris(phosphiniminato) ligands (P_3tren) have been prepared via the Staudinger reaction depicted in Scheme 2.1, where PR_3 = PMe_3, PMe_2Ph, $PMePh_2$, and PPh_3. When bound to metals, these ligands impose similar geometries as tmpa, but with different ligand field effects. Support for the assignment of enhanced anionic character to the phosphinimine nitrogens is provided by both the pK_a values of protonated phosphinimines and natural bond order (NBO) analysis of simplified phosphinimines.

Phopshinimines are often used as strong neutral organic bases due their commercial availability and because their p*K*a values can range from 26 to 50 allowing for a multitude of uses.[17,18] We measured *N*-adamantyl-trimethyliminophosphorane to have a pK_a of 26.2 through titration of the base with DBU-H^+. The high basicity (on par

with, or stronger than, the strong neutral bases DBU, TMG, and TBD) can be attributed to increased anionic character at the nitrogen atom.[19] Dyson and coworkers have shown that the natural population analysis (NPA) charges from NBO calculations of simple phosphinimines support an ionic bonding model between nitrogen and phosphorous.[20] Using a modified basis set that reproduces Dyson's results, *N*-methyl-trimethyliminophosphorane ($MeN{=}PMe_3$) was calculated to have a charge of -1.14 at nitrogen, while the PMe_2Ph, $PMePh_2$, and PPh_3 derivatives have charges of -1.11 at nitrogen (Figure 2.3). The NPA charge value is similar for all four simplified phosphinimines, supporting an ionic bonding model with build-up of anionic charge on the nitrogen atom.

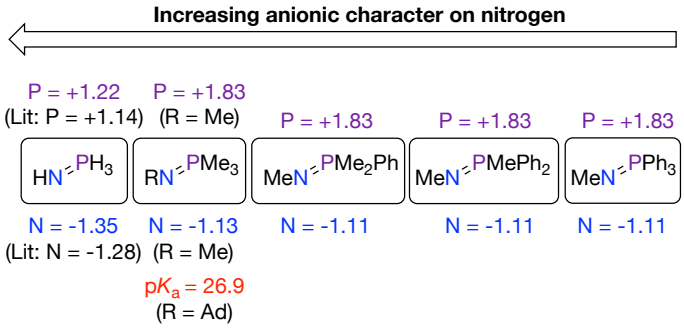

Figure 2.3 Zwitterionic character of phosphinimies and pentamethylguanidine shown through natural population analysis charge (blue/purple), and pK_a values in MeCN (red).

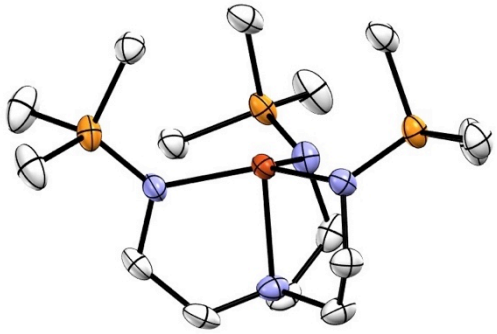

Figure 2.4 Molecular structure of 1-PMe_3 with thermal ellipsoids set to 50%. Hydrogen atoms and $B(C_6F_5)_4^-$ counteranion omitted for clarity Crystals grown from Et_2O at -35 °C.

The series of copper(I) complexes, **1-(PMe_3, PMe_2Ph, $PMePh_2$, PPh_3)**, were synthesized in THF at room temperature by combining the P_3tren ligand with 1.0 equiv of $CuBArF_{20}$•4MeCN ($BArF_{20}$ = $B(C_6F_5)_4^-$) or, in the case of **1-PPh_3**, 0.5 equiv of $[CuOTf]_2$•C_6H_6 (Scheme 2.1). NMR spectroscopic data of all complexes in MeCN-d_3 reveal C_{3v} symmetry in the NMR timescale. Notably, all complexes share a triplet and a doublet of triplets near 3 ppm in their ^{1}H NMR spectra for the two signals from the ethylene backbone, and they feature a single $^{31}P\{^1H\}$ signal in the range of 20-25 ppm that shifts upfield with an increasing number of phenyl groups on phosphorus. The NMR data further give no indication that the 18 e^- complexes **1** bind coordinating solvents, like THF, MeCN or EtCN. This view is supported by the crystallographic data for these compounds, which revealed the presence of trigonal pyramidal metal centers with an open coordination site located *trans* to the amino nitrogen of the ligand. That said, the varying steric profile of the secondary coordination sphere complicates investigation into

the steric versus electronic role that the ligand plays in preventing axial coordination. However, we note that the most reducing X-tmpa-Cu(I) analogue (X = Me_2N, $E_{1/2}$ = -0.70 V) fails to bind solvent, while the less reducing analogues (X = OMe, H, Me, ^{t}Bu; $E_{1/2}$ = *ca*. -0.45 V) readily bind nitriles to form trigonal bipyramidal complexes. The similarity in the secondary coordination spheres about the X-tmpa-Cu(I) complexes suggest that an electronic effect is responsible for controlling the propensity of Cu(I) complexes in this coordination sphere to bind nitriles.

2.2.2 Cyclic Voltammetry

The electrochemical behavior of the Cu(I) complexes was analyzed using cyclic voltammetry (CV) under a dry, N_2 atmosphere in ^{i}PrCN (IBN). As shown in Figure 2.5, **1-(PMe_3, PMe_2Ph, $PMePh_2$, PPh_3)** all demonstrate *quasi*-reversible oxidations, with $E_{1/2}$ values of -780, -740, -630, and -370 mV (vs. Fc/Fc^+) respectively. The redox potentials for these complexes are extremely reducing for Cu(I) centers, highlighting the effects of enhanced anionic charge at the phosphinimine nitrogen atoms. Furthermore, a trend is observed in which the incorporation of more electron-donating groups at phosphorous yields a more anionic phosphinimine nitrogen donor, correlating with a more reducing copper center (as indicated by the measured redox potentials). To the best of our knowledge, **1-PMe_3** has the most negative Cu(I)/Cu(II) redox potential for a trigonal pyramidal copper complex that has been reported to date.

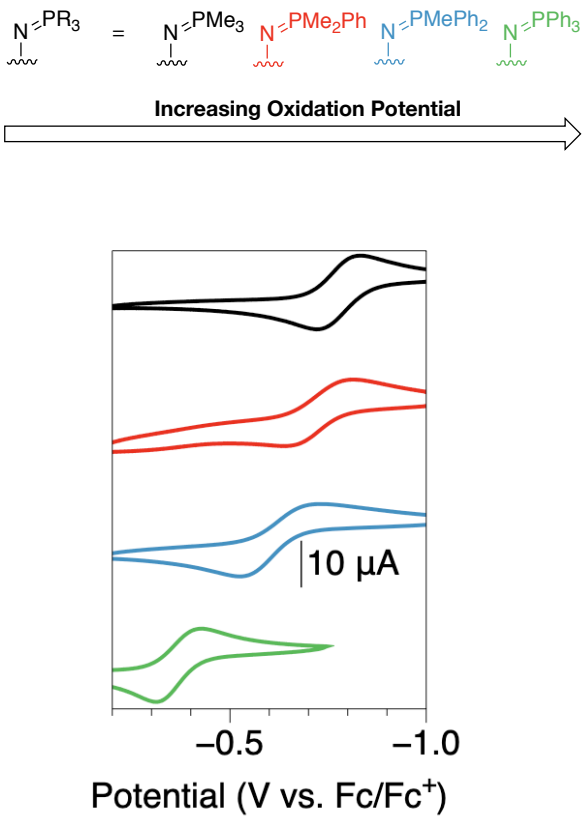

Figure 2.5 CV traces of 1-PMe_3 (black, $E_{1/2}$ = -780 mV; ΔE_p = 68 mV), 1-PMe_2Ph (red, $E_{1/2}$ = -740 mV; ΔE_p = 116 mV), 1-$PMePh_2$ (blue, $E_{1/2}$ = -630 mV; ΔE_p = 187 mV), and 1-PPh_3 (green, $E_{1/2}$ = -370 mV; ΔE_p = 66 mV) Conditions: 200 mV/s, 100 mM NBu_4PF_6, 1 mM analyte, IBN, Pt electrode.

Consistent with the facile access to Cu(II) implied by these electrochemical data, chemical oxidations of **1-PMe_3** with trityl chloride and silver triflate provided Cu(II) complexes supported by P_3tren. Single crystals of the resulting dark green oxidation products were grown from diethyl ether at -78 °C. Crystallographic analysis revealed trigonal bipyramidal Cu(II) centers containing either a bound chloride (**3PMe_3-Cl**) or triflate (**3PMe_3-OTf**) ion. In **3-Cl**, a modest shortening of the Cu-N_{ax} bond by 0.07 Å was

observed, along with an elongation of one Cu-N_{eq} by 0.12 Å compared to **1-PMe_3**; all other bonds and angles remained similar. A similar trend is seen in differences between Cu(I) and Cu(II) tmpa complexes, where the Cu-N_{ax} shortens in Cu(II) complexes and one Cu-N_{eq} bond elongates in Cu(II) complexes.[21-23] On average all bond lengths are shorter by a minimum of 0.08 Å in tmpa complexes.

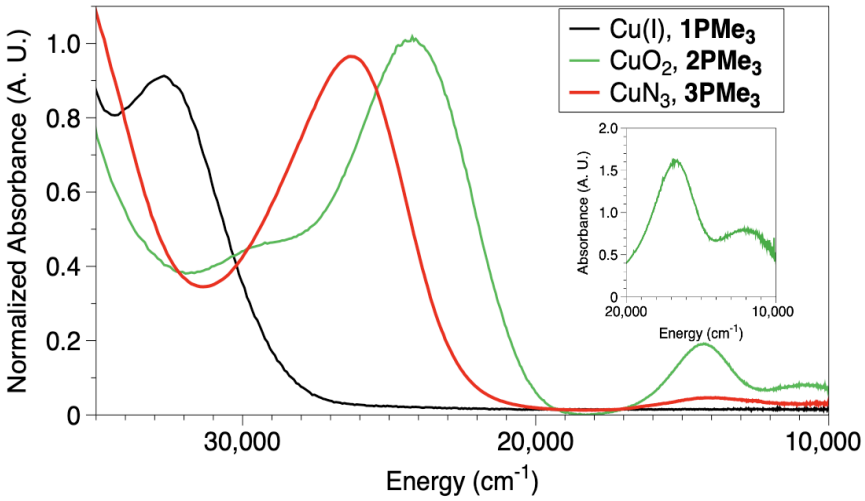

Figure 2.6 UV/vis spectrum of compounds 1-PMe_3 (-100 °C, 0.5 mM, THF, black), 2-PMe_3 (-100 °C, 0.5 mM, THF, green), and 4-PMe_3 (20 °C, 0.25 mM, MeCN, red). Absorbances normalized for differing concentrations.

2.2.3 Formation of End-On Superoxide Complexes

Treatment of pale yellow THF solutions of **1-(PMe_3, PMe_2Ph)** with excess dioxygen at -100 °C results in the rapid formation of a vivid green solution, the color of which persists at low temperature (Scheme 2.1). The low temperature (-100 °C) UV/vis spectra of these compounds display intense features at 24,200 cm^{-1} (ε = ~3,500 $M^{-1}cm^{-1}$), 14,300 cm^{-1} (ε = ~800 $M^{-1}cm^{-1}$), and 10,500 cm^{-1} (ε = ~100 $M^{-1}cm^{-1}$), characteristic of the

formation of an end-on cupric superoxide complex (Figure 2.6). All known five-coordinate end-on cupric superoxides reported in the literature display similar absorptions in the range of 22,600-26,000 cm^{-1}, with extinction coefficients between 1,000 and 3,000 $M^{-1}cm^{-1}$.[4,24] In a further effort to confirm the assignment of the proposed LMCT feature at 24,200 cm^{-1} in **2**, the cupric azide complex **4-PMe$_3$** was synthesized, wherein the azide moiety acts as a surrogate for the superoxide ligand in **2**. An overlay of the UV/vis spectra of **2-PMe$_3$** and **4-PMe$_3$** (λ_{max} = 26,000 cm^{-1}, ε = 3,145 $M^{-1}cm^{-1}$) is shown in Figure 2.3, and the LMCT energies and extinction coefficients are found to be qualitatively similar, consistent with literature reports of cupric superoxides and their cupric azide counterparts.

While **1-PMe$_3$** and **1-PMe$_2$Ph** reacted quickly with O_2 (< 20 s), **1-PMePh$_2$** and **1-PPh$_3$** behaved differently. **1-PPh$_3$** did not react with O_2, as judged by the lack of observable changes in the mixtures UV/vis trace upon addition of O_2 at -100 or 20 °C. **1-PMePh$_2$** reacted much slower with O_2 compared to the essentially instantaneous reactions observed for **1-PMe$_3$** and **1-PMe$_2$Ph**. Monitoring the absorption profile of a solution of **1-PMePh$_2$** treated with 1 atm of O_2 at -100 °C revealed that formation of **2-PMePh2** occurred a minimum of 550 times slower than for **2-PMe$_3$** and **2-PMe$_2$Ph** (see Figure S2.12). This rate was convenient for obtaining a first-order rate constant, determined to be 2.6 x 10^{-3} s^{-1}. Considering that trigonal bipyramidal copper(I) complexes with more positive Cu(I)/Cu(II) redox couples are known to form superoxides at low temperatures, we attribute the lack of formation for **1-PPh$_3$** and slow formation for **1-PMePh$_2$** to the

steric profile about the open coordination site on the Cu(I) complexes, not because of the more positive redox couples for **1-PPh$_3$** and **1-PMePh$_2$**.[15,16]

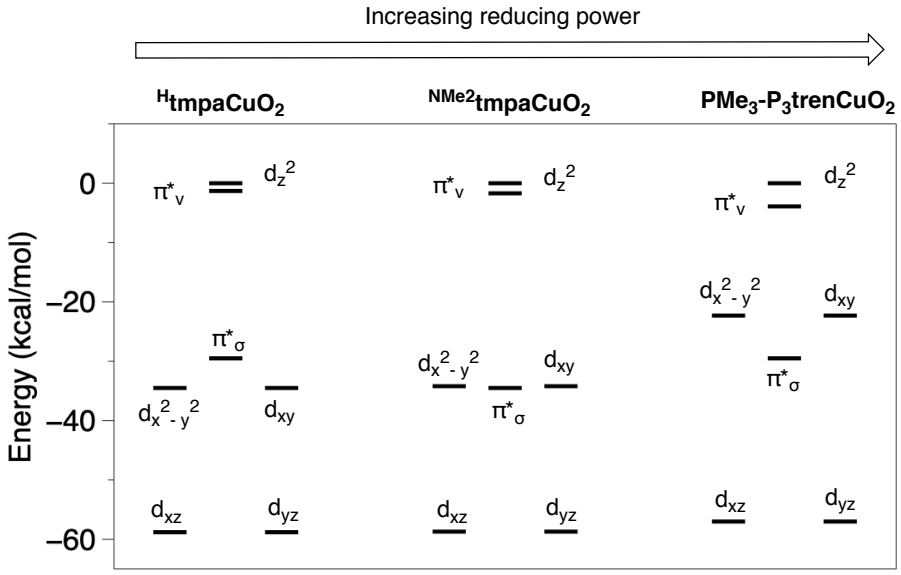

Figure 2.7 DFT calculated β (spin down) MO diagram for Cu(I) complexes. HOMO is highest shown orbital for each complex.

2.2.4 DFT Calculations

Spin unrestricted DFT geometry optimizations and TD-DFT calculations were performed on **1-(PMe$_3$, PMe$_2$Ph, PMePh$_2$, PPh$_3$)**, tmpaCu(I), ^{NMe2}tmpaCu(I), and their cupric superoxides to gain insight into the impact of the strong donor properties of P_3tren on the electronic structures of the Cu complexes.[25] Calculations on the Cu(I) series of complexes revealed a trend in ligand field splitting that correlates with the redox potential of complexes. In the most reducing complex, **1-PMe$_3$**, the $d_{x^2-y^2}/d_{xy}$ manifold is the highest occupied molecular orbital (HOMO), appearing at +6.1 kcal/mol from d_{z^2} (Figure 2.7). To lower energies, the d_{xz}/d_{yz} set are found a *ca*. -14 kcal/mol from d_{z^2}. **1-PMe$_2$Ph,**

$PMePh_2$, PPh_3 have an identical orbital ordering but with a $d_{x^2-y^2}/d_{xy}$-to-d_{z^2} gap of ~ +2 kcal/mol. For tmpaCu(I) and ^{NMe2}tmpaCu(I), d_{z^2} is the HOMO and $d_{x^2-y^2}/d_{xy}$ lie at -7.0 (tmpa) and -2.2 (^{NMe2}tmpa) kcal/mol (Figure 2.7). The increase in the relative energy of $d_{x^2-y^2}/d_{xy}$ in the (P_3tren)Cu(I) complexes may be attributed to the better σ-donor properties of P_3tren ligand. This raises the energy of the d-orbitals in the equatorial plane, resulting in more negative oxidation potentials.

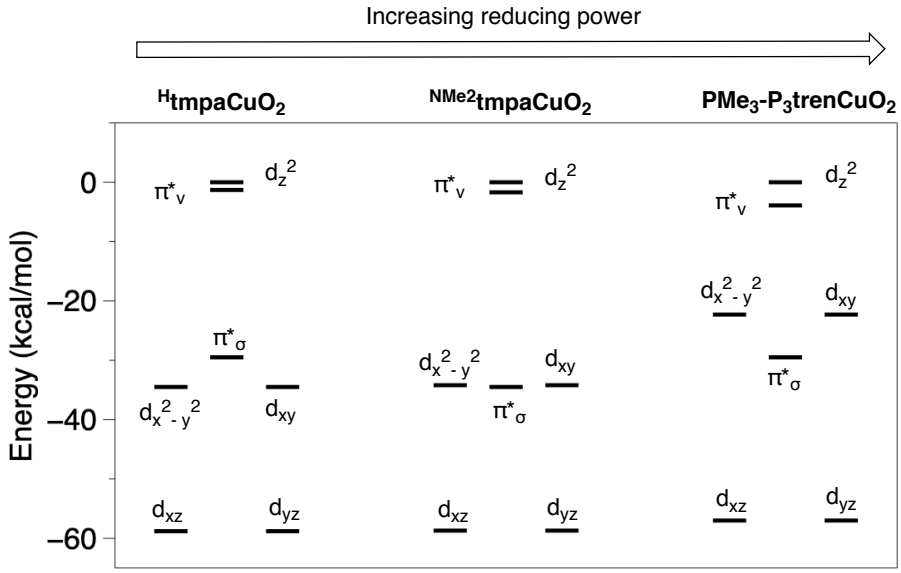

Figure 2.8 DFT calculated β (spin down) MO diagram for CuO_2 complexes. HOMO for 1-PMe_3 and ^{NME2}tmpa is the $d_{x^2-y^2}$. HOMO for tmpa is π^*_σ.

Examination of the orbital energies and orbital ordering of the cupric superoxides reveals similar trends. An energy level diagram of the computed orbitals of **2-PMe_3** can be seen in Figure 2.9. Again, in the (P_3tren)Cu complexes **2-(PMe_3, PMe_2Ph, $PMePh_2$, PPh_3)** the $d_{x^2-y^2}$ and d_{xy} are the HOMO while in the tmpa complexes the π^*_σ is the HOMO with the $d_{x^2-y^2}$ and d_{xy} being the next highest in energy (Figure 2.8). This is again

consistent with the hypothesis that the P_3tren ligand is a stronger σ-donor than tmpa.

Table 2.1 TDDFT calculated transitions of CuO_2 complexes.

Complex	Transition	Energy (cm^{-1})
1-PMe$_3$	$\pi^*_\sigma \rightarrow d_z^2$	23,250
1-PMe$_3$	$d_{xy}/d_{xz} \rightarrow d_z^2$	19,900
1-PMe$_3$	$d_{x^2-y^2}/d_{xy} \rightarrow d_z^2$	8,500
^{NMe2}tmpa	$\pi^*_\sigma \rightarrow d_z^2$	20,000
^{NMe2}tmpa	$d_{xy}/d_{xz} \rightarrow d_z^2$	19,000
^{NMe2}tmpa	$d_{x^2-y^2}/d_{xy} \rightarrow d_z^2$	12,700
^{H}tmpa	$\pi^*_\sigma \rightarrow d_z^2$	23,000
^{H}tmpa	$d_{xy}/d_{xz} \rightarrow d_z^2$	20,500
^{H}tmpa	$d_{x^2-y^2}/d_{xy} \rightarrow d_z^2$	14,250

TD-DFT calculations on the superoxides complexes match well with experimental data (Table 2.1 and experimental). Notably, in all complexes, an intense LMCT for the π^*_σ to d_z^2 is calculated to lie between 20,000 and 25,000 cm^{-1}. To lower energies, transitions are found for $d_{xz}/d_{yz} \rightarrow d_z^2$ in the range of 15,500-18,000 cm^{-1}. A final d→d transition for $d_{x^2-y^2}/d_{xy} \rightarrow d_z^2$ is calculated for **2-(PMe$_3$, PMe$_2$Ph, PMePh$_2$, PPh$_3$)** to occur at ~8,500 cm^{-1}, while superoxides complexes of ^{NMe2}tmpa and tmpa are predicted to exhibit transitions at 12,700 cm^{-1} and 14,000 cm^{-1} respectively. Experimental UV/vis data match these TD-DFT trends; **2-PMe$_3$** and **2-PMe$_2$Ph** exhibit absorptions at ~10,500 cm^{-1}, whereas the lowest energy feature for ^{NMe2}tmpaCuO_2 occurs at 13,000 cm^{-1}.[29,30] These data again support the view that the $d_{x^2-y^2}/d_{xy}$ set are raised in energy by the P_3tren

ligand set due to the enhanced σ-donating ability of the phosphinimine ligands.

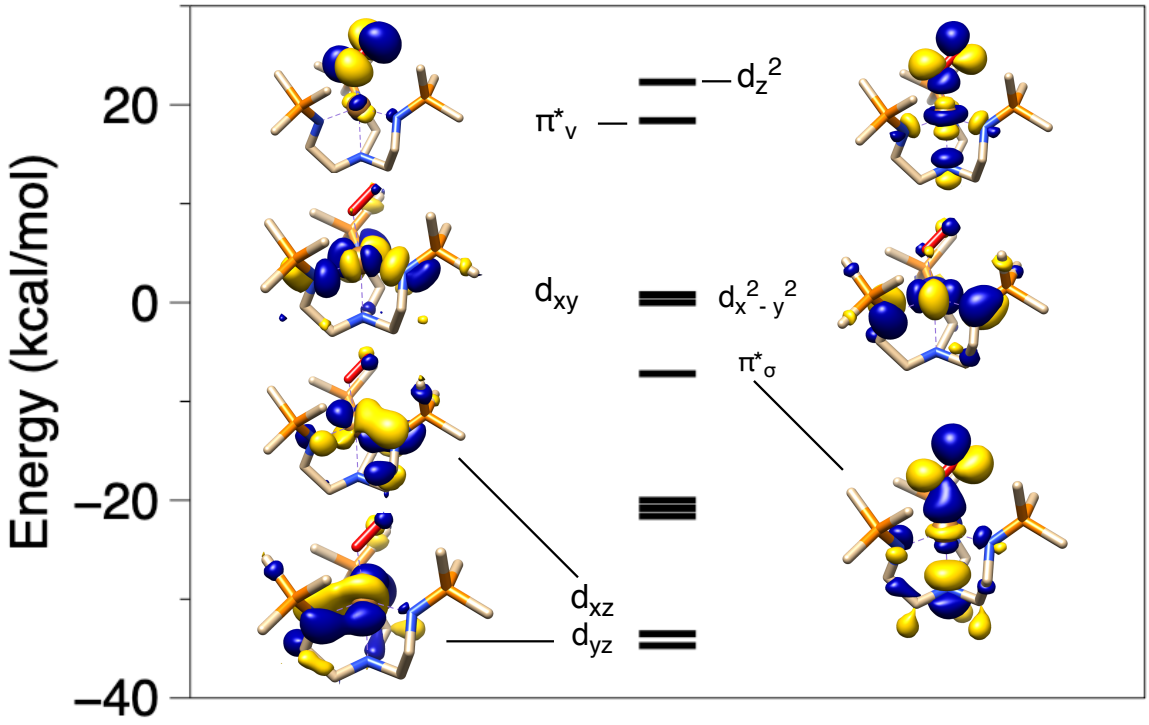

Figure 2.9 DFT calculated β (spin down) MO diagram for 1-PMe_3.

2.2.5 Proton-Coupled Electron Transfer (PCET) Reactivity of 2

PCET from organic substrates containing C-H, O-H, N-H, or S-H bonds is a typical reaction paradigm for superoxides.[24] Indeed, several cupric superoxides have been shown to perform PCET from 2,6-di-*tert*-butyl-4-methoxyphenol to form the corresponding phenoxyl radical and 2,6-di-*tert*-butyl-1,4-benzoquinone in various ratios.[27] The Karlin group has performed detailed kinetic studies to elucidate the mechanism of this reaction.[5] They proposed that after PCET between the substrate and

one equiv of the cupric superoxide, a second equiv of cupric superoxide attacks the *para* position of the phenoxyl radical. Water then attacks the phenoxyl/superoxide complex to form a cupric hydroxide and a hydroxide at the *para* position of the phenol, which then loses methanol and forms 2,6-di-*tert*-butyl-1,4-benzoquinone.

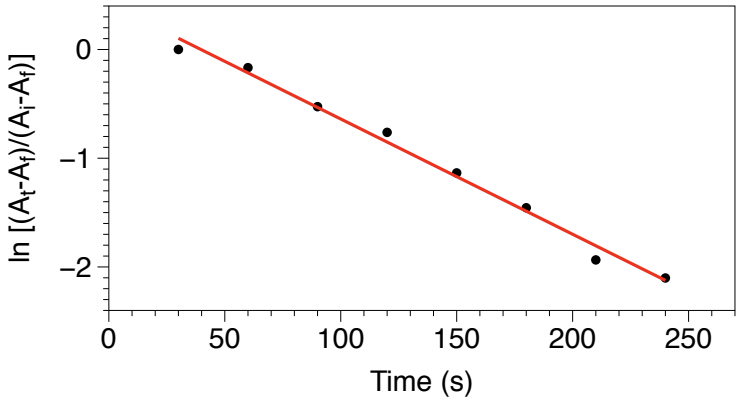

(a)

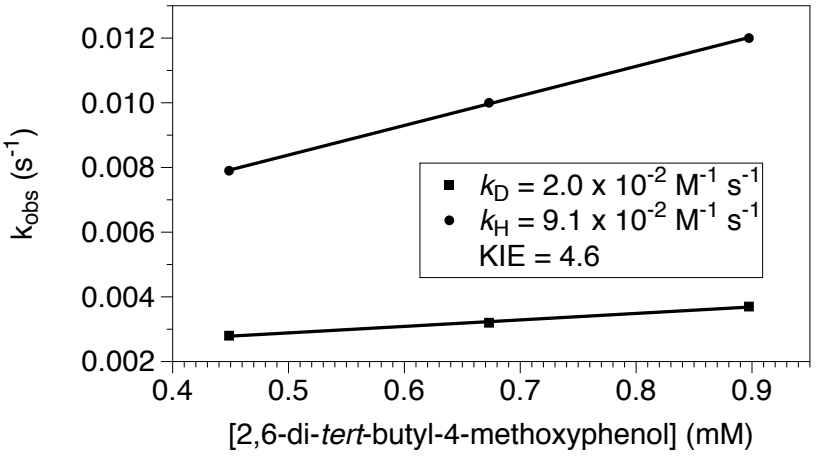

(b)

Figure 2.10 (a) Pseudo-first-order plot obtained by monitoring the treatment of **2-PMe$_2$Ph** (0.52 mM) with 1.5 equiv of 2,6-di-*tert*-butyl-4-methoxyphenol in THF at 173 K. (b) Plot of k_{obs} vs. concentration of substrate to determine second-order rate constant and KIE; proteo (circles), deutero (squares).

Upon treatment of degassed solutions of either **2-PMe$_3$** or **2-PMe$_2$Ph** , that has been sparged N_2, with a precooled THF solution of 2,6-di-*tert*-butyl-4-methoxyphenol at -100 °C, the LMCT transition decays rapidly, and characteristic UV/vis features of 2,6-di-*tert*-butyl-4-methoxyphenoxyl radical are observed to form. Stirring a solution of excess **2** with 2,6-di-*tert*-butyl-4-methoxyphenol for extended periods of time (2-24 h), followed by removal of solvent *in vacuo* does not result in the formation of 2,6-di-*tert*-butyl-1,4-benzoquinone as indicated by NMR spectroscopy. The addition of water to this system results in hydrolysis of the P_3tren ligand scaffold, preventing a direct comparison with the proposed reaction mechanism described above.

Evidence for a PCET process as the mechanism for 2,6-di-*tert*-butyl-4-methoxyphenoxyl radical formation by **2** was obtained through kinetic isotope experiments between **2** and both proteo (-OH) and deutero (-OD) 2,6-di-*tert*-butyl-4-methoxyphenol and comparison to literature. These kinetic experiments were run under pseudo-first order conditions at -100 °C by monitoring the decay of the d-d bands at 14,300 cm^{-1}.[28] These data fit first order kinetics with respect to **2**, providing a series of rate constants that were linear with respect to substrate concentration (see experimental).

Second order rate constants for both the proteo and deutero analogues were obtained, allowing for a determination of a kinetic isotope effect (KIE) of 3.0 for the reaction with **2-PMe$_3$** and 4.6 for the reaction with **2-PMe$_2$Ph** (Figure 2.10 shows data for **2-PMe$_2$Ph**, see experimental for data corresponding to **2-PMe$_3$**). This magnitude of KIE is consistent with either a PCET or a proton transfer event being operative in the rate determining step for the conversion of phenol to phenoxyl radical in the presence of **2**. These KIE values are similar to KIE values reported for other cupric superoxides, which were further shown to undergo asynchronous PCET processes, in which the electron transfer partially precedes proton transfer.[5]

2.2.6 Formation of heteroleptic di(cupric)peroxide (5)

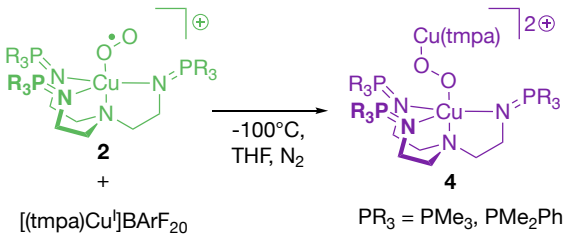

Scheme 2.2 Synthesis of heteroleptic trans-1,2-dicupricperoxide species.

For tmpa-ligated cupric superoxides, thermal decomposition has been shown to proceed through the formation of di(cupric)-1,2-μ-peroxide complexes, which display characteristic features in the visible spectrum at ~20,000 and ~16,666 cm^{-1}. Upon monitoring the thermal decomposition of **2-(PMe$_3$, PMe$_2$Ph)** at various temperatures (-40 to -120 °C), no such complex is ever observed to form, suggesting that such a species is either transient, or unable to form at all. Even upon addition of **1-(PMe$_3$,**

PMe_2Ph) to a degassed solution of **2-(PMe_3, PMe_2Ph)** at -100 °C, there are no new absorbance features as observed via UV-vis spectroscopy. However, addition of an alternative copper(I) complex, [tmpa-Cu]$BArF_{20}$, to a degassed solution of **2-(PMe_3, PMe_2Ph)** at -100 °C results in the immediate loss of the LMCT feature associated with **2** (~24,200 cm^{-1}), concomitant with the growth of new features at ~20,000 cm^{-1} (ε = ~860 $M^{-1}cm^{-1}$) and ~16,666 cm^{-1} (ε = ~570 $M^{-1}cm^{-1}$) (Figure 2.11). Based on the characteristic energies of these new features, the product is assigned as a heteroleptic di(cupric)-1,2-μ-peroxide complexes **5-(PMe_3, PMe_2Ph)**, in which a peroxide fragment bridges between (P_3tren)Cu(II) and tmpa-Cu(II) centers (Scheme 2.2). The extinction coefficients of the features associated with **5** are too low to result from simple transfer of the O_2 fragment to [tmpa-Cu]$BArF_{20}$ to create the reported homoleptic di(cupric)-1,2-μ-peroxide complex. Further, the intensities of the features at ~20,000 and ~16,666 cm^{-1} increase over time, and when O_2 is reintroduced into the system, the LMCT transition at ~24,200 cm^{-1} reappears, with no other changes to the spectra. This is likely due to initial formation of a heteroleptic P_3tren/tmpa di(cupric)peroxide which slowly forms the homoleptic tmpa di(cupric)peroxide and (P_3tren)Cu(I). Control reactions confirm that adventitious O_2 is not present to an appreciable extent under these reaction conditions (see experimental for details).

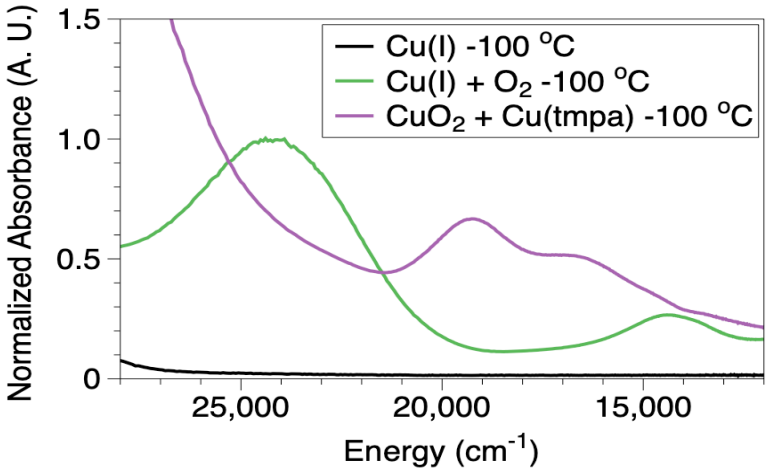

Figure 2.11 UV/vis spectra of compounds 1 (black), 2 (green), and 3 (purple).

2.2.7 Comments on Thermal Decomposition of 2

Mononuclear cupric superoxides reported in the literature typically exhibit half-lives ($t_{1/2}$) too fast to be studied with methods other than stopped-flow UV/vis spectroscopy at temperatures ranging from -125 to -85 °C.[15,16] The decomposition of these superoxides is evident by the loss of the LMCT transition and appearance of the spectroscopic signature of the homoleptic di(cupric)peroxides. There are a few examples of superoxides for which homoleptic di(cupric)superoxide signals are not seen. This has been attributed to either a more reducing copper center or hydrogen bonding in the secondary coordination sphere.[5,29,31] Quantitative data on the thermal stabilities of these compounds are not always available, but $[(^{NMe2}tmpa)Cu(O_2)]^+$ has been reported to have a $t_{1/2}$ = 4 h in THF at -85 °C and $[(^{OMe}tmpa)Cu(O_2)]^+$ a $t_{1/2}$ = 3 h in MeTHF at -90 °C.

The $[(P_3tren)Cu(O_2)]^+$ system similarly decomposes with loss of the LMCT feature, but no new features of significant intensity were observed during or after decomposition. After complete loss of the LMCT, the solution is retains a green color and upon evaporation of the solvent, a paramagnetic green solid is formed. The lack of new signals during decomposition is indicative that no concentrated amounts of homoleptic P_3tren di(cupric)peroxide complexes are formed.

The most reducing derivative of complex **2**, **2-PMe$_3$** ($E_{1/2}$ = -780 mV), is comparatively robust ($t_{1/2}$ = 38.5 h) at -100 °C, consistent with the proposal that more cathodic Cu(I/II) redox potentials favor the binding of O_2. Accordingly, **2-PMe$_2$Ph** ($E_{1/2}$ = 740 mV) shows a shorter half-life of ~2 h under the same conditions. Monitoring the decay of **2-PMe$_3$** at -85 °C provides a direct comparison to the stability of the dimethylamino-substituted tmpa cupric superoxide, which was shown to decay with a half-life of ~4 h. Under these conditions, the $t_{1/2}$ for **2-PMe$_3$** is 32 h, and **2-PMe$_3$** maintains a surprising degree of stability up to -40 °C, at which point the half-life was found to be 1.4 h (Figure 2.12).

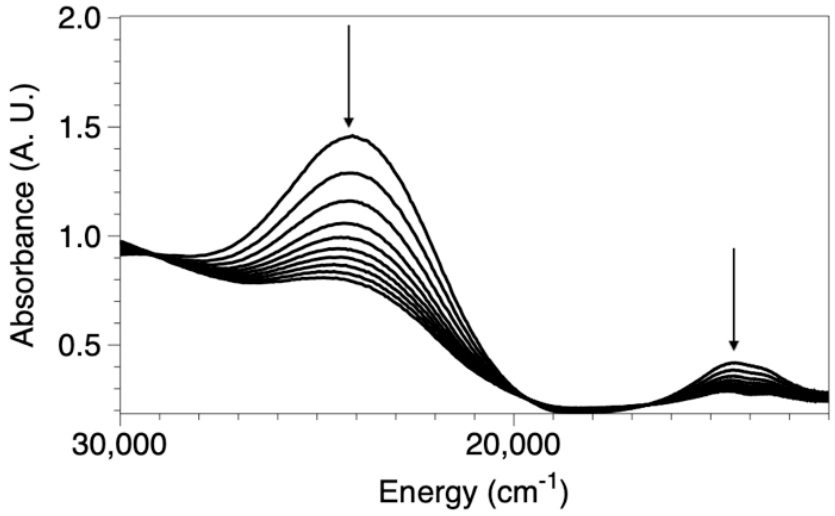

Figure 2.12 (A) UV/vis spectra of $2PMe_3$ (0.5 mM) showing decay at -40 °C.

Although the formation of a homoleptic di(cupric)-1,2-μ-peroxide complex is not observed for this system, the thermal decomposition rate data are consistent with a second-order dependence on Cu. Removal of excess O_2 from the reaction cuvette by sparging with dry N_2 results in a 10-fold increase in the rate of decomposition of **2**. A further rate enhancement is observed on addition of a precooled solution of **1** to a degassed solution of **2**. Both of these observations are consistent with a decomposition mechanism that involves the initial reformation of **1** via dissociation of O_2 from **2**, followed by rate limiting coupling of **1** to **2**. This view is further supported by an Eyring analysis of the UV/vis-monitored decomposition of **2-PMe$_2$Ph** at various temperatures (T = -90, -95, -100 °C). The resulting activation parameters ($\Delta H^{\ddagger}$ = 9.9 kcal/mol; $\Delta S^{\ddagger}$ = -16.4 cal/(mol•K)) are consistent with a rate-limiting, bimolecular transition state. As alluded to earlier, it appears that more cathodic Cu(I/II) redox couples for **1** effectively

slow the decomposition of **2** by shifting the equilibrium constant for O_2 binding in a direction that minimizes the concentration of **1** in solution.

2.3 Conclusion

A novel class of tren-based tris(phosphiniminato) ligands (P_3tren) were synthesized and used to bind copper(I) ions. The resulting complexes (**1-(PMe_3, PMe_2Ph, $PMePh_2$, PPh_3)**) show remarkable reducing power, courtesy of the high degree of anionic character located on the phosphinimine nitrogen atoms. This ligand framework allows for straight-forward tuning of the Cu(I)/Cu(II) couple ($\Delta E_{1/2}$ = 350 mV) through modulation of the substituents bound to phosphorous. The most reducing analogue, **1-PMe_3**, displays a Cu(I/II) redox couple at -780 mV, which, to the best of our knowledge, is the most negative potential reported for a trigonal pyamidal complex. Analysis of DFT studies highlighted the strong σ-donating ability of the P_3tren ligand, which led to a reordering the ligand field splitting compared to structurally analogous, trigonal pyramidal Cu(I) complexes.

Treating the series of copper(I) complexes (**1-(PMe_3, PMe_2Ph, $PMePh_2$)**) with dioxygen at low temperatures resulted in the formation of end-on-coordinated superoxide complexes of Cu(II) (**2-(PMe_3, PMe_2Ph, $PMePh_2$)**), as evidenced both by the observation of characteristic features in the electronic spectra and by reactivity studies with 2,6-di-*tert*-butyl-4-methoxyphenol. Notably, KIE values of 3 and 4.5 were measured for the reaction of **2-PMe_3** and **2-PMe_2Ph** with 2,6-di-*tert*-butyl-4-methoxyphenol respectively, indicating either a PCET or deprotonation event as the rate-determining

step. A PCET mechanism is favored as a result of the asynchronous PCET mechanisms that are known for related cupric superoxides, but a proton-transfer mechanism cannot be ruled out based on the available data.

The importance of the Cu(I/II) redox potential on the thermal stability of solutions of **2** was highlighted through a correlation of stability and reduction potential of the precursor copper(I) complex ($t_{1/2}$(**2-PMe$_3$**) > $t_{1/2}$(**^{Me2N}tmpaCuO$_2^+$**) > $t_{1/2}$(**2-PMe$_2$Ph**)). The decomposition of **2** is consistent with the mechanism that has been proposed previously for the thermal decomposition of ^{NMe2}tmpa and involves the loss of O_2 to form **1**, followed by a rate-limiting interaction between **1** and **2**. This analysis is supported by UV/vis studies aimed at measuring the thermodynamic and kinetic properties of this system, resulting in a mechanistic pathway that provides a simple explanation for enhanced stability, wherein a more negative Cu(I/II) redox couple perturbs the O_2 binding equilibrium to favor the superoxide **2**, thereby minimizing the concentration of **1**, which is necessary to form the di(cupric)-1,2-μ-peroxide involved in decomposition. Ultimately, the tris(phosphinimine) ligands reported herein show remarkable potential for their ability to create electron-rich Cu(I) centers, and studies are underway in the group both to further increase the reducing power of the copper(I) complexes through substitution of more electron-donating groups at phosphorous and to investigate the bond-activation and polymerization chemistry that results from this redox character.

2.4 References

1. Allen, S. E.; Walvoord, R. R.; Padilla-Salinas, R.; Kozlowski, M. C. *Chem. Rev.* **2013**, 113, 6234

2. Solomon, E. I.; Heppner, D. E.; Johnston, E. M.; Ginsbach, J. W.; Cirera, J.; Qayyum, M.; Kiever-Emmons, M. T.; Kjaergaard, C. H.; Hadt, R. G.; Tian, L. Chem. Rev. 2014, 114, 3659

3. Solomon, E. I.; Ginsbach, J. W.; Heppner, D. E.; Kieber-Emmons, M. T.; Kjaergaard, C. H.; Smeets, P. J.; Tian, L.; Woertink, J. S. *Faraday Discuss.* **2011**, 148, 11

4. Mirica, L. M.; Ottenwaelder, X.; Stack, T. D. P. *Chem. Rev.* **2004**, 104, 1013

5. Lee, J. Y.; Peterson, R. L.; Ohkubo, K.; Garcia-Bosch, I.; Himes, R. A.; Woertink, J.; Moore, C. D.; Solomon, E. I.; Fukuzumi, S.; Karlin, K. D. *J. Am. Chem. Soc.* **2014**, 136, 9925

6. (a) Xie, L.; van der Donk, W. A. *PNAS* **2001**, 98 (23), 12863 (b) Marshall, N. M.; Garner, D. K.; Wilson, T. D.; Gao, Y.-G.; Robsinson, H.; Nilges, M. J.; Lu, Y.; *Nature* **2009**, 462 (7269), 113.

7. Shook, R. L.; Borovik, A. S. *Inorg. Chem.* **2010**, 49, 3646.

8. Cook, S. A.; Borovik, A. S. *Acc. Chem. Res.* **2015**, 48, 2407.

9. Creutz, S. E.; Peters, J. C. *Chem. Sci.* **2017**, 8, 2321.

10. Mann, S. I.; Heinisch, T.; Ward, T. R.; Borovik, A. S. *J. Am. Chem. Soc.* **2017**, 139, 17289.

11. Dhar, D.; Yee, G. M.; Tolman, W. B. *Inorg. Chem.* **2018**, 57, 9794.

12. Zhang, C. X.; Kaderli, S.; Costas, M.; Kim, W.; Neuhold, Y.; Karlin, K. D.; Zuberuhler, A. D. *Inorg. Chem.* **2003**, 42, 1807.

13. Ribelli, T. G.; Fantin, M.; Daran, J.; Augustine, K. F.; Poli, R.; Matyzaszewski, K. *J. Am. Chem. Soc.* **2018**, 140, 1525.

14. It has been shown that there is a linear correlation between the catalyst $E_{1/2}$ and the natural log of the polymerization equilibrium constant, such that more negative potentials leads to a more active catalyst.

15. Zhang, C. X.; Kaderli, S.; Costas, M.; Kim, W.; Neuhold, Y.; Karlin, K. D.; Zuberuhler, A. D. *Inorg. Chem.* **2003**, 42, 1807.

16. Weitzer, M.; Schindler, S.; Brehm, G.; Schneider, S.; Hörmann, E.; Jung, B.; Kaderli, S.; Zuberbühler, A. D. *Inorg. Chem.* **2003**, 42, 1800

17. *Superbases for Organic Synthesis: Guanidines, Amidines, Phosphazenes and Related Organocatalysts*; Ishikawa, T., Ed.; Wiley: Chichester, U.K., 2009.

18. Kalijurand, I.; Saame, J.; Rodima, T.; Koppel, I.; Koppel, I. A.; Kogel, J. F.; Sundermeyer, J.; Kohn, U.; Coles, M. P.; Leito, I. *J. Phys. Chem. A* **2016**, 120, 2591.

19. Wittmann, H.; Raab, V.; Schorm, A.; Plackmeyer, J.; Sundermey er *J. Eur. J. Inorg.*

Chem. **2001**, 1937

20. Chaplin, A. B.; Harrison, J. A.; Dyson, P. J. Inorg. Chem. **2005**, 44 (23), 8407

21. Lucas, H. R.; Meyer, G. J.; Karlin, K. D. *J. Am. Chem. Soc.* **2010**, 132, 12927

22. Wei, N.; Murthy, N. N.; Karlin, K. D. *Inorg. Chem.* **1994**, 33 (26), 6093

23. Kim, S.; Lee, J. Y.; Cowley, R. E.; Ginsbach, J. W.; Siegler, M. A.; Solomon, E. I.; Karlin, K. D. *J. Am. Chem. Soc.* **2015**, 137, 2796.

24. Elwell, C. E.; Gangnon, N. L.; Neisen, B. D.; Dhar, D.; Spaeth, A. D.; Yee, G. M.; Tolman, W. B. *Chem. Rev.* **2017**, 117, 2059.

25. $TMG_3trenCuO_2$ was also calculated so that it could be used as a standard compared to Karlin and Solomon group calculations, which were performed using the B3LYP functional.[26] TDDFT matched extremely well with reported findings but further analysis of the orbitals showed that their was a different ordering of orbitals between functionals. In B3LYP the π^*_σ was calculated as the HOMO not the $d_{x^2-y^2}$ and d_{xy}. While we acknowledge these differences we still believe the broad general trends of orbital energies between P_3tren and tmpa corroborated by UV/vis and TDDFT are acceptable when using B97-D3.

26. Woertink, J. S.; Tian, L.; Maiti, D.; Lucas, H. R.; Himes, R. A.; Karlin, K. D.; Neese, F.; Würtele, C.; Holthausen, M. C.; Bill, E.; Sundermeyer, J.; Schindler, S.; Solomon, E. I. *Inorg. Chem.* **2010**, 49, 9450

27. (a) Maiti, D.; Lee, D.-H.; Gaoutchenova, K.; Würtele, C.; Holthausen, M. C.; Narducci Sarjeant, A. A.; Sundermeyer, J.; Schindler, S.; Karlin, K. D. *Angew. Chem. Int. Ed.* **2008**, 47, 82. (b) Lee, J. Y.; Peterson, R. L.; Ohkubo, K.; Garcia-Bosch, I.; Himes, R. A.; Woertink, J.; Moore, C. D.; Solomon, E. I.; Fukuzumi, S.; Karlin, K. D. *J. Am. Chem. Soc.* **2014**, 136, 9925 (c) Peterson, R. L.; Himes, R. A.; Kotani, H.; Suenobu, T.; Tian, L.; Siegler, M. A.; Solomon, E. I.; Fukuzumi, S.; Karlin, K. D. *J. Am. Chem. Soc.* **2011**, 133, 1702

28. (a) Peterson, R. L.; Himes, R. A.; Kotani, H.; Suenobu, T.; Tian, L.; Siegler, M. A.; Solomon, E. I.; Fukuzumi, S.; Karlin, K. D. *J. Am. Chen. Soc,* **2011***,* 133, 1702 (b) Komiyama, K.; Furutachi, H.; Nagatoma, S.; S.; Hashimoto, A.; Hayashi, H.; Fujinami, S.; Suzuki, M.; Kitagawa, T. *Bull.Chem. Soc. Jpn.* **2004**, 77, 59 (c) Chaudhuri, P.; Hess, M.; Weyhermuller, T.; Wieghardt, K. *Angew. Chem. Int. Ed.* **1999**, 38 (8), 1095

29. Maiti, D.; Fry, H. C.; Woertink, J. S.; Vance, M. A.; Solomon, E. I.; Karlin, K. D. *J. Am. Chem. Soc.* **2007**, 129, 264

30. Data for ^{NMe2}tmpa reported to 11,111 cm^{-1} with the lowest energy feature at 13,000 cm^{-1}.

31. Bhadra, M.; Lee, J. Y. C.; Cowley, R. E.; Kim, S.; Siegler, M. A.; Solomon, E. I.; Karlin, K. D. *J. Am. Chem. Soc.* **2018**, 140 (29), 9042.

2.5 Experimental

General Considerations

All reactions containing transition metals were performed under an inert atmosphere of N_2 using standard Schlenk line or glovebox techniques unless addition of O_2 is noted. UHP-grade O_2 (99.99%) was purchased from Airgas and dried over a column of Drierite before use. All solvents (THF, acetonitrile, *n*-pentane, *n*-hexane, and diethyl ether) were dried by passage through a column of activated alumina and stored over 4 Å molecular sieves under an inert atmosphere. Deuterated solvents (CD_3CN and C_6D_6) were dried over CaH_2, isolated via vacuum transfer, and stored under an inert atmosphere over 4 Å sieves. ^{1}H, $^{13}C\{^{1}H\}$, $^{31}P\{^{1}H\}$, $^{19}F\{^{1}H\}$, spectra were recorded on Bruker DMX300, UNI400, or BioDRX500 spectrometers. All chemical shifts (δ) are reported in units of ppm and referenced to the residual protio-solvent resonance for proton and carbon chemical shifts. External H_3PO_4 or $CFCl_3$ were used for referencing ^{31}P and ^{19}F chemical shifts. Elemental analyses were performed by Midwest Microlab, LLC or at the University of Pennsylvania on a Costech ECS 4010 analyzer in the Earth & Environmental Science Department at the University of Pennsylvania. Low-temperature UV/vis spectra were collected on a Cary 60 spectrophotometer equipped with a Unisoku USP-203A cryostat using a 1 cm cuvette. Accurate mass measurement data were acquired on Waters instruments. Waters software calibrates the instrument and reports the data by use of neutral atomic masses; the mass of the electron is not included. 2-chloro-*N*,*N*-bis(2-chloroethyl)ethanammonium chloride was synthesized following the literature

procedure.[1] All chemicals, unless specifically mentioned, were purchased from Fisher Scientific.

Syntheses

2-azido-*N*,*N*-*bis*(2-azidoethyl)ethanamine (tris(azido)tren). Tris(azido)tren was prepared according to a modification of the literature procedure.[2] 2-chloro-*N*,*N*-bis(2-chloroethyl)ethanammonium chloride (1.6 g, 6.64 mmoles) was combined with sodium azide (2.4 g, 36.92 mmoles) in DMSO (50 mL) open to the air. The reaction mixture was heated to 92 ^{o}C for 8 h. Upon cooling, deionized water (300 mL) was added, and the resulting aqueous mixture was treated with sodium carbonate until the solution became alkaline (3.2 g). The aqueous mixture was extracted with diethyl ether (3 x 200 mL), and the combined organic layers were washed with deionized water (3 x 100 mL), followed by brine (100 mL). The ethereal solution was dried over sodium sulfate, then concentrated to ~30 mL under reduced pressure. *Extreme caution was taken to ensure that the solution was not evaporated to dryness.* The ethereal solution was then transferred to a Schlenk flask and degassed through three freeze-pump-thaw cycles. Calcium hydride was added under a positive stream of N_2, and the heterogeneous mixture was stirred vigorously for two days at room temperature. The solution was filtered through a plug of Celite on a Schlenk filter. The product, 2-azido-*N*,*N*-bis(2-azidoethyl)ethanamine, was used without further purification under the assumption that the reaction provided a quantitative yield. All azide waste and byproducts were quenched by dissolving sodium nitrite (~5 g) in DI H_2O (~100 mL) and adding glacial aceting acid (~1 mL) and adding the azide waste slowly to this mixture. Vigorous bubbling occurs

instantly and slow addition is needed. Once completely added, the waste was allowed to sit in a ventilated hood overnight before siposing into proper waste streams.

^{Me3}P$_3$tren. A diethyl ether (30 mL) solution of 2-azido-*N*,*N*-bis(2-azidoethyl)ethanamine (6.64 mmoles) was cooled to 0 ^{o}C, and an equal volume of THF (30 mL) was added via cannula transfer. Trimethylphosphine (2.03 mL, 19.92 mmoles) was added quickly via syringe. The resulting Et_2O/THF solution was warmed to room temperature and stirred for 6 h while open to a mineral oil bubbler to prevent a buildup of pressure due to N_2 evolution. The volatile materials were then removed *in vacuo*, and the resulting white solid was washed with *n*-hexane. The resulting white solid was dried under vacuum for 30 minutes (1.5 - 1.8 g, 62 - 74%). **^{1}H NMR** (400 MHz, C_6D_6, 300 K): δ 3.62 (dt, 6H, $^3J_{HH}$ = 8 Hz, $^3J_{PH}$ = 24 Hz), δ 3.18 (t, 6H, ^3J = 8 Hz), δ 0.92 (d, 27H, ^2J = 12 Hz) ppm. **^{31}P{^{1}H} NMR** (162 MHz, C_6D_6, 300K): δ 3.11 (s) ppm. **MH$^+$** = 354.22 (calc. 354.22).

^{Me2Ph}P$_3$tren. A diethyl ether (30 mL) solution of 2-azido-*N*,*N*-bis(2-azidoethyl)ethanamine (6.64 mmoles) was cooled to -78 ^{o}C, and an equal volume of THF (30 mL) was added via cannula transfer. Dimethylphenylphosphine (2.83 mL, 19.92 mmoles) was added quickly via syringe. The resulting Et_2O/THF solution was warmed to room temperature and stirred for 6 h while open to a mineral oil bubbler to prevent a buildup of pressure due to N_2 evolution. The volatile materials then removed *in vacuo* to generate a clear, viscous oil. The product was crystallized from diethyl ether at -78 ^{o}C, and crystals were isolated through cannula filtration. Upon warming to room temperature, the crystals melted into an oil, which was washed extensively with *n*-hexane to remove

any residual phosphine. The product was further dried under vacuum for a minimum of 30 minutes. (62%). **^{1}H NMR** (400 MHz, C_6D_6, 300K) δ 7.62 (m, 6H), δ 7.09 (m, 9H), δ 3.69 (dt, 6H, $^{3}J_{HH}$ = 8 Hz, $^{3}J_{PH}$ = 20 Hz) ppm, δ 3.29 (t, 6H, ^{3}J = 8 Hz), δ 1.21 (d, 18H, ^{2}J = 12 Hz). **^{13}C{^{1}H} NMR** (101 MHz, C_6D_6, 300K) δ 137.3, δ 136.2, δ 130.4, δ 62.9, δ 45.1, δ 40.5, δ 16.1 **^{31}P{^{1}H} NMR** (162 MHz, C_6D_6, 300K) δ 2.37 (s) ppm. **MH^{+}** = 540.59 (calc. 540.61)

^{MePh2}P$_3$tren. A diethyl ether (30 mL) solution of 2-azido-*N*,*N*-bis(2-azidoethyl)ethanamine (6.64 mmoles) was cooled to -78 ^{o}C, and an equal volume of THF (30 mL) was added via cannula transfer. Methyldiphenylphosphine (3.71 mL, 19.92 mmoles) was added quickly via syringe. The resulting Et_2O/THF solution was warmed to room temperature and stirred for 6 h while open to a mineral oil bubbler to prevent a buildup of pressure due to N_2 evolution. The volatile materials were then removed *in vacuo*, and the resulting pale oil was triturated with *n*-hexane. The *n*-hexane was filtered off, and the resulting oily solid was dried under vacuum for a minimum of 30 minutes to produce a tan solid (63%). **^{1}H NMR** (400 MHz, C_6D_6, 300K) δ 7.67 (m, 12H), δ 7.37 (m, 6H), δ 7.05 (m, 12H), δ 3.68 (m, 6H) ppm, δ 3.28 (t, 6H, ^{3}J = 8 Hz), δ 1.55 (d, 9H, ^{2}J = 20 Hz) . **^{31}P{^{1}H} NMR** (162 MHz, C_6D_6, 300K) δ 2.13 (s) ppm. **MH^{+}** = 664.75 (calc. 664.75)

^{Ph3}P$_3$tren. A diethyl ether (30 mL) solution of 2-azido-*N*,*N*-bis(2-azidoethyl)ethanamine (6.64 mmoles) was cooled to -78 ^{o}C, and an equal volume of THF (30 mL) was added via cannula transfer. Triphenylphosphine (dried under vacuum) (5.22, 19.92 mmoles) was dissolved in a small amount of THF (~2 mL) under N_2 and added

quickly via a cannula. The resulting Et_2O/THF solution was warmed to room temperature and stirred for 6 h while open to a mineral oil bubbler to prevent a buildup of pressure due to N_2 evolution. The volatile materials were then removed *in vacuo*, and the resulting solid was washed with *n*-hexane. Then extracted with ether and allowed to sit at -20 ^oC for any dissolved triphenylphosphine to crystallize out. The solution was filtered cold and the volatile materials were then removed *in vacuo*. The resulting solid was dried under vacuum for a minimum of 30 minutes to produce a tan solid (55%). **^{1}H NMR** (400 MHz, C_6D_6, 300K) δ 7.0-7.8 (m, 45H), δ 3.65 (m, 6H) ppm, δ 3.28 (t, 6H, ^3J = 8 Hz). **^{31}P{^{1}H} NMR** (162 MHz, C_6D_6, 300K) δ 1.87 (s) ppm. **MH^+** = 664.75, found 664.75

General procedure for copper(I) complexes (1). [Tetrakis(acetonitrile)copper(I)][tetrakis(pentafluorophenyl)borate] ($CuBArF_4$-20·4MeCN) (400 mg, 0.44 mmoles) was dissolved in THF (30 mL) in a Schlenk flask, and cooled to -78 ^oC. One equiv of P_3tren (0.44 mmoles) dissolved in THF (20 mL) was cannula transferred to the reaction flask, resulting in the formation of a pale yellow solution. The reaction mixture was warmed to room temperature and stirred for 3 h. Volatile materials were removed in vacuo, resulting in a white (**1-PMe_3**) or pale yellow (**1-(PMe_2Ph, $PMePh_2$, PPh_3)**) foam. Product was extracted with diethyl ether (30 mL) and filtered through celite. Diethyl ether was removed *in vacuo*, and the resulting solids were washed with *n*-hexane. Products were dried under vacuum for a minimum of 30 minutes.

1-PMe_3. White powder, 72% yield. Single crystals of X-ray quality were grown from diethyl ether at -35 ^oC. **^{1}H NMR** (400 MHz, CD_3CN, 300K) δ 2.99 (dt, 6H, $^3J_{HH}$ = 6

Hz, $^{3}J_{PH}$ = 16 Hz), δ 2.51 (t, 6H, ^{3}J = 4 Hz), δ 1.49 (d, 27H, ^{2}J = 16 Hz) ppm. **^{31}P{^{1}H} NMR** (162 MHz, C_6D_6, 300K) δ 24.39 (s) ppm. **Anal. Calcd.** for $C_{39}H_{39}BCuF_{20}N_4P_3$: C, 42.16; H, 3.54; N, 5.04. **Found**: C, 42.52; H, 3.56; N, 5.00.

1-PMe$_2$Ph. Yellow solid, 74% yield. **^{1}H NMR** (400 MHz, CD_3CN, 300K) δ 7.4-7.85 (m, 15H), 3.00 (dt, 6H, $^{3}J_{HH}$ = 6 Hz, $^{3}J_{PH}$ = 18 Hz), δ 2.52 (t, 6H, ^{3}J = 6 Hz), δ 1.72 (d, 18H, ^{2}J = 12 Hz) ppm. **^{13}C{^{1}H} NMR** (101 MHz, C_6D_6, 300K) δ 132.8, δ 131.4, δ 129.7, δ 68.1, δ 45.4, δ 26.1, δ 15.7 ppm. **^{31}P{^{1}H} NMR** (162 MHz, C_6D_6, 300K) δ 22.7 (s) ppm. **UV/vis** 296 nm (ε = ~20,800 $M^{-1}cm^{-1}$), 373 nm (ε = ~10,200 $M^{-1}cm^{-1}$) **IR** FTIR (KBr plate) 3533, 3466, 3358, 3048, 2961, 2895, 2826, 1594, 1435, 1414, 1290, 1261, 1160, 1110, 1046, 1010, 932, 915, 801, 719, 670, 615 cm^{-1}

1-PMePh$_2$ Yellow solid, 69% yield. **^{1}H NMR** (400 MHz, CD_3CN, 300K) δ 7.2-7.9 (m, 30H), 3.03 (dt, 6H, $^{3}J_{HH}$ = 6 Hz, $^{3}J_{PH}$ = 18 Hz), δ 2.54 (t, 6H, ^{3}J = 6 Hz), δ 1.79 (d, 9H, ^{2}J = 12 Hz) ppm. **^{31}P{^{1}H} NMR** (162 MHz, C_6D_6, 300K) δ 21.5 (s) ppm.

1-PPh$_3$ Yellow solid, 80% yield. **^{1}H NMR** (400 MHz, CD_3CN, 300K) δ 7.0-8.0 (m, 45H), 3.06 (dt, 6H, J_{HH} = 6 Hz, J_{PH} = 18 Hz), δ 2.57 (t, 6H, J = 6 Hz) ppm. **^{31}P{^{1}H} NMR** (162 MHz, C_6D_6, 300K) δ 20.3 (s) ppm.

3-Cl. Triphenylmethyl chloride (70 mg, 0.25 mmoles) dissolved in THF (3 mL) was added to a stirred solution of **2-PMe$_3$** (279 mg, 25 mmoles) in THF (5 mL) at room temperature. An immediate color change from pale yellow to vibrant green was observed. The reaction mixture was stirred at room temperature for 1 h, followed by removal of solvent *in vacuo*. The resulting green foam was washed extensively with *n*-hexane, which

removed trityl radical/Gomberg's dimer as confirmed by NMR spectroscopy. The remaining green solid was dried under vacuum for 30 minutes, and X-ray quality crystals were grown from diethyl ether at -78 ^{o}C. See X-ray data below. **NMR** shows no signals **UV/vis** 280 nm (ε = ~20,000 $M^{-1}cm^{-1}$), 650 nm (ε = ~140 $M^{-1}cm^{-1}$), 720 nm (ε = ~100 $M^{-1}cm^{-1}$)

4-PMe$_3$. A solution of **3-Cl** (100 mg, 0.087 mmoles) in MeCN (20 mL) was prepared in a Schlenk flask. Sodium azide (6 mg, 0.092 mmoles) was ground by mortar and pestle, and a slurry in MeCN (10 mL) was transferred to the flask containing **3-Cl**. The resulting slurry was stirred overnight (8 hrs.) at room temperature. Excess sodium azide and sodium chloride were removed by filtration through celite, and the solvent of the filtrate was removed *in vacuo*. The vividly green solid was washed with *n*-hexane, and X-ray quality single crystals were grown from diethyl ether at -78 ^{o}C. **NMR** shows no signals **UV/vis** 384 nm (ε = ~3,145 $M^{-1}cm^{-1}$), 700 nm (ε = ~200 $M^{-1}cm^{-1}$)

Electrochemistry:

Cyclic voltammetry and square-wave voltammetry measurements were carried out using a BASi Epsilon Eclipse electrochemistry analyzer. All electrochemistry was performed in an N_2 atmosphere glovebox. A platinum disk was used as the working electrode. A platinum wire was used as the counter electrode. The reference electrode was $Ag/AgNO_3$ in MeCN. The measurements were performed at room temperature under an N_2 atmosphere in an MeCN solution containing 0.1 M tetrabutylammonium

hexafluorophosphate, which was recrystallized four times from ethanol and dried under vacuum, and 1 mM copper complex.

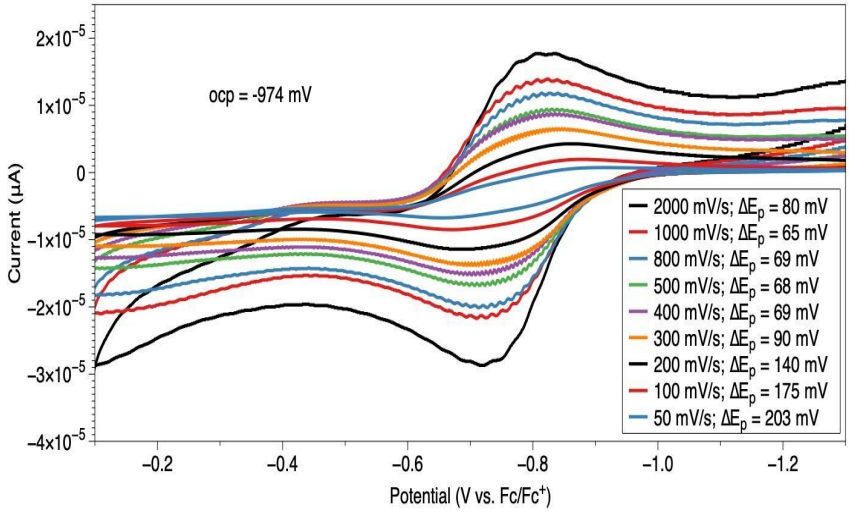

Figure S2.1 Cyclic voltammograms of **1-PMe$_3$**.

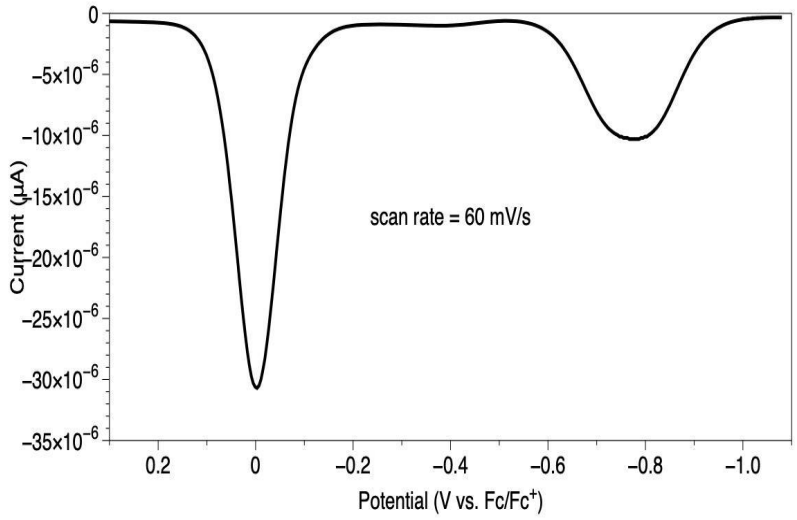

Figure S2.2 Square-wave voltammogram of **1-PMe$_3$** with added ferrocene set to 0 V.

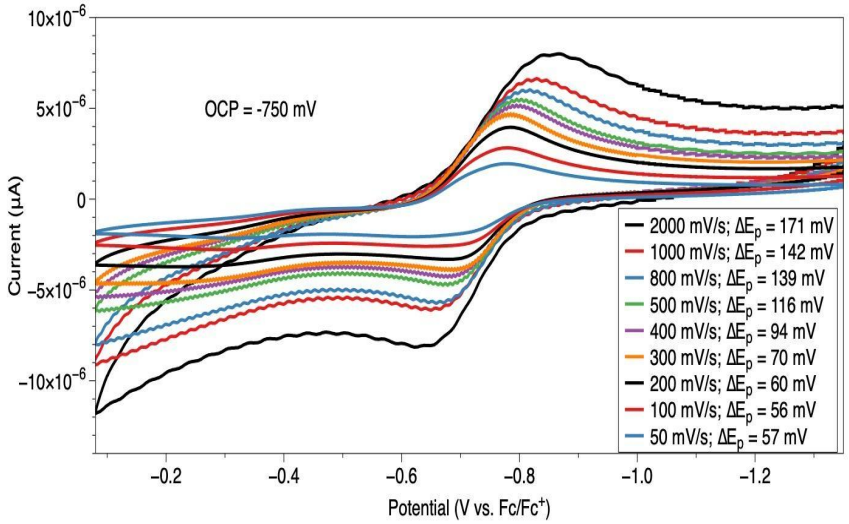

Figure S2.3 Cyclic voltammograms of **1-PMe$_2$Ph**.

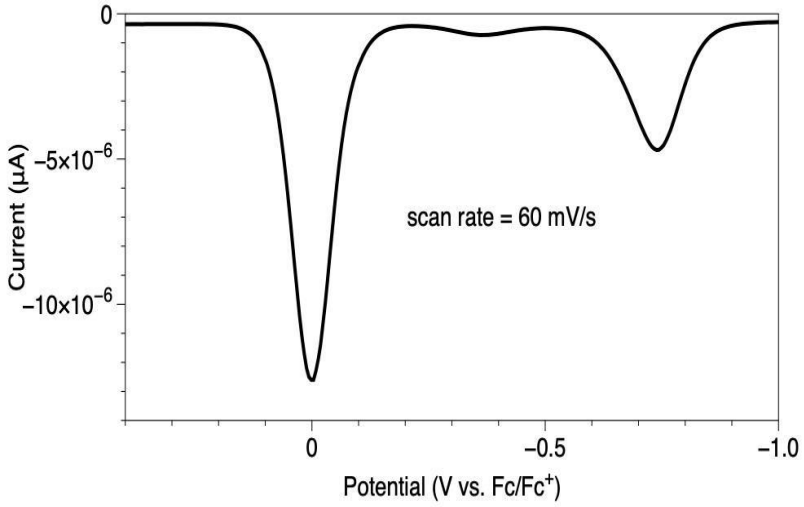

Figure S2.4 Square-wave voltammogram of **1-PMe$_2$Ph** with added Ferrocene set to 0 V.

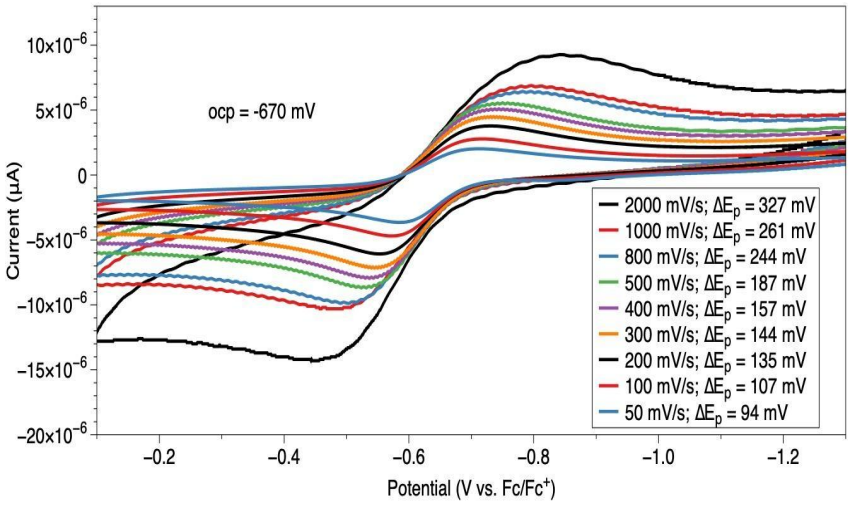

Figure S2.5 Cyclic voltammograms of **1-PMePh$_2$**.

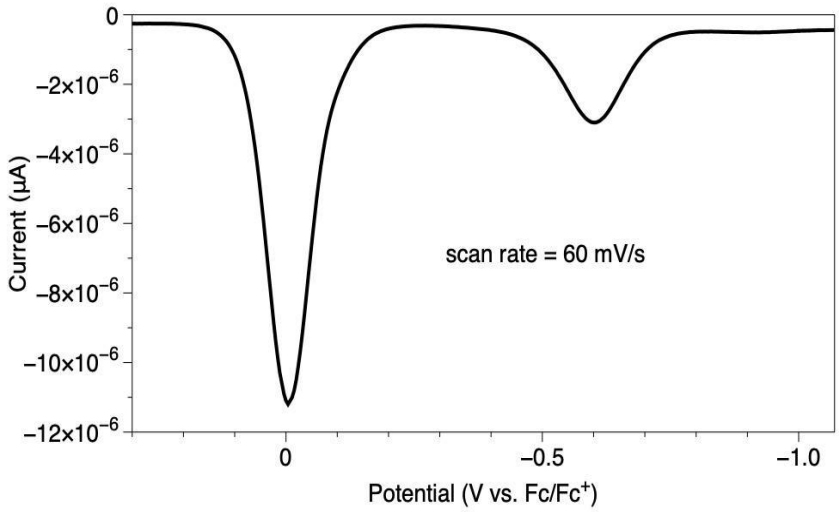

Figure S2.6 Square-wave voltammogram of **1-PMePh$_2$** with added Ferrocene set to 0 V.

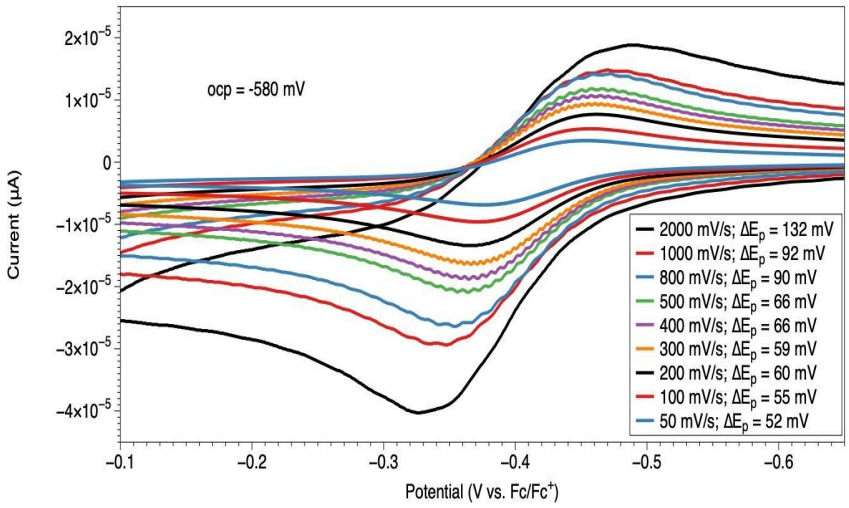

Figure S2.7 Cyclic voltammograms of **1-PMePh$_2$**.

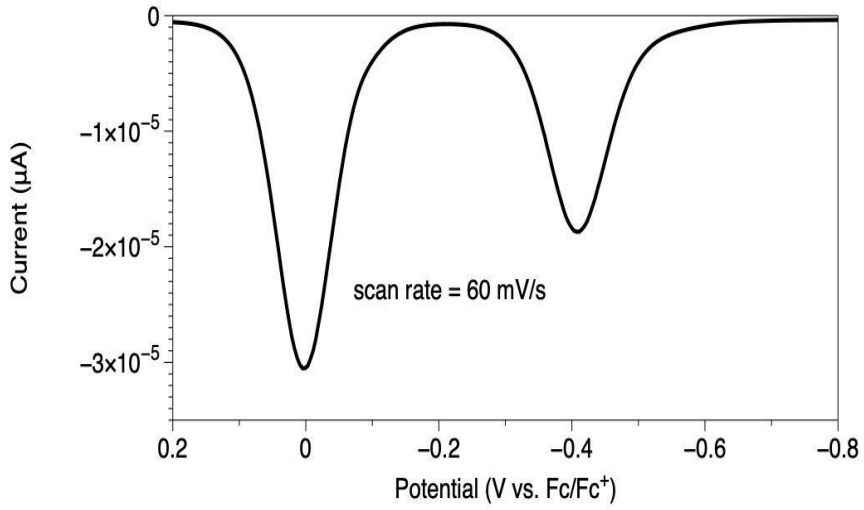

Figure S2.8 Square-wave voltammogram of **1-PMePh$_2$** with added Ferrocene set to 0 V.

Generation of 2-PMe_3 and 2-PMe_2Ph:

In the glovebox, a solution of **2** in THF (3 mL, 0.5 mM) was prepared and transferred to a 1 cm, long-neck cuvette and capped with a Teflon septum. The cuvette was placed in the UV/vis cryostat within a stream of nitrogen, and a spectrum was recorded at 22 °C. The sample was then cooled to -100 °C and spectra were taken to confirm that the sample was unchanged. Dry O_2 (100%) was bubbled through the cold solution for 10 seconds, then spectra were recorded.

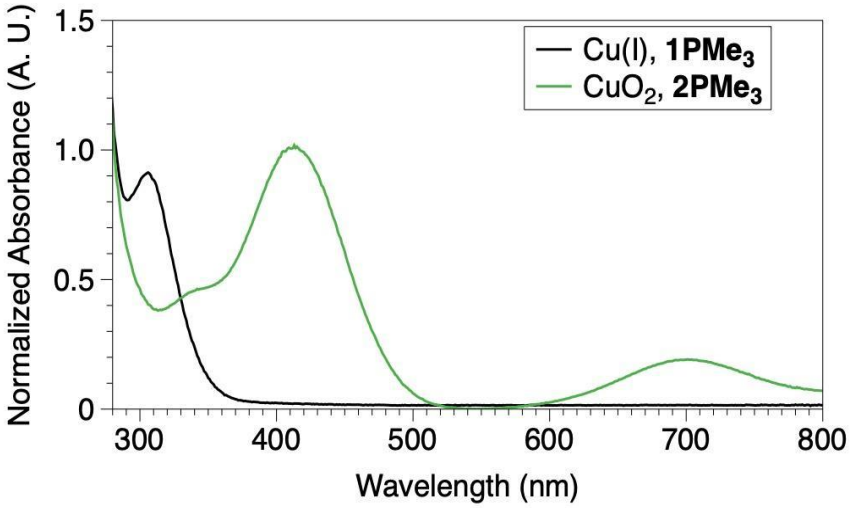

Figure S2.9 UV/vis at -100 °C for **1-PMe_3** and **2-PMe_3** after adding O_2.

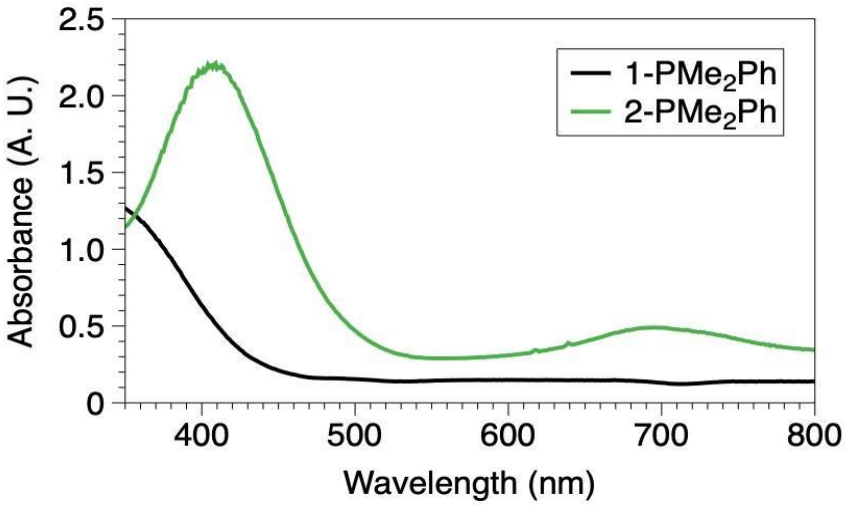

Figure S2.10 UV/vis at -100 °C for **1-PMe$_2$Ph** and **2-PMe$_2$Ph** after adding O_2.

Generation of 2-PMePh$_2$:

In the glovebox, a solution of **2** in THF (3 mL, 0.5 mM) was prepared and transferred to a 1 cm, long-neck cuvette and capped with a Teflon septum. The cuvette was placed in the UV/vis cryostat within a stream of nitrogen, and a spectrum was recorded at 22 °C. The sample was then cooled to -100 °C and spectra were taken to confirm that the sample was unchanged. Dry O_2 (100%) was bubbled through the cold solution for 10 seconds, then spectra were recorded.

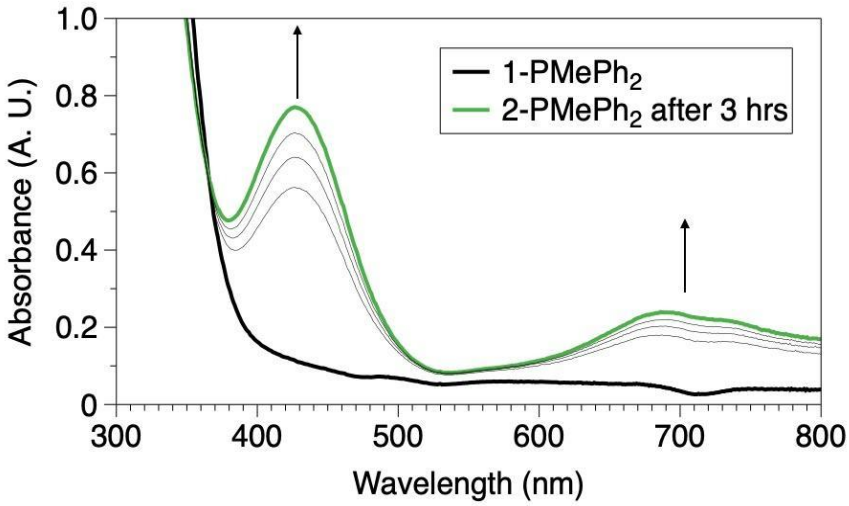

Figure S2.11 UV/vis at -100 °C for **1-PMePh$_2$** and **2-PMePh$_2$** after adding O_2, time points at 15 min, 30 min, and 1 h shown in black.

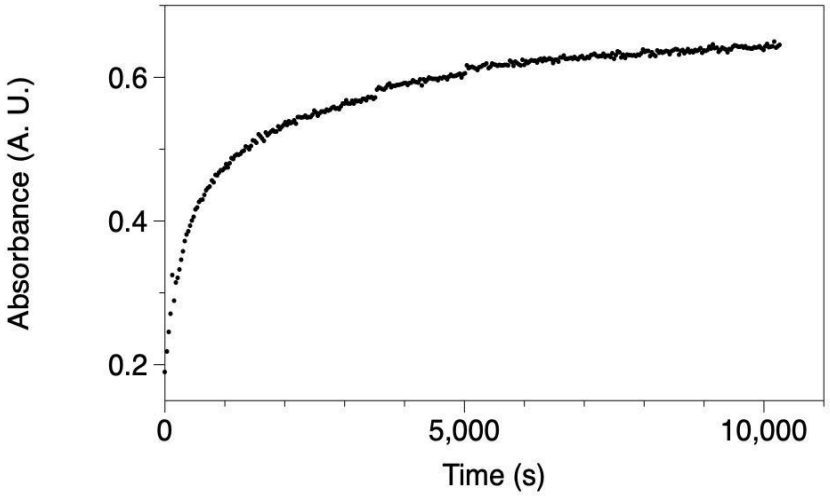

Figure S2.12 Absorbance value for peak ~400nm for **2-PMePh$_2$** after the addition of O_2.

Generation of 2 and reaction with 2,6-di-tert-butyl-4-methoxyphenol:

In the glovebox, a solution of **2** in THF (3 mL, 0.5 mM) was prepared and transferred to a 1 cm, long-neck cuvette and capped with a Teflon septum. The cuvette

was placed in the UV/vis cryostat within a stream of nitrogen, and a spectrum was recorded at 22 °C. The sample was then cooled to -100 °C and spectra were taken to confirm that the sample was unchanged. Dry O_2 (100%) was bubbled through the cold solution for 10 seconds, then spectra were recorded. The solution was then sparged with dry N_2 for 30 seconds and the substrate (pre cooled to -94 °C) was immediately added by transferring from a Schlenk tube with a syringe (100 μL). Spectra were taken every 30 seconds for 1 h. Pseudo-first-order rate plots analyzing the first 10% of loss of absorbance were performed by observing the disappearance of a 700 nm d-d bands to obtain plots of $\ln[(A - A_f)/(A_i - A_f)]$ versus time (seconds), which were found to be linear.

Figure S2.13 Pseudo-first-order plots for the reactions of **2-PMe$_2$Ph** (0.5 mM) and 2,6-di-tert-butyl-4-methoxyphenol to determine pseudo-first-order rate constants (k_{obs}).

Phenol (mM)	k_{obs} (s^{-1}) Trial 1	k_{obs} (s^{-1}) Trial 2	k_{obs} (s^{-1}) Trial 3	k_{obs} (s^{-1}) Average	Std. dev.
0.5	0.0079	0.0079	0.008	0.0079	5.7×10^{-5}
0.75	0.0096	0.01	0.0106	0.010	5.0×10^{-4}
1.0	0.0112	0.0123	0.0119	0.012	5.6×10^{-4}

Representative trial for each concentration:

0.5 mM:

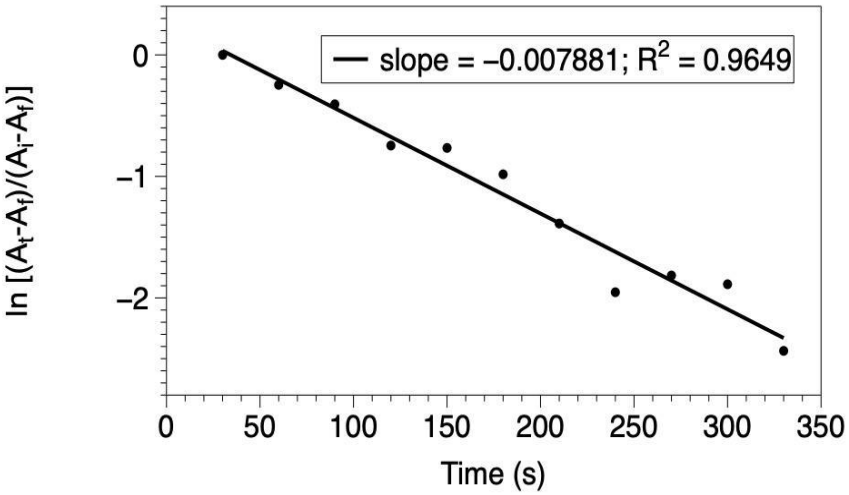

0.75 mM:

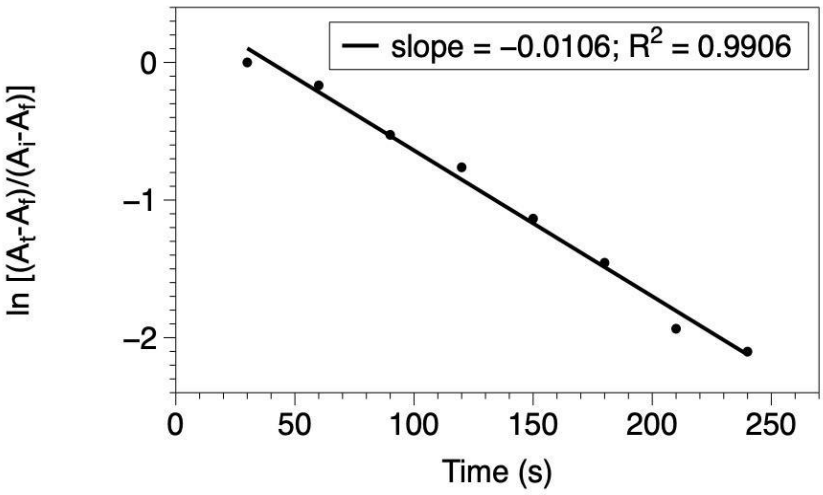

1.0 mM:

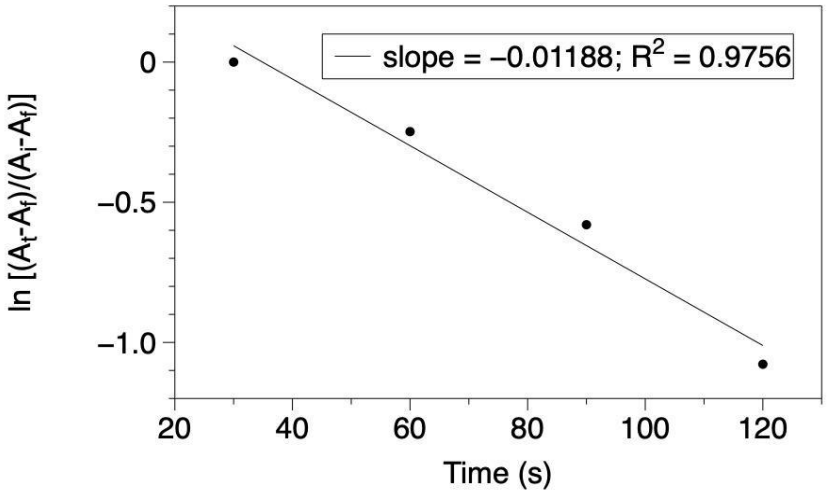

Figure S2.14 Pseudo-first-order plots for the reactions of **2-PMe$_2$Ph** (0.5 mM) and deutoro-2,6-di-tert-butyl-4-methoxyphenol (OD) to determine pseudo-first-order rate constants (k_{obs}).

Phenol (mM)	k_{obs} (s^{-1}) Trial 1	k_{obs} (s^{-1}) Trial 2	k_{obs} (s^{-1}) Trial 3	k_{obs} (s^{-1}) Average	Std. dev.
0.5	0.0028	0.0029	0.0026	0.0028	1.5×10^{-4}
0.75	0.003	0.0031	0.0035	0.0032	2.6×10^{-4}
1.0	0.0036	0.0039	0.0036	0.0037	1.7×10^{-4}

Representative trial for each concentration:

0.5 mM:

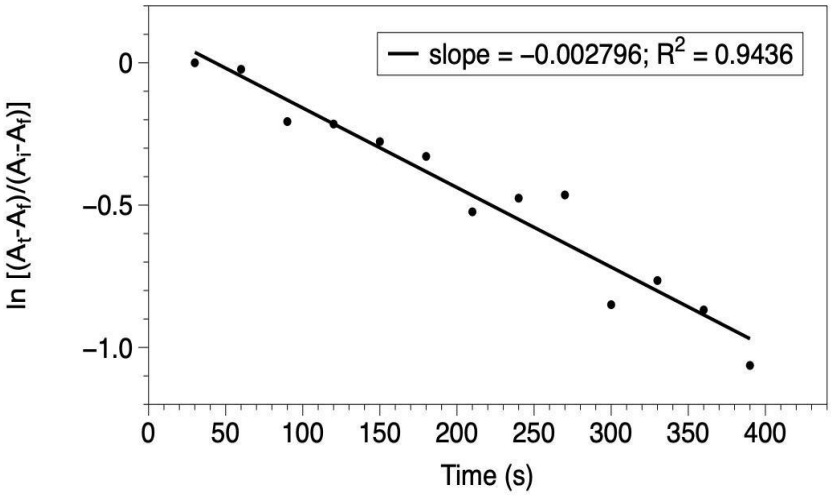

0.75 mM:

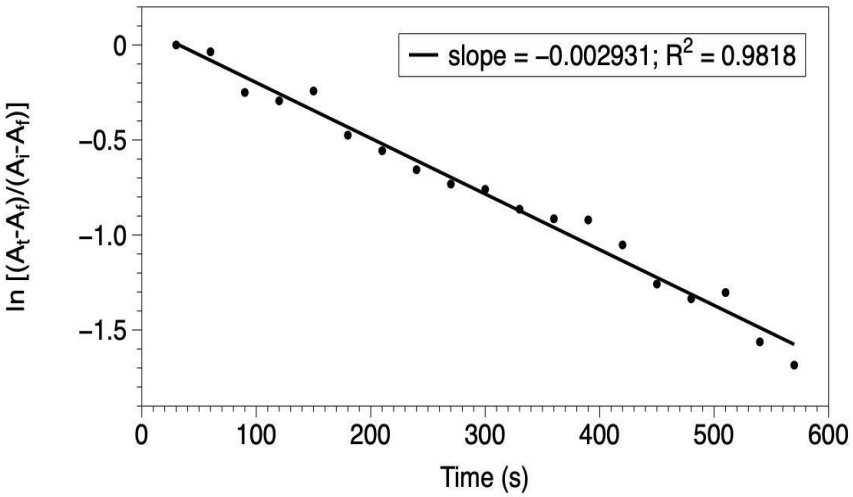

1.0 mM:

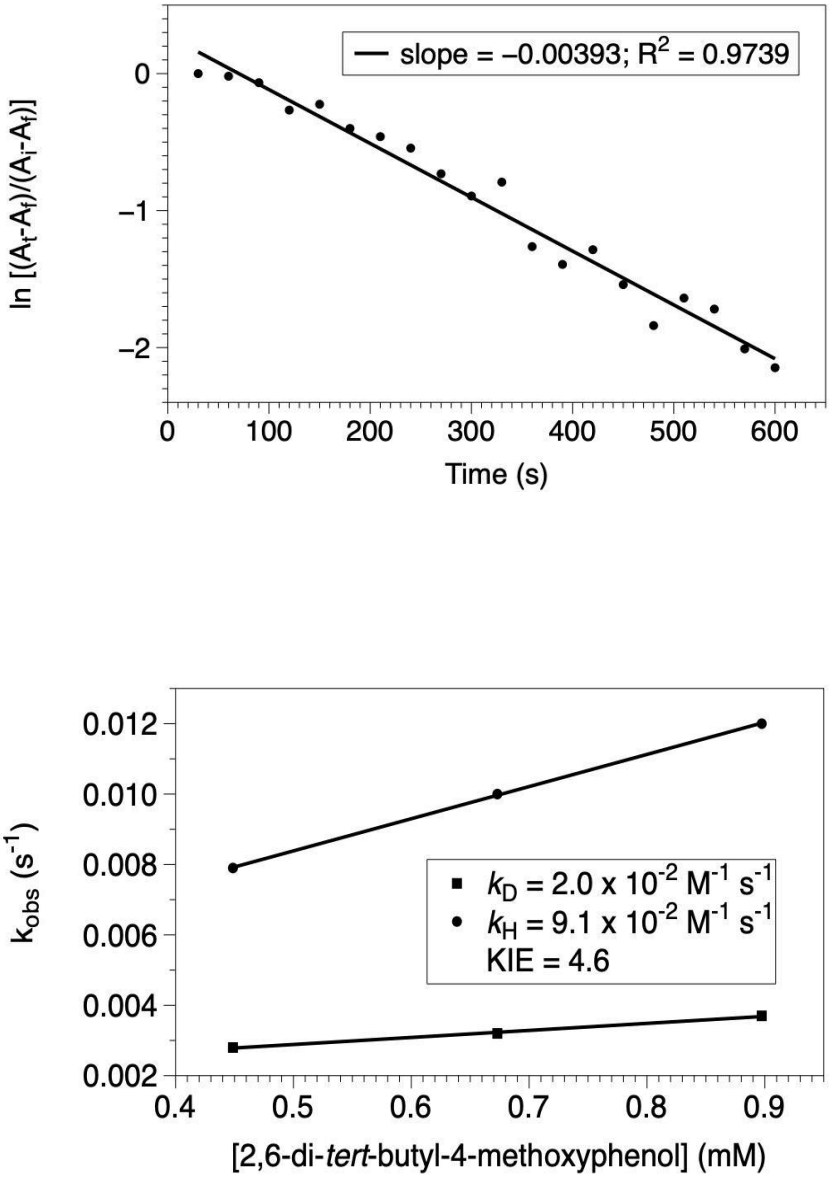

Figure S2.15 Plot of k_{obs} vs. concentration of substrate to determine second-order rate constant and KIE; proteo (circles), deutero (squares) for **2-PMe$_2$Ph**.

Figure S2.16 Pseudo-first-order plots for the reactions of **2-PMe$_3$** (0.5 mM) and 2,6-di-tert-butyl-4-methoxyphenol to determine pseudo-first-order rate constants (k_{obs}).

Phenol (mM)	k_{obs} (s^{-1}) Trial 1	k_{obs} (s^{-1}) Trial 2	k_{obs} (s^{-1}) Trial 3	k_{obs} (s^{-1}) Average	Std. dev.
0.5	0.0023	0.0026	0.0025	0.0025	0.00015

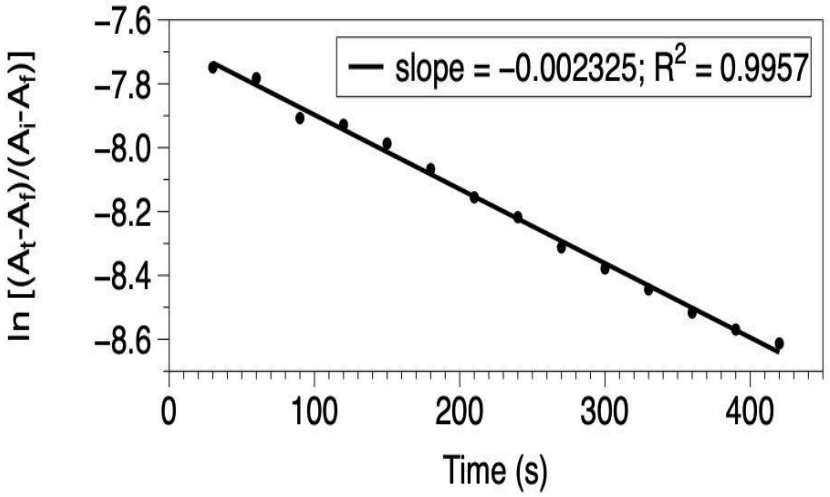

Figure S2.17 Pseudo-first-order plots for the reactions of **2-PMe$_3$** (0.5 mM) and deutoro-2,6-di-tert-butyl-4-methoxyphenol (OD) to determine pseudo-first-order rate constants (k_{obs}).

Phenol (mM)	k_{obs} (s^{-1}) Trial 1	k_{obs} (s^{-1}) Trial 2	k_{obs} (s^{-1}) Trial 3	k_{obs} (s^{-1}) Average	Std. dev.
0.5	0.0008	0.0008	0.0009	0.0008	0.00006

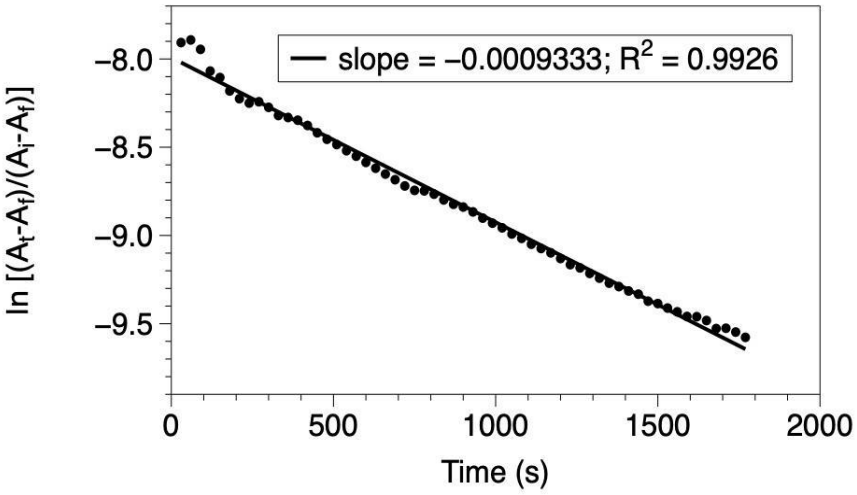

Thermal Decomposition Studies under O_2:

Procedure

In the glovebox, a solution of **2** in THF (3 mL, 0.5 mM) was prepared and transferred to a 1 cm, long-neck cuvette and capped with a Teflon septum. The cuvette was placed in the UV/vis cryostat within a stream of nitrogen, and a spectrum was recorded at 22 °C. The sample was then cooled to -100 °C and spectra were taken to

confirm that the sample was unchanged. Dry O_2 (100%) was bubbled through the cold solution for 10 seconds, then spectra were recorded. The decomposition of the 400 nm LMCT was tracked every 30 seconds for 1 h. For decomposition at higher temperature, the temperature was changed immediately after addition of O_2. After it reached the higher temperature, the solution was allowed to equilibrate for 30 seconds before data collection. Pseudo-first-order rate plots analyzing the first 10% of loss of absorbance were performed by observing the disappearance of a 700 nm d-d bands to obtain plots of $\ln[(A - A_f)/(A_i - A_f)]$ versus time (seconds), which were found to be linear.

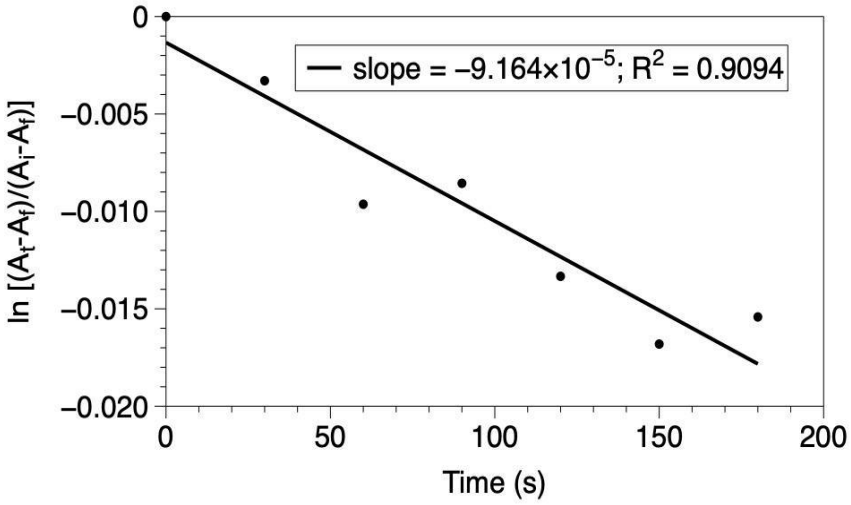

Figure S2.18 Pseudo-first-order plots for the decomposition of **2-PMe$_2$Ph** (0.5 mM) at -100 °C under O_2 to determine pseudo-first-order rate constants (k_{obs}).

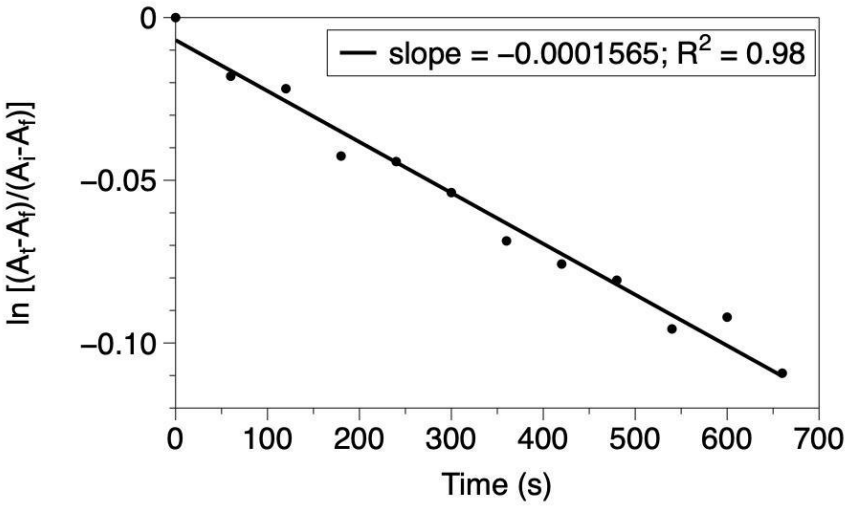

Figure S2.19 Pseudo-first-order plots for the decomposition of **2-PMe$_2$Ph** (0.5 mM) at -85 °C under O_2 to determine pseudo-first-order rate constants (k_{obs}).

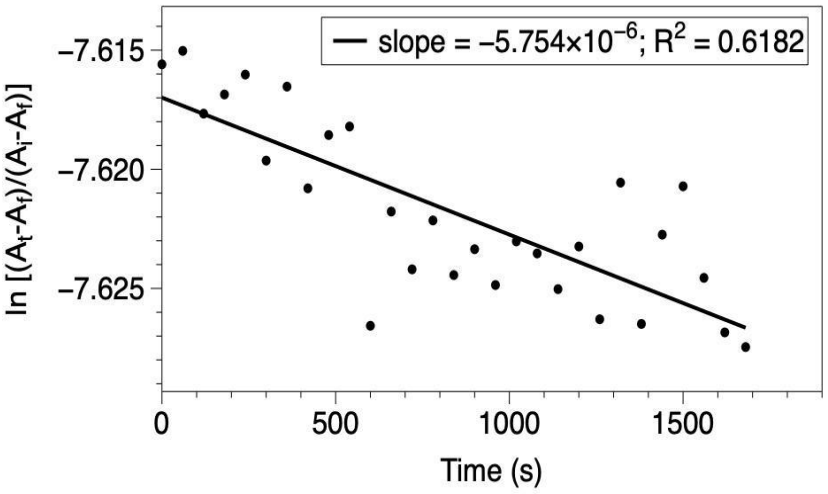

Figure S2.20 Pseudo-first-order plots for the decomposition of **2-PMe$_3$** (0.5 mM) at -100 °C under O_2 to determine pseudo-first-order rate constants (k_{obs}).

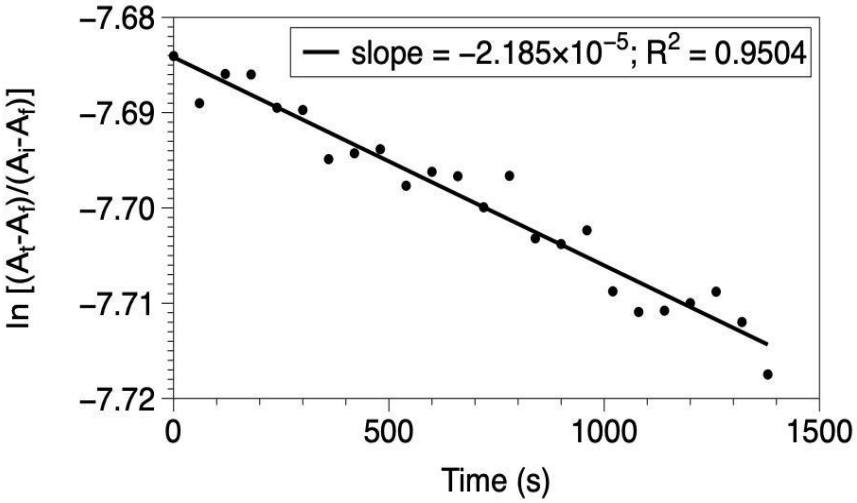

Figure S2.21 Pseudo-first-order plots for the decomposition of **2-PMe$_2$Ph** (0.5 mM) at -80 °C under O_2 to determine pseudo-first-order rate constants (k_{obs}).

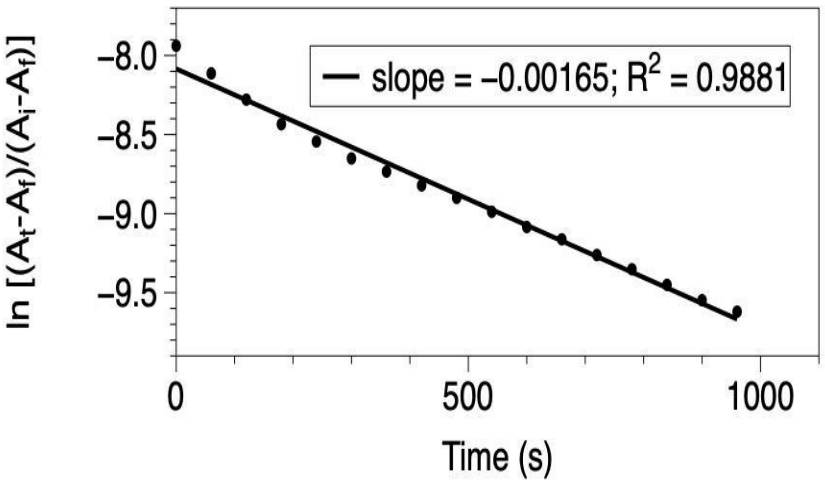

Figure S2.22 Pseudo-first-order plots for the decomposition of **2-PMe$_2$Ph** (0.5 mM) at -80 °C under O_2 to determine pseudo-first-order rate constants (k_{obs}).

Thermal Decomposition Studies under N_2:

Procedure

In the glovebox, a solution of **2** in THF (3 mL, 0.5 mM) was prepared and transferred to a 1 cm, long-neck cuvette and capped with a Teflon septum. The cuvette was placed in the UV/vis cryostat within a stream of nitrogen, and a spectrum was recorded at 22 °C. The sample was then cooled to -100 °C and spectra were taken to confirm that the sample was unchanged. Dry O_2 (100%) was bubbled through the cold solution for 10 seconds, then spectra were recorded. The solution was then sparged with dry N_2 for 30 seconds The decomposition of the 400 nm LMCT was tracked every 30 seconds for 1 h. For decomposition at higher temperature, the temperature was changed immediately after addition of O_2 and before N_2 sparging. After it reached the higher temperature, the solution was allowed to equilibrate for 30 seconds before data collection. Pseudo-first-order rate plots analyzing the first 10% of loss of absorbance were performed by observing the disappearance of a 700 nm d-d bands to obtain plots of $\ln[(A - A_f)/(A_i - A_f)]$ versus time (seconds), which were found to be linear.

Representative trial for each temperature:

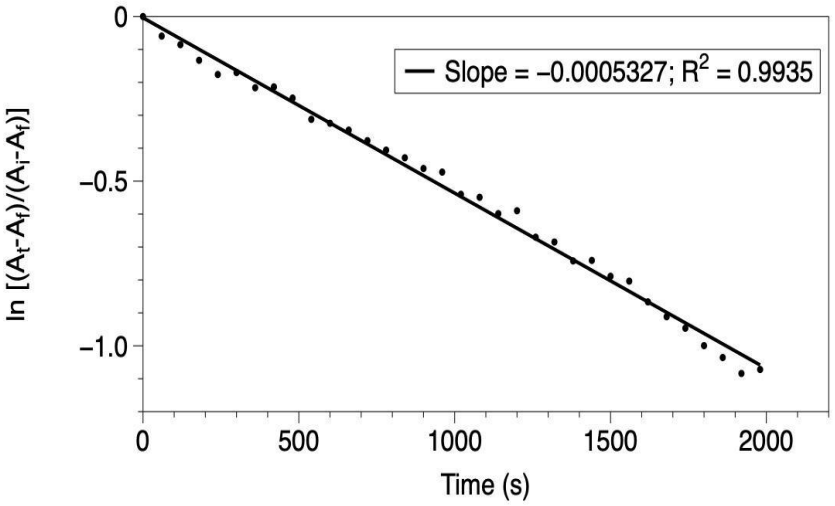

Figure S2.23 Pseudo-first-order plots for the decomposition of **2-PMe$_2$Ph** (0.5 mM) at -100 °C under N_2 to determine pseudo-first-order rate constants (k_{obs}).

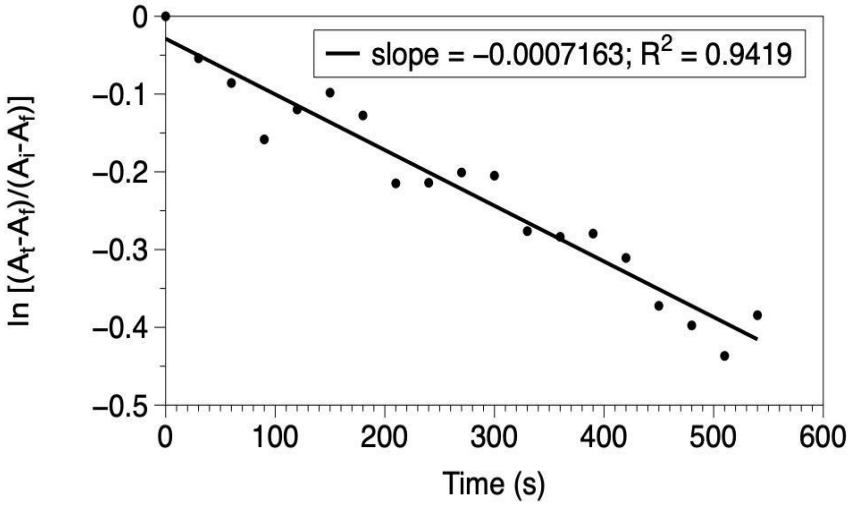

Figure S2.24 Pseudo-first-order plots for the decomposition of **2-PMe$_2$Ph** (0.5 mM) at -95 °C under N_2 to determine pseudo-first-order rate constants (k_{obs}).

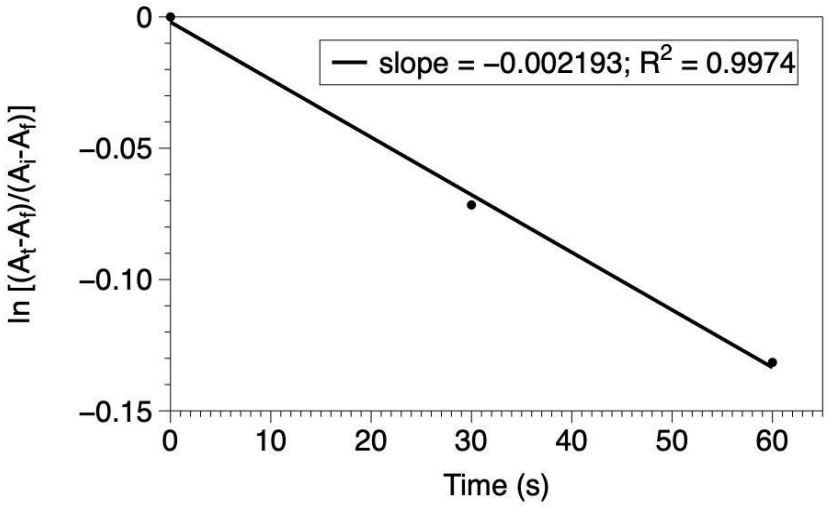

Figure S2.25 Pseudo-first-order plots for the decomposition of **2-PMe$_2$Ph** (0.5 mM) at -90 °C under N_2 to determine pseudo-first-order rate constants (k_{obs}).

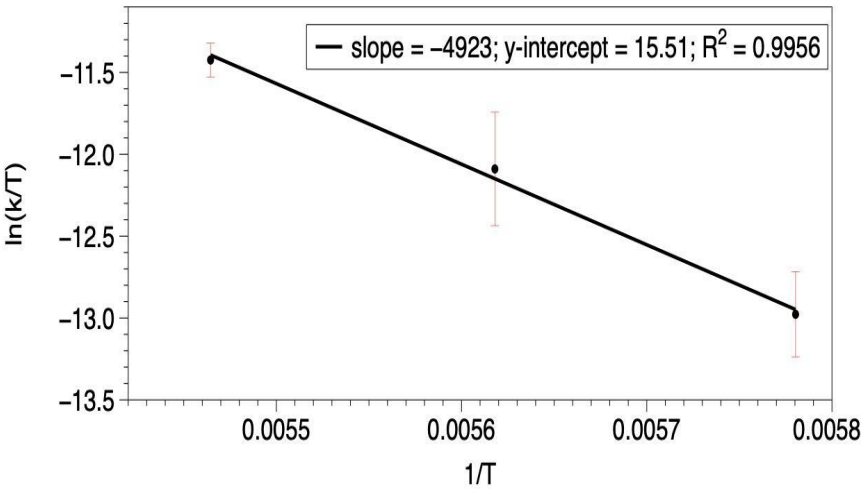

$\Delta H^{\ddagger}$ = 9.9 kcal/mol

$\Delta S^{\ddagger}$ = -16.4 cal/mol

Figure S2.26 Eyring plots for the decomposition of **2-PMe$_2$Ph** (0.5 mM) under N_2.

Heteroleptic bis(cupric)peroxide formation

Procedure

In the glovebox, a solution of **1-(PMe_3, PMe_2Ph)** in THF (2 mL, 0.75 mM) was prepared and transferred to a 1 cm, long-neck cuvette and capped with a Teflon septum. The cuvette was placed in the UV/vis cryostat within a stream of nitrogen, and a spectrum was recorded at 22 °C. The sample was then cooled to -100 °C and spectra were taken to confirm that the sample was unchanged. Dry O_2 (100%) was bubbled through the cold solution for 10 seconds, then spectra were recorded, followed by sparging with N_2 for 30 s. A precooled (-94 ^oC) solution of TMPA-$CuBArF_4$ (1 mL, 1.5 mM) was cannula transferred directly into the cuvette, and UV-vis spectra were immediately recorded.

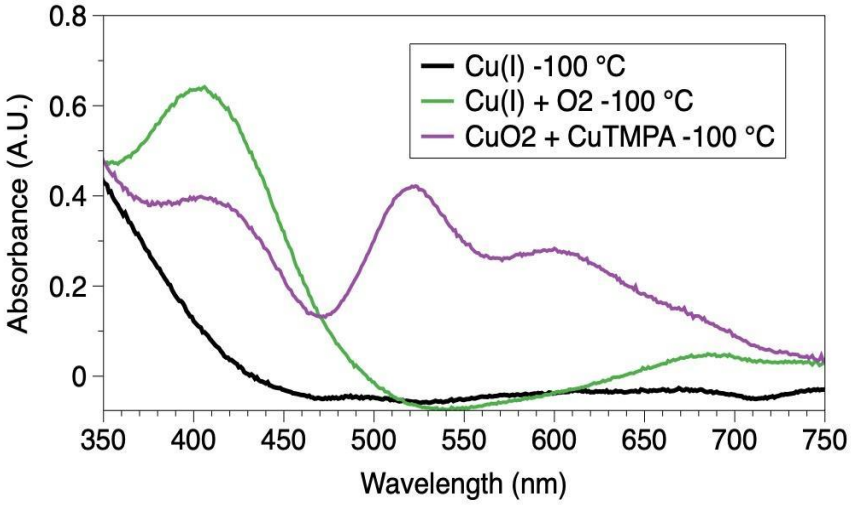

Figure S2.27 UV-vis spectra of compounds **1-PMe_2Ph** (black), **2-PMe_2Ph** (green), and **3-PMe_2Ph** (purple).

Control Procedure

In the glovebox, neat THF was transferred to a 1 cm, long-neck cuvette and capped with a Teflon septum. The cuvette was placed in the UV/vis cryostat within a stream of nitrogen, and a spectrum was recorded at 22 °C. The sample was then cooled to -100 °C and spectra were taken to confirm that the sample was unchanged. Dry O_2 (100%) was bubbled through the cold solution for 10 seconds, then spectra were recorded, followed by 2 minutes of sparging with dry N_2 in order to remove excess O_2. A precooled (-94 ^oC) solution of TMPA-CuBArF$_4$ (1 mL, 1.5 mM) was cannula transferred directly into the cuvette, and UV-vis spectra were immediately recorded. No intensity corresponding to the homoleptic bis(cupric)peroxide complex (TMPA-Cu-O-O-Cu-TMPA) was observed by UV-vis.

Experiments to conclude no formation of a homoleptic bis(cupric)peroxide

Procedure

In the glovebox, a solution of **1-(PMe_3, PMe_2Ph)** in THF (2 mL, 0.75 mM) was prepared and transferred to a 1 cm, long-neck cuvette and capped with a Teflon septum. The cuvette was placed in the UV/vis cryostat within a stream of nitrogen, and a spectrum was recorded at 22 °C. The sample was then cooled to -100 °C and spectra were taken to confirm that the sample was unchanged. Dry O_2 (100%) was bubbled through the cold solution for 10 seconds, then spectra were recorded, followed by 30 seconds of sparging with dry N_2 in order to remove excess O_2, and spectra were obtained to confirm the formation of **1-(PMe_3, PMe_2Ph)**. A precooled (-94 ^oC) solution of **1-(PMe_3,**

PMe_2Ph) (1 mL, 1.5 mM) was cannula transferred directly into the cuvette, and UV-vis spectra were immediately recorded. No new features were seen but signals for **2-(PMe_3, PMe_2Ph)** decreased faster.

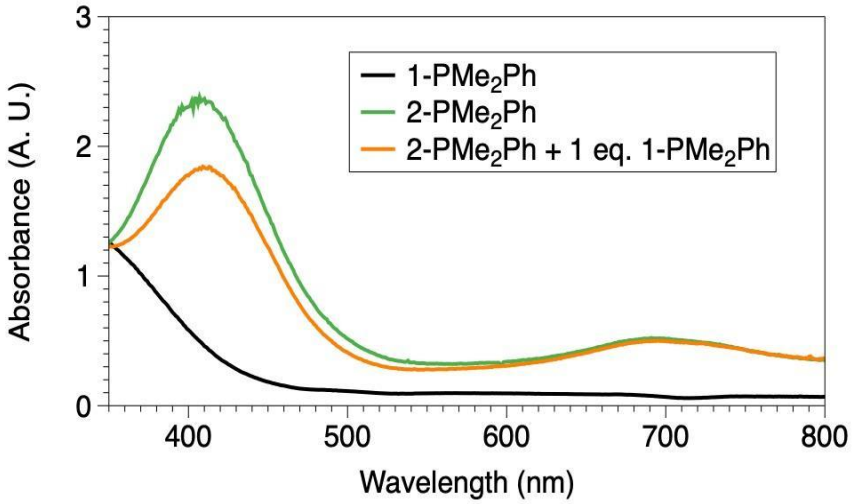

Figure S2.28 UV-vis spectra of compounds **1-PMe_2Ph** (black), **2-PMe_2Ph** (green), and after addition of 1 equiv Of **1-PMe_2Ph** (orange).

Kinetics of enhanced rate of decomposition upon addition of 1 equiv of 1-PMe_2Ph

Procedure

In the glovebox, a solution of **2** in THF (3 mL, 0.5 mM) was prepared and transferred to a 1 cm, long-neck cuvette and capped with a Teflon septum. The cuvette was placed in the UV/vis cryostat within a stream of nitrogen, and a spectrum was recorded at 22 °C. The sample was then cooled to -100 °C and spectra were taken to confirm that the sample was unchanged. Dry O_2 (100%) was bubbled through the cold solution for 10 seconds, then spectra were recorded. A spectrum was recorded to ensure

proper oxygenation by analyzing the peak ~400 nm. The solution was then sparged with dry N_2 for 30 seconds and the **1-PMe$_2$Ph** (pre cooled to -94 °C) was immediately added by transferring from a Schlenk tube with a syringe (100 μL). Spectra were taken every 30 seconds for 1 h. Pseudo-first-order rate plots analyzing the first 10% of loss of absorbance were performed by observing the disappearance of a 700 nm d-d bands to obtain plots of $\ln[(A - A_f)/(A_i - A_f)]$ versus time (seconds), which were found to be linear.

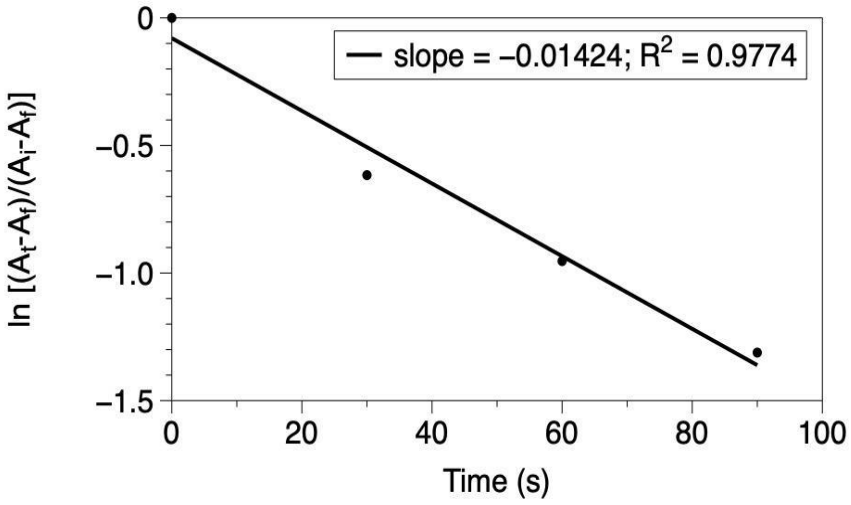

Figure S2.29 Pseudo-first-order plots for the decomposition of **2-PMe$_2$Ph** (0.5 mM) upon addition of 1 equiv of **1-PMe$_2$Ph** at -100 °C under N_2 to determine pseudo-first-order rate constants (k_{obs}).

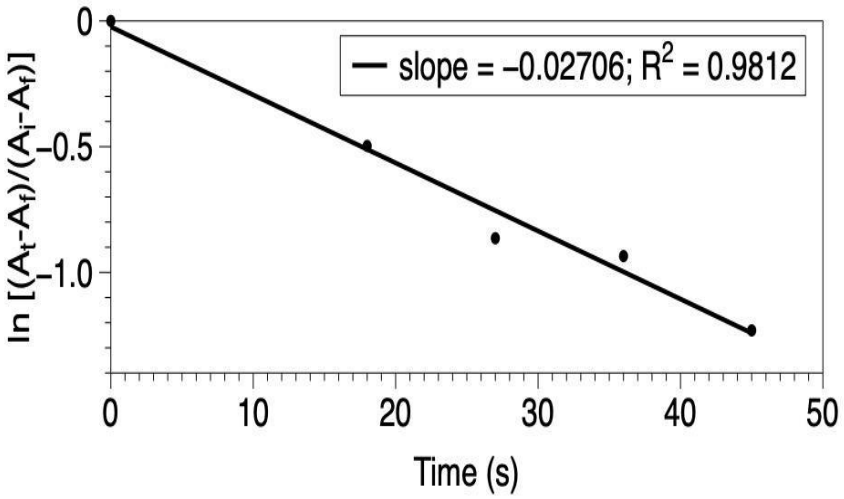

Figure S2.30 Pseudo-first-order plots for the decomposition of **2-PMe$_2$Ph** (0.5 mM) upon addition of 1 equiv of **1-PMe$_2$Ph** at -95 °C under N_2 to determine pseudo-first-order rate constants (k_{obs}).

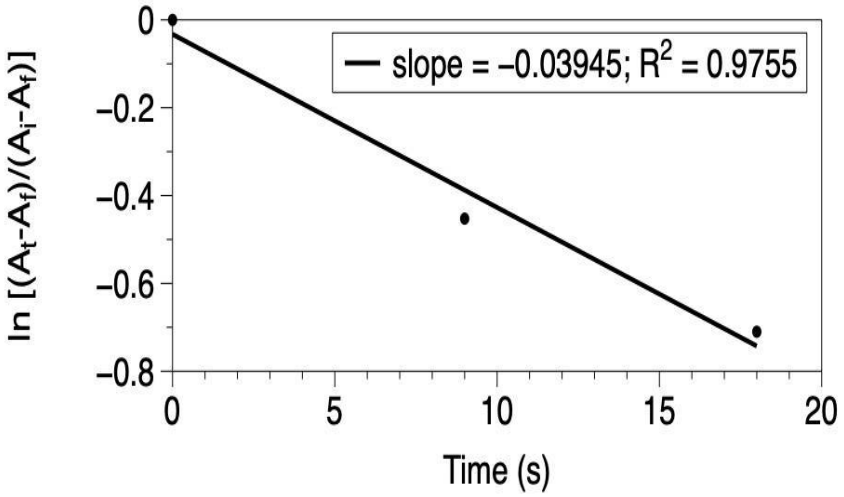

Figure S2.31 Pseudo-first-order plots for the decomposition of **2-PMe$_2$Ph** (0.5 mM) upon addition of 1 equiv of **1-PMe$_2$Ph** at -90 °C under N_2 to determine pseudo-first-order rate constants (k_{obs}).

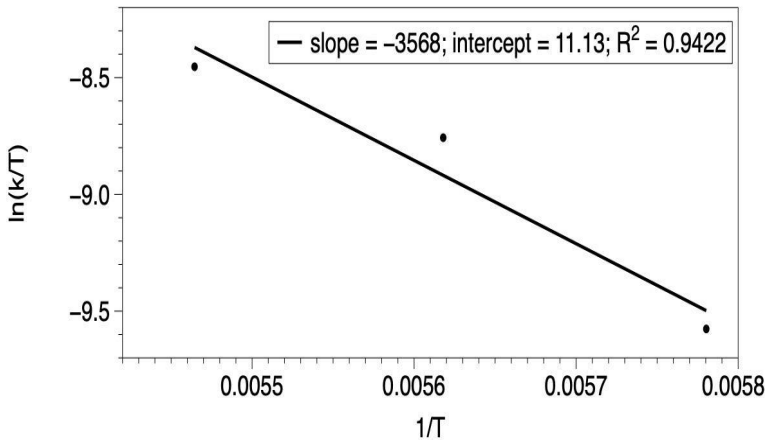

$\Delta H^{\ddagger}$ = 7.1 kcal/mol; $\Delta S^{\ddagger}$ = -25.1 cal/mol

Figure S2.32 Eyring plot for the decomposition of **2-PMe$_2$Ph** (0.5 mM) upon addition of 1 equiv of **1-PMe$_2$Ph** at -90 °C under N_2 to determine pseudo-first-order rate constants (k_{obs}).

Crystallographic analysis

X-ray intensity data were collected on a Bruker D8QUEST[3] CMOS area detector or a on a Bruker APEXII CCD area detector, employing graphite-monochromated Mo-Kα radiation (λ=0.71073Å) at a temperature of 100K. Rotation frames were integrated using SAINT[4], producing a listing of unaveraged F^2 and $\sigma(F^2)$ values. The intensity data were corrected for Lorentz and polarization effects and for absorption using SADABS[5]. The structure was solved by direct methods - ShelXS-97[6]. There was a region of disordered solvent for which a reliable disorder model could not be devised; the X-ray data were corrected for the presence of disordered solvent using SQUEEZE[7]. Refinement was by full-matrix least squares based on F^2 using SHELXL-2017[8]. All reflections were

used during refinement. The weighting scheme used was $w=1/[\sigma^2(F_o^2)+ (0.0369P)^2 + 9.9284P]$ where $P = (F_o^2 + 2F_c^2)/3$. Non-hydrogen atoms were refined anisotropically and hydrogen atoms were refined using a riding model.

X-Ray Structure Data

Table S2.1 Summary of Structure Determination of 1-PMe_3.

Empirical formula	$C_{38}H_{37}BCuF_{20}N_4P_3$
Formula weight	1096.99
Temperature/K	100
Crystal system	triclinic
Space group	P
a	13.4430(19)Å
b	14.253(2)Å
c	14.599(2)Å
α	93.503(7)°
β	105.397(6)°
γ	107.916(6)°
Volume	2534.8(6)$Å^3$
Z	2
d_{calc}	1.456 g/cm^3
μ	0.631 mm^{-1}
F(000)	1120.0
Crystal size, mm	0.17 × 0.14 × 0.08
2θ range for data collection	2.93 - 55.068°

Index ranges	$-15 \leq h \leq 17$, $-18 \leq k \leq 18$, $-18 \leq l \leq 18$
Reflections collected	43606
Independent reflections	11597[R(int) = 0.0372]
Data/restraints/parameters	11597/0/622
Goodness-of-fit on F^2	1.012
Final R indexes [I>=2σ (I)]	$R_1 = 0.0367$, $wR_2 = 0.0873$
Final R indexes [all data]	$R_1 = 0.0558$, $wR_2 = 0.0964$
Largest diff. peak/hole	0.55/-0.57 $eÅ^{-3}$

Table S2.2 Summary of Structure Determination of 1-PPh_3.

Empirical formula	$C_{65}H_{65}N_4O_4F_3P_3SCu$
Formula weight	1211.72
Temperature/K	100
Crystal system	triclinic
Space group	P
a	10.6937(4)Å
b	10.7364(4)Å
c	25.1952(10)Å
α	88.365(2)°
β	83.658(2)°
γ	83.887(2)°
Volume	2858.25(19)$Å^3$

Z	2
d_{calc}	1.408 g/cm^3
μ	0.566 mm^{-1}
F(000)	1264.0
Crystal size, mm	0.28 × 0.08 × 0.05
2θ range for data collection	3.254 - 55.15°
Index ranges	-13 ≤ h ≤ 13, -13 ≤ k ≤ 13, -32 ≤ l ≤ 32
Reflections collected	71105
Independent reflections	13007[R(int) = 0.0567]
Data/restraints/parameters	13007/178/760
Goodness-of-fit on F^2	1.051
Final R indexes [I>=2σ (I)]	R_1 = 0.0641, wR_2 = 0.1554
Final R indexes [all data]	R_1 = 0.0904, wR_2 = 0.1693
Largest diff. peak/hole	2.29/-0.84 eÅ^{-3}

Table S2.3 Summary of Structure Determination of 3-PMe_3.

Empirical formula	$C_{43}H_{49}BCuF_{20}N_7OP_3$
Formula weight	1227.15
Temperature/K	100
Crystal system	monoclinic
Space group	$P2_1/c$
a	16.5506(10)Å
b	20.5218(13)Å

c	15.8428(10)Å
β	105.663(3)°
Volume	5181.2(6)$Å^3$
Z	4
d_{calc}	1.573 g/cm^3
μ	0.629 mm^{-1}
F(000)	2492.0
Crystal size, mm	0.43 × 0.25 × 0.23
2θ range for data collectio	5.754 - 55.21°
Index ranges	-21 ≤h≤ 21, -26 ≤k≤ 26, -20 ≤l≤ 20
Reflections collected	129735
Independent reflections	11995[R(int) = 0.0550]
Data/restraints/parameters	11995/0/696
Goodness-of-fit on F^2	1.051
Final R indexes [I>=2σ (I)	R_1 = 0.0318, wR_2 = 0.0722
Final R indexes [all data]	R_1 = 0.0410, wR_2 = 0.0771
Largest diff. peak/hole	0.43/-0.58 $eÅ^{-3}$

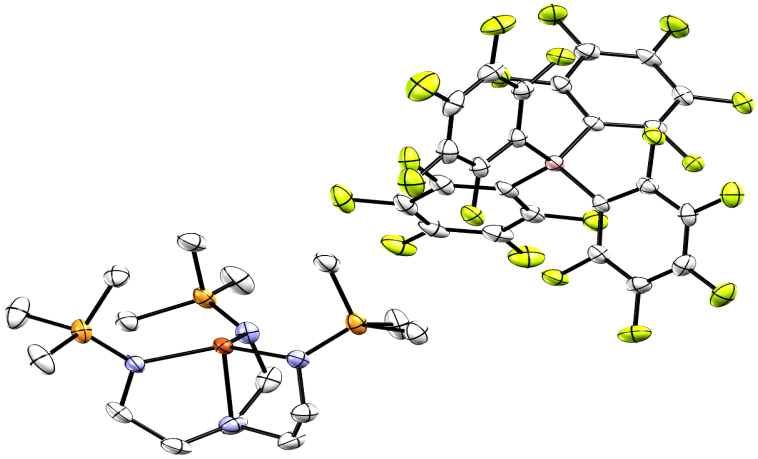

Figure S2.33 Molecular structure of **1-PMe$_3$** with thermal ellipsoids at 50 % probability. All hydrogen atoms were omitted for clarity.

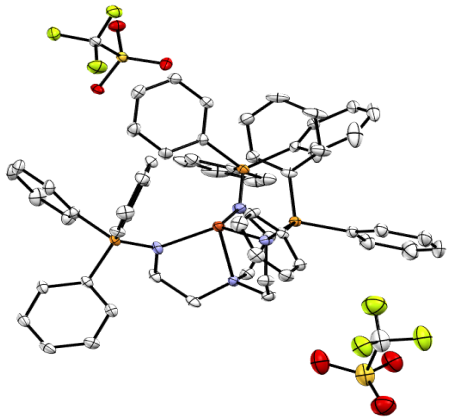

Figure S2.34 Molecular structure of **1-PPh$_3$** with thermal ellipsoids at 50 % probability. Co-crystallized THF and all hydrogen atoms were omitted for clarity.

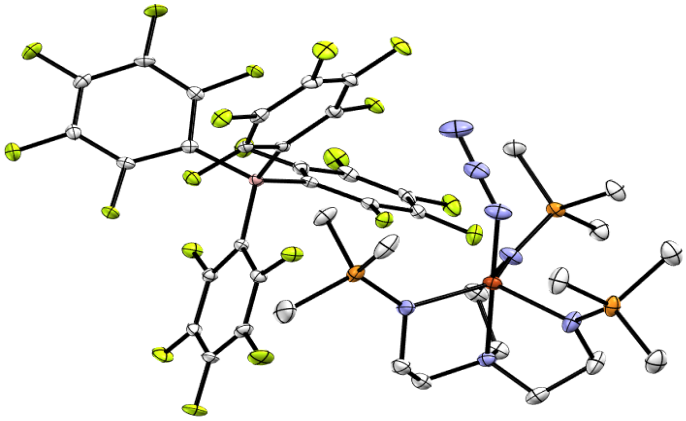

Figure S2.35 Molecular structure of **3-PMe$_3$** with thermal ellipsoids at 50 % probability. Co-crystallized Et_2O and all hydrogen atoms were omitted for clarity.

Table 4: Important Crystallographic Bond Lengths (Å) and Angles (°).

	1-PMe$_3$	**1-PPh$_3$**	**3-PMe$_3$**
Cu-N$_{ap}$	2.1986(17)	2.236(3)	2.1254(14)
Cu-N$_{eq}$ (avg.)	2.0453(17)	2.066(3)	2.0729(14)
N$_{ap}$-Cu-N$_{eq}$ (avg.)	85.03(7)	83.21(12)	82.25(6)
N$_{eq}$-Cu-N$_{eq}$ (avg.)	119.26(7)	118.62(12)	118.2(6)
N-P (avg.)	1.5832(18)	1.584(3)	1.5871(15)
Cu-N$_{azide}$			2.0036(15)
Cu-N$_{azide}$-N$_{azide}$			123.74(13)

Computational Details

All density functional theory (DFT) calculations were performed with the ORCA program package, v3.0.3.[9] Geometry optimizations were carried out at the unrestricted B97-D3 level of DFT. The def2-TZVP basis sets and the def2-TZVP/J auxiliary basis sets (used to expand the electron density in the resolution-of-identity (RI) approach) were used for all atoms except hydrogen. All hydrogens were described using the def2-SVP basis sets and def2-SV/J auxiliary basis sets.[10] The SCF calculations were tightly converged ($1x10^{-8}$ E_h in energy, $1x10^{-7}$ E_h in the density change, and $5x10^{-7}$ in the maximum element of the DIIS error vector). In all cases the geometries were considered converged after the energy change was less than $1x10^{-6}$ E_h, the gradient norm and maximum gradient element were smaller than $3x10^{-4}$ E_h-Bohr^{-1} and $1x10^{-4}$ E_h-Bohr^{-1}, respectively, and the root-mean square and maximum displacements of all atoms were smaller than $6x10^{-4}$ Bohr and $1x10^{-3}$ Bohr, respectively. Numerical frequency calculations were used to verify that the calculated structures represented either local minima (ground states) or saddle points (transition states) on the potential energy surface. The reported energies are Gibbs free energies, calculated for 298.15 K and 1.00 atm, as obtained from numerical frequency calculations on the optimized geometries. The natural bond orbital (NBO) analysis was carried out using the NBO 6.0 program,[11] ran through Orca 3.0. For all MO diagrams presented we held the d_z^2 orbital constant at 0 kcal/mol, where the z-axis is along the Cu-N_{ax} bond.

TDDFT

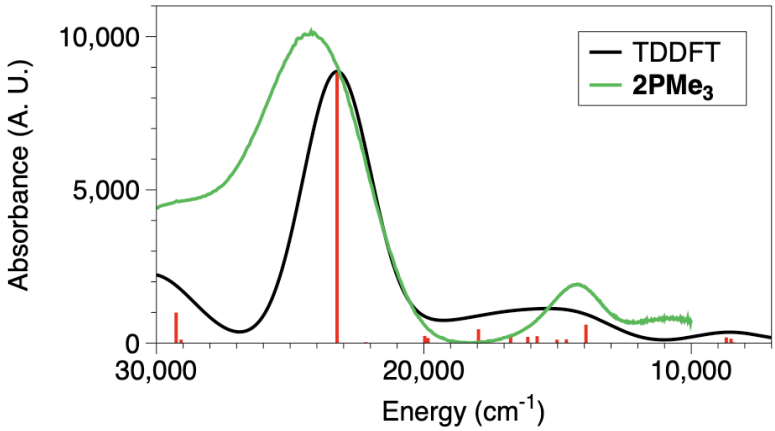

Figure S2.36 Computed UV/vis spectra and transitions for **2-PMe$_3$** with experimental UV/vis data.

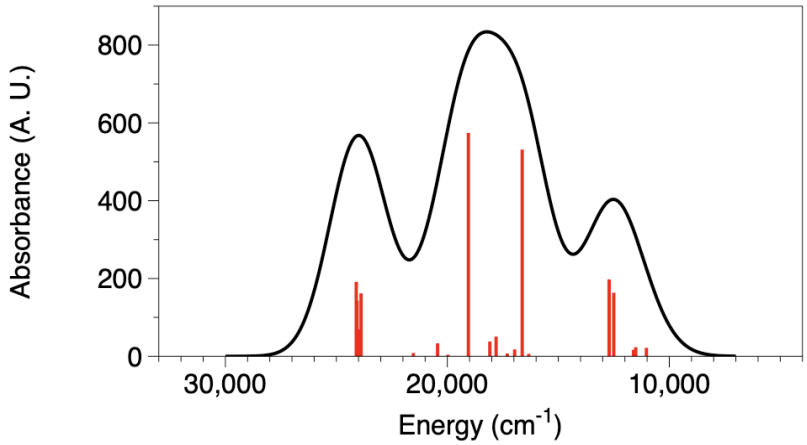

Figure S2.37 Computed UV/vis spectra and transitions for ^{NMe2}**TMPA(CuO$_2$)**.

References

1. Shao, F.; Cahier, B.; Rivière, E.; Guillot, R.; Guihéry, N.; Campbell, V. E.; Mallah, T.; *Inorg. Chem.* **2017**, *56* (3), 1104.

2. Caraballo, R.; Saleeb, M.; Bauer, J.; Liaci, A. M.; Chandra, N.; Storm, R. J.; Frangsmyr, L.; Qian, W.; Stehle, T.; Arnberg, N.; Elofsson ***Org. Biomol. Chem.*** **2015**, 13, 9194.

3. APEX2 2014.11-0: Bruker-AXS, Madison, Wisconsin, USA (2014).

4. SAINT v8.34A: Bruker-AXS, Madison, Wisconsin, USA (2014).

5. SADABS v2014/5: Krause, L., Herbst-Irmer, R., Sheldrick, G.M. & Stalke, D., J. Appl. Cryst., 48, 3-10 (2015).

6. SHELXS-97: Sheldrick, G.M., Acta Cryst., A64, 112-122 (2008).

7. PLATON (v110917): Spek, A.L., Acta Cryst., D65, 148-155 (2009).

8. SHELXL-2017/1: Sheldrick, G.M., Acta Cryst., A71, 3-8 (2015).

9. Neese, F. *WIREs Comput. Mol. Sci.* **2012**, 2, 73.

10. (a) Schaefer, A.; Horn, H.; Ahlrichs, R. *J. Chem. Phys.* **1992**, 97, 2571; (b) Schaefer, A.; Huber, C.; Ahlrichs, R. *J. Chem. Phys.* **1994**, 100, 5829; (c) Weigend, F.; Ahlrichs, R. *Phys. Chem. Chem. Phys.* **2005**, 7, 3297; (d) Weigend, F. *Phys. Chem. Chem. Phys.* **2006**, 8, 1057.

11. NBO 6.0. E. D. Glendening, J. K. Badenhoop, A. E. Reed, J. E. Carpenter, J. A. Bohmann, C. M. Morales, C. R. Landis, and F. Weinhold, Theoretical Chemistry Institute, University of Wisconsin, Madison (2013)]

Chapter 3: Mechanism for the Catalytic Dehydrogenation of Indoline to Indole by Tripodal Phosphinimine Copper Complexes and O_2 with Metal-Ligand Cooperativity

3.1 Introduction

Indoles are pivotal substructures in many biological and industrial chemicals.[1] The main strategy to form indoles is through dehydrogenation of indolines, although C-N coupling strategies have also been developed.[2] While several early dehydrogenation routes were effective, many used stoichiometric oxidants, gave major undesired side products, or produced hazardous waste such as MnO_2.[3] Because of these drawbacks, several groups in the last decade have found alternative synthetic routes that are more selective and exhibit improved atom economy.[4] Notably, Stahl and coworkers have identified several systems that perform the catalytic dehydrogenation of nitrogen heterocycles, including indoline, with O_2 as the oxidant.[5] These systems include a heterogenous cobalt oxide material on nitrogen-doped carbon as well as a homogeneous ruthenium catalyst that requires a cobalt salophen co-catalyst. Despite these initial successes, little information is available on the mechanisms by which metal complexes may use O_2 to perform the oxidation of indolines to indoles, hampering the development of superior catalysts with improved performance, cost, and selectivity.

Copper-based catalysts offer a non-toxic alternative to noble metals, and methods have been developed for the selective oxidation of indolines by Cu-based systems for the synthesis of complex pharmaceutical precursors. However, these system required stoichiometric oxidants such as *tert*-butylhydroperoxide and *tert*-butylperacetate that

yield organic byproducts.[4a,b] To date, one Cu:O_2 system has been reported for the catalytic, aerobic oxidation of indolines, $CuCl(pyr)_x$ in methylene chloride.[3d] A limited substrate scope and a kinetic study were used to propose a rate law of rate = k_{obs}[indoline][catalyst][O_2]. Based on the faster rate of indoline oxidation when using CuCl compared to $CuCl_2$, the authors proposed that oxygenation of a Cu(I)/indoline adduct must be rate limiting.[6]

Herein, we report the catalytic oxidation of a variety of indolines, using a tren-based tris(dimethylphenylphosphiniminine) ligand (P_3tren) copper(I) complex. We have previously reported that a cupric superoxide supported by this ligand framework can perform the abstraction of a hydrogen atom from 2,6-di-*tert*-butyl-4-methoxyphenol.[7] Indolines present a particular challenge for oxidation by cupric superoxides owing the strong N–H and C–H bonds within the five-membered ring. Calculated gas-phase bond dissociation energies (BDEs) of 86.9 and 87.6 kcal/mol, respectively, have been reported,[8] using a methodology that was shown to be reliable for predicting the experimental BDEs within indole. The high indoline BDEs are notable because cupric superoxides have previously only been shown to abstract a hydrogen atom from a substrate with a BDE of ~83 kcal/mol.[9] To overcome this difference, our system was engineered to allow for metal-ligand cooperativity, such that the phosphinimine arms could either act as a base to deprotonate indoline or hydrogen bond with the NH of indoline as a way to orient indoline for C–H activation by the superoxide. Detailed below are experiments that illustrate the importance of metal-ligand cooperativity to indoline dehydrogenation.

3.2 Results and Discussion

3.2.1 Results from Catalysis

The treatment of various indoles with a catalytic amount of [(P_3tren)Cu][$BArF_{20}$] (**1**) in THF or MeCN under 1 atm of O_2 at room temperature (RT) afforded indoles in good yields and with high selectivity (Table 3.1). For example, in MeCN, **1** (20 mol %) catalyzes the quantitative oxidation of indoline to indole over 7 h at RT (entry 1). When the solvent was switched to THF, the reaction still provided high conversion over 7 h, yielding 90 % indole (entry 2). Quantitative conversion in THF was reached with longer reaction time (entry 3). Attempts to lower the catalyst loading led to higher turnover numbers (TONs) but lower overall conversion (entries 4-6). All further reactions were therefore run at 20 mol % loading of **1** in MeCN-d_3 at RT for 14 h on an NMR scale.

The roles of copper and ligand were investigated with various control experiments (Table 3.2). First, the P_3tren ligand was found to be crucial to catalysis. Replacement of P_3tren with the parent tren ligand, tris(2-aminomethyl)amine, severely reduced indole formation (entries 1-3). Second, copper needs to be included to observe indoline dehydrogenation (entries 1, 4). Finally, it was found that a (P_3tren)Cu(II) complex with weakly coordinate anions was also able to effect turnover (entry 5). Concordantly, when (P_3tren)Cu(OTf_2) is used as a stoichiometric oxidant in the absence of O_2, the indoline dehydrogenation still proceeds in 45% yield (entry 6) or in 92 % yield when the concentration of (P_3tren)Cu(OTf_2) is doubled (entry 7).[9] However, preliminary studies suggest that (P_3tren)Cu(OTf_2)-mediated indoline dehydrogenation proceeds through an

alternative mechanism and will thus not be described further as it relates to the present study.[10]

Table 3.1 Selected optimization of indoline oxidation.[a]

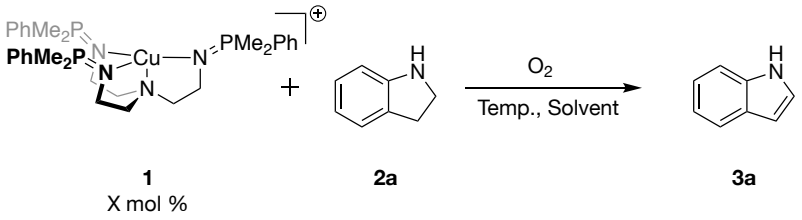

1
X mol %

2a

3a

Entry	Cu mol %	Solvent	T (°C)	Time	Yield[b]	TON
1	20	MeCN	20	7 h	100 %	5
2	20	THF	20	7 h	90 %	4.5
3	20	THF	20	14 h	100 %	5
4	5	MeCN	20	14 h	60 %	12
5	1	MeCN	20	14 h	13 %	13
6	0.1	MeCN	20	14 h	5.4 %	54

[a]By comparison of ^{1}H NMR spectra with published data. [b]By integration of product in ^{1}H NMR spectra versus 1,3,5-trimethoxybenzene internal standard.

Variations to the electron donating or withdrawing nature of substituents at the 5- and 6-positions of the indoline rings were used to provide *para*- and *meta*-substituent effects on the dehydrogenation reaction (Figure 3.1). Quantitative conversion was reached with indolines bearing strong electron donating groups, e.g. methoxy groups, at either the 5-(**3b**) or 6- (**3c**) position to their respective indoles. Lower conversions were obtained when electron-withdrawing groups were employed in the 5- (nitro, **3d**, 38 %) or 6- (nitro, **3e**, 30 %; trifluoromethyl, **3f**, 35 %) positions. The low yields for the electron poor substrates are attributed to slower reaction rates, which allow for catalyst

decomposition. Increased reaction times do not lead to improved yields, and the phosphinimine arms of P_3tren are known to be hydrolytically sensitive. Specific data on the relative rates of these reactions will be described below.

Table 3.2 Selected controls of indoline oxidation.[a]

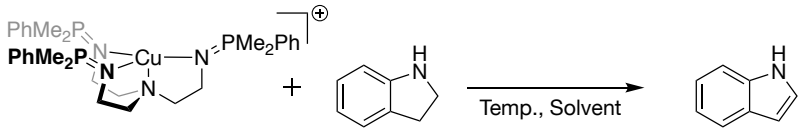

1
X mol %

2a

3a

Entry	Ligand	Cu Source	catalyst mol %	O_2	Yield[b]
1	none	none	0	Yes	0 %
2	none	$CuBArF_{20}$	20	Yes	23 %
3	tren	$CuBArF_{20}$	20	Yes	25 %
4	P_3tren	none	20	Yes	0 %
5	P_3tren	$Cu(OTf)_2$	20	Yes	100 %
6	P_3tren	$Cu(OTf)_2$	100	No	45 %
7	P_3tren	$Cu(OTf)_2$	200	No	92%

[a] By comparison of ^{1}H NMR spectra with published data. [b] By integration of product in ^{1}H NMR spectra versus 1,3,5-trimethoxybenzene internal standard.

When methyl groups were employed at either the 1- (**3g**) , 2- (**3h**), 3- (**3i**), or 2,3- (**3j**) positions, little to no indoles were formed. In the case of 1-methylindoline, 0% indole was formed and all starting indoline could be recovered (**3g**). For the 2-methyl, 3-methyl or 2,3-dimethylindoline (**3h**, **3i**, **3j**), starting material was consumed but no products could be positively identified by NMR spectroscopy. GC/MS analysis of these latter reactions gave multiple peaks, some of which exhibited fragments consistent with the addition of one oxygen atom (**3h**, **3i**) or two oxygen atoms (**3j**). The oxygen could

possibly have inserted into the C-H or C-C bond of the methyl groups but no further analysis was performed because of the complexity of these reactions.[11]

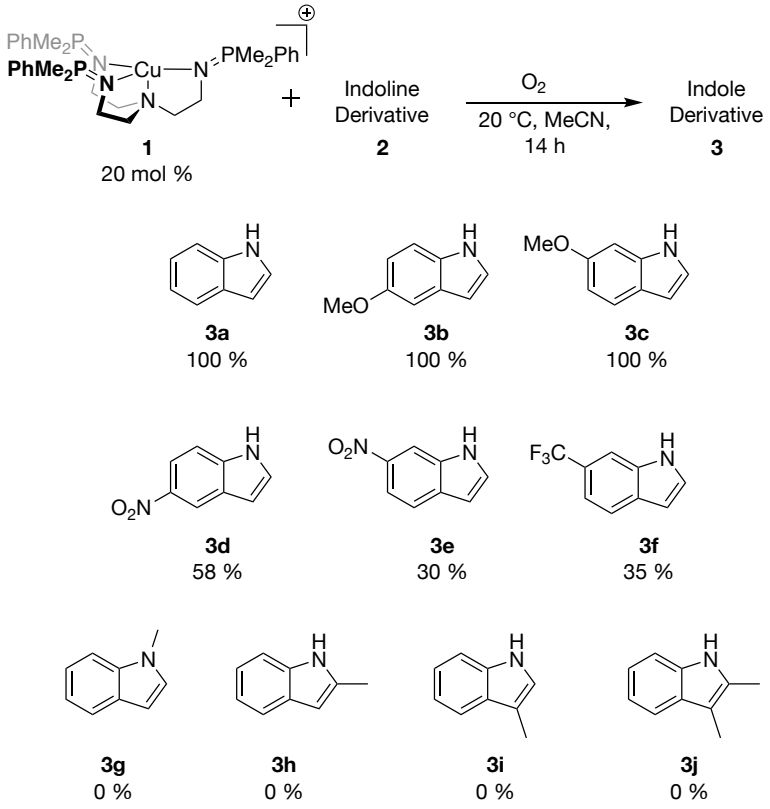

[a]By comparison of ^{1}H NMR spectra with published data. [b]By integration of product in ^{1}H NMR spectra versus 1,3,5-trimethoxybenzene internal standard.

Figure 3.1 Scope of indolines for oxidation to indole.

3.2.2 Mechanistic Studies

3.2.2.1 Background

The successful mediation of indoline dehydrogenation by [(P_3tren)Cu][$BArF_{20}$] prompted an investigation into the mechanism of the reaction. We sought to answer four major questions: 1) what is the rate law of the reaction; 2) what is the overall

stoichiometry of the reaction; 3) what is the rate determining step (RDS) of the reaction; and 4) what are the active catalytic species in the reaction? The first question aims to give insight into the stoichiometry of the rate-determining step, which will aid in analysis of the remaining questions. The second question is aimed at determining the fate of the oxygen containing species at the end of the catalytic cycle. This is expected to give insight into how the cycle can turn over and establish the overall stoichiometry. Next, the nature of the rate determining step will be discussed, focusing on which bonds are activated by the basic phosphinimine arms, in a metal-ligand cooperative manner, to aid in proton coupled electron transfer (PCET) with the oxygen moiety. The nature of the PCET type process will also be discussed. Finally, we have previously shown that (P_3tren)Cu can be treated with O_2 at low temperatures to form an end-on superoxide. The competency of this end-on superoxide for indoline dehydrogenation will be discussed and compared to RT reactions to lend credence to our assignment of a cupric superoxide as the active species at RT.

3.2.2.2 Kinetics

Kinetic studies were undertaken to establish the rate law of the catalytic reaction. Under 1 atm of O_2, the rate constants, k_{obs}, were determined by monitoring the decay of indoline signals by ^{1}H NMR spectroscopy.[12] The order of reagents was determined by testing three different concentrations for each. A plot of k_{obs} vs. [Cu] showed a linear dependence on the initial concentration of Cu in the range of 1.1-2.3 mM (Figure 3.2a), indicative of the reaction being first order in [(P_3tren)Cu(I)]. Similarly, a plot of k_{obs} vs. [indoline] showed a linear dependence over indoline concentrations of 1.1-2.3 mM

(Figure 3.2b), indicating that the reaction is also first order in [indoline]. Finally, the rate dependence on [O_2] was examined. Under initial headspace pressures of 0.01 atm (0.99 atm N_2), 1 atm, and 2 atm O_2, all reactions gave the same k_{obs} of -7 x 10^{-7} s^{-1}. All of these pressures exceed that needed to saturate MeCN-d_3 with O_2, making the [O_2] in solution dependent on the spinning rate of the NMR tube (see experimental for more details).[9] When the amount of added O_2 was decreased to ~0.5 equiv (0.1 atm of 1% O_2 in N_2), the k_{obs} lowered to -4 x 10^{-7} s^{-1}. The exact order of O_2 could not be determined from these data, but the positive correlation between [O_2] and rate suggests that a rate law of the form rate = k_{obs}[(P_3tren)Cu(I)][indoline][O_2]^x (x > 0) is appropriate.

3.2.2.3 Stoichiometry Determination

We next sought to determine the fate of the H_2-equivalent that is removed from indoline. Aerobic oxidation chemistry may proceed through either a 2 e^-, 2 H^+ process to generate H_2O_2 or a 4 e^-, 4 H^+ to form H_2O. Under optimized reaction conditions with the parent indoline as the substrate, 6 % hydrogen peroxide was detected after five minutes. This is lower than the 18 % yield of indole that was found by ^{1}H NMR spectroscopy after five minutes.[13] After fifteen minutes, 0 % hydrogen peroxide could be detected. These observations confirm that hydrogen peroxide is a reaction product but that H_2O_2 does not persist under the reaction conditions.

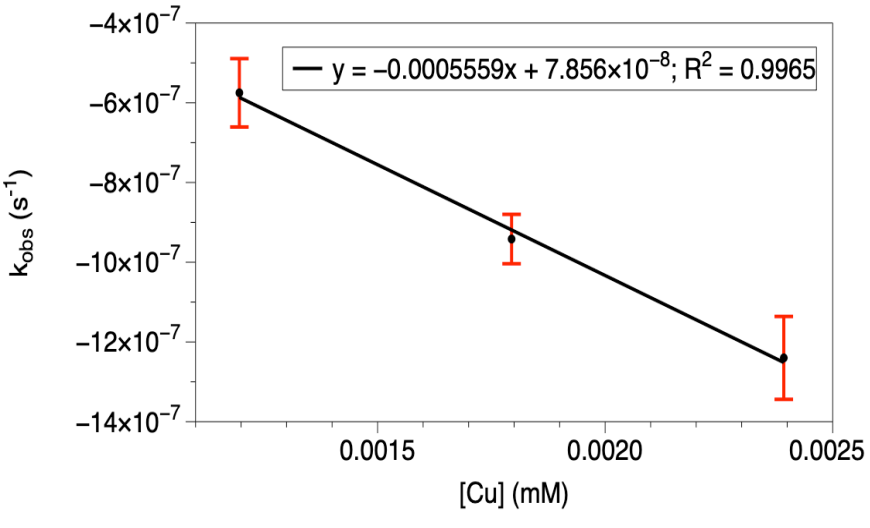

(a)

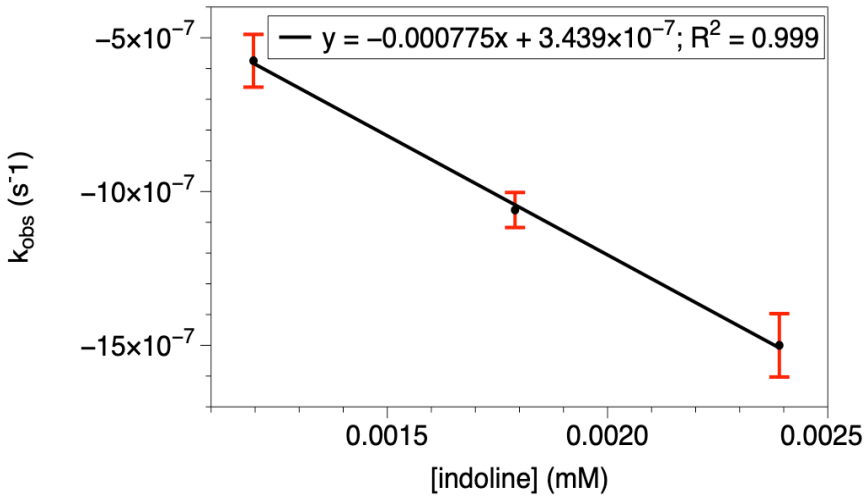

(b)

Figure 3.2 Dependence of the reaction rate on (a) copper concentration and (b) indoline concentration.

Table 3.3 Selected controls of indoline oxidation using H_2O_2 as the oxidant.[a]

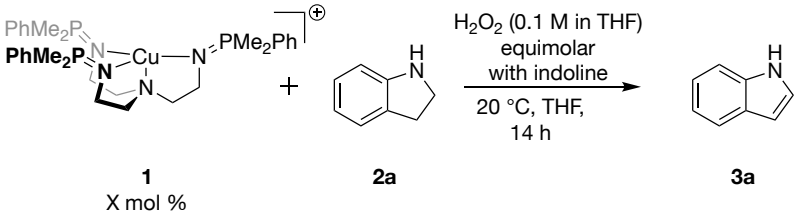

1
X mol %

2a

3a

Entry	Cu Source	Cu mol %	Yield
1	none	none	0 %
2	$(P_3tren)CuBArF_{20}$	20 %	19 %
3	$(P_3tren)CuBArF_{20}$	100 %	18 %

[a]By comparison of ^1H NMR spectra with published data. [b]By integration of product in ^1H NMR spectra versus 1,3,5-trimethoxybenzene internal standard.

A series of control reactions using H_2O_2 as the oxidant were performed to gauge its ability to perform indoline dehydrogenation, either in the presence or absence of Cu salts (Table 3.3). When indoline was treated with 1 equiv of H_2O_2 (0.1 M in THF), the indoline was completely consumed and formed a complex mixture of products. However, indole formation was not detected (entry 1). When $(P_3tren)Cu(I)$ was used at 20 mol % loading, only 18 % (entry 2) of indole is formed while at 100 mol % loading, only 19 % (entry 3) indole was formed. This indicates that hydrogen peroxide is a competent oxidant but is not solely responsible for the dehydrogenation of indoline.

3.2.2.4 Synthetic Observations and Deuterium Labeling

As part of our substrate screen, we noted the different reaction outcomes when placing methyl groups at the 1(N)-, 2-, or 3-positions of the indoline ring. The inclusion of methyl groups on the 2- and 3-positions of the ring led to a wide range of products,

presumably due to oxidation of the methyl substituents. However, the *N*-methyl substrate (**2g**) failed to provide conversion away from the starting material, indicating that the substrate was unable to perform a critical step in initiating activation by the Cu catalyst. We propose that the importance of the NH group could either result from an initial proton coupled electron transfer (PCET) to form an aminyl radical, as has been proposed in the literature,[3d] or the NH group may be necessary for an acid-base interaction with (P_3tren)Cu prior to indoline activation.

Reaction rate monitoring with ND-indoline and NH-indoline afforded a KIE of 1, which suggests that any activation of the N–H bond of indoline is not part of the rate determining step (RDS). This contrasts with a KIE study on isotopic substitution at the α-position of the indoline ring. The use of α-D_2-indoline as a substrate afforded a KIE of 2.36. This value is in good agreement with other KIE values reported for Cu/O_2 chemistry and provides support for the view that either deprotonation or a PCET involving an α-C–H bond of indoline is rate determining.[8]

To further investigate the role of the N–H substitution on the ability of (P_3tren)Cu to activate indolines, we sought to understand the interaction of indoline and (P_3tren)Cu under anaerobic conditions. A series of variable temperature (VT) $^{31}P\{^1H\}$ NMR studies were conducted. In the absence of indoline, the VT $^{31}P\{^1H\}$ NMR spectra of (P_3tren)Cu remain unchanged over the available temperature range (-63 to 27 °C), exhibiting a singlet at 22.7 ppm. On addition of 1.0 equiv of indoline, two new signals evolve below -23 °C, one at ~40 ppm and another ~33 ppm in a 1:2 ratio, respectively, with a 1:1.85 ratio for the ~33/22.7 ppm peaks. As the temperature is further decreased, the 40 ppm

peak shifts downfield (0.4 ppm over 40 °C), and the 33 ppm peak shifts upfield (2.3 ppm over 40 °C), while the peak for (P_3tren)Cu(I) remains at 22.7 ppm across the temperature region. While decreasing the temperature, we also observed an increase in the ratio of the 40/33 ppm signals to the signal at 22.7 ppm with a maximum ratio of 1:1.3 at -63 °C. Here it is important to note that when 1 equiv of $HBArF_{24}{\cdot}2Et_2O$ was added to (P_3tren)Cu(I), we observed two new signals, one at 47 ppm and another at 34 ppm in an integral ratio of 1:2, respectively. These signals were assigned as one protonated P_3tren arm (47 ppm) and two Cu-bound P_3tren arms (34 ppm). The correspondence between these signals to those observed in mixtures of indoline and (P_3tren)Cu(I) led us to hypothesize that these solutions form an equilibrium between the starting materials and an adduct between the NH of indoline and one of the phosphinimine arms of the ligand. This view is also consistent with the observation that lower temperatures lead to higher concentrations of the adduct, as expected for system that is entropically disfavored.

The nature of the (P_3tren)Cu(I):indoline adduct could span a hydrogen-bonding interaction to full deprotonation and generation of a Cu(I) indolinide. We favor a hydrogen-bonding interaction for the following reasons. ^{1}H NMR spectroscopic data on mixtures of indoline with either free ligand or (P_3tren)Cu(I) at 20 °C show no loss of N-H peak intensity or change in chemical shift. As the sample is cooled to -63 °C, the signal for the indoline NH proton retains its intensity but gradually shifts downfield by 0.34 ppm. In contrast, if stronger bases such as nBuLi or KH are used, indoline can be fully deprotonated. Further, the pK_a of related complexes are known. Indole has an estimated pK_a of 34.5 in MeCN, as extrapolated from a measured pK_a of 22.1 in

DMSO,[14] and the pK_a of *N*-adamantyl-trimethyliminophosphorane was found to be 26.2 through titration of the base with DBU-H$^+$.[7] These data suggest that an arm of P_3tren may be basic enough to form a complex with the NH of indoline but not lead to full deprotonation.

3.2.2.5 Hammett Analysis

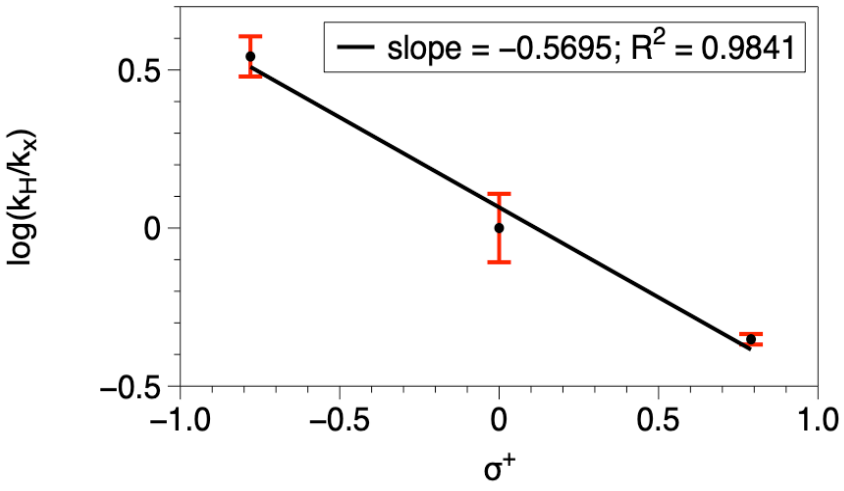

Figure 3.3 Hammett correlation plot for the catalytic dehydrogenation of indoline by (P_3tren)Cu(I) under O_2.

To further parse the electronic effects of indoline substitutions, rate constants, k_{obs}, were determined by ^{1}H NMR spectroscopy for 5-nitroindoline, indoline, and 5-methoxyindoline. A linear relationship was observed in a Hammett plot for the catalytic dehydrogenation of these three indolines using σ^+ values (Figure 3.3), resulting in a ρ-value of −0.57. This negative ρ-value is consistent with a buildup of positive charge on indoline during the rate-determing step, which was shown above to involve cleavage of the α-C–H bond. Furthermore, the observation that substrates with electron

withdrawing groups are dehydrogenated more slowly is particularly relevant since it lends evidence that the rate-determining step involves PCET, not deprotonation, the latter of which would result in the buildup of anionic charge on indoline in the RDS.

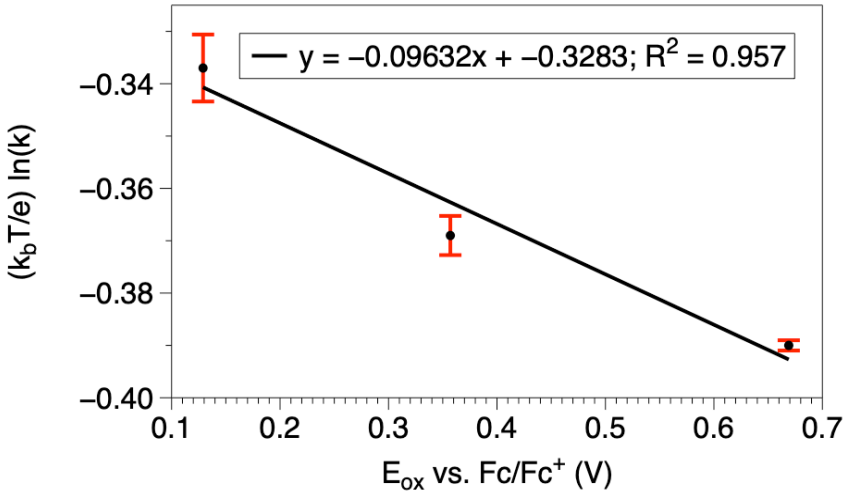

Figure 3.4 Plot of (k_BT/e) ln(k) versus E_{ox} for the catalytic dehydrogenation of indoline by 1 under O_2.

Related Cu/O_2 systems have been gated by the electron transfer portion of the PCET process for phenol substrates,[9] but the description of this PCET process as an asynchronous ET-PT or as an HAT cannot be answered by data from the Hammett analysis. The Karlin group has previously distinguished between the two pathways by plotting (k_BT/e)ln(k) vs. E_{ox}. Slopes near -0.05 represent an HAT process, and those between -0.5 and -1.0 represent an asynchronous ET-PT process. For context, positive slopes are obtained for a proton-transfer-gated process. Karlin and coworkers studied the PCET reaction of phenols with [(DMM-tmpa)$Cu^{II}(O_2^{\bullet-})]^+$ [DMMtmpa = tris((4-methoxy-3,5-dimethylpyridin-2-yl)methyl)-amine] and found a slope of -0.29, which was

determined to represent an HAT process with a modest amount of leading electron-transfer character.[9] The plot of $(k_BT/e)\ln(k)$ vs. E_{ox} for the present catalytic dehydrogenation of indolines exhibited a slope of -0.096, consistent with an HAT process with a minor amount of leading electron transfer.

3.2.2.6 Stoichiometric Indoline Reactivity with P_3tren-Cupric Superoxide

Considering the assembled mechanistic data and our previous observation that the formation of 2:1 Cu:O_2 complexes supported by P_3tren are thermodynamically unfavorable,[7] we hypothesize that a 1:1 Cu:O_2 adduct is the most likely active species. Our group has previously characterized an end-on cupric superoxide supported by P_3tren (**4**) that displays significant stability at low-temperatures. This species exhibits a characteristic LMCT band at *ca*. 400 nm by UV/vis spectroscopy, and it was shown to perform the net abstraction of a hydrogen atom from 2,6-di-*tert*-butyl-4-methoxyphenol to yield the phenoxyl radical. We thus sought to determine if **4** would be competent for indoline dehydrogenation.

Complex **4** was generated at -94 °C, then treated with 1.0 equiv of indoline. The mixture was stirred at this temperature for 1, 2 or 3 h before all volatile materials were removed under vacuum while maintaining the flask temperature below -94 °C. Analysis of the crude reaction mixtures by ^{1}H NMR spectroscopy revealed indole yields of 8 %, 15 % and 18 %, respectively. The modest increase in yield between the 2 h and 3 h time points is attributable to the thermal decomposition of **4**, as the half-life of **4** is 30 min, under N_2 at -95 °C.[7] Finally, we

note that **4** does not react with 1-methylindoline under these reaction conditions, as is the case for the catalytic conditions described above.

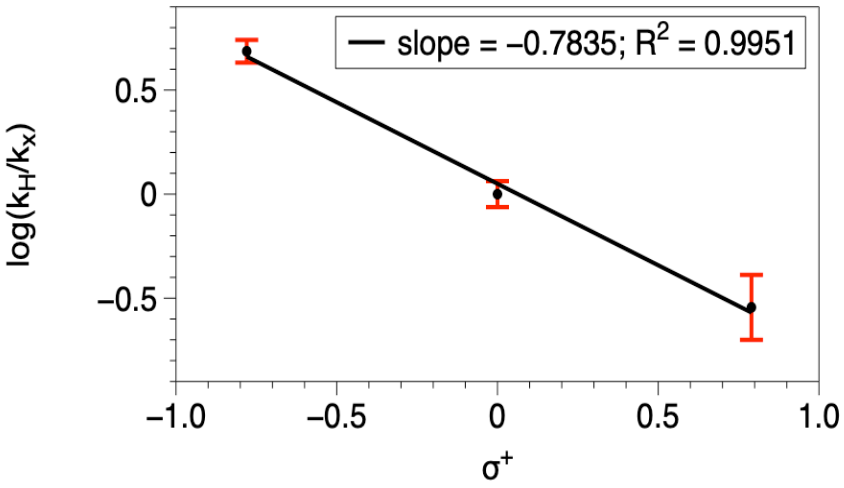

Figure 3.5 Hammett correlation plot for the catalytic dehydrogenation of indoline by cupric superoxide, 4, at -100 °C in THF.

To further determine the extent to which the dehydrogenation of indolines by **4** at low temperatures is related to the catalytic indoline oxidation chemistry performed at room temperature, we analyzed the rates by which various substituted indolines caused the decay of **4**. The superoxide was generated at -100 °C in THF by treating $[(P_3tren)Cu][BArF_{20}]$ with O_2, then the cuvette was sparged with N_2 and the solution was treated with 1 equiv of 5-nitroindoline, indoline, or 5-methoxyindoline. Tracking the decay of the *ca*. 400 nm LMCT band corresponding to **4** allowed for determination of reaction rate constants, k_{obs}, at -100 °C. A Hammett plot of the resulting data revealed a values of ρ = -0.78 (Figure 3.5). This ρ-value is similar to that obtained at RT (ρ = -0.57) and correlates with a build-up of positive charge on

indoline in the transition state of the RDS. Related variable-temperature Hammett analyses show similar changes in ρ with temperature; examples show a $|\Delta\rho| = 0.06$ to 0.1 with a change in temperature of 15 °C, and steeper slopes are observed at lower temperatures.[15]

The slower reaction rates at lower temperatures allowed us to perform an Eyring analysis over the temperature range of -100 to -85 °C on the oxidation chemistry mediated by **4**. Doing so revealed $\Delta H^{\ddagger}$ = 1.7 kcal/mol and $\Delta S^{\ddagger}$ = -61 cal/K-mol. The large-negative $\Delta S^{\ddagger}$ indicates the presence of a highly ordered transition state, as expected for the movement of a dissociated phosphinimine arm that is hydrogen bonding to indoline into a geometry that is suitable for HAT to the O_2 fragment.[16]

3.2.2.7 Reaction Mechanism

Scheme 3.1 shows a proposed mechanism for the catalytic dehydrogenation of indoline by (P_3tren)Cu (**1**) and O_2. First, indoline coordinates to P_3tren through H-bonding of the indoline N-H with the phosphinimine arm. Experimental evidence for this interaction was shown through VT NMR spectroscopy of (P_3tren)Cu and indoline, which at lower temperatures exhibited both downfield shifts of the indoline N–H signal with no loss of intensity and a signal near that of protonated (P_3tren)Cu in samples $^{31}P\{^{1}H\}$ NMR spectrum. Also, 1-methylindoline was not dehydrogenated by the (P_3tren)Cu:O_2 system, suggesting that the N-H of indoline may to integral in substrate activation.

The next step in the proposed mechanism involves oxidation of Cu(I) by O_2 to form an end-on cupric superoxide, which without indoline bound, has been shown to

have an equilibrium that lies towards the CuO_2 species.[7] For the low temperature reaction, we hypothesize that when (P_3tren)Cu(I) is formed in the equilibrium with O_2 bound, that indoline can bind to (P_3tren)Cu(I) and then be oxidized by a similar mechanism as at RT. From the indoline-bound cupric superoxide, rate-determining α-C–H bond activation occurs, as supported by KIE studies. From here, another net hydrogen atom transfer from the β-C–H bond forms indole and hydrogen peroxide. Dissociation of indole and H_2O_2 regenerates (P_3tren)Cu(I). No experimental data are available on the β-C–H bond activation; it may occur directly via hydrogen atom transfer to the proximal oxygen or indirectly though rebound of the indoline radical.

3.3 Conclusion

The catalytic, aerobic oxidation of indoline by the cuprous P_3tren complex, [(P_3tren)Cu][$BArF_{20}$], was found to proceed in high yields with a variety of electronically diverse indolines. Mechanistic studies of the catalytic reaction revealed metal-ligand cooperativity, wherein one phosphinimine arm forms a hydrogen-bonding interaction with the N-H bond of indoline, allowing for activation of the α-C–H bond. It was further found that α-C–H bond activation was rate limiting and proceeds through an HAT process with leading electron transfer from indoline to Cu before proton transfer. Finally, similar mechanistic parameters were determined for independently synthesized P_3tren cupric superoxide complexes. This lends support to the notion of an end-on superoxide being the active species in catalysis.

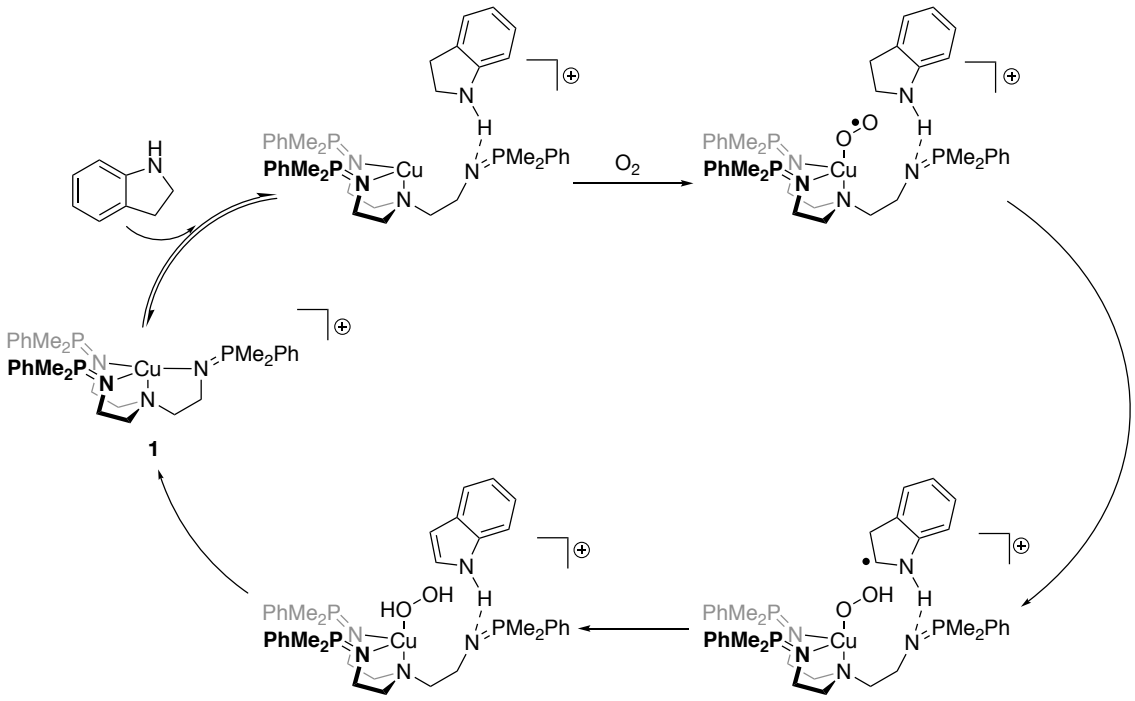

Scheme 3.1 Proposed reaction mechanism.

3.4 References

1. (a) Gribble, G. W. *Indole Ring Synthesis: From Natural Products to Drug Discovery* Wiley: USA. (b) Kochanowska-Karamyan, A. J.; Hamann, M. T. *Chem. Rev.* **2010**, 110, 4489.

2. (a) Ganton, M. D.; Kerr, M. A. *Org. Lett.* 2005, 7, 21, 4777 (b) LeStrat, F.; Murphy, J. A.; Hughes, M. *Org. Lett.* **2002**, 4, 16, 2735.

3. (a) R. Than and E. Rapoport, Tetmhedron, 23 (1967) 3823. (b) A. B. A. Jansen, J. M. Jonhson and J. R. Surtee, J. Chem. Sot., (1964) 5573. (c) A. Inada, Y. Nakamura and Y. Morita, Chem. Lett., (1980) 1287. (d) Balogh-Hergovich, E.; Speier, G. *J. Mol. Cat.* **1986**, 37, 309. (e) Tilstam, U.; Harre, M.; Heckrodt, T.; Weinmann, H. *Tetrahedron Lett.*

2001, 42, 5385. (f) Kamata, K.; Kasai, J.; Yamaguchi, K.; Mizuno, N. *Org. Lett.* **2004**, 6, 3577. (g) Song, Z.; Samanta, R.; Antonchick, A. P. *Org. Lett.* **2013**, 15, 5662.

4. (a) Peng, F.; McLaughlin, M.; Liu, Y.; Mangion, I.; Tschaen, D. M.; Xu, Y. *J. Org. Chem.* **2016**, 81, 10009. (b) Yayla, H. G.; Peng, F.; Mangion, I. K.; McLaughlin, M.; Campeau, L.; Davies, I. W.; DiRocco, D. A.; Knowles, R. R. *Chem. Sci.* **2016**, 7, 2066. (c) Gandeepan, P.; Koeller, J.; Ackermann, L. *ACS Catal.* **2017**, 7, 1030.

5. (a) Li, B.; Wendlandt, A. E.; Stahl, S. S. *Org. Lett.* **2019**, 21, 1176. (b) Iosub, A. V.; Stahl, S. S. *Org. Lett.* **2015**, 17, 4404.

6. Allen, S. E.; Walvoord, R. R.; Padilla-Salinas, R.; Kozlowski, M. C. *Chem. Rev.* **2013**, 113, 6234.

7. McCollom, S. P.; Weberg, A. B.; Thierer, L. M.; Gau, M. R.; Carrol, P. J.; Tomson, N. C. *in preparation*

8. da Silva, M. A. V. R.; Cabral, J. I. T. A.; Gomes, J. R. B. *J. Phys. Chem. A* **2008**, 112, 12263.

9. (a) Lopes, M.; Mota, M.; Belo, I. *Chem. Eng. Technol.* **2013**, 36, 10, 1779. (b) Kirk, T. V.; Marques, M.; Radhakrishnan, A. N. P.; Szita, N. *J. Chem. Technol. Biotechnol.* 2016, 91, 823.

10. We would like to note a few things for the oxidation of indoline using (P_3tren)Cu(II) salts. First, (P_3tren)Cu(Br_2) does not oxidize indoline under O_2 or N_2 pointing towards needing an open coordination site since crystals of PMe_3-(P_3tren)Cu(OTf_2) show not

triflate binding. Second, we note that while the oxidation of indoline by (P_3tren)Cu(OTf_2) is interesting, we believe it is proceeding through a unique mechanism separate from the studies on (P_3tren)Cu(I) catalytic chemistry. Because of this introductory studies into this mechanism were conducted but are incomplete and a separate story from this chapter.

11. (a) Kuo, H. H.; Mauk, A. G. *PNAS* **2012**, 109 (35), 13966 (b) Linhares, M.; Rebelo, S. L. H.; Simoes, M. M. Q.; Silva, A. M. S.; Neves, M. G. P. M. S.; Cavaleiro, J. A. S.; Freire, C. *Applied Catalysis A: General* **2014**, 470 (30), 427

12. Indole formation was not tracked because the signals were too small for the first several percent. As the reaction progresses, indole and indoline have complementary concentrations (i.e. 50:50; 30:70, etc.) therefore tracking indoline is expected to give a suitable k_{obs}.

13. (a) Maiti, D.; Lee, D.-H.; Gaoutchenova, K.; Würtele, C.; Holthausen, M. C.; Narducci Sarjeant, A. A.; Sundermeyer, J.; Schindler, S.; Karlin, K. D. *Angew. Chem. Int. Ed.* **2008**, 47, 82. (b) Lee, J. Y.; Peterson, R. L.; Ohkubo, K.; Garcia-Bosch, I.; Himes, R. A.; Woertink, J.; Moore, C. D.; Solomon, E. I.; Fukuzumi, S.; Karlin, K. D. *J. Am. Chem. Soc.* **2014**, 136, 9925 (c) Peterson, R. L.; Himes, R. A.; Kotani, H.; Suenobu, T.; Tian, L.; Siegler, M. A.; Solomon, E. I.; Fukuzumi, S.; Karlin, K. D. *J. Am. Chem. Soc.* **2011**, 133, 1702

14. Kutt, A.; Leito, I.; Kaljurand, I.; Soovali, L.; Vlasov, V. M.; Yagupolski, L. M.; Koppel I. A. *J. Org. Chem.* **2006**, 7, 17, 2829.

15. (a) Marlier, E. E.; Macaranas, J. A.; Marell, D. J.; Dunbar, C. R.; Johnson, M. A.; DePorre, Y.; Miranda, M. O.; Neisen, B. D.; Cramer, C. J.; Hillmyer, M. A.; Tolman, W. B. *ACS Catal.* 2016, 6, 2, 1215. (b) Jabir, S.; Ashgar, B. H.; Mansoor, S. S. *Orient. J. Chem.* **2017**, 33(1), 288. (c) Hapeler, L. G. *Can. J. Chem.* **1971**, 49, 2803.

16. (a) Mader, E. A.; Davidson, E. R.; Mayer, J. M. *J. Am. Chem. Soc.* **2007**, 129 (16), 5153. (b) West, B.; Castillo, S. R.; Sit, A.; Mohamed, S.; Lowe, B.; Joblin, C.; Bodi, A.; Mayer, P. M. *Phys. Chem. Chem. Phys.* **2018**, 20, 7195.

3.5 Experimental

General Considerations

All reactions containing transition metals were performed under an inert atmosphere of N_2 using standard Schlenk line or glovebox techniques unless addition of O_2 is noted. UHP-grade O_2 (99.99%) was purchased from Airgas and dried over a column of Drierite before use. All solvents (THF, acetonitrile, *n*-pentane, *n*-hexane, and diethyl ether) were dried by passage through a column of activated alumina and stored over 4 Å molecular sieves under an inert atmosphere. Deuterated solvents (CD_3CN and C_6D_6) were dried over CaH_2, isolated via vacuum transfer, and stored under an inert atmosphere over 4 Å sieves. ^{1}H, $^{13}C\{^{1}H\}$, $^{31}P\{^{1}H\}$, $^{19}F\{^{1}H\}$, spectra were recorded on Bruker DMX300, UNI400, or BioDRX500 spectrometers. All chemical shifts (δ) are reported in units of ppm and referenced to the residual protio-solvent resonance for proton and carbon chemical shifts. External H_3PO_4 or $CFCl_3$ were used for referencing ^{31}P and ^{19}F chemical shifts. Elemental analyses were performed by Midwest Microlab, LLC or at the

University of Pennsylvania on a Costech ECS 4010 analyzer in the Earth & Environmental Science Department at the University of Pennsylvania. Low-temperature UV/vis spectra were collected on a Cary 60 spectrophotometer equipped with a Unisoku USP-203A cryostat using a 1 cm cuvette. Accurate mass measurement data were acquired on Waters instruments. Waters software calibrates the instrument and reports the data by use of neutral atomic masses; the mass of the electron is not included. (P_3tren)Cu(I), ND, and α-D_2-indoline were synthesized following literature procedure.[1,2] All chemicals, unless specifically mentioned, were purchased from Fisher Scientific.

General procedure for optimized RT oxidations

20 mg (0.015 mmol) of the PMe_2Ph-derived version of [(P_3tren)Cu][$BArF_{20}$] was dissolved in 1 mL of acetonitrile in a 50 mL Schlenk tube. Indoline (or derivatives) were added to the Schlenk tube under N_2. (P_3tren)Cu and indoline were stirred for 5 min then 1 atm of O_2 was added to the schlenk flask. The reaction was stirred for 14 h. Volatile materials were removed *in vacuo* and reactions were redissolved in MeCN-d_3 with an added internal standard (1,3,5-trimethoxybenzene).

Characterization of Organic Substrates for Substrate Scope

All indoles and indolines were purchased from commercial sources and used without further purification, except for the following. 3-methylindoline and 2,3-dimethylindoline were synthesized by reduction of the substituted indoles according to literature procedures.[3,4] No ^{1}H NMR data were available in the literature for any indolines or indoles in MeCN-d_3 and is therefore presented below.

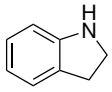 **Indoline 2a**: **^{1}H NMR** (300 MHz, CD_3CN) δ 7.05 (d, ^3J = 6 Hz, 1H), 6.94 (t, ^3J = 9 Hz, 1H), 6.59 (q, ^3J = 6 Hz, 2H), 4.30 (s, 1H), 3.45 (t, ^3J = 6 Hz, 2H), 2.94 (q, ^3J = 6 Hz, 2H) ppm.

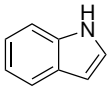 **Indole 3a**: **^{1}H NMR** (300 MHz, CD_3CN) δ 9.29 (s, 1H), 7.59 (d, ^3J = 9 Hz, 1H), 7.44 (d, ^3J = 6 Hz, 1H), 7.26 (t, ^3J = 3 Hz, 1H), 7.14 (t, ^3J = 3 Hz, 1H), 7.05 (t, ^3J = 3 Hz, 1H), 6.38 (m, 1H) ppm.

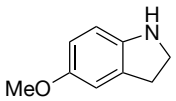 **5-Methoxyindoline 2b**: **^{1}H NMR** (300 MHz, CD_3CN) δ 6.73 (s, 1H), 6.47-6.58 (m, 2H), 4.06 (s, 1H), 3.67 (s, 3H), 3.42 (t, ^3J = 6 Hz, 2H), 2.92 (t, ^3J = 6 Hz, 2H) ppm.

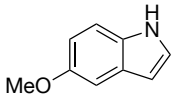 **5-Methoxyindole 3b**: **^{1}H NMR** (300 MHz, CD_3CN) δ 9.26 (s, 1H), 7.31 (d, ^3J = 12 Hz, 1H), 7.21 (s, 1H), 7.07 (d, ^3J = 1 Hz, 1H), 6.77 (dd, ^3J = 6 Hz, 1 Hz, 1H), 6.38 (s, 1H), 3.78 (s, 3H) ppm. $\mathbf{M}^+$ = 147.07 (calc. 147.07)

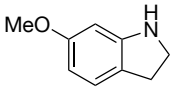

6-Methoxyindoline 2c: **^{1}H NMR** (300 MHz, CD_3CN) δ 6.92 (d, 1H), 6.12-6.18 (m, 2H), 4.32 (s, 1H), 3.62 (s, 3H), 3.46 (t, ^3J = 6 Hz, 2H), 2.86 (t, ^3J = 6 Hz, 2H) ppm.

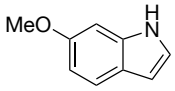

6-Methoxyindole 3c: **^{1}H NMR** (300 MHz, CD_3CN) δ 9.26 (s, 1H), 7.45 (d, ^3J = 12 Hz, 1H), 7.14 (m, 1H), 6.98 (m, 1H), 6.72 (dd, ^3J = 6 Hz, 1 Hz, 1H), 6.40 (s, 1H), 3.83 (s, 3H) ppm. $\mathbf{M}^+$ = 147.07 (calc. 147.07)

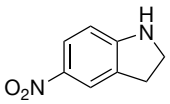

5-Nitroindoline 2d: **^{1}H NMR** (300 MHz, CD_3CN) δ 7.83-7.97 (m, 2H), 6.49 (d, ^3J = 6 Hz, 1H), 5.48 (s, 1H), 3.67 (t, ^3J = 6 Hz, 2H), 3.06 (t, ^3J = 6 Hz, 2H) ppm.

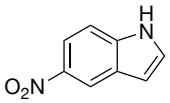

5-nitroindole 3d: **^{1}H NMR** (300 MHz, CD_3CN) δ 9.93 (s, 1H), 8.57 (d, ^3J = 1 Hz, 1H), 8.04 (m, 2H), 7.46 (d, ^3J = 1 Hz, 1H), 6.72 (d, ^3J = 1 Hz, 1H), 6.40 (s, 1H) ppm.

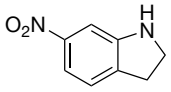

6-Nitroindoline 2e: **^{1}H NMR** (300 MHz, CD_3CN) δ 7.46 (dd, ^3J = 10 Hz, 4 Hz, 1H), 7.27 (d, ^3J = 3 Hz, 1H), 7.19 (dt, ^3J = 9 Hz, 1 Hz, 1H), 4.81 (s, 1H), 3.59 (t, ^3J = 9 Hz, 2H), 3.05 (t, ^3J = 9 Hz, 2H) ppm.

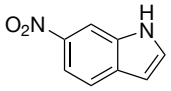

6-Nitroindole 3e (10-153): **^{1}H NMR** (300 MHz, CD_3CN) δ 10.00 (s, 1H), 8.40 (s, 1H), 7.94 (d, ^3J = 6 Hz, 1H), 7.50-7.71 (m, 2H), 6.65 (s, 1H), ppm.

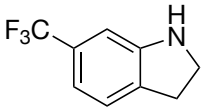

6-Trifluoromethylindoline 2f: **^{1}H NMR** (300 MHz, CD_3CN) δ 7.18 (d, ^3J = 6 Hz, 2H), 6.87 (d, ^3J = 6 Hz, 1H), 6.77 (s, 1H), 4.64 (s, 1H), 3.53 (t, ^3J = 6 Hz, 2H), 3.01 (t, ^3J = 6 Hz, 2H) ppm.

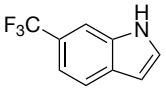

6-Trifluoromethylindole 3f: **^{1}H NMR** (300 MHz, CD_3CN) δ 9.80 (s, 1H), 7.46 (d, ^3J = 2 Hz, 1H), 7.25-7.34 (m, 2H), 7.08 (d, ^3J = 3 Hz, 1H), 6.89 (s, 1H), 6.59 (d, ^3J = 1 Hz, 1H) ppm. $\mathbf{M}^+$ = 185.05 (calc. 185.05)

General Procedure for RT Kinetics

1 mg (0.00077 mmol) of [(P_3tren)Cu][$BArF_{20}$] was dissolved in 600 μL of MeCN-d_3. 2 mg of indoline (or indoline derivate) was dissolved in 100 μL of MeCN-d_3

and an appropriate aliquot (1 eq, 2 eq, etc.) was added to the copper-containing solution along with 1,3,5-trimethoxybenzene as an internal standard (usually around 3 mg). This solution was placed in a J-Young tube, which was sealed, then used to lock and shim in the NMR instrument prior to introduction of the O_2. The solution was then frozen and the headspace was evacuated and refilled with dry O_2. The solution was placed in RT H_2O to thaw for 30 s, after which time NMR spectra were collected every minute. Plots of [indoline] vs. time can be seen below, which show the first 10 % of indoline loss.

Figure S3.1 Plots for the reactions of [(P_3tren)Cu][$BArF_{20}$] and indoline (1.2 mM) to determine rate constants (k_{obs}) and reaction order of Cu.

Cu (mM)	k_{obs} (s^{-1}) Trial 1	k_{obs} (s^{-1}) Trial 2	k_{obs} (s^{-1}) Trial 3	k_{obs} (s^{-1}) Average	Std. dev.
1.2	-5.05×10^{-7}	-5.48×10^{-7}	-6.71×10^{-7}	-5.75×10^{-7}	8.58×10^{-8}
1.8	-9.41×10^{-7}	-8.80×10^{-7}	-1.00×10^{-6}	-9.42×10^{-7}	8.58×10^{-8}
2.4	-1.20×10^{-6}	-1.17×10^{-6}	-1.36×10^{-6}	-1.24×10^{-6}	1.04×10^{-7}

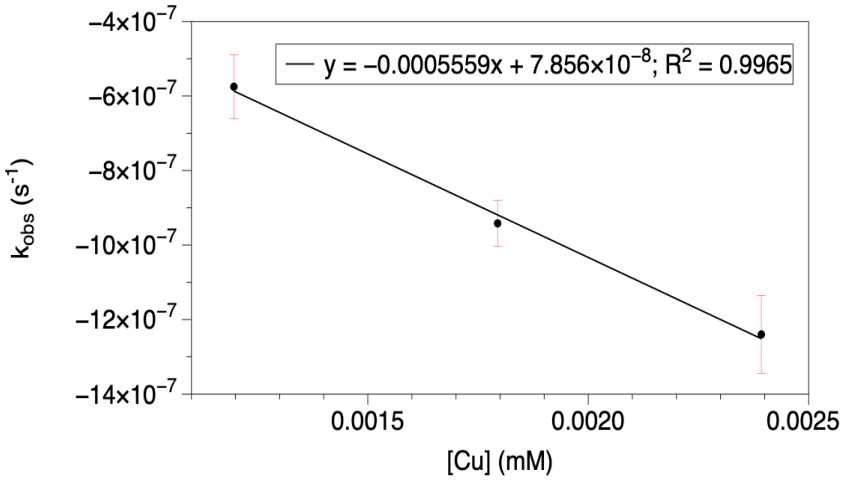

Example kinetic run for 1.2 mM [(P_3tren)Cu][$BArF_{20}$] over the first 10% of the reaction:

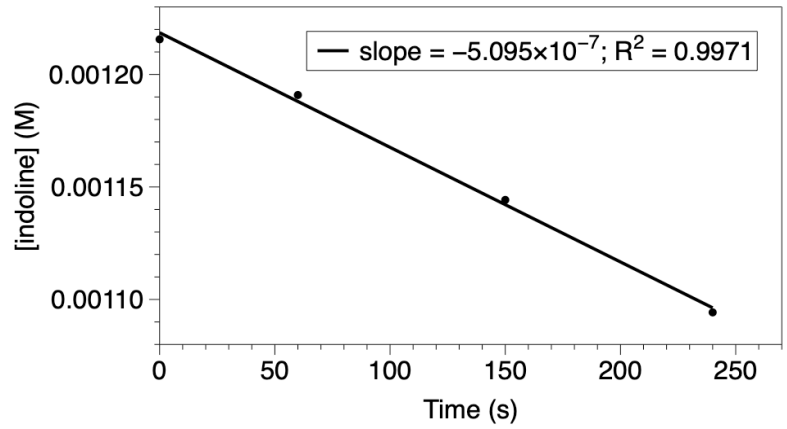

Full run of 1.2 mM [(P_3tren)Cu][$BArF_{20}$] and indoline over the first 10% of the reaction:

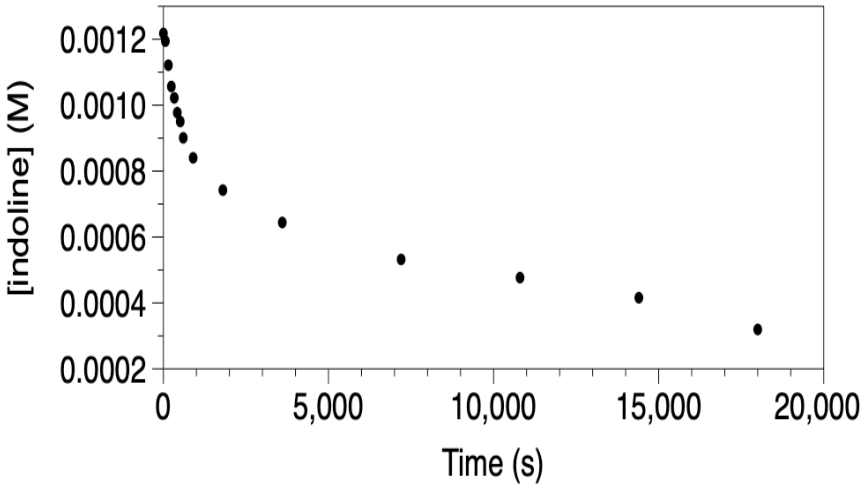

Example kinetic run for 1.8 mM [(P_3tren)Cu][$BArF_{20}$] over the first 10% of the reaction:

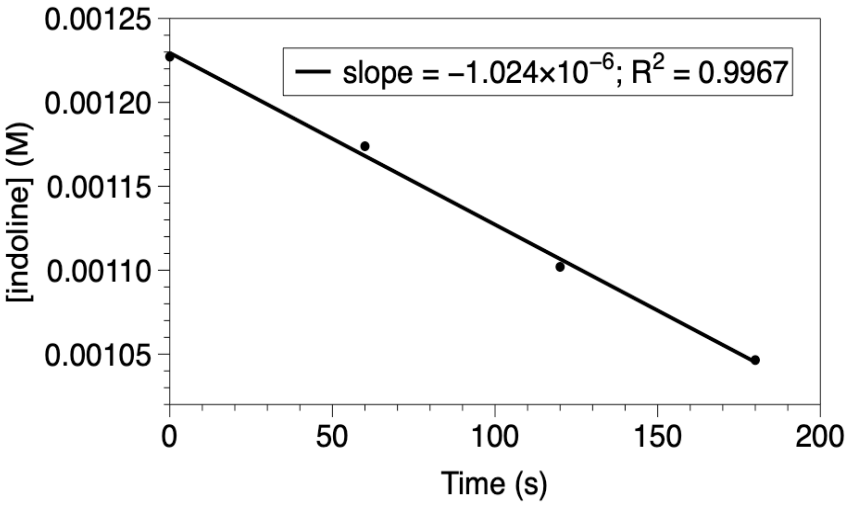

Example kinetic run for 2.4 mM [(P_3tren)Cu][$BArF_{20}$] over the first 10% of the reaction:

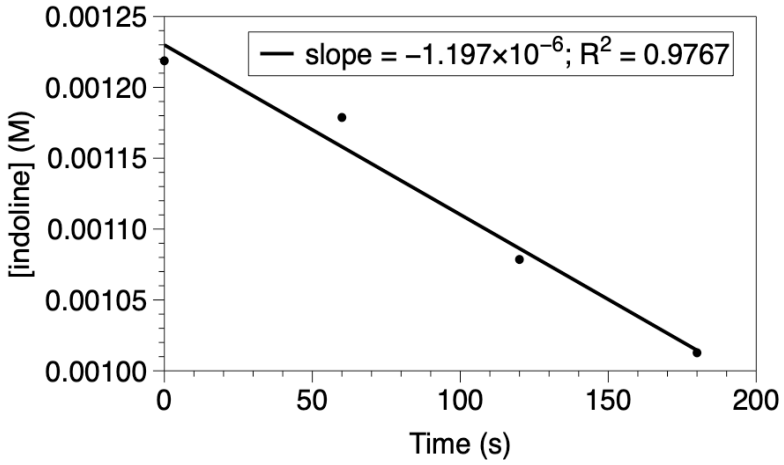

Figure S3.2 Plots for the reactions of [(P_3tren)Cu][$BArF_{20}$] (1.2 mM) and indoline to determine rate constants (k_{obs}) and reaction order of indoline.

Indoline (mM)	k_{obs} (s^{-1}) Trial 1	k_{obs} (s^{-1}) Trial 2	k_{obs} (s^{-1}) Trial 3	k_{obs} (s^{-1}) Average	Std. dev.
1.2	-5.05×10^{-7}	-5.48×10^{-7}	-6.71×10^{-7}	-5.75×10^{-7}	8.58×10^{-8}
1.8	-1.12×10^{-6}	-1.04×10^{-6}	-1.00×10^{-6}	-1.05×10^{-6}	5.70×10^{-8}
2.4	-1.59×10^{-6}	-1.39×10^{-6}	-1.53×10^{-6}	-1.50×10^{-6}	1.03×10^{-7}

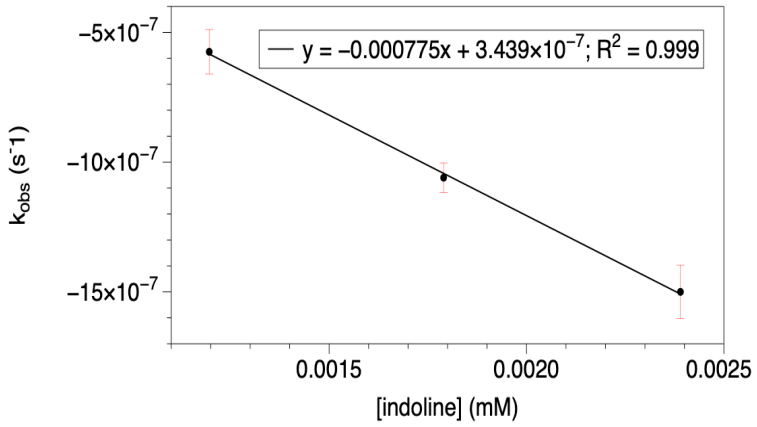

Example kinetic run for 1.2 mM indoline over the first 10% of the reaction:

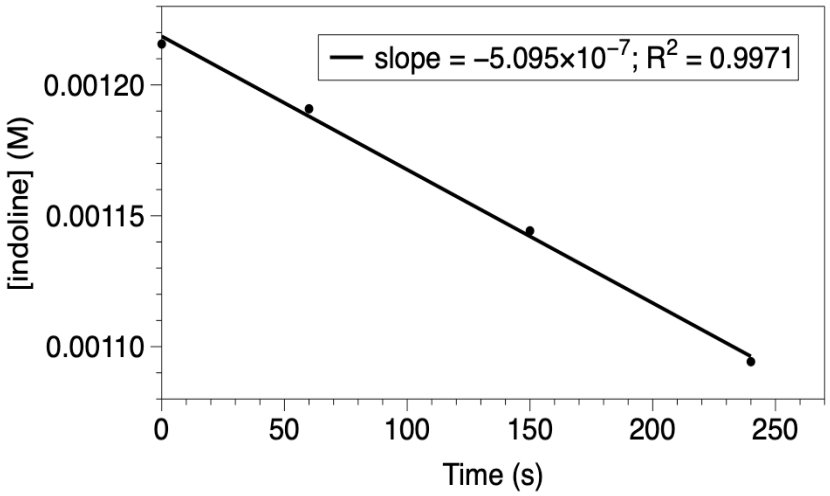

Example kinetic run for 1.8 mM indoline over the first 10% of the reaction:

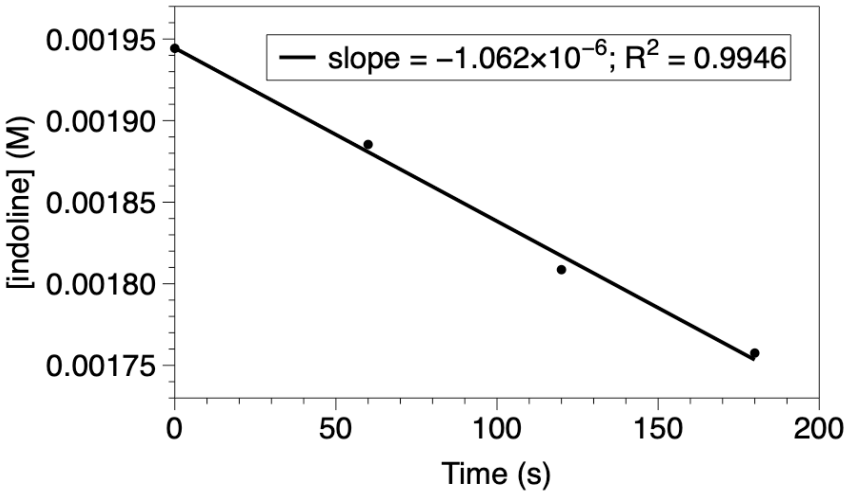

Example kinetic run for 2.4 mM indoline over the first 10% of the reaction:

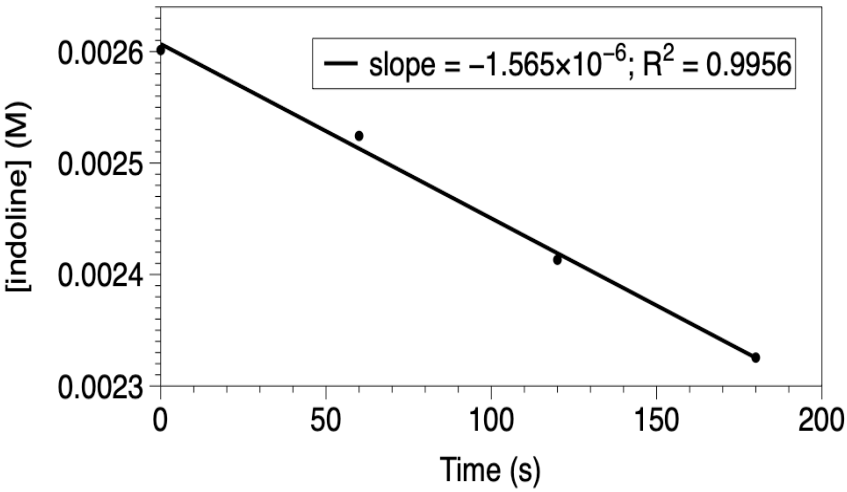

Figure S3.3 Plots for the reactions of [(P_3tren)Cu][$BArF_{20}$] (1.2 mM) and 5-methoxyindoline (1.2 mM) to determine rate constants (k_{obs}) for Hammett plot.

5-methoxyindoline (mM)	k_{obs} (s^{-1}) Trial 1	k_{obs} (s^{-1}) Trial 2	k_{obs} (s^{-1}) Trial 3	k_{obs} (s^{-1}) Average	Std. dev.
1.2	-2.48×10^{-6}	-2.03×10^{-6}	-1.51×10^{-6}	-2.01×10^{-6}	4.84×10^{-7}

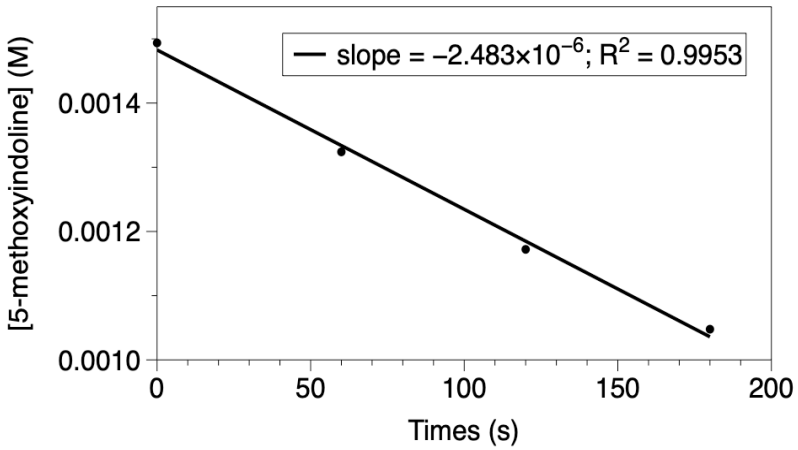

Figure S3.4 Plots for the reactions of [(P_3tren)Cu][$BArF_{20}$] (1.2 mM) and 5-nitroindoline (1.2 mM) to determine rate constants (k_{obs}) for Hammett plot.

5-nitroindoline (mM)	k_{obs} (s^{-1}) Trial 1	k_{obs} (s^{-1}) Trial 2	k_{obs} (s^{-1}) Trial 3	k_{obs} (s^{-1}) Average	Std. dev.
1.2	-2.49×10^{-7}	-2.51×10^{-7}	-3.23×10^{-7}	-2.74×10^{-7}	4.21×10^{-8}

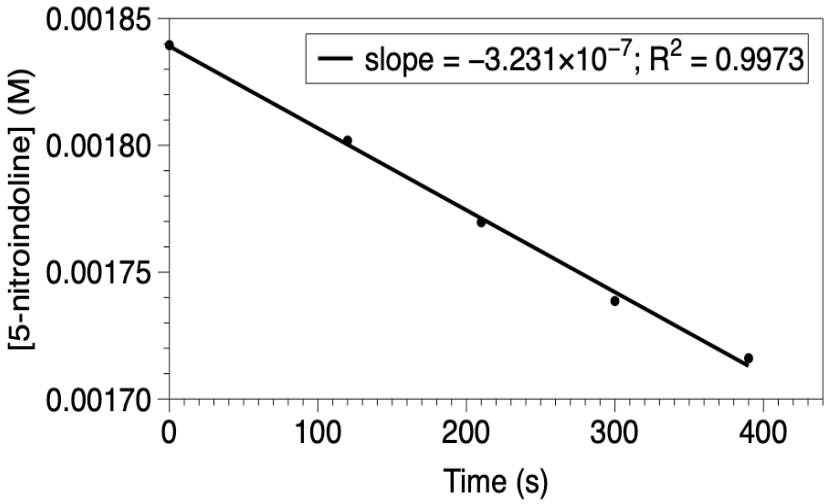

Figure S3.5 Plots for the reactions of $[(P_3tren)Cu][Otf_2]$ (2.4 mM) and indoline (1.2 mM) to determine rate constants (k_{obs}).

O_2	k_{obs} (s^{-1}) Trial 1	k_{obs} (s^{-1}) Trial 2	k_{obs} (s^{-1}) Trial 3	k_{obs} (s^{-1}) Average	Std. dev.
Yes	-4.57×10^{-7}	-4.33×10^{-7}	-4.64×10^{-7}	-4.51×10^{-7}	1.63×10^{-8}
No	-1.41×10^{-7}	-1.61×10^{-7}	-1.13×10^{-7}	-1.38×10^{-7}	2.41×10^{-8}

With O_2 over the first 10% of the reaction:

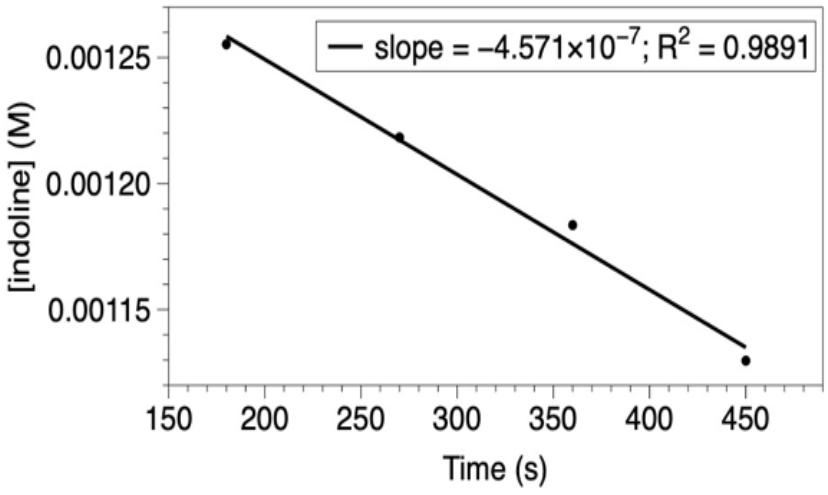

Without O_2 over the first 10% of the reaction:

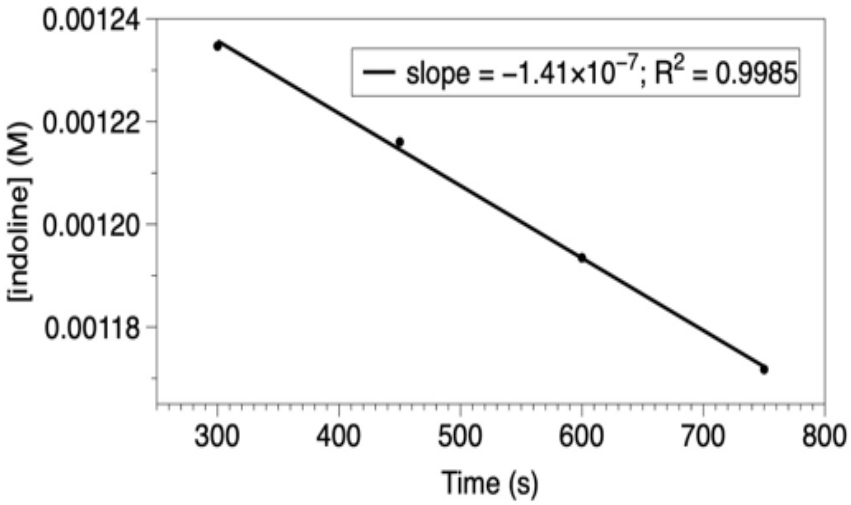

Figure S3.6 Plots for the reactions of [(P_3tren)Cu][$BArF_{20}$] (1.2 mM) and indoline (1.2 mM) with variable pressures of O_2 to determine rate constants (k_{obs}).

O_2 (atm)	k_{obs} (s^{-1}) Trial 1	k_{obs} (s^{-1}) Trial 2	k_{obs} (s^{-1}) Trial 3	k_{obs} (s^{-1}) Average	Std. dev.
1 atm	-5.05×10^{-7}	-5.48×10^{-7}	-6.71×10^{-7}	-5.75×10^{-7}	8.58×10^{-8}
2 atm	-5.95×10^{-7}	-5.46×10^{-7}	-6.07×10^{-7}	-5.82×10^{-7}	3.42×10^{-8}
1 % O_2 in 99 % N_2 at 1 atm	-5.18×10^{-7}	-6.52×10^{-7}	-5.85×10^{-7}	-5.85×10^{-7}	6.71×10^{-8}
1 % O_2 in 99 % N_2 at 0.1 atm	-3.32×10^{-7}	-4.04×10^{-7}	-4.28×10^{-7}	-3.88×10^{-7}	4.97×10^{-8}

1 atm O_2 over the first 10% of the reaction:

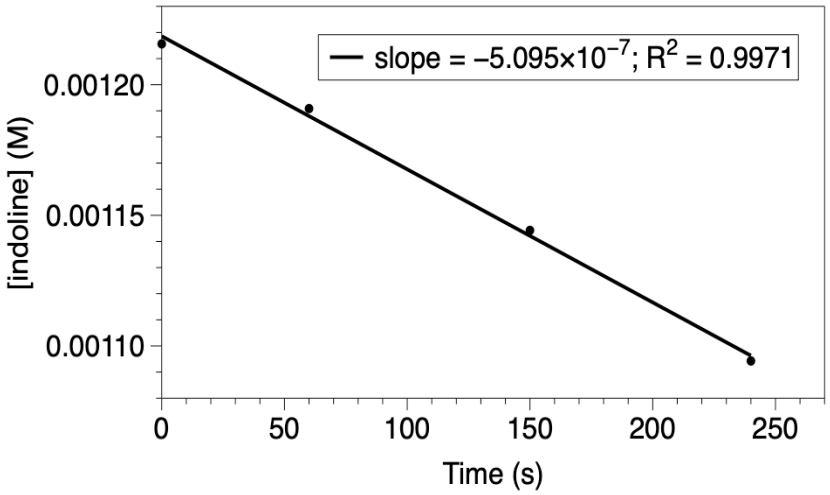

2 atm O_2 over the first 10% of the reaction:

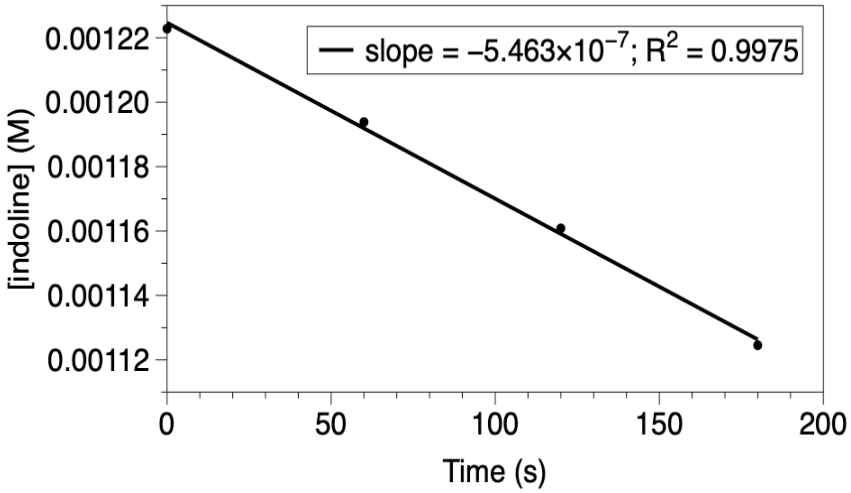

1 % O_2 in 99 % N_2 at 1 atm over the first 10% of the reaction:

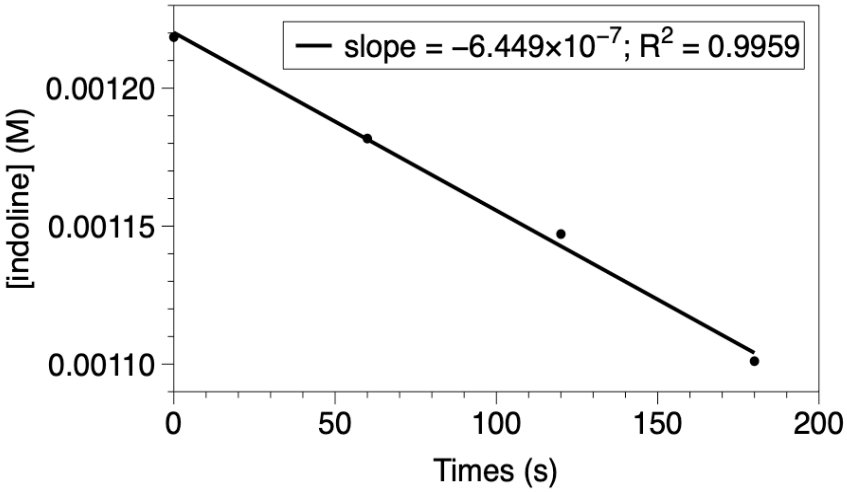

1 % O_2 in 99 % N_2 at 0.1 atm over the first 10% of the reaction:

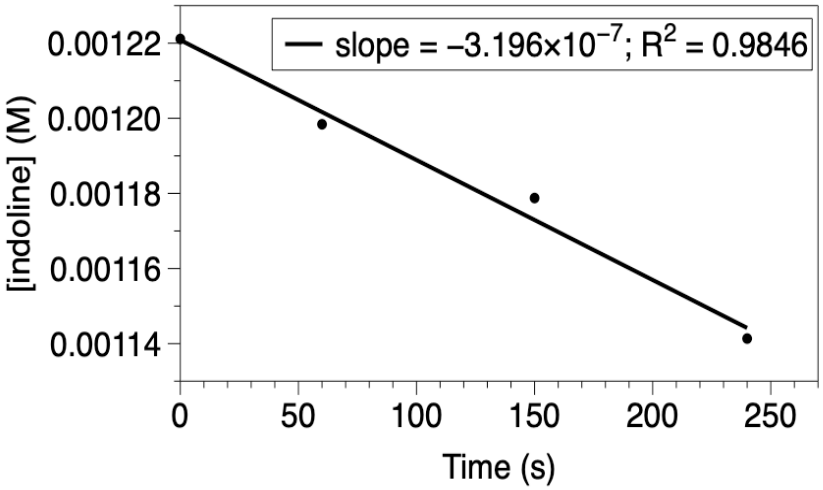

Figure S3.7 Plots for the reactions of [(P_3tren)Cu][$BArF_{20}$] (1.2 mM) and deuterated indolines (1.2 mM) determine rate constants (k_{obs}) for KIE values.

Indoline (1.2 mM)	k_{obs} (s^{-1}) Trial 1	k_{obs} (s^{-1}) Trial 2	k_{obs} (s^{-1}) Trial 3	k_{obs} (s^{-1}) Average	Std. dev.	KIE
ND	-6.33×10^{-7}	-6.32×10^{-7}	-6.59×10^{-7}	-6.41×10^{-7}	1.50×10^{-8}	1
α-D_2	-3.30×10^{-7}	-2.57×10^{-7}	-1.43×10^{-7}	-2.43×10^{-7}	9.40×10^{-8}	2.36

ND over the first 10% of the reaction:

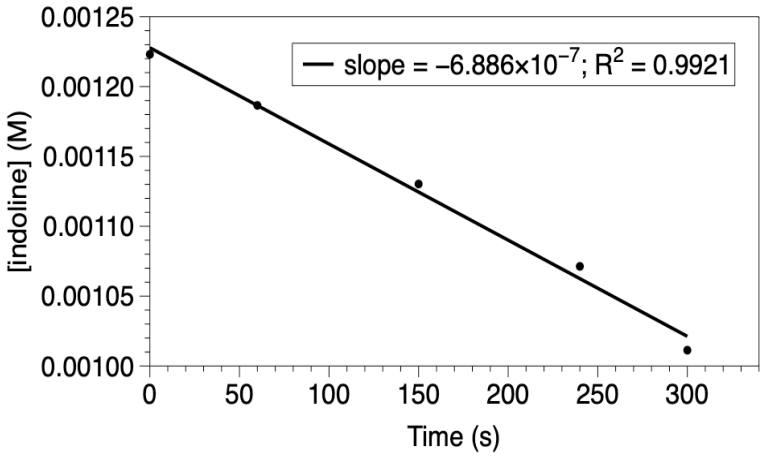

α-D_2 over the first 10% of the reaction:

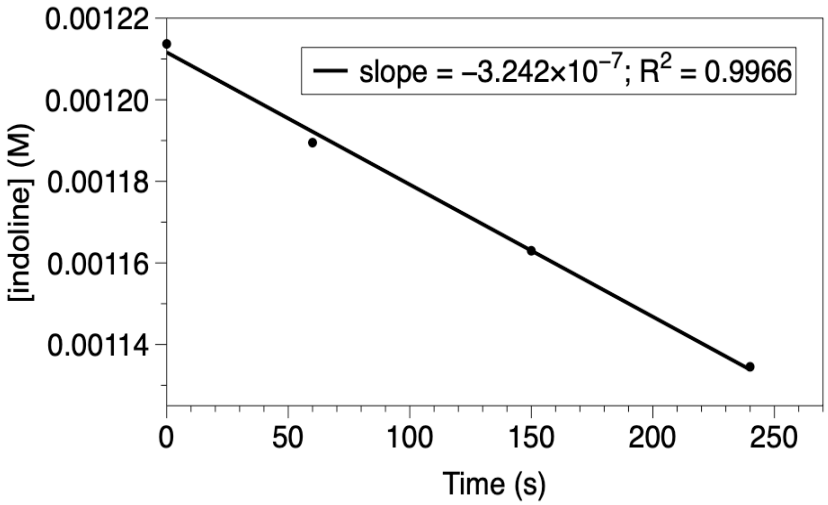

General Procedure for Low-Temperature Kinetics

In the glovebox, a solution of $[(P_3tren)Cu][BArF_{20}]$ in THF (3 mL, 0.5 mM) was prepared and transferred to a 1 cm, long-neck cuvette and capped with a Teflon septum. The cuvette was placed in the UV/vis cryostat within a stream of nitrogen, and a spectrum was recorded at 22 °C. The sample was then cooled to -100 °C and spectra were taken to confirm that the sample was unchanged. Dry O_2 (100%) was bubbled through the cold solution for 10 seconds, then spectra were recorded. The solution was then sparged with dry N_2 for 30 seconds and the substrate (pre cooled to -94 °C) was immediately added by transferring from a Schlenk tube with a syringe (100 μL). Spectra were taken every 30 seconds for 1 h. Pseudo-first-order rate plots analyzing the first 10% of loss of absorbance were performed by observing the disappearance of a 400 nm LMCT to obtain plots of $\ln[(A - A_f)/(A_i - A_f)]$ versus time (seconds), which were found to be linear.

Note: The rate of $[(P_3tren)Cu][BArF_{20}]$ (0.5 mM) decomposition at -100 °C has an average of $k_{obs} = -0.004\ s^{-1}$.[1] This value was subtracted from all indoline values for analysis but numbers shown here are before subtraction.

Figure S3.8 Plots for the reactions of $[(P_3tren)Cu][BArF_{20}]$ (0.5 mM) and indoline (0.5 mM) to determine rate constants (k_{obs}).

Indoline	k_{obs} (s^{-1}) Trial 1	k_{obs} (s^{-1}) Trial 2	k_{obs} (s^{-1}) Trial 3	k_{obs} (s^{-1}) Average	Std. dev.
indoline	-0.0012	-0.0011	-0.0010	-0.0011	0.0001
5-methoxyindoline	-0.0036	-0.0036	-0.0034	-0.0035	0.0001
5-nitroindoline	-0.0007	-0.0005	-0.0006	-0.0006	0.0001

Indoline over the first 10% of the reaction:

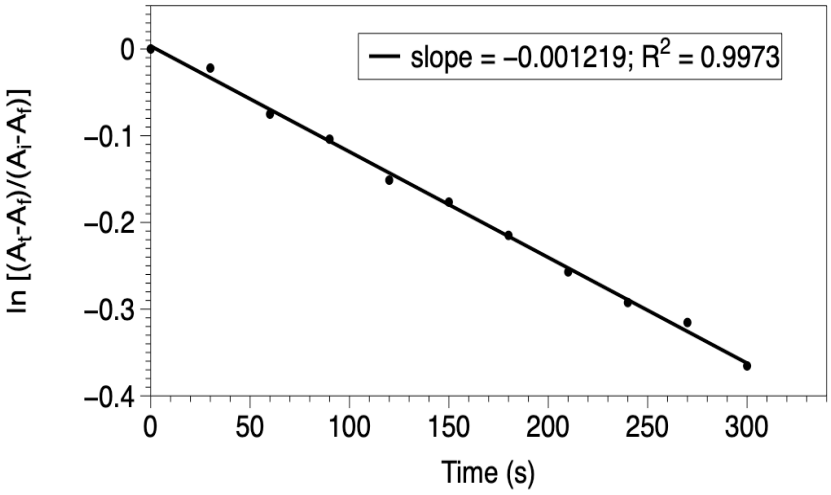

5-methoxyindoline over the first 10% of the reaction:

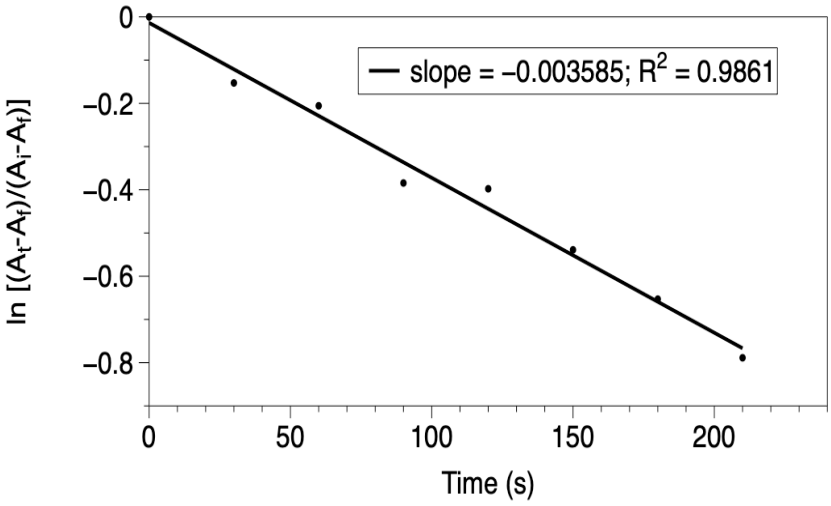

5-nitroindoline over the first 10% of the reaction:

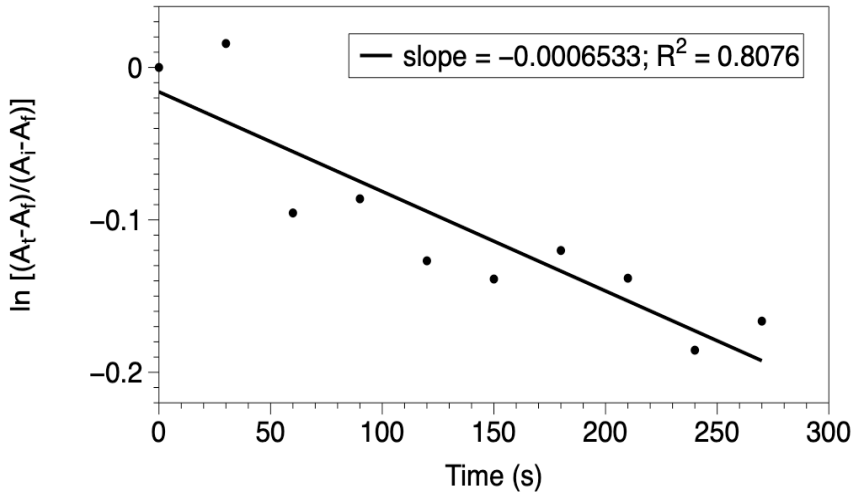

Figure S3.9 Plots for the reactions of $[(P_3tren)CuO_2][BArF_{20}]$ (0.5 mM) and indoline (0.5 mM) to determine rate constants (k_{obs}).

Note: The rate of $[(P_3tren)Cu][BArF_{20}]$ (0.5 mM) decomposition at -100 °C has an average of k_{obs} = -0.0004 s^{-1}. At -95 °C the decomposition has an average of k_{obs} = -0.0007 s^{-1}. At -85 °C the decomposition has an average of k_{obs} = -0.001 s^{-1}. These values were subtracted from all indoline values for analysis but numbers shown here are before subtraction.[1,10]

Temperature (°C)	k_{obs} (s^{-1}) Trial 1	k_{obs} (s^{-1}) Trial 2	k_{obs} (s^{-1}) Trial 3	k_{obs} (s^{-1}) Average	Std. dev.
-100	-0.0012	-0.0011	-0.0010	-0.0011	0.0001
-95	-0.0014	-0.0015	-0.0013	-0.0014	0.0001
-85	-0.0018	-0.0017	-0.0016	-0.0017	0.0001

-100 °C over the first 10% of the reaction:

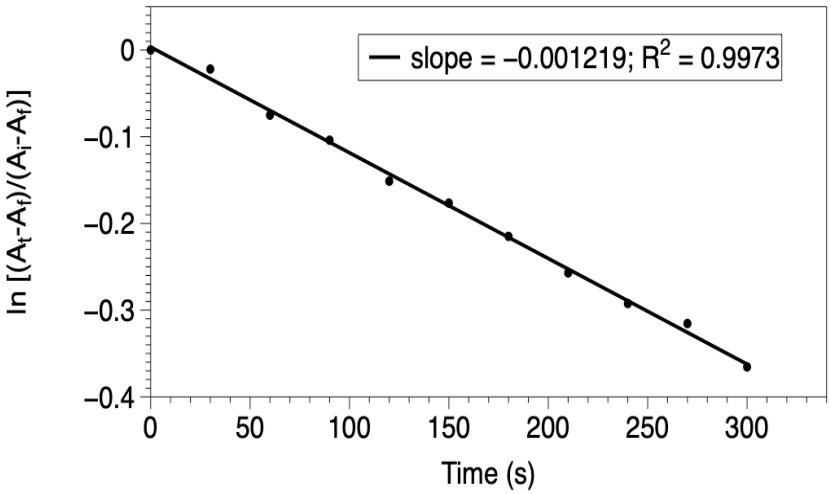

-95 °C over the first 10% of the reaction:

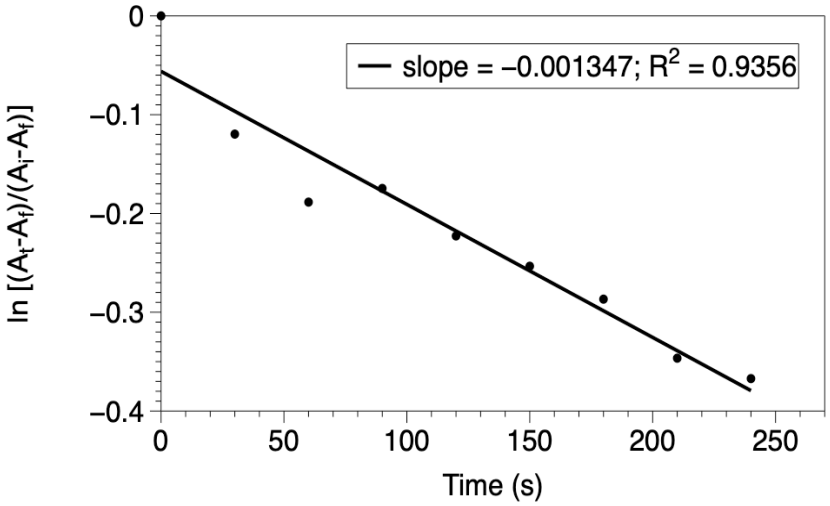

-85 °C over the first 10% of the reaction:

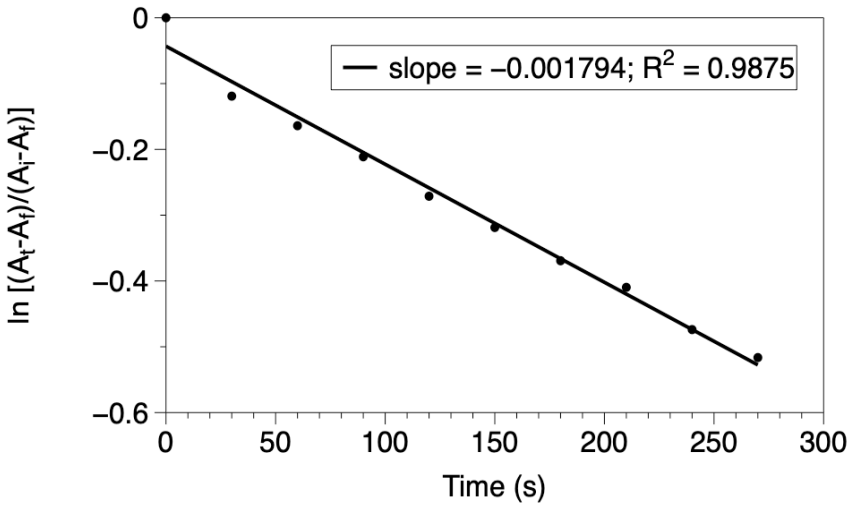

Eyring Plot:

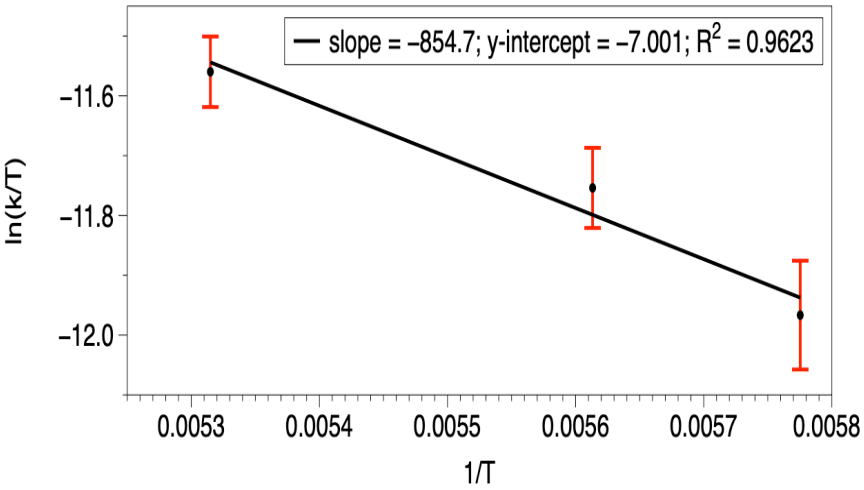

$\Delta H^{\ddagger}$ = 1.7 kcal/mol, $\Delta S^{\ddagger}$ = -61 cal/K, $\Delta G(298)^{\ddagger}$ = 20 kcal/mol

VT NMR General Procedure

10 mg (0.0077 mmol) of [(P_3tren)Cu][$BArF_{20}$] were dissolved in 600 µL of isbutyronitrile (IBN). IBN was used because of its similary polarity and binding ability as acetonitrile but much lower melting point. To the Cu(I) solution was added 1 eq (1 µL, 0.0077 mmol) of indoline. NMR spectra were taken at every 10 °C.

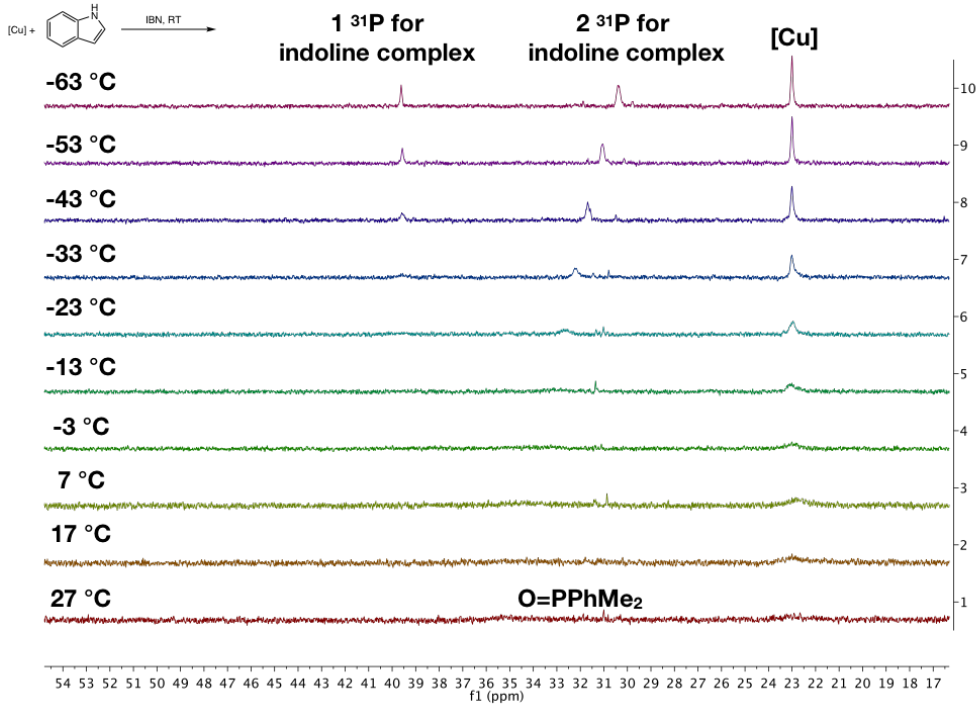

Figure S3.10 VT ^{31}P NMR of [(P_3tren)Cu][$BArF_{20}$] + indoline in IBN

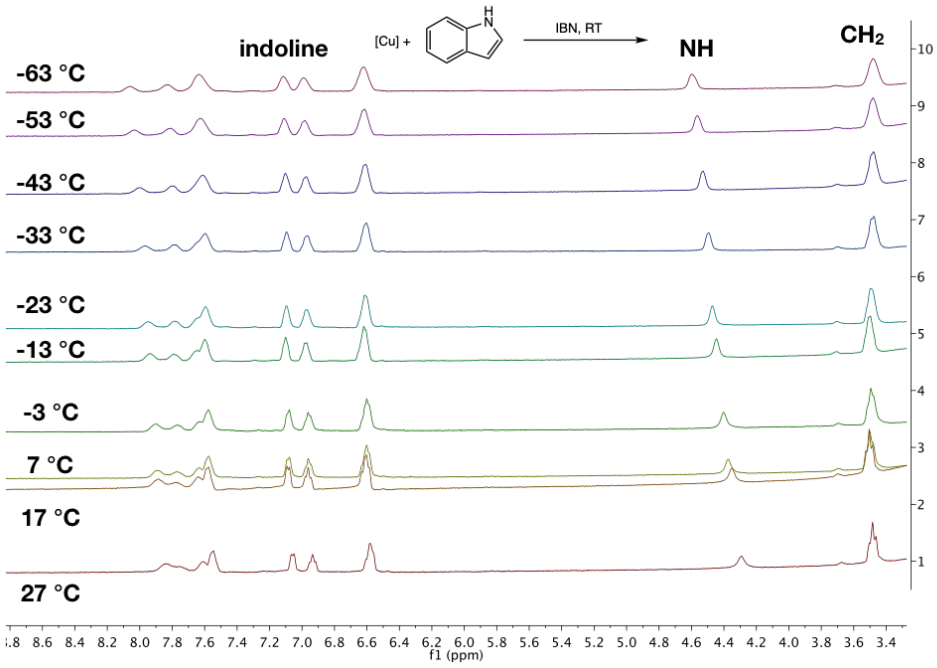

Figure S3.11 VT ^{1}H NMR of [(P_3tren)Cu][$BArF_{20}$] + indoline in IBN.

NMR of Protonated P_3trenCuBArF$_{20}$

10 mg (0.0077 mmol) of [(P_3tren)Cu][$BArF_{20}$] were dissolved in 600 µL of isbutyronitrile (IBN). 1 eq of $HBArF_{24}(Et_2O)_2$ (0.0077 mmol, 7.8 mg) was added to the solution. The yellow solution immediately bleached. NMR spectra were then recorded.

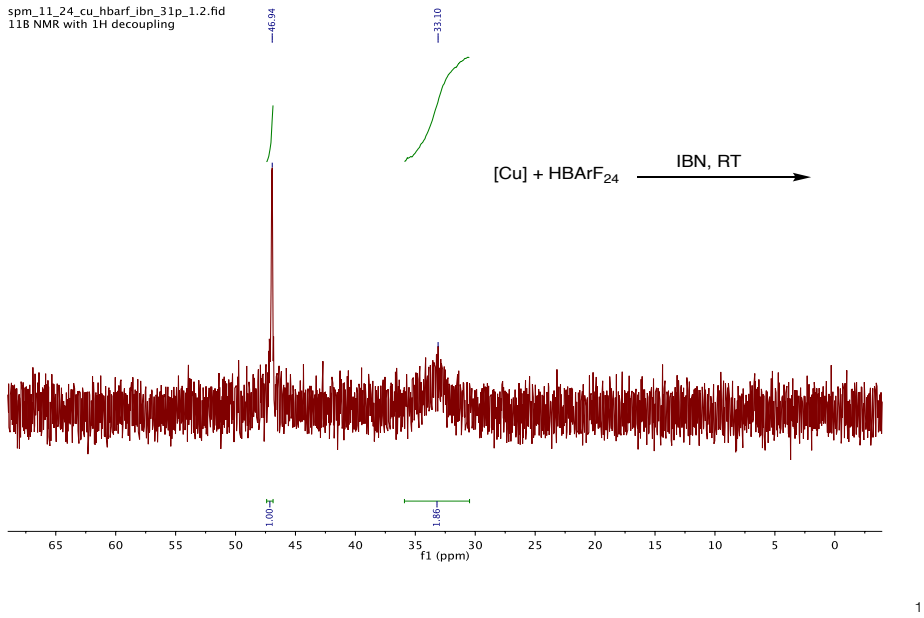

Figure S3.12 ^{1}H NMR of [(P_3tren)Cu][$BArF_{20}$] + 1 equiv of $HBArF_{24}(Et_2O)_2$

H_2O_2 Detection

Iodometry: Procedure for hydrogen peroxide detection was followed from literature sources.[5,6] First, 2.0 mg (0.00015 mmol) of [(P_3tren)Cu][$BArF_{20}$] were dissolved in 1.0 mL of MeCN. Indoline was then added and stirred for 5 min. 1 atm of O_2 was added to the 50 mL Schlenk tube. After 5 and 15 minutes the volatile materials were evaporated *in vacuo*. Under N_2 and in the dark, 1.0 mL of MeCN was added to redissolve all solids in a glovebox. 100 µL of solution was added to 3.00 mL of NaI saturated MeCN that had been previously degassed. The UV−vis spectrum of this solution displayed the formation of triiodide (I_3^-) at 362 nm, and the yield was calculated by comparing with standard H_2O_2 solutions of known concentration. Of note is that [(P_3tren)Cu][$BArF_{20}$], [(P_3tren)Cu][OTf_2],

[(P_3tren)Cu][$BArF_{20}$] + 1, 2, or 3 equiv of $HBArF_{24}(Et_2O)_2$, or [(P_3tren)Cu][OTf_2] + 1, 2, or 3 equiv of $HBArF_{24}(Et_2O)_2$ do not oxidize I^- to I_3^-.

F254 TLC Plates: F254 TLC plates are specially designed for hydrogen peroxide to appear as a colored spot under 254 nm light. Reaction mixtures generated exactly as above were run simultaneously as a standard H_2O_2 solution in MeCN. The plate was run with a 2:1 THF:*n*-hexane mixture and H_2O_2 appears at an R_f value of 0.54.

Electrochemistry

Cyclic voltammetry and square-wave voltammetry measurements were carried out using a BASi Epsilon Eclipse electrochemistry analyzer. All electrochemistry was performed in an N_2 atmosphere glovebox. A platinum disk was used as the working electrode. A platinum wire was used as the counter electrode. The reference electrode was $Ag/AgNO_3$ in MeCN. The measurements were performed at room temperature under an N_2 atmosphere in an MeCN solution containing 0.1 M tetrabutylammonium hexafluorophosphate, which was recrystallized four times from ethanol and dried under vacuum, and 1 mM copper complex.

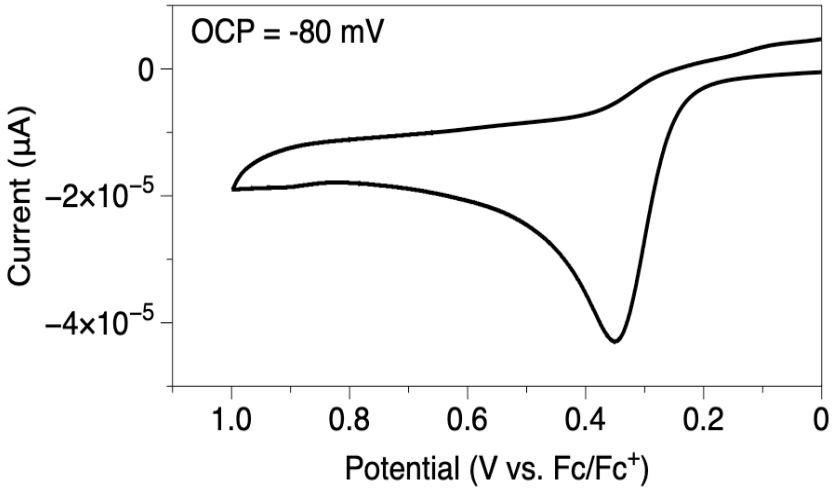

Figure S3.13 Cyclic voltammogram of indoline at 200 mV/s

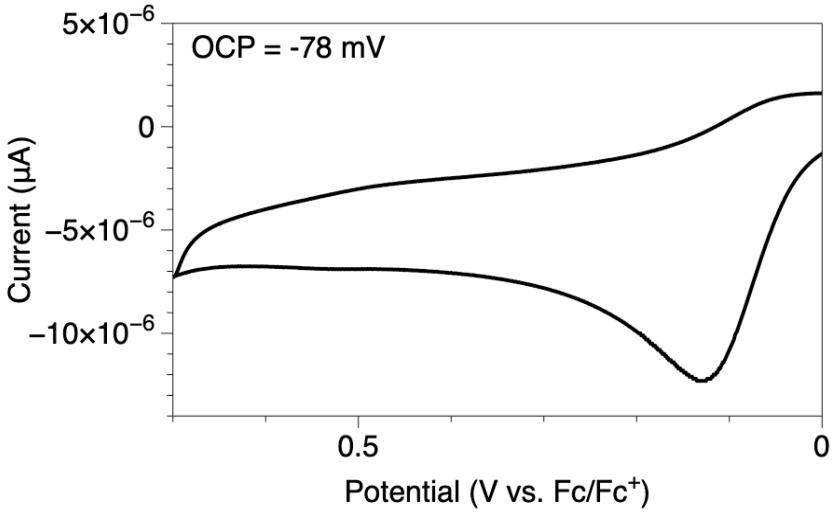

Figure S3.14 Cyclic voltammogram of 5-methoxyindoline at 200 mV/s

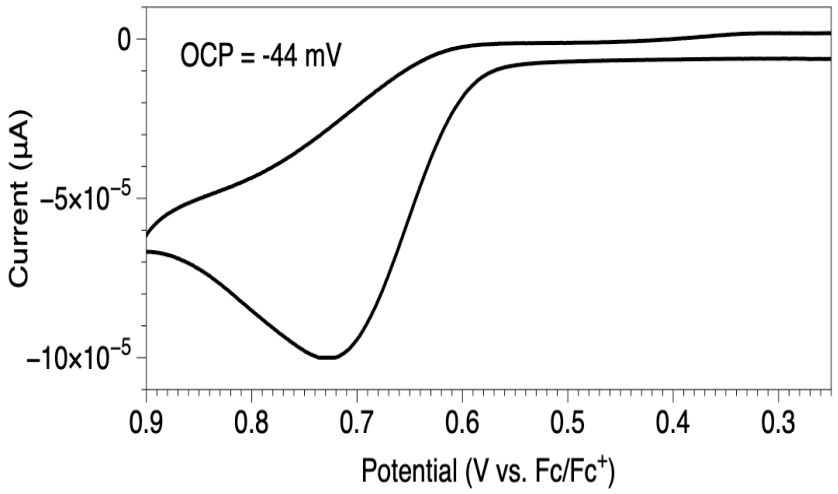

Figure S3.15 Cyclic voltammogram of 5-nitroindoline at 200 mV/s

Determination of O_2 Concentration During RT Catalytic Experiments

There are no direct literature reports on the solvation rate of O_2 at 1 atm in an NMR tube. Several literature references can be pieced together to form conclusive evidence that the catalytic reactions are saturated with O_2 within the timeframe of the appreciable turnover. First, the maximum concentration of O_2 in acetonitrile at RT under 1 atm of O_2 pressure is *ca.* 10 mM, which corresponds to 6×10^{-6} mol for our experiments. The amount of copper used was 7.7×10^{-7} mol, 8-fold less than the amount available at saturation.[8] Secondly, we have not found examples of studies investigating the behaviour of gaseous diatomics dissolving in acetonitrile in the absence of stirring, but ethylene has been studied for this purpose and found to exhibit a volumetric mass transfer coefficient of 2.8×10^{-4} m/s. Using the mass transfer coefficient equation, this equals 3.1×10^{-8} mol of O_2 dissolved within 2 min, i.e. the first catalytic data point. This is roughly 25-fold less than needed to reach 1 equiv.[8] However, the experiments

for this chapter were conducted with the NMR tube spinning at a rate of 1,200 revolutions per minute.[8,9] Several studies have been conducted on the effect of stirring rate on O_2 solvation in solvents such as water and THF. THF has a 10-fold larger mass transfer coefficient than water. These studies found that with stirring, the surface area of the solvent provides a negligible perturbation on the mass transfer coefficient. This results in mass transfer values expressed simply in terms of s^{-1}. Stirring rates of up to 600 rpm were found in the literature, and a linear relationship was found over several stirring rates compared to the mass transfer coeffieinct. Using this linear relationship for O_2 dissolving in THF and extrapolating for 1200 rom, coefficient of 20 min^{-1} was extraploted.[8] This correlates to a gradient of 3.7 x 10^{-4} mol/min, a value that is well in excess of that needed for the solvent to remain saturated with O_2.

References

1. McCollom, S. P.; Weberg, A. B.; Thierer, L. M.; Gau, M. R.; Carrol, P. J.; Tomson, N. C. *in preparation*
2. Yi, C. S.; Lee, D. W. *Organometallics* **2009**, 28, 4, 947.
3. Xie, W.; Li, B.; Wang, B. *J. Org. Chem.* **2016**, 81, 2, 396.
4. Yang. Y.; Wang, C. *Chem. Eur. J.* **201**9, 25, 8245.
5. Lee, J. Y.; Peterson, R. L.; Ohkubo, K.; Garcia-Bosch, I.; Himes, R. A.; Woertink, J.; Moore, C. D.; Solomon, E. I.; Fukuzumi, S.; Karlin, K. D. *J. Am. Chem. Soc.* **2014**, 136, 9925.
6. Kim, S.; Saracini, C.; Siegler, M. A.; Drichko, N.; Karlin, K. D. Inorg. Chem. 2012, 51, 12603−12605.

7. Li, Q.; Batchelor-McAuley, C.; Lawrence, N. S.; Hartshorne, R. S.; Compton, R. G. *Journal of Electroanalytical Chemistry* **2013**, 688, 328.

8. Buser, J. Y.; Luciani, C. V. *React. Chem. Eng.* **2018**, 3, 442.

9. Lopes, M.; Mota, M.; Belo, I. *Chem. Eng. Technol.* **2013**, 36, 1779.

10. (a) Dole, M.; Hsu, C. S.; Patel, V. M.; Patel, G. N. *J. Phys. Chem.* **1975**, 79 (23), 2473. (b) Kunishita, A.; Kubo, M.; Sugimoto, H.; Ogura, T.; Sato, K.; Takui, T.; Itoh, S. *J. Am. Chem. Soc.* **2009**, 131, 2788.

Chapter 4: Additive Free Catalytic Oxidation of Alcohols by Tripodal Phosphinimine Copper Complexes and O_2 with Metal-Ligand Cooperativity

4.1 Introduction

The development of reactions that exhibit high atom-economy and use non-toxic reagents continues to be a driving force in catalysis science.[1] Great strides have been made towards using non-toxic transition metals to perform important transformations, but many systems still employ wasteful stoichiometric additives and harsh reaction conditions. Generally, these types of systems have ligands on the transition metal that play a pivotal role in tuning the properties of the metal center but do not participate in bond-making or bond-breaking processes.[2-4] The design of ligands that can perform the role of common additives facilitating catalytic turnover has the potential to greatly reduce the production of chemical waste.

Examples of this metal-ligand cooperatively strategy are common in nature. Metalloenzymes have finely tuned ligand environments that aid in the activation of a wide variety of substrates.[5] For example, Zn-dependent alcohol dehydrogenases use nicotinamide adenine dinucleotide (NAD^+) in the ligand environment to accept a hydride from alcohols bound to Zn.[6-11] Another enzyme that uses metal-ligand cooperativity is galactose oxidase, which has a copper active site and a ligand-stabilized phenoxyl radical. This radical is key to the abstraction of a hydrogen atom from a Cu(II)-bound alkoxide.[12, 13] If, like enzymes, we can harness the power of metal-ligand cooperativity, we can generate important chemicals with higher efficiency and lower environmental impact.

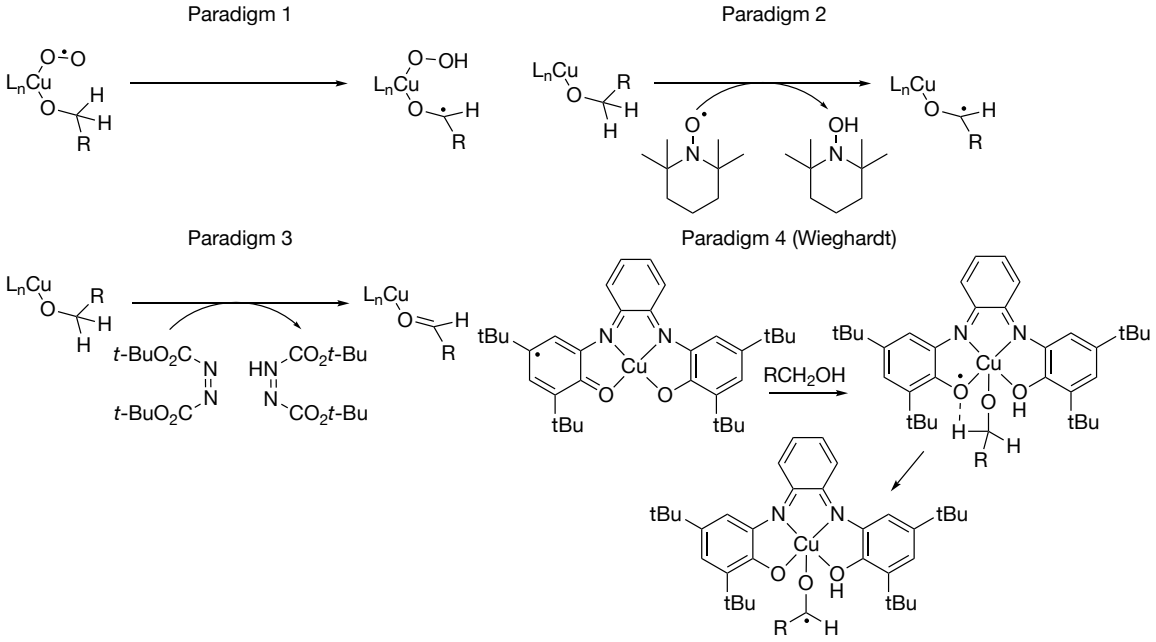

Scheme 4.1 Mecahanism paradigms for Cu/O_2 alcohol oxidation.

The oxidation of alcohols to aldehydes and ketones is a reaction that has potential to make use of metal-ligand cooperativity, as seen with the enzymatic examples above. Examples are known in the literature of using copper as an inexpensive and non-toxic metal for promoting the aerobic oxidation of alcohols.[14] While this catalytic chemistry can be performed in high yields under mild conditions, a major drawback to these systems is their need for the use of organic additives, which create additional waste products. Two exceptions are known and will be described below in detail.

Copper-mediated alcohol oxidation chemistry can be classified into four mechanistic types (Paradigms 1-4, Scheme 4.1). In Type 1, a copper-bound superoxide ligand abstracts a hydrogen atom from a ligated alkoxide.[15] In Type 2, a superoxide

surrogate (e.g. TEMPO) abstracts a hydrogen atom from an alkoxide bound to copper(II), with O_2 serving to regenerate TEMPO radical from TEMPOH.[16] Notably, the Stahl group has elegantly studied and optimized this system to oxidize a wide array of substrates in high yield under mild conditions.[17] In mechanism Type 3, a hydride anion acceptor abstracts a hydride from an alkoxide bound to copper(I).[18] Finally, in mechanism Type 4, ligands that mimic galactose oxidase use a phenolic radical bound to copper to abstract a hydrogen atom from an alkoxide bound to copper(II).[19]

Of note are two related systems developed by the Wieghardt group. These ligand architectures mimic galactose oxidase and are the sole examples of copper catalysts for the aerobic oxidation of alcohols that do not require added base or co-catalysts (Paradigm 4, Scheme 4.1).[20, 21] These ligands are proposed to use phenoxide groups bound to Cu(II) to deprotonate an alcoholic substrate, forming a Cu(II)-alkoxide and phenol. From there, a phenoxyl radical on the ligand is proposed to perform rate-determining hydrogen atom transfer. Subsequent oxygenation turns-over the catalytic cycle by forming hydrogen peroxide and regenerating the phenoxyl radical and phenoxide. As Wieghardt first showed, the way to improve the oxidation of alcohols to aldehydes or ketones in a green manner using copper, is to use a ligand that can either fully deprotonate the alcohol or coordinate the alcohol and help activate the C-H bonds for hydrogen atom transfer.

Herein, we report the base-free catalytic oxidation of alcohols, primarily benzylic, using O_2 and a tren-based tris(phosphiniminato) ligand (P_3tren) copper(I) complex. Our group has previously shown that (P_3tren)Cu (Scheme 4.2) employs metal-ligand cooperativity in the oxidation of indoline using O_2.[22] We hypothesized that one of the

phosphinimine arms coordinates the N–H bond of indoline, which aids in the activation of the indoline toward rate-limiting abstraction of an α-C–H hydrogen atom. We have also found that (P_3tren)Cu can be treated with O_2 at low temperatures to form an end-on superoxide that undergoes PCET reactivity with 2,6-di-*tert*-butyl-4-methoxyphenol and indoline.[23] Considering that substrates below will be shown to be oxidized without additives, due to metal-ligand cooperativity, and furthermore form similar byproducts to other known superoxide active species reactions, we hypothesize the chemistry below also proceeds through a cupric suproxide, but further studies are needed to confirm this.

4.2 Results and Discussion

4.2.1 Synthesis of Copper(I) Precursors

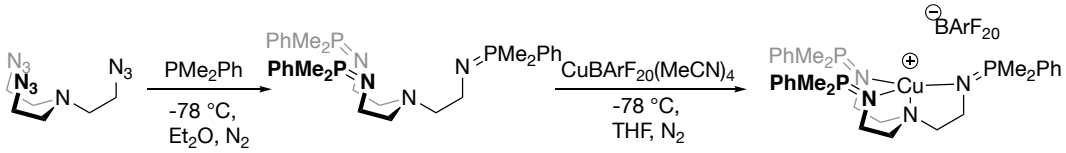

Scheme 4.2 Synthesis of P_3tren by the Staudinger reaction and [(P_3tren)Cu][$BArF_{20}$].

The synthesis of the potassium iodide bound-ligand, P_3tren (**3**), was carried out in three steps (Scheme 4.3). First, a frozen solution of tris(2-aminoethyl)amine (tren) and triethylamine (10 equiv), in THF, was layered with 3 equiv of chloromethylphenylphosphine. Doing so generates the monophosphorylated tren, **1**, in moderate yields. The low reaction temperatures are needed to minimize formation of diphosphorylated products, which predominate at higher reaction temperatures. Next, **1** was methylated at -78 °C with three equiv of methyl iodide to form the

tris(phosphonium) salt, **2**, in quantitative conversion of both the mono and diphosphorylated starting material formed in the first step. Finally, **2** was deprotonated in the presence of 4 equiv of potassium hydride in pyridine at -41 °C, yielding pure **3** in 28 % yield over all steps. Due to the bound potassium iodide, metalation with various copper sources (CuCl, $CuBF_4$, and CuOTf) led to complexes with a mixture of anions. To ensure the isolation of a pure copper complex, copper(I) iodide was treated with a stoichiometric amount of **3** in THF, yielding a colorless precipitate (KI) and a yellow solution of [(P_3tren)Cu]I, **4**, which formed in quantitative yield.

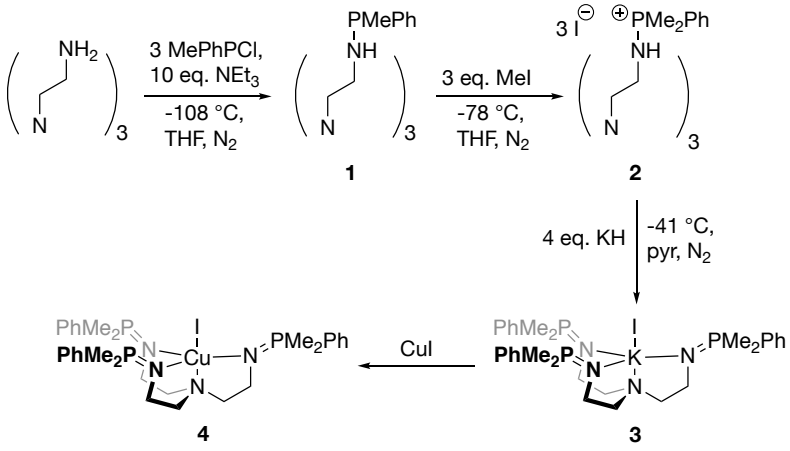

Scheme 4.3 Synthesis of P_3tren(KI) through three step synthesis.

4.2.2 Optimization of Benzyl Alcohol Oxidation

Treatment of benzyl alcohol with a catalytic amount of **4** in MeCN under 1 atm O_2 was found to generate benzaldehyde in the absence of added base (Table 4.1). Importantly, no over oxidation to benzoic acid was observed. For example, **4** (20 mol %) catalyzes the oxidation of benzyl alcohol in 32 % yield over 14 h at 20 °C. An increase in the temperature to 50 °C provided a modest increase in the yield (39 %), but longer

reaction times (up to 20 h) afforded no further improvement. The use of THF or DCM as solvent prevented conversion to the benzaldehyde product. Copper complex precipitated out of solution as a green solid when using THF. In DCM, the copper(I) species turned green before the addition of O_2, possibly due to oxidation of the copper. Furthermore, when $[(P_3tren)Cu]Cl_2$ was generated *in situ* and used in place of **4**, no reaction was

Table 4.1 Selected optimization of benzyl alcohol oxidation.[a]

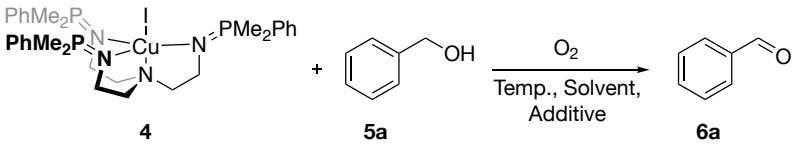

Entry	Cu mol %	Solvent	T (°C)	Time (h)	Additive	Yield
1	20	MeCN	20	14	None	32 %
2	20	MeCN	50	14	None	39 %
3	20	MeCN	50	20	None	40 %
4	20	THF	50	14	None	0 %
5	50	THF	50	14	None	1 %
6	20	DCM	40	14	None	0 %
7	5	MeCN	50	14	None	20 %
8	0.1	MeCN	50	14	None	0.5 %
9	20	MeCN	50	14	3 Å mole. sieve	60 %
10	20	MeCN	50	14	Cs_2CO_3	8 %
11	20	MeCN	50	14	NEt_3	32 %

observed (see experimental for control experiments). Attempts to lower the catalyst loading gave mixed success, as higher TONs were seen at 5 and 0.1 mol % loading, but lower overall yields were obtained. During the course of optimization, the formation of dimethylphenylphosphine oxide was observed by $^{31}P\{^{1}H\}$ NMR spectroscopy. This byproduct is hypothesized to form upon hydrolysis of the copper complex with water. To slow down the hydrolysis, 3 Å molecular sieves were added to the reaction, which enhanced the yield of benzaldehyde to 60 %. Finally, stoichiometric amounts of base were evaluated. The two bases tested, Cs_2CO_3 and NEt_3, are the most common bases used for alcohol oxidation in Cu/O_2 systems.[14] However, no positive effects were found by adding base, and the yield of benzaldehyde worsened in the case of Cs_2CO_3. Overall, optimized conditions for further studies involved 20 mol % loading in MeCN at 50 °C with 3 Å molecular sieves.

4.2.3 Reaction Scope

The substrate scope of benzyl alcohol oxidation was next determined. Experiments were conducted using high-throughput experimentation (HTE) at 1 μmol of **4** in MeCN, with one bead of 3 Å molecular sieves (average of 5.5 mg per bead), under 1 atm of O_2, at 50 °C. The reaction mixtures were then analyzed by GC/MS. Benzyl alcohol was repeated as a substrate to ensure the yield was comparable to the scaled-up reaction (10 mmol **4**). Under the HTE conditions, benzyl alcohol was oxidized to benzaldehyde in a similar yield, 64 % (**6A**) (Figure 4.1). When a substrate with weaker C- H bonds, benzoin, was tested, the oxidized product, benzil (**6B**), was formed in quantitative yield.

Next, electronic effects were studied using substrates with either electron-withdrawing or electron-donating groups in the *para*-, *meta*-, or *ortho*-positions of the benzyl arene rings. Strongly electron-donating groups (e.g. methoxy, **6C**, 58 %) and weakly electron withdrawing group (e.g. bromide, **6D**, 58 %) in the *para*-position led to similar yields as for **6A**. However, when strongly electron-withdrawing groups, like nitro (**6E**), are used at the *para* position, the yield dropped to 47 %. A similar trend occurs when these electron donating/withdrawing groups are located at the *meta*- or *ortho*-positions (**6F-6J**). This is comparable to what was observed when this system was used to perform indoline dehydrogenation. A decrease in yield on inclusion of electron-withdawing substituents indicated rate-determining hydrogen atom transfer.

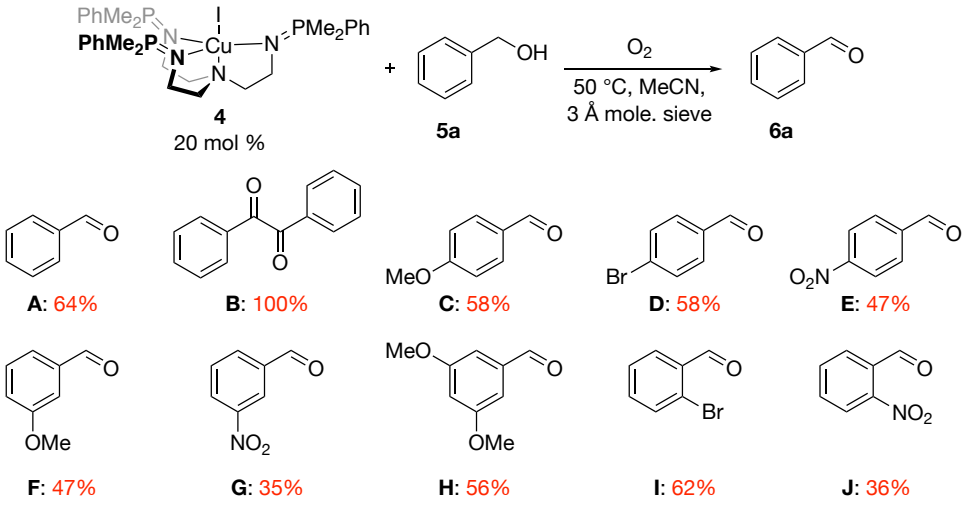

Figure 4.1 Scope of benzyl alcohols for oxidation to benzaldehydes.

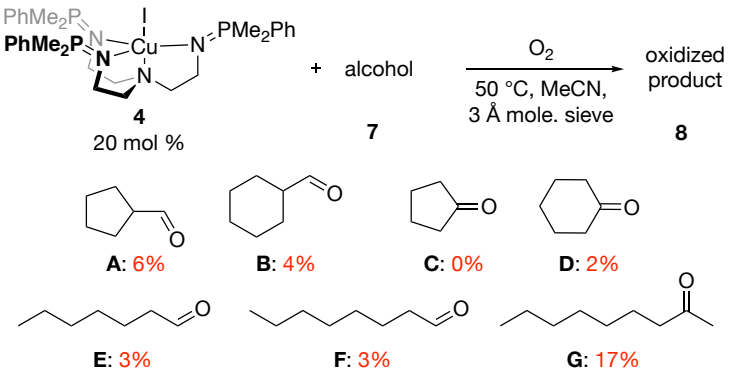

Figure 4.2 Scope of saturated alcohols for oxidation to aldehydes and ketones.

Non-benzylic alcohols provided poor yields of aldehyde and ketone products under the optimized catalytic conditions (Figure 4.2). When cycloakyl methanol derivates were used, with varying ring group size, little to no conversion of aldehyde was seen (**7A-D**). If 1° aliphatic alcohols, such as 1-heptanol (**7E**) or 1-octanol (**7F**), were used, low yields were again observed (3%). A modest improvement in yield was seen when 2-octanol (**7G**) was used (17%). These substrates are likely not able to be oxidized as easily as benzyl alcohols due to their stronger C–H bonds.

4.2.4 Byproduct Analysis for Mechanistic Interpretation

The final substrates that were tested were phenols, catechols, and hydroquinones. These aromatic alcohols are well documented in the literature as substrates for oxidation by Cu:O_2 systems without the addition of base or other additives. For catechols and hydroquinones, known Cu:O_2 systems are understood to proceed through two net hydrogen atom transfer steps to form 1,2-benzoquinone (**10a**) and 1,4-benzoquinone (**10c**), respectively. When catechol and hydroquinone were tested as substrates for oxidation by [(P_3tren)Cu]I, it was found that catechol did not oxidize into 1,2-

benzoquinone (**10a**), where all starting material was observed by GC/MS. Interestingly, when 2,4-di-*tert*-butylcatechol was tested, 44 % yield forming **10b** was determined. The intricacies of this steric dependence are outside of the scope of this metal-ligand cooperativity aimed study, and therefore were not studied further. When hydroquinone was submitted to catalytic ocnditions, clean quantitative conversion into 1,4-benzoquinone (**10c**) was observed. (Table 4.2).

Table 4.2 Substrate scope for catechol and hydroquinones.

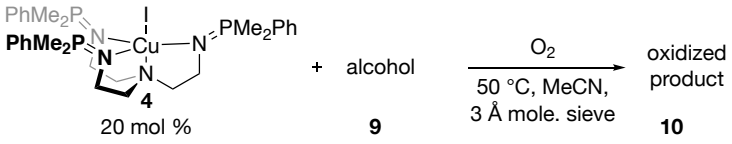

Starting Material	Product	Yield
 **9a**	 **10a**	0 %
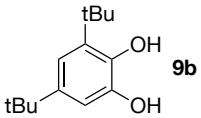 **9b**	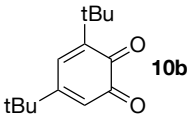 **10b**	44 %
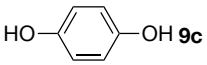 **9c**	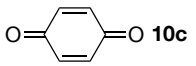 **10c**	100 %

For phenols, literature Cu/O_2 systems perform net hydrogen atom transfers to form phenoxyl radicals, which can then C-C couple through *ortho* or *para* unprotected sites. For our system, similar reaction patterns were observed, in which a variety of phenols with different substitution patterns were able to be oxidized to several different type of products depending on substitution on the aryl ring. If a single *ortho* site was

unprotected by using 2,4-di-*tert*-butylphenol, **11a**, then C-C coupling products through the unprotected *ortho* site were observed in moderate yield. Similarly, if the *para* site was left unprotected by using 2,5-di-*tert*-butylphenol, **11b**, then C-C coupling through the *para* position and $2e^-/2H^+$ oxidations were observed to form diphenoquinone-type compounds, specifically 3,3',5,5'-tetra-*tert*-butyldiphenoquinone.

We found divergent reactivity with tri-substituted phenols compared to literature catalytic Cu/O_2 systems. The use of 2,4,6-tri-*tert*-butylphenol (**11d**) and 2,6-di-*tert*-butyl-4-methoxyphenol (**11c**) as substrates yielded 2,6-di-*tert*-butyl-1,4-benzoquinone in 15 % and 52 % yields, respectively. All other catalytic Cu/O_2 systems form C-C or C-O coupled products through the *para* position for these two substrates.[14] However, there are three known stoichimetric systems that have also formed benzoquinones from tri-substituted phenols, of which two have been well characterized as end-on copper superoxide active species.[24-26] Further, the Karlin group performed a detailed mechanistic study in which they found that hydrogen peroxide is formed for both substrates in addition to methanol for 2,6-di-*tert*-butyl-4-methoxyphenol and isobutene for 2,4,6-tri-*tert*-butylphenol (see experimental for mechanism). The same byproducts were found when performing the oxidation in the presence of **4**. The formation of H_2O_2 was confirmed by F254 TLC plates and by iodometry. This gives credence to the hypothesis that the active species from the combination of **4** and O_2 is also a cupric superoxide.

Table 4.3 Substrate scope for phenols.

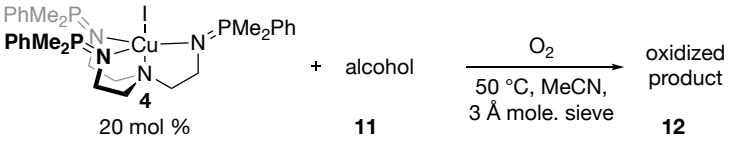

Starting Material	Product	Yield
11a 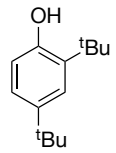	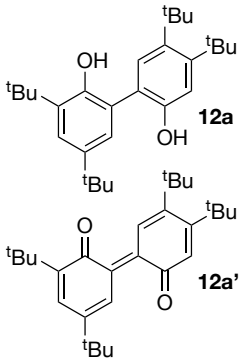 **12a** **12a'**	30 % 30 %
11b 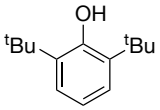	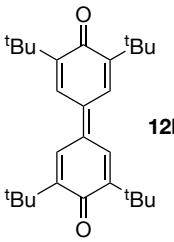 **12b**	28 %
11c 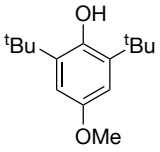	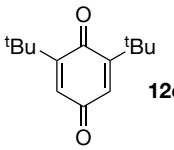 **12c**	52 %
11d 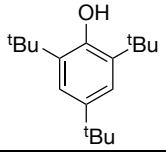	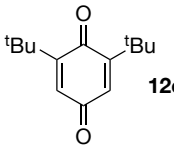 **12e**	15 %

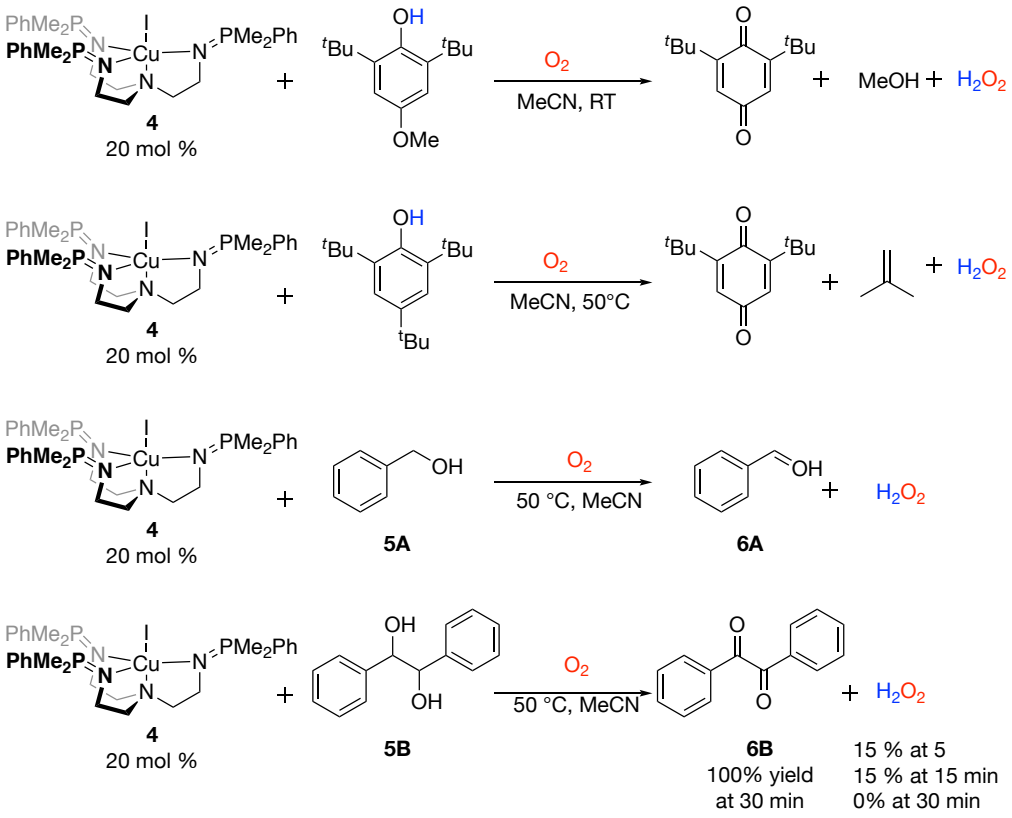

Figure 4.3 Byproducts observed in catalytic alcohol oxidations.

Notably, the Karlin systems are not catalytic, and catalyst death occurs due to formation of cupric hydroxides. The system implemented in this study does show catalytic turnover, and the while hydrogen peroxide is seen for (P_3tren)Cu and in the Karlin system, for (P_3tren)Cu it may indicate that **4** can be regenerated, as proposed in indoline dehydrogenation.

Consideirng the catalytic oxidation of phenol systems can be linked to known superoxides through byproduct analysis, similar studies were extedended to benzyl alcohols. In the catalytic oxidation of benzyl alcohol and benzoin, hydrogen peroxide formation was also confirmed by using F254 TLC plates and quantified by iodometry for

the benzoin reaction. During the oxidation of benzoin, H_2O_2 production was quantified over time, with 15 % H_2O_2 observed at 5 and 15 min, while at 30 min, 0 % H_2O_2 and 100 % benzil were observed. This highlights that H_2O_2 was produced and was the byproduct derived from O_2. Considering the similarity between byproducts of the oxidation of phenols or benzyl alcohols and well-studied literature examples/previous indoline chemistry, the active species for phenols and benzyl alcohols may be a cupric superoxide. Hydrogen peroxide also provides a source of water for the hydrolysis of the phosphinimine arms, leading to catalyst death. At 50 °C, H_2O_2 is unstable and decomposes into water and oxygen. Furthermore, molecular sieves have been shown to increase the rate of decomposition of H_2O_2.[27]

While hydrogen peroxide could be decomposing in this time frame due to heat and sieves, we also tested to see if H_2O_2 could be a viable oxidant for the oxidation of benzoin using (P_3tren)Cu. When one equiv of hydrogen peroxide was treated with a mixture of benzoin and **4**, 27% yield of benzil was formed with ~70% benzoin remaining. When **4** was excluded, only 10% yield of benzil was formed along with a mixture of unidentifiable products. These yields are much lower than the quantitative conversion that is seen when O_2 is used as the oxidant. Therefore, hydrogen peroxide can be a suitable oxidant for this chemistry and is likely participating in this manner, but the main oxidant is O_2.

4.3 Conclusion

Overall, the oxidation of benzyl alcohol and related substrates can be performed in a green manner using the (P_3tren)Cu system. We propose that the inclusion of a basic phosphinimine arm allows for metal-ligand cooperativity, in which the basic arm can aid in mediating the activation of substrates while copper can bind O_2 and aid in selective and direct bond activation to form hydrogen peroxide. Notably, this is only the third copper system that can perform this type of reaction without any additives, such as base or TEMPO. To distinguish this chemistry from the Wieghardt system, we have given circumstantial evidence that (P_3tren)Cu goes through a cupric superoxide mechanism (Type 1, Scheme 4.1) for alcohol oxidation. This is unique from the Wieghardt systems, which are proposed to undergo oxidase type chemistry in which O_2 regenerates active, oxidized metal complexes.

4.4 References

1. Sheldon, R. A.; Arends, I. W. C. E.; ten Brink, G.; Dijksman, A. *Acc. Chem. Res.* **2002** 35, 9, 774.

2. Khusnutdinova, J. R.; Milstein, D. *Angew. Chem. Int. Ed.* **2015**, 54, 12236.

3. Beller, M., Bolm, C., Eds. Transition Metals for Organic Synthesis; Wiley-VCH: Weinheim, 2004.

4. Gunanathan, C.; Milstein, D. *Acc. Chem. Res.* **2011**, 44, 8588.

5. Wodrich, M. D.; Hu, X. *Nat. Rev. Chem.* **2017**, 2 (99), 1.

6. Eklund, H., Plapp, B. V., Samama, J.-P. & Brädén, C.-I. *J. Biol. Chem.* **1982**, 257, 14349.

7. Cook, P. F. & Cleland, W. W. *Biochemistry* **1981**, 20, 1805

8. Eklund, H. et al. *J. Mol. Biol.* **1976**, 102, 27.

9. Ramaswamy, S., Eklund, H. & Plapp, B. V. *Biochemistry* 1994, 33, 5230.

10. Inoue, J., Tomioka, N., Itai, A. & Harayama, S. *Biochemistry* **1998**, 37, 3305.

11. Yu, M.-J. & Chen, S.-L. *Chemistry* **2017**, 23, 7545.

12. Ito, N.; Phillips, S. E. V.; Stevens, C.; Ogel, Z. B.; McPherson, M. J.; Keen, J. N.; Yadav, K. D. S.; Knowles, P. F. *Nature* **1991**, 350, 87.

13. Whittaker, M. M.; Whittaker, J. W. *Biochemistry* **2001**, 40, 7140.

14. Allen, S. E.; Walvoord, R. R.; Padilla-Salinas, R.; Kozlowski, M. C. *Chem. Rev.* **2013**, 113, 6234.

15. (a) Liang, L.; Rao, G.; Sun, H.-L.; Zhang, J.-L. *Adv. Synth. Catal.* **2010**, 352, 2371. (b) Lahtinen, P.; Ahmad, J. U.; Lankinen, E.; Pihko, P.; Leskelä, M.; Repo, T. *J. Mol. Catal. A: Chem.* **2007**, 275, 228. (c) Jallabert, C.; Lapinte, C.; Riviere, H. *J. Mol. Catal.* **1982**, 14, 75.

16. Semmelhack, M. F.; Schmid, C. R.; Cortés, D. A.; Chou, C. S. *J. Am. Chem. Soc.* **1984**, 106, 3374.

17. Hoover, J. M.; Ryland, B. L.; Stahl, S. S. *ACS Catal.* **2013**, 311, 2599.

18. Markó, I. E.; Giles, P. R.; Tsukazaki, M.; Brown, S. M.; Urch, C. *Science* **1996**, 274, 2044.

19. (a) Mukherjee, C.; Pieper, U.; Bothe, E.; Bachler, V.; Bill, E.; Weyhermüller, T.; Chaudhuri, P. *Inorg. Chem.* **2008**, 47, 8943. (b) Maheswari, P. U.; Hartl, F.; Quesada, M.; Buda, F.; Lutz, M.; Spek, A. L.; Gamez, P.; Reedijk, J. *Inorg. Chim. Acta* **2011**, 374, 406. (c) Chaudhuri, P.; Hess, M.; Flörke, U.; Wieghardt, K. *Angew. Chem., Int. Ed.* **1998**, 37, 2217.

20. Chaudhuri, P.; Hess, M.; Weyhermuller, T.; Wieghardt, K. *Angew. Chem. Int. Ed.* **1999**, 38 (8), 1095.

21. Chaudhuri, P.; Hess, M.; Muller, J.; Hildenbrand, K.; Bill, E.; Weyhermuller, T.; Wieghardt, K. *J. Am. Chem. Soc.* **1999**, 121 (41), 9599

22. McCollom, S. P.; Weberg, A. B.; Thierer, L. M.; Gau, M. R.; Carrol, P. J.; Tomson, N. C. *in preparation*

23. McCollom, S. P.; Tomson, N. C. *in preparation*

24. Lee, J. Y.; Peterson, R. L.; Ohkubo, K.; Garcia-Bosch, I.; Himes, R. A.; Woertink, J.; Moore, C. D.; Solomon, E. I.; Fukuzumi, S.; Karlin, K. D. *J. Am. Chem. Soc.* **2014**, 136, 9925

25. Maiti, D.; Lee, D.; Gaoutchenova, K.; Wurtele, C.; Holthausen, M. C.; Sarjeant, A. A. N.; Sundermeyer, J.; Schindler, S.; Karlin, K. D. *Angew. Chem. Int. Ed.* **2008**, 47, 82

26. Yadav, A.; Mathur, P. *Inor. Chim. Acta.* **2015**, 435, 206

27. Zhou, H.; Shen, Y. F.; Wang, J. Y.; Chen, X.; O'young, C.-L.; Suib, S. L. *J. Catal.* **1998**, 176, 321.

4.5 Experimental

General Considerations

All reactions containing transition metals were performed under an inert atmosphere of N_2 using standard Schlenk line or glovebox techniques unless addition of O_2 is noted. UHP-grade O_2 (99.99%) was purchased from Airgas and dried over a column of Drierite before use. All solvents (THF, acetonitrile, *n*-pentane, *n*-hexane, and diethyl ether) were dried by passage through a column of activated alumina and stored over 4 Å molecular sieves under an inert atmosphere. Deuterated solvents (CD_3CN and C_6D_6) were dried over CaH_2, isolated via vacuum transfer, and stored under an inert atmosphere over 4 Å sieves. ^1H, $^{13}C\{^1H\}$, $^{31}P\{^1H\}$, $^{19}F\{^1H\}$, spectra were recorded on Bruker DMX300, UNI400, or BioDRX500 spectrometers. All chemical shifts (δ) are reported in units of ppm and referenced to the residual protio-solvent resonance for proton and carbon chemical shifts. External H_3PO_4 or $CFCl_3$ were used for referencing ^{31}P and ^{19}F chemical shifts. Elemental analyses were performed by Midwest Microlab, LLC or at the University of Pennsylvania on a Costech ECS 4010 analyzer in the Earth & Environmental Science Department at the University of Pennsylvania. Accurate mass measurement data were acquired on Waters instruments. Waters software calibrates the instrument and reports the data by use of neutral atomic masses; the mass of the electron is not included. All chemicals, unless specifically mentioned, were purchased from Fisher Scientific.

Ligand Synthesis

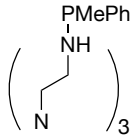

1 2 mL (0.014 mol) of tris(2-aminoethyl)amine were dissolved in 50 mL of THF. 15 equiv of triethylamine (28.4 mL, 0.204 mol) were added to the THF, and the solution was stirred for 10 min. The solution was then frozen in liquid nitrogen and 3 equiv of neat methylphenylphosphine chloride (6.48 g, 0.041 mol) was layered on top of the frozen solution. The mixture was allowed to thaw in a RT waterbath. After stirring the solution overnight, the THF was filtered from the triethylammonium salt and the volatile materials were removed *in vacuo*. The oil was extracted with hexanes and the volatile materials were removed *in vacuo*. Mixtures of mono and di phosphorylation were observed by ^{31}P NMR at ~30 ppm and ~45 ppm respectively with the monophosphoyrlated product as a majority in C_6D_6 . Because of the large impurity though analytical data is not presented for this compound as the next step was significantly easier to purify.

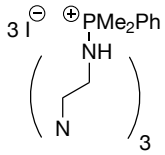

2 3.65 g (0.0071 mol) of **1** were dissolved in 50 mL of THF and cooled to -78 °C in a dry ice/acetone batch. 3 equiv of methyl iodide (1.3 mL, 0.0214 mol) were added dropwise to the solution. The solution was warmed to RT and allowed to stir overnight where **2** precipitates out of solution. The THF was filtered and the solid was washed with THF in 100 % yield (6.9 g). Note that the diphosphorylated product also can be

methylated and the solid obtained contains a mixture of mono- and diphosphorylated products that are resolved after the next step.

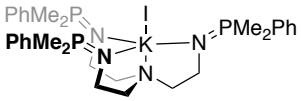

3

7.04 g of **2** (0.0071 mol) were dissolved in pyridine and cooled to -40 °C. A mixture of KH (4 equiv, 1.14 g, 0.0284 mol) in pyridine was added to the cooled solution of **2**. The reaction was stirred for 1 h at RT when bubbling stopped occurring. The solution was filtered and the volatile materials were removed *in vacuo*. The solid was extracted with THF and precipitated at -20 °C in 28 % yield (1.1 g). Crystals can be grown by THF/pentane vapor diffusion. **^{1}H NMR** (300 MHz, $CDCl_3$, 300K) δ 7.63 (m, 6H), δ 7.21-7.30 (m, 10H), δ 3.21 (dt, ^{3}J = 6 Hz, 2 Hz, 6H) , δ 2.66 (t, ^{2}J = 2 Hz, 6H) ppm. **^{31}P{^{1}H} NMR** (121.49 MHz, $CDCl_3$, 300K) δ 12.35 (s) ppm. **MH^+** = 720.15 (calc. 720.15)

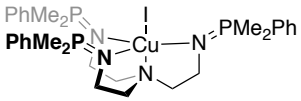

4

0.530 g of **3** (0.00096 mol) were dissolved in 50 mL THF and solid copper iodide (0.182 g, 0.00096 mol) was added to the solution. The solution was stirred overnight, during which time to color turned yellow and a white precipitate, KI, formed. The solution was filtered; the volatile materials evaporated *in vacuo*; and the solid was washed with diethyl ether. **^{1}H NMR** (400 MHz, CD_3CN, 300K) δ 7.4-7.85 (m,

18H), 2.99 (dt, 6H, $^{3}J_{HH}$ = 6 Hz, $^{3}J_{PH}$ = 18 Hz), δ 2.52 (t, 6H, ^{3}J = 6 Hz), δ 1.72 (d, 18H, ^{2}J = 12 Hz) ppm. **$^{13}C\{^{1}H\}$ NMR** (101 MHz, C_6D_6, 300K) δ 132.8,δ 131.4, δ 129.7, δ 68.1, δ 45.4, δ 26.1, δ 15.7 ppm **$^{31}P\{^{1}H\}$ NMR** (162 MHz, C_6D_6, 300K) δ 22.8 (s) ppm. **EA** IS NMR shows 2 % O=PPhMe$_2$ and 92% **4**; Anal. calc. for 92% $C_{30}H_{45}N_4P_4CuI$ and 2 % $C_8H_{11}OP$ (found): C, 45.6 (45.2); H, 5.83 (5.42); N 6.80 (6.20). **UV/vis** 296 nm (Ɛ = ~20,800 $M^{-1}cm^{-1}$), 373 nm (Ɛ = ~10,200 $M^{-1}cm^{-1}$) **IR** FTIR (KBr plate) 3533, 3466, 3358, 3048, 2961, 2895, 2826, 1594, 1435, 1414, 1290, 1261, 1160, 1110, 1046, 1010, 932, 915, 801, 719, 670, 615 cm^{-1}.

General Procedure for Catalytic Reactions Run on Schlenk line (i.e. Optimizations)

20 mg (0.026 mmol) of dimethylphenyl-(P_3tren)Cu(I)I was dissolved in 1 mL of acetonitrile (or THF) in a 50 mL Schlenk tube. Alcohols were added to the Schlenk tube under N_2. (P_3tren)Cu and alcohols were stirred for 5 min then 1 atm of O_2 was added to the Schlenk flask. The reaction was stirred for 14 h unless specified. Volatile materials were removed *in vacuo* and reactions were redissolved in MeCN-d_3 with added internal standard, 1,3,5-trimethoxybenzene or mesitylene.

High-Throughput Experimental Methods

Experiments were set up inside a glovebox under a nitrogen atmosphere. One 24-well aluminum block containing 1 mL glass vials were predosed with dimethylphenyl-(P_3trenCu)(I)I (1 μmol) in MeCN. The volatile materials were removed to dryness using a J-Kem blow down block and a parylene stir bar was then added to each reaction vial. The alcohols (5 μmol each) were dosed into the

reaction vials (100 μmol, 0.05 M) at RT. The well plate was sealed and placed in a dessicator. The dessicator was evacuated and refilled with O_2. The system was sparged with O_2 for 5 min, then the well plate was sealed and heated with stirring at 50 ^oC for 14 h. After 14 h the well plate was opened and diluted to 1 mL with MeCN and all solutions were filtered. Into a separate 96-well GC block was added 700 μL of acetonitrile, followed by 50 μL of the diluted reaction mixtures. The GC block was then sealed with a silicon-rubber storage mat and mounted on an automated GC/MS instrument for analysis.

H_2O_2 Detection

Iodometry: Procedure for hydrogen peroxide detection was followed from literature sources.[4,5] First, 2.0 mg (0.027 mmol) of [(**P_3tren)Cu]I** (20 mol % loading) were dissolved in 1.0 mL of MeCN. Alcohol was then added and stirred for 5 min. 1 atm of O_2 was added to the 50 mL Schlenk tube. After 5, 10, or 15 minutes the volatile materials were evaporated *in vacuo*. Under N_2 and in the dark, 1.0 mL of MeCN was added to redissolve all solids in a glovebox. 100 μL of solution was added to 3.00 mL of NaI saturated MeCN that had been previously degasses. The UV−vis spectrum of this solution displayed the formation of triiodide (I_3^-) at 362 nm, and the yield was calculated by comparing with a standard H_2O_2 solution of known concentrations. Of note is that [(P_3tren)Cu]I, [(P_3tren)Cu]Br_2, [(P_3tren)Cu]I + 1, 2, or 3 equiv of $HBArF_{24}(Et_2O)_2$, or [(P_3tren)Cu]Br_2 + 1, 2, or 3 equiv of $HBArF_{24}(Et_2O)_2$ do not oxidize I^- to I_3^-.

F254 TLC Plates: F254 TLC plates are specially designed for hydrogen peroxide to move on them and to appear has a colored spot under 254 nm light. Reaction mixtures generated exactly as above were run simultaneously as a standard H_2O_2 solution in MeCN. The plate was run with a 2:1 THF:*n*-hexane mixture and H_2O_2 appears at an R_f value of 0.54.

Detection of Isobutylene

First, 2.0 mg (0.027 mmol) of [(P_3tren)Cu]I were dissolved in 1.0 mL of MeCN in a headspace GC/MS vial. 2,4,6-tri-*tert*-butylphenol (35.0 mg, 0.13 mmol) was then added and stirred for 5 min. 1 atm of O_2 was added to the headspace GC/MS vial with a needle. The reaction was tested at 5 min, 10 min, 30 min, and 1 h where isobutylene was detected at all timepoints.

Detection of Methanol

First, 2.0 mg (0.027 mmol) of [(P_3tren)Cu]I were dissolved in 600 μL of MeCN-d_3 in a J-young tube. 2,6-di-*tert*-butyl-4-methoxyphenol (31.8 mg, 0.13 mmol) was then added and stirred for 5 min. The solution was frozen and the headspace was evacuated and refilled with 1 atm of O_2. The reaction was tracked by NMR where a peak for methanol was seen to grow in.

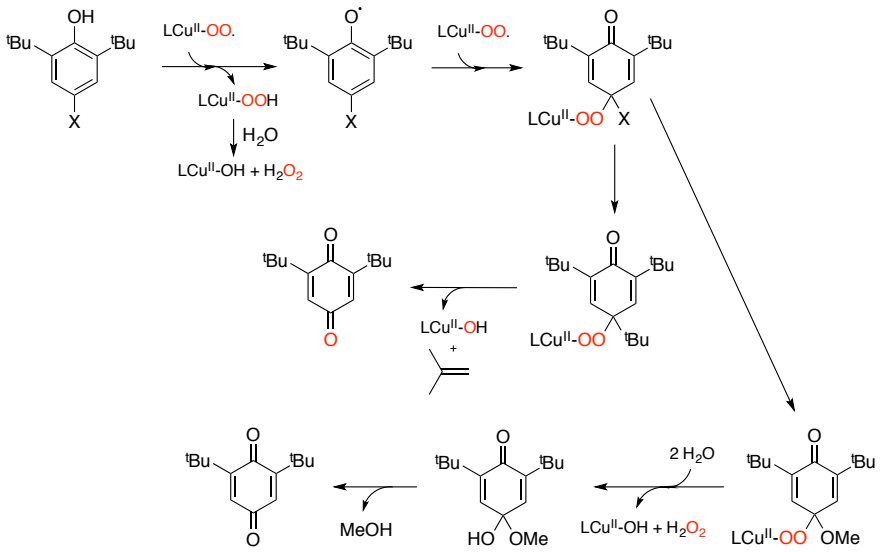

Figure S4.1 Proposed mechanism for cupric superoxide coversion of phenol to benzoquinone.[1]

Table S4.1 Selected controls of benzyl alcohol oxidation.

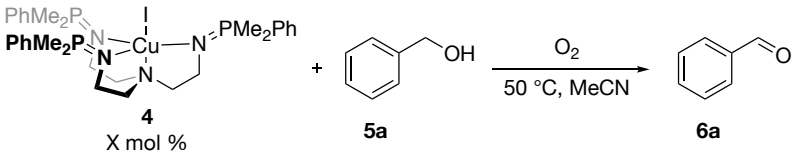

Entry	Ligand	Cu Source	catalyst mol %	O_2	Yield
1	none	none	0	Yes	0 %
2	none	CuI	20	Yes	0 %
3	tren	CuI	20	Yes	17 %
4	P_3tren	none	20	Yes	0 %
5	P_3tren	$Cu(Cl)_2$	20	Yes	0 %
6	P_3tren	$Cu(Cl)_2$	100	No	0 %
7	P_3tren	$Cu(OTf)_2$	100	Yes	0 %

$Cu(Cl)_2$ and $Cu(OTf)_2$ where generated in situ for catalysis testing. Cu(II) salt was mixed with ligand, **3**, giving green solutions and a white precipitate. Solutions where filtered and catalysis was started under optimized conditions.

References

1. Lee, J. Y.; Peterson, R. L.; Ohkubo, K.; Garcia-Bosch, I.; Himes, R. A.; Woertink, J.; Moore, C. D.; Solomon, E. I.; Fukuzumi, S.; Karlin, K. D. *J. Am. Chem. Soc.* **2014**, 136, 9925

Chapter 5: Aryl Fluoride Activation Through Palladium Magnesium Bimetallic Cooperation: A Synthetic and Computational Study[†]

5.1 Introduction

C–F bonds have garnered widespread attention as challenging and attractive targets for materials science, pharmaceuticals, and agrochemicals.[1] At a bond strength of 126 kcal/mol, the C–F bond in fluorobenzene is among the strongest in organic chemistry, and as a result, it is considerably more difficult to cleave than the C–Cl bond in aryl chlorides (96 kcal/mol). Due in large part to this high bond strength, aryl fluorides are inert in the presence of most cross-coupling catalysts. Therefore, if aryl fluorides can be selectively activated, then new synthetic pathways can be envisioned where the aryl fluoride is transformed in the later stages of the synthesis after any harsh condition synthetic steps have been completed.[1c,2]

Few cases are known of palladium catalysts reacting with aryl fluorides.[3] Modes of activation (Figure 5.1) include the η^6-coordination of the aryl fluoride to transition metals complexes such as $Cr(CO)_3$,[3d,3e] the use of aryl fluorides with strongly electron withdrawing groups,[3b,3g] and the use of directing groups to position the palladium in close proximity to the C–F bond.[3c] In the lone example of Pd catalyzed cross-coupling of unactivated aryl fluorides, Dankwardt described use of $Pd(dba)_2$ (5 mol%)/ PCy_2Ph (7.5 mol%) with 3 equiv of ArMgCl at 80 ^oC

[†] Portions of this chapter are reproduced from a soon to be submitted manuscript from authors: Wu, C.; McCollom, S. P.; Zhipeng, Z.; Tomson, N. C.; Walsh, P. J. please note all non-DFT experiments were conducted by Chen Wu and Zhipeng Zhang.

for 2.5 days.[3a] The coupling products were formed with an average GC yield of 47% (6 substrates), limiting the potential utility of this process. One exception was a reaction conducted under microwave irradiation in THF at 150 ^{o}C, which led to 98% GC yield.

While few advances have been made in palladium-catalyzed cross-coupling chemistry with aryl fluorides, several examples are known in which nickel is able to promote this chemistry. The Ni chemistry typically requires bulky and electronic-rich ligands.[4] However, Nakamura and co-workers developed a unique strategy to activate C–F bonds for nickel cross-coupling using a hydroxyphosphine ligand in which an alkoxy-bridged Ni–Mg heterobimetallic complex was proposed as key to Ar–F activation (Figure 5.2).[5] While this nickel catalyst, at 5 mol % loading, can activate a wide array of aryl fluorides in good yields, the major drawback is that the only ligand the Nakamura group found to successfully catalysed the reaction is one they newly synthesized over multiple steps. Therefore, it would be advantageous to use a similar heterobimetallic theory to activate aryl fluorides, but using ligands that are more readily available. Towards this end we focused on Pd, as there are decades of research on a wide variety of phosphine ligands geared toward Pd cross-coupling catalysis.

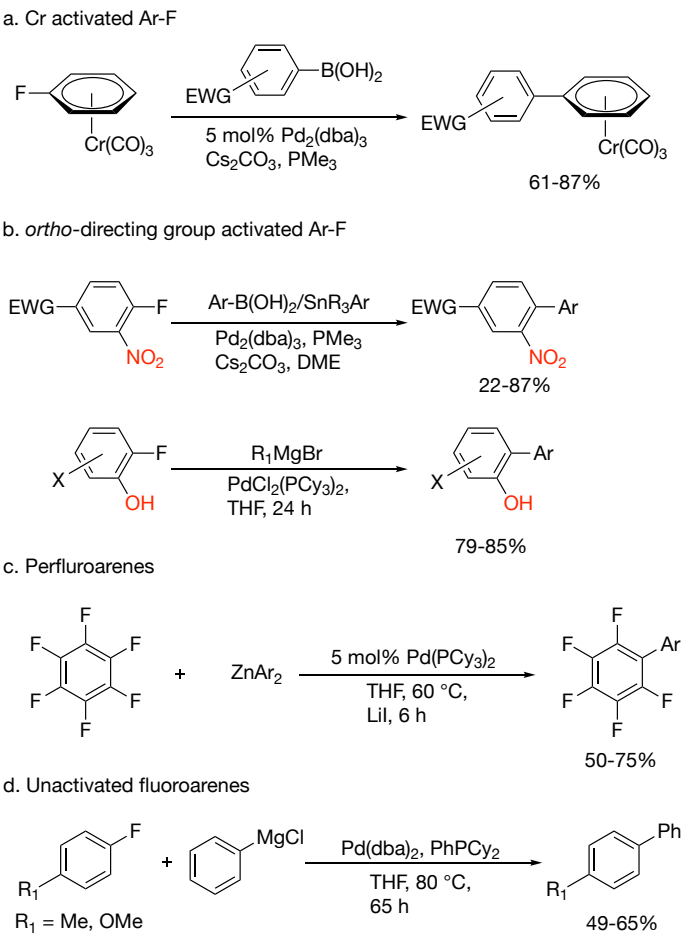

Figure 5.1 Literature examples of Pd-catalyzed cross-coupling reactions with aryl fluorides.

In regards as to which phosphines to focus on, we geared our search to address a major outstanding problem in the heterobimetallic activation of C–X bonds, which is control over the placement of the Lewis acidic main group metal in the vicinity of the transition metal.[6] Our group envisioned harnessing cation-π interactions to place the Lewis acidic metal in proximity to the nucleophilic metal to aid in the heterobimetallic activation. We have prior success using the Bronsted acidic (NIXANTPHOS)Pd complexes (Figure 5.2, far left) designed by van

Lewuuen and coworkers.[7] Under the basic reaction conditions used for the coupling of diarylmethanes with aryl chlorides, the NIXANTPHOS N–H (pKa ~21 in DMSO) was deprotonated, generating an anionic ligand that binds potassium to the nitrogen and the aromatic π-system. This catalyst oxidatively adds unactivated aryl chlorides at room temperature, indicating a substantial decrease in activation energy compared to other palladium catalysts bearing bidentate ligands.[8] We hypothesized that the exceptional reactivity of this system stems from the cooperativity between the main group metal and the palladium catalyst. Further support for cooperativity between the main group metal and Pd in the M(NIXANTPHOS)Pd-based system (M = main group) has been disclosed in the chemoselective functionalization of 2-benzylfuran[9] and in the arylation of toluene.[10]

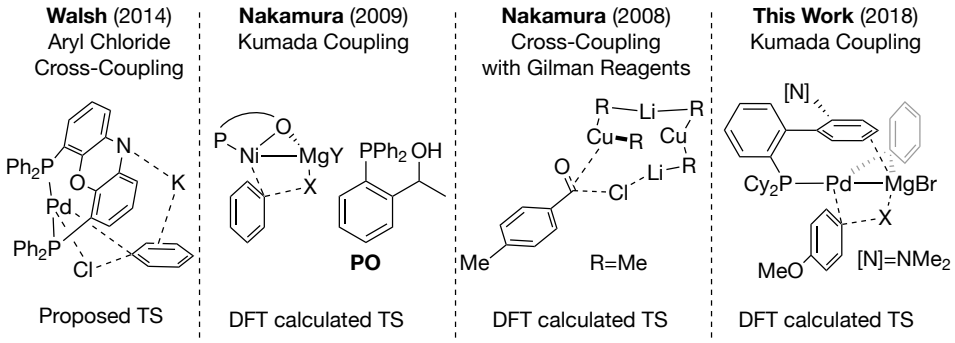

Figure 5.2 Key transitions states for heterobimetallic cooperativity.

Building on this precedent, we sought a class of ligands that would promote the activation of Ar–F bonds through a heterobimetallic activation process. A high-throughput experimentation screen of Pd-catalyzed Kumada-Tamao-Corriu (KTC)

cross-coupling reactions with a variety of potential auxiliary ligands allowed us to identify a class of phosphines that promote Ar–F bond activation under mild conditions and short reaction times. Following initial mechanistic studies, density functional theory (DFT) calculations were used to support the proposal that the magnesium of the Grignard reagent is intimately involved in the oxidative addition of the C–F bond. These findings point to a novel mechanism for the oxidative addition step in Kumada-Tamao-Corriu (KTC) cross-coupling reactions.

5.2 Results and Discussion

5.2.1 Catalyst Identification and Optimization

The KTC cross-coupling reaction between 4-fluorobiphenyl, **1a**, and 4-*tert*-butyl-phenyl magnesium bromide (**2a**) was used as a test reaction. A ligand screen was performed using high-throughput experimentation conditions (10 μmol of **1a**, 25 μmol of **2a**, 10 mol % of $Pd(OAc)_2$, 20 mol % for monodentate phosphines, 10 mol % for bidentate ligands, 80 °C, THF for 16 h). Of the 48 screened phosphine ligands the most promising were cataCXium PCy, DavePhos and CyJohnPhos, all of which share a similar structural motif of two cyclohexyl groups and one biphenyl-type group. Notably, without added phosphine ligand, $Pd(OAc)_2$ alone provided an assay yield of 22 % under these conditions, while the exclusion of $Pd(OAc)_2$ from the reaction mixture gave 0 % yield.

These three ligands were then optimized on laboratory scale (0.1 mmol) with 5 mol % loading of $Pd(OAc)_2$ (Table 5.1, entry 1–3). CyJohnPhos and DavePhos gave similar assay yields (89–90 % AY) with cataCXium PCy lagging

Table 5.1 Selected optimization of coupling between 1a and 2a.[a]

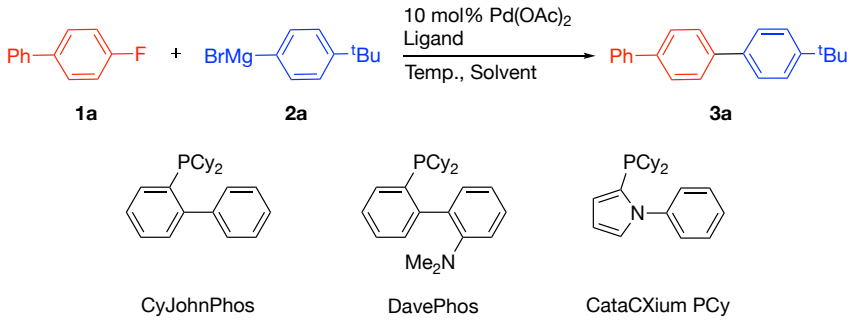

Entry	Ligand	Pd/Ligand (mol %)	Solvent	**1a:2a**	T (°C)	Assay Yield[b]
1	cataCXium PCy	5/20	THF	1:2.5	80	45%
2	DavePhos	5/20	THF	1:2.5	80	89%
3	CyJohnPhos	5/20	THF	1:2.5	80	90%
4	DavePhos	5/20	DME	1:2.5	80	98%
5	CyJohnPhos	5/20	DME	1:2.5	80	89%
6	DavePhos	5/10	DME	1:2.5	80	100%
7	DavePhos	5/10	DME	1:2.5	50	100%
8	DavePhos	5/10	DME	1:2.5	25	33%
9	DavePhos	2.5/5	DME	1:2.5	50	74%
10	DavePhos	5/10	DME	1:2	50	75%
11[c]	DavePhos	5/10	DME	1:2.5	50	100% (99%)

[a] Reactions conducted on a 0.1 mmol scale at 0.1 M. [b] Assay yields determined by ^{1}H NMR spectroscopy of the crude reaction mixture using CH_2Br_2 as the internal standard. [c] Isolated yield after chromatographic purification and 4 h reaction time.

(45 % AY). Changing the solvent from THF to dimethoxyethane (DME) resulted in an increase in AY to 98 % with DavePhos (entry 4) and no change with CyJohnPhos (89 % AY, entry 5). Attempts at lowering the ligand loading and the temperature were found to be successful with optimization at a 5:10 mol % Pd:L ratio and a 50 °C reaction temperature (entries 6-9). When the ratio of Grignard reagent to electrophile (Mg:ArX) was reduced to 2.0, the yield dropped to 75 % (entry 10). Finally, further optimization for reaction time found that the reaction was complete within 4 h under the optimized conditions from entry 7 and a 99 % isolated yield was determined (entry 11).

5.2.2 Reaction Scope

The substrate scope of aryl fluorides with 4-*tert*-butyl phenylmagnesium bromide was next determined. Aryl fluorides bearing weak electron donating groups at the para position, such as phenyl, or strong electron donating groups, like methoxy and *N,N*-dimethylamino, provided high yields of the products **3a**, **3b**, and **3c** in 99, 95, and 91 %, respectively. Aryl fluoride reagents bearing electron withdrawing groups at the meta position, such as carboxylic acid (**1d**), also allowed for successful coupling in 99 % yield. However, when strong electron withdrawing groups at the para position were used, such as trifluoromethyl (**1e**), no coupling products were observed.[18] Sterically hindered aryl fluorides such as 1-fluoro naphthalene or 2-methyl and 2-methoxy groups were also tested but only gave moderate yield (around 50 %) and there was difficulty in isolating them by chromotography. When a higher reaction temperature (80 °C) and an alternative

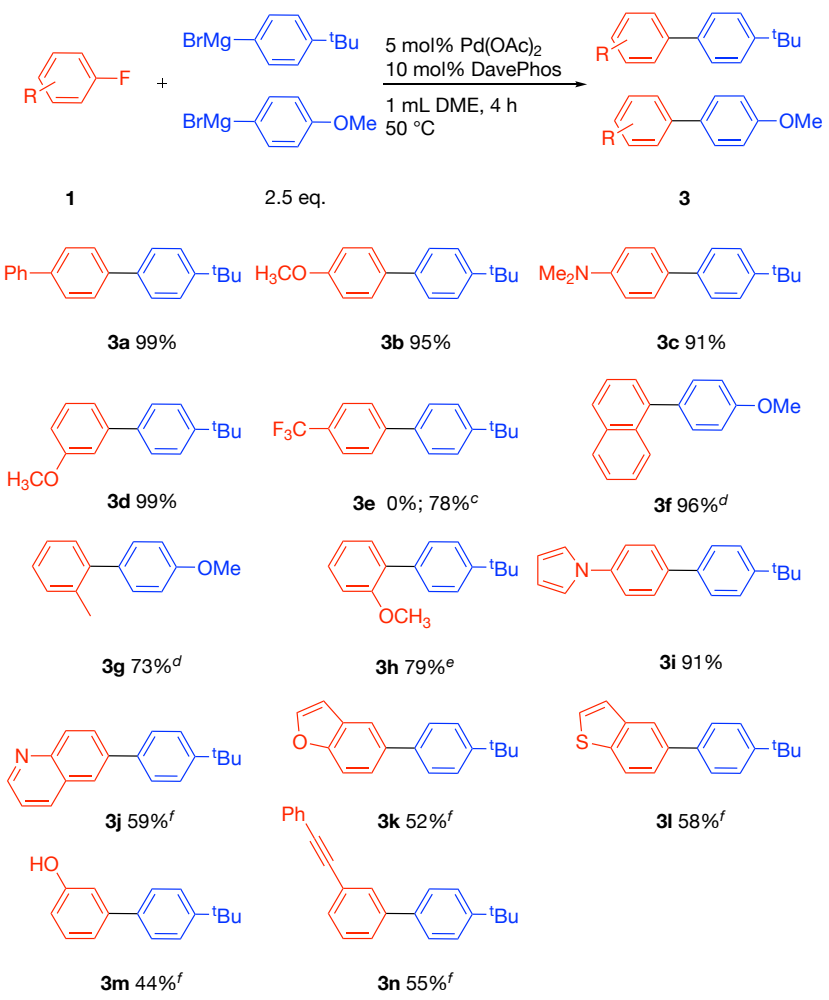

Figure 5.3 Scope of aryl fluorides with aryl Grignard reagents.[a,b]

[a] Reactions conducted on a 0.1 mmol scale at 0.1 M. [b] Isolated yields after chromatographic purification. [c] NIXANTPHOS (7.5 mol %), 80 °C, 12 h. [d] 4-Methoxyphenylmagnesium bromide (2.5 equiv), 80 °C, 12 h. [e] 80 °C, 12 h. [f] $Pd(OAc)_2$ (10 mol %), CyJohnPhos (20 mol %), 80 °C, 12 h and 3.5 equiv Grignard reagent for **3l**.

Grignard reagent (4-methoxyphenylmagnesium bromide, to aid in chromatographic isolation) were used, the desired products **3f–3h** were isolated in 73–96 % yield. Heterocyclic substrates, including 1-(4-fluorophenyl)-1*H*-pyrrole (**1i**), 6-fluoroquinoline (**1j**), 5-fluorobenzofuran (**1k**) and 5-fluorobenzothiophene (**1l**) were examined but only 1-(4-fluorophenyl)-1*H*-pyrrole gave product (**3j**, 91 % yield) using DavePhos. Switching the ligand to CyJohnPhos allowed for the remaining heterocyclic substrates to be successfully coupled in moderate yields. Finally, substrates bearing hydroxyl (**1m**) and alkynyl (**1n**) groups were also tested. DavePhos again gave low yields for these substrates but the related CyJohnPhos provided products **3m** and **3n** in 44 and 55 % yields, respectively.

5.2.3 Mechanistic Insights

In Pd-mediated KTC cross-coupling chemistry, the accepted turnover-limiting step (TLS) involves the oxidative addition of the Ar–X prior to transmetallation by a Grignard reagent.[11] However, the inability of typical $L_1Pd(0)$ complexes to oxidatively add Ar–F bonds prompted further investigation into the means by which the present system is able to mediate this transformation.

Competition experiments were conducted using equimolar mixtures of 4-*tert*-butoxychlorobenzene and 4-methoxyfluorobenzene with varying amounts of phenylmagnesium bromide. These were catalyzed by 5 mol% $Pd(OAc)_2$ and 10 mol% DavePhos in 1 mL DME at 50 ^{o}C for 4 h (Table 5.3). If the Grignard reagent is not involved in (or before) the TLS, then we expect to see a clear preference for the

activation of the aryl chloride at all Grignard to substrate ratios, as it will undergo oxidative addition faster than the aryl fluoride.

Table 5.2 Competitive experiments between aryl fluorides and aryl chlorides.

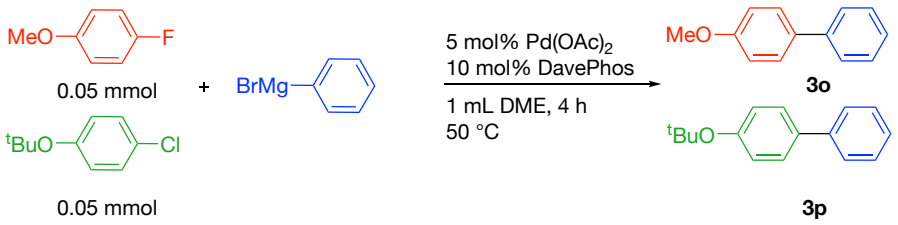

Entry	PhMgBr:ArX	**F** (mmol)	**Cl** (mmol)	**F**:**Cl**
1	0.1:1	0.000	0.0019	0.0
2	0.25:1	0.0039	0.0114	0.34
3	0.5:1	0.0162	0.0248	0.66
4	0.75:1	0.0243	0.0225	1.08
5	1:1	0.0416	0.0385	1.08
6	1.5:1	0.0446	0.0425	1.05
7	2:1	0.0485	0.0462	1.05
8	2.5:1	0.0447	0.0453	0.99

There were several interesting observations from these competition experiments. First, we observed only C–Cl bond activation product, **3p**, at Grignard to substrate ratios of 0.1:1. Secondly, the ratio of C–F activation product (**3o**) to C–Cl activation product (**3p**) increases when the Grignard to substrate ratios are increased from 0.1:1 to 1:1 with the ratio of C–F to C–Cl activation

leveling off at around 1.0 after a 0.5:1 Grignard to substrate ratio. Third, when the reaction was run at the optimized conditions, with a Grignard to substrate ratio of 2.5:1, the ratio of C–F to C–Cl activation is 1.0.

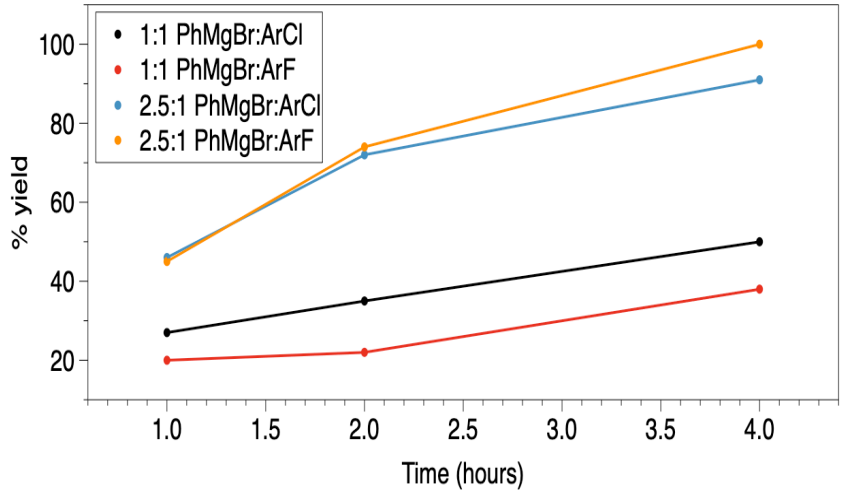

Figure 5.4 Non-competition Time Course Experiments at Mg:ArX Ratios of 1:1 and 2.5:1.

Finally, we conducted time course experiments tracking the formation of **3o** from Ar–F and Ar–Cl in a non-competition manner under optimized conditions. At a Mg:ArX ratio of 1:1, a faster reaction rate was observed for Ar–Cl (1hr, 27%; 4 hr, 50%) compared to Ar–F (1hr, 20%; 4 hr, 38%) (Figure 5.4). However, when the Mg:ArX ratio was increased to 2.5:1, the rates both increased and became more equal between Ar–Cl (1hr, 46%; 4 hr, 91%) and Ar-F (1hr, 45%; 4 hr, 100%) (Figure 5.4).

Taken together, these data suggest that a non-traditional KTC mechanism is being accessed at high Mg:ArX concentration ratios. This dependence on the ratio

of concentrations indicate that it may be possible for both PhMgBr and Ar–X to associate with Pd(0), with Ar–X association leading to a traditional KTC mechanism for Ar–Cl, which is favored at low Grignard to substrate ratios, and PhMgBr association leading to an alternative pathway for both Ar–Cl and Ar–F at high Grignard to substrate ratios.

5.2.4 Computational Study

We next turned to DFT computations to inform our understanding of the manner in which this system is able to promote Ar–F cross coupling. Of the 48 screened phosphine ligands, the three that were most successful share a common structural motif that includes two cyclohexyl groups and one biphenyl-type unit. We chose one of these (DavePhos) as a case study for identifying a mechanism that is able to account for the experimental data.

The monophosphine Pd(0) complex (DavePhos)Pd (**4**) was found to be stabilized by an intramolecular η^2-π-interaction between Pd and the *o*-aryl group of the phosphine (denoted as Ar_P). For complex **4**, this interaction creates a 14 e^- metal center and provides a 17 kcal/mol stabilization. Minor changes to the Pd-P bond length and the Pd-P-C_{ipso} angle compared to those in the 12 e^- L_1Pd isomer indicate that Ar_P binding to Pd does not result in significant structural changes to the ligand backbone. In addition to Ar_P, the coordination of other donors present in the reaction mixture (DME, DavePhos, arenes) provided stabilization with respect to **4**. These include the adduct of **4** with the biphenyl C–C coupling product 4-methoxybiphenyl (**3o**), which forms the Pd(0)-biphenyl adduct **5**. The free energy

of **5** plus those of PhMgBr, ArCl, and ArF is used to define the zero point on the energy surfaces described below.

The traditional cross-coupling catalytic cycle involves the formation of an adduct between an aryl halide and the Pd(0) species **4** (Figure 5.5). This could be envisioned to occur along the catalytic cycle via either dissociation of **3o** from **5**, followed by association of ArX, or by associative substitution of ArX for **3o**. Stahl, Landis, and co-workers have used kinetic experiments and DFT studies to show that a 14 e^- Pd complex undergoes associative ligand exchange involving η^2-bound olefins, with activation barriers of 10-14 kcal/mol.[12] In the present example, attempts to locate transition states for either dissociative or associative ligand exchange processes were unsuccessful. The coordination sphere about Pd in **7** is too hindered to accommodate an additional π-arene interaction, but ring-slippage of **3o** or dissociation of Ar_P could be envisioned to create enough space for binding ArX prior to dissociation of **3o**. A dissociative pathway is also feasible; loss of **3o** from **5** is endergonic by 10.0 kcal/mol and requires minimal reorganization of the coordination sphere about Pd, indicating that 10 kcal/mol may be considered a lower bound for the ligand exchange process.

The ligand exchange process yields the π-ArX complexes **6X** (**X** = **F**, **Cl**), which exhibit Pd-C_{ArX} distances of *ca*. 2.21 Å (**6Cl**) and 2.40 Å (**6F**) as well as η^2 Pd-Ar_P distances of *ca*. 2.83 Å (**6Cl**) and 2.81 Å (**6F**). The subsequent Ar–X oxidative addition transition states (**TS1X**) were located at +9.5 (**TS1Cl**) and +22.9 (**TS1F**) kcal/mol from **6X**. The significant difference in energy between the rate-determining steps for this catalytic cycle are in line with the conventional

understanding that monophosphine Pd complexes undergo facile Ar–Cl oxidative addition and slower Ar–F cleavage. The geometries of **TS1X** exhibit typical three-centered TS character, in line with significant Pd–C and Pd–X bond formation as well as C–X bond cleavage.

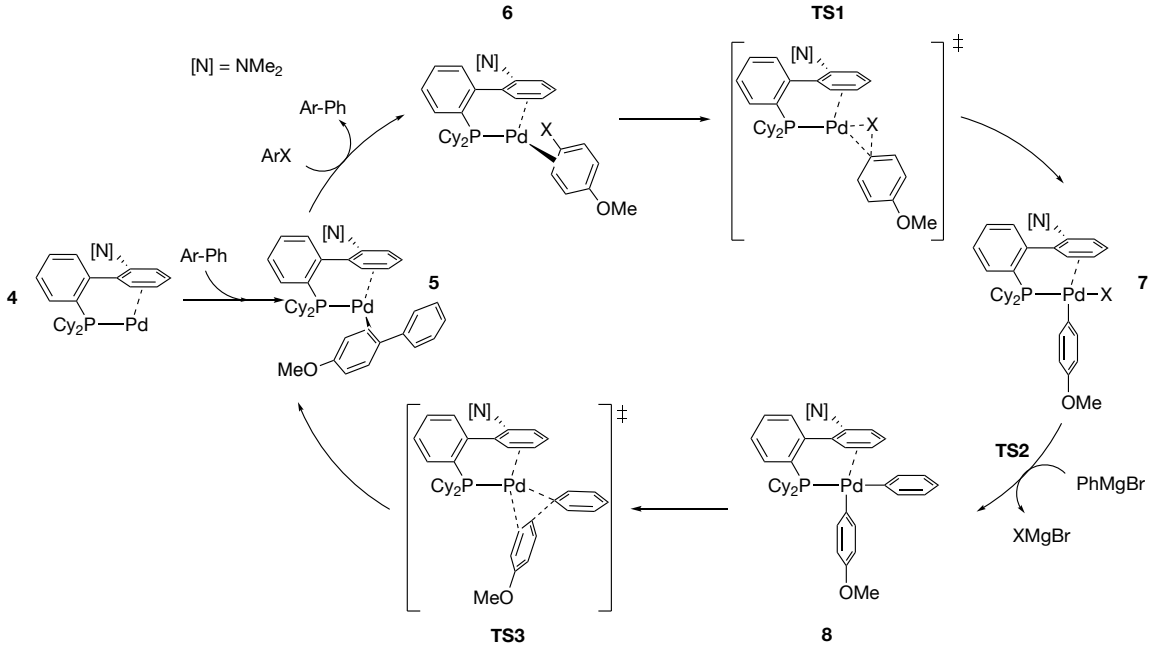

Figure 5.5 Kumada coupling pathway.

The oxidative addition steps lead to the formation of Ar–Pd(II)–X compounds (**7X**). Evaluation of the various possible isomers of **TS1X** and **7X** revealed both a kinetic and thermodynamic preference for placing the halide *trans* to the phosphine. The products **7Cl** (-22.0 kcal/mol from **6Cl**) and **7F** (-8.3 kcal/mol from **6F**) exhibited T-shaped core geometries with added η^2 cation-π interactions between Pd and Ar_P, which complete square-planar coordination environments about the Pd(II) metal centers. Repeated attempts to locate a

transition state for transmetallation (**TS2X**) were unsuccessful. Transmetallation has been shown to be turnover-limiting for Suzuki[13] and Stille[14] couplings, but oxidative addition is thought to be turnover-limiting for the more closely related Negishi coupling reactions.[15,16] For transmetallation to be turnover-limiting, the putative **TS2X** steps would need to lie >30 kcal/mol above **7X**. For comparison, the computed barrier to transmetallation in the aforementioned Negishi cycle is *ca*. 10 kcal/mol from the oxidative addition product.

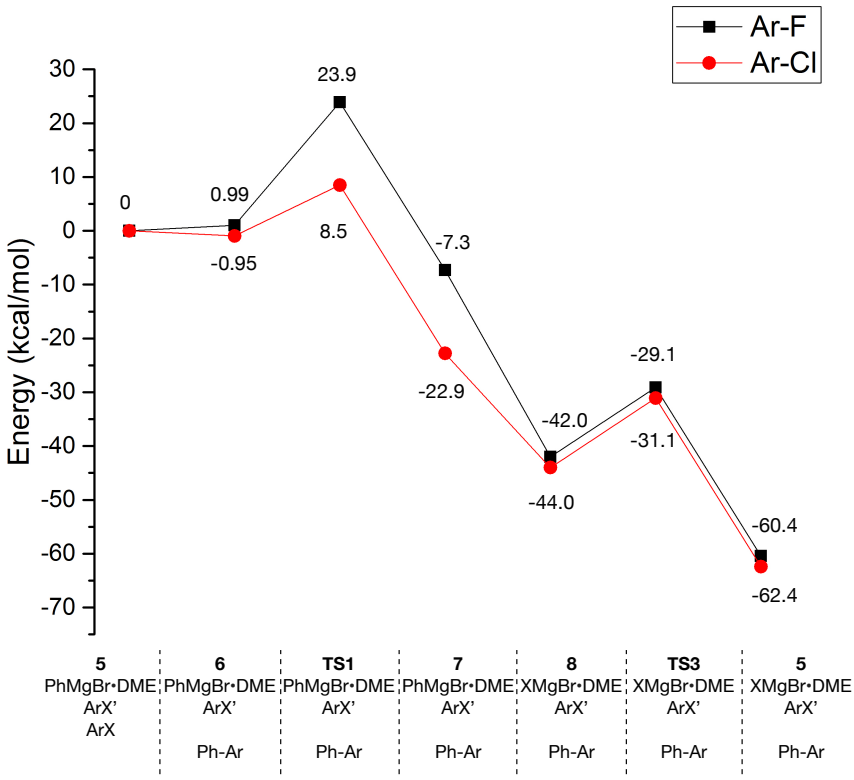

Figure 5.6 Potential energy diagram for the Kumada cycle.

The product of transmetallation with PhMgBr yields the Ar–Pd(II)–Ph species, **8**, and MgBrX. Compound **8** again exhibits an η^2 cation-π interaction

between Pd and Ar_P (Pd–Ar_P = *ca.* 2.77 Å). Reductive elimination (**TS3**) is calculated to be facile (-30.1 kcal/mol versus **6**) *en route* to regenerating the Pd(0) species **5**, which closes the catalytic cycle.

The calculations thus predict that the rate of the traditional KTC pathway is turnover-limited at the oxidative addition step during Ar–F activation and that either the oxidative addition or arene exchange steps are turnover-limiting for Ar–Cl activation. The predicted kinetic preference for Ar–Cl bond activation ($\Delta\Delta G^{\ddagger}$ = 15.4 kcal/mol) contrasts with the competitive Ar–F and Ar–Cl bond activation observed experimentally, suggesting that an alternative pathway may be operative. The traditional KTC pathway also does not account for the experimental observation that Ar–F cross-coupling depends on the relative concentration of Grignard to electrophile, which suggests that the Grignard reagent may compete with the electrophile for binding to Pd(0).

Examples are known of alkyl magnesium complexes forming Lewis acid-base adducts with Fe, Co, Ni, and Cu. In most cases, the alkyl group stabilizes the heterobimetallic core by bridging between the two metal centers ($d_{M–Mg}$ = *ca*. 2.6 Å), but in some examples, an alkylated metal center has been shown to form an unsupported dative interaction with Mg. While no examples are known of Pd(0) binding to Mg, Pd(0) acts as a base for other Lewis acidic metal centers. We and others have previously shown that cation-π interactions can be used to house Lewis acidic metals near a Pd center, and Mg(II) has been shown to form intramolecular cation-π interactions.[17] In addition, a handful of reports of heterobimetallic activation of Ar–X electrophiles have been reported in the literature. The most

salient example involved a Ni-Mg heterobimetallic complex.[3c] In this case, the proposed reaction coordinate included a nickel hydroxyphosphine complex that coordinated Mg through the alkoxide donor. The close proximity of the two metal centers allowed for the simultaneous activation of Ar–X substrates through the concerted delivery of X to Mg and Ar to Ni (Figure 5.8). Transition states were identified for X = $OP(O)(OMe)_2$, $OC(O)NMe_2$, OMe, and SMe, but attempts to locate transition states for aryl halide activation (X = F, Cl, Br) were unsuccessful.

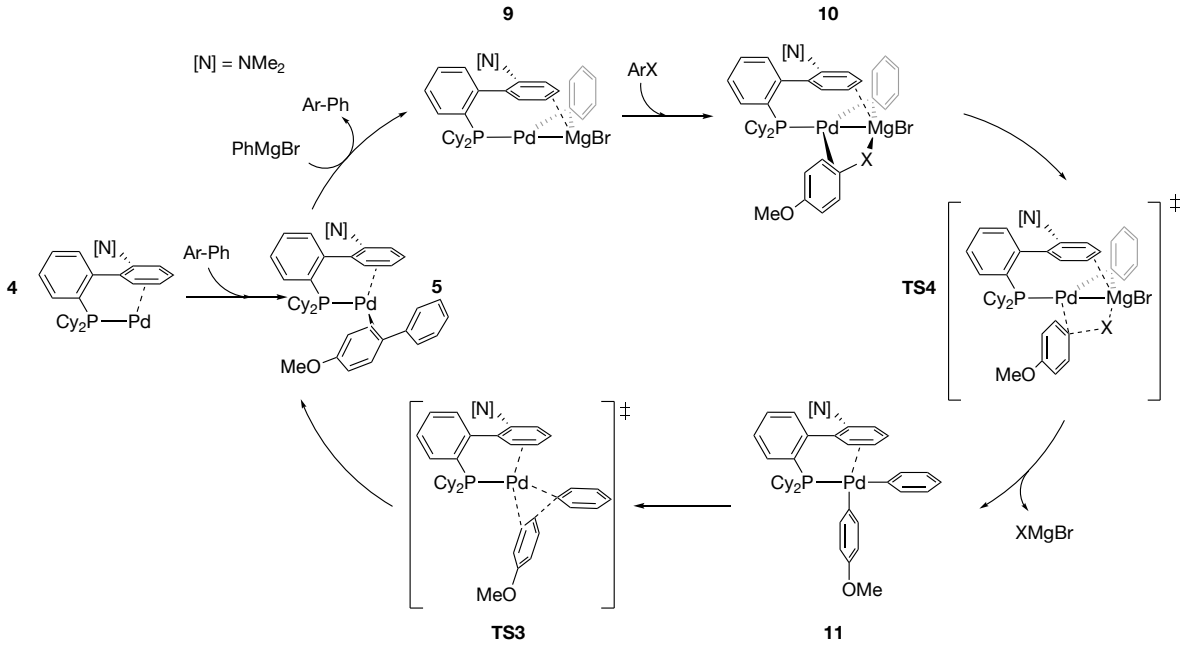

Figure 5.7 Heterobimetallic cycle.

With DavePhos as a supporting ligand, the interaction between Pd(0) (**5**) and PhMgBr was computed to be highly exergonic (ΔG = -23.2 kcal/mol), generating a heterobimetallic palladate species, **9**. Compound **9** features a Pd-Mg distance of 2.44 Å that is supported with both a μ-phenyl bridge (Pd-C_{ipso} = 2.11

Å, Mg-C_{ipso} = 2.35 Å; <Pd-C_{ipso}-C_{para} = 158.2°) and an η^2 cation-π interaction between Mg and the biphenyl portion of the phosphine ligand. The Mg-C_π distances of *ca.* 2.79 Å are comparable with crystallographically characterized compounds that share the η^2 cation-π motif (Mg-C_π distances of *ca.* 2.62 Å).

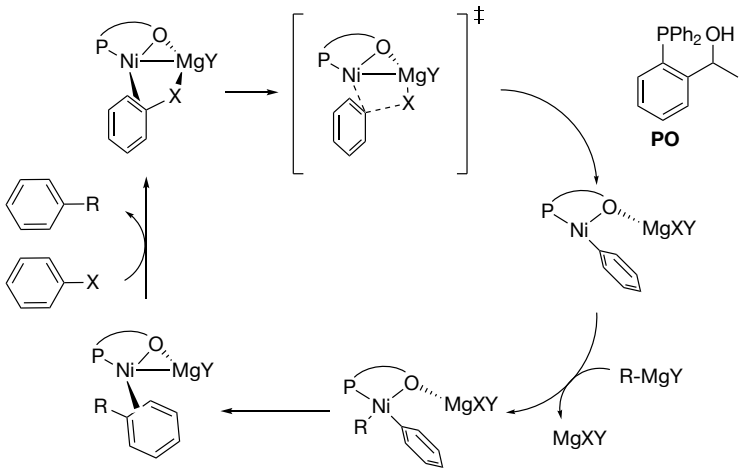

Figure 5.8 Nakamura group proposed Mg/Ni cooperative activation of ArX.

The formally anionic Pd(0) center of **9** adopts a T-shaped geometry, with the μ-phenyl *ipso* carbon located *trans* to the phosphine (<P-Pd-C_{ipso} = 170.3°) and the Mg center *cis* to the phosphine (<P-Pd-Mg = 117.8°). This geometry did not provide a viable pathway for approach of ArX that would allow for cooperative action by Pd and Mg; however, a scan of the P–Pd–C_{ipso} angle from 175° to 100° revealed a flat potential energy surface. The MgBr unit trails the μ-phenyl group as the P–Pd–C_{ipso} angle is varied, leading to a *trans*-disposed Mg center at <P–Pd–C_{ipso} = 100° in a structure that lies 4.5 kcal/mol higher in energy than the ground

state geometry. Ar_P has migrated at this point, regenerating an η^2 π-interaction with Pd(0).

The addition of ArX to **9** results in the arene complexes **10X**. In this case, however, the position of Mg allows for a concurrent dative interaction from the halide to Mg (Mg–Cl = 2.57 Å; Mg–F = 2.14 Å). Ar_P returns to Mg in **10X**, forming cation-π interactions at distances of *ca.* 2.92 Å (Cl) and 2.83 Å (F). The modest increase in free energy on formation of **10X** (+12.9 kcal/mol vs. {**9** + Ar–X}) masks the substantial activation of the aryl halides, which both exhibit 0.11 Å increases in the Ar–X bond distances and pyramidalization of the ArX *ipso* carbon (sum of angles about C_{ipso} = 343.2°; <Pd-C_{ipso}-C_{para} = 107.3°). Nakamura and co-workers used constrained geometry scans to support the notion that aryl halide bond activation is nearly barrierless in the Ni:Mg heterobimetallicsystem. In the present system, the transition states for Ar–X bond cleavage (**TS4X**) were located and found to exhibit exceedingly small activation energies with respect to **10X**: +0.2 kcal/mol for **TS4Cl** and +1.1 kcal/mol for **TS4F**. The structures of **TS4X** are similar to those of **10X**, in accord with Hammond's postulate (Figure 5.9). Both of the Ar–X distances in **TS4X** are elongated by 0.32 Å from **10X**, while the Mg–X and Pd–$C_{ipso(ArX)}$ distances decrease by 0.11 Å, as expected for Ar–X bond breaking and Pd–Ar/Mg–X bond formation. We note that Ar_P retains η^2 cation-π interactions of *ca.* 2.9 Å with Mg in the transition states. We were unable to locate intermediates following **TS4X** that retain MgBrX in the coordination sphere of Pd. Presumably, oxidation to Pd(II) weakens the Pd–Mg interaction such that salt loss requires a negligible amount of energy. The resulting Ph-Pd(II)-Ar species (**8**,

described above) undergoes reductive elimination through the previously described three-centered transition state (**TS3**), calculated to lie >20 kcal/mol lower in energy than **TS4X**.

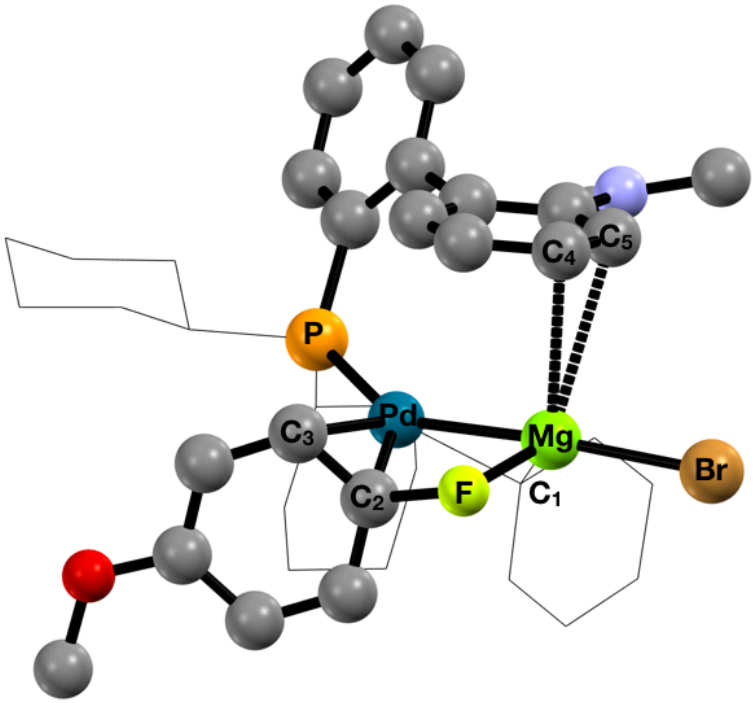

Figure 5.9 DFT opyimized structure of **TS4F**; all hydrogen atoms were removed for clarity. Important bond lengths (Å) and angles (deg): Pd-C1 2.166, Pd-C2 2.076, Pd-C3 2.474, Pd-Mg 2.610, Pd-P 2.381, F-C2 1.683, Mg-C1 2.320, Mg-C4 2.798, Mg-C5 3.044, F-Mg-Br 107.1, Pd-Mg-C1 51.7, C2-F-Mg 96.3.

On evaluation of the full energy surface provided in Figure 5.10, we are left with the conclusion that either the exchange of Ph-Ar product for PhMgBr (**5→9**) or the association of ArX to the Grignard-bound Pd(0) complex (**9→10**) is

turnover-limiting. As mentioned above, $\mathbf{TS_{9\rightarrow 10}}$ would need to lie >23 kcal/mol higher in energy than **9**, a significant value for a ligand association process. Thus, we propose that $\mathbf{TS_{5\rightarrow 9}}$ is turnover-limiting for the heterobimetallic pathway and that this transition state is of comparable energy to the ligand exchange process in the KTC pathway (Figure 5.6, $\mathbf{TS_{5\rightarrow 6}}$). It was found experimentally that increasing the Grignard concentration mitigated the difference in rates of formation of Ar–F and Ar–Cl coupling products. This suggests that at low Grignard to subsrate ratios, the KTC pathway is favoured, yielding higher proportions of Ar–Cl activation products than Ar–F activation products. However, with high Grignard to substrate ratios, the available Pd(0) in solution is shunted to a heterobimetallic pathway that is turnover-limited by ligand exchange. This is consistent with the results of the competition experiment, which found that Ar–F and Ar–Cl activation occurred at comparable rates under high Grignard to substrate ratio conditions. While Ar–X activation ceased to be turnover-limiting in the heterobimetallic mechanism, it is still worth highlighting the dramatic stabilization offered by the heterobimetallic mechanism (*i.e.* **TS1** vs. **TS4**). The transition state energy for the Ar–Cl activation step was decreased by 18.5 kcal/mol, and the $\Delta G^{\ddagger}$ for Ar–F decreased by 33.0 kcal/mol when PhMgBr was used to assist in Ar–F bond cleavage.

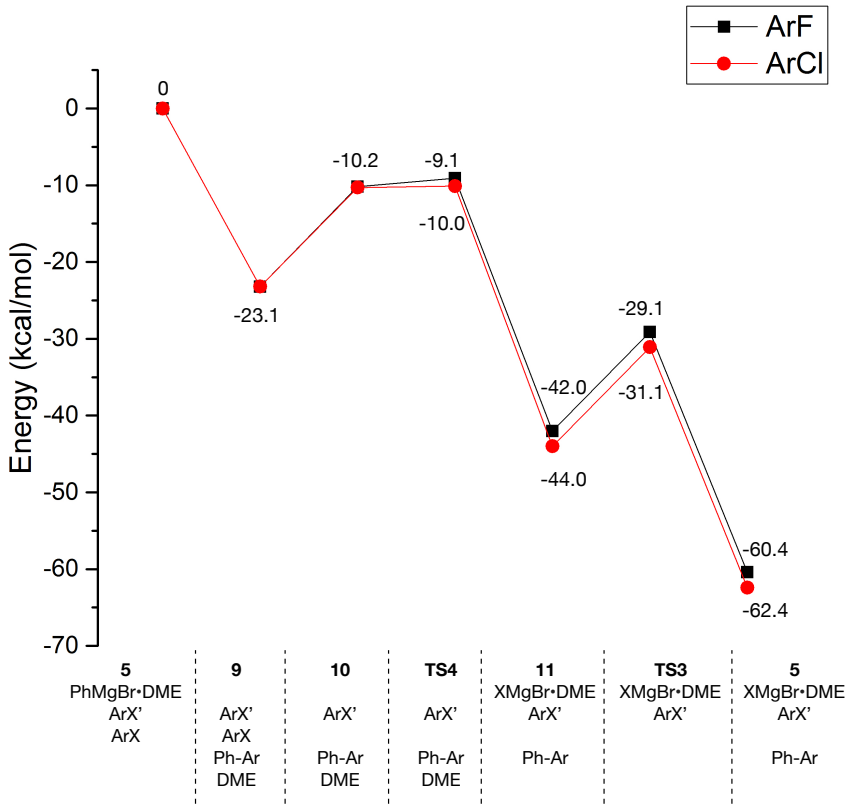

Figure 5.10 Potential energy diagram for the heterobimetallic pathway.

5.2.5 Experimental Support for Heterobimetallic Mechanism

Additional experimental work was used to support the proposed heterobimetallic mechanism. The constrained structure of **TS4** brought about through phosphorus coordination to Pd and biphenyl binding to Mg places one of the phosphine's cyclohexyl groups along a portion of the π-face of the aryl halide. Thus, an increase in the steric bulk of the electrophile was proposed to result in diminished catalytic activity, in contrast to traditional KTC cycles, which are known to exhibit limited rate effects due to variations in the steric profile of the electrophile.[11b] Both 2,6-dimethyl-1-fluorobenzene and 3,5-dimethyl-1-

fluorobenzene were evaluated as substrates for the reaction of 2.5:1 Grignard to substrate ratios. The use of 3,5-dimethyl-1-fluorobenzene resulted in a slower reaction rate (80% yield after 4 h, compared to 99% after 4 h for 4-phenyl-1-fluorobenzene), and the use of 2,6-dimethyl-1-fluorobenzene under identical conditions halted the reaction entirely.

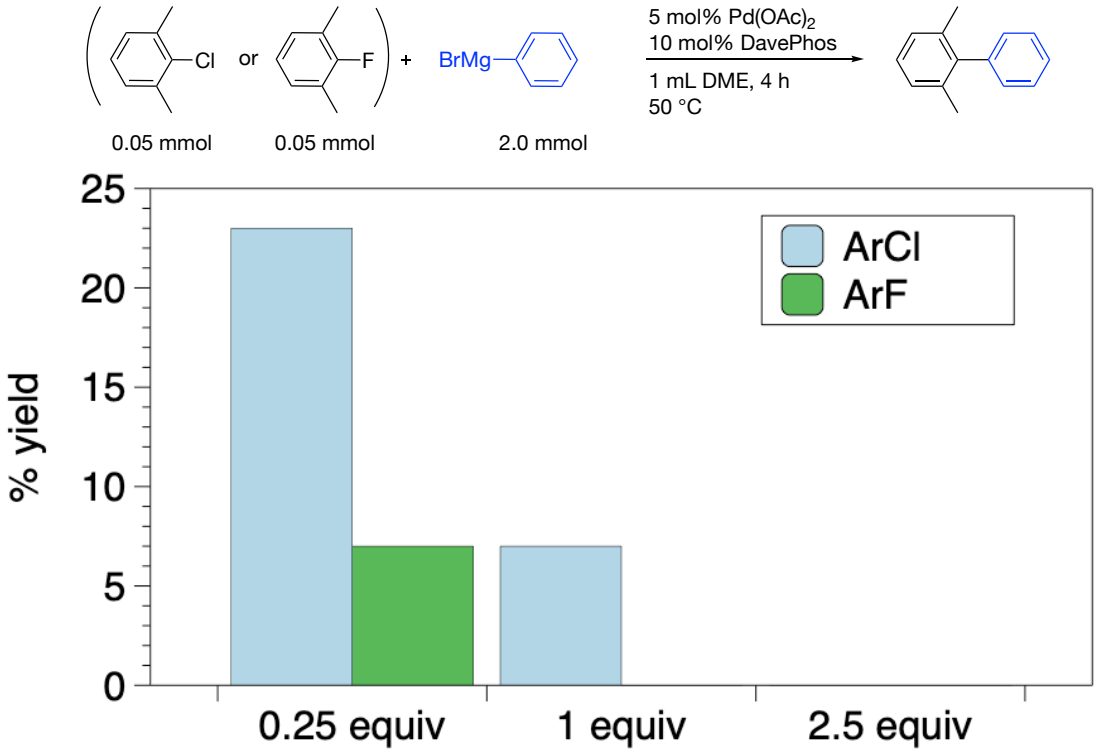

Figure 5.11 Non-competition Experiments at Mg:ArX Ratios of 0.25:1, 1:1 and, 2.5:1 using 2,6-dimethyl-1-fluorobenzene or 2,6-dimethyl-1-chlorobenzene.

To further probe the proposed switching of mechanisms from KTC to heterobimetallic based on Grignard to substrate ratio, 2,6-dimethyl-1-fluorobenzene and 2,6-dimethyl-1-chlorobenzene were tested at different ratios in a non-competition manner (Figure 5.11). At a Grignard to substrate ratio of 0.25:1,

coupling from Ar–Cl predominated with a 23 % yield compared to 7 % yield for the Ar–F experiment. When the Grignard to substrate ratio was raised to 1:1 both yields decreased with 2% and 0% for Ar–Cl and Ar–F respectively, while at a 2.5:1 ratio no product was seen for Ar–Cl or Ar–F. These finding corroborate the hypothesis that at low Grignard to substrate ratios that Ar–X will go through the KTC mechanism and Ar-Cl proceeds at a faster rate where there is no steric hinderance to oxidative addition from the 2,6-dimethyl groups. If the Grignard to substrate ratio is increased then the heterobimetallic pathways begins to be favoured and because of the congested TS for Ar–X bond activation, a 2,6-dimethyl substituted Ar–X can not access the Pd center for activation.

Further, the proposed Pd:Mg heterobimetallic structure was supported through the use of a novel phosphine architecture, $Cy_2P(o\text{-Bn-}C_6H_4)$, in which an *ortho* position on the aryl ring of Cy_2PPh was substituted with a benzyl group. Under the optimized reaction conditions described above, this ligand provided a significant yield enhancement over the reaction run under phosphine-free conditions (71% vs. 22%) (Figure 5.13). Additional evidence for $Cy_2P(o\text{-Bn-}C_6H_4)$ going through a similar heterobimetallic mechanism was obtained using DFT computations. A TS (**TS4F-OB)** nearly identical to **TS4F** was obtained with the $Cy_2P(o\text{-Bn-}C_6H_4)$ ligand. **TS4F** and **TS4-OB** have similar changes in comparison to their respective arene complexes **10F** and **10F-OB** (Figure 5.12). **TS4F-OB** exhibits elongation of the Ar–F by 0.22 Å (vs. 0.32 Å in **TS4F**), while the Mg-F distance decreases by 0.18 Å (vs. 0.11 Å in **TS4F**) and Pd–$C_{ipso(ArX)}$ distance decreases by 0.12 Å (vs. 0.11 Å in **TS4F**) as expected for Ar–F bond breaking and

Pd–Ar/Mg–X bond formation. Finally, Ar_P retains η^2 cation-π interactions of *ca.* 2.9 Å with Mg in both **TS4F** and **TS4-OB**.

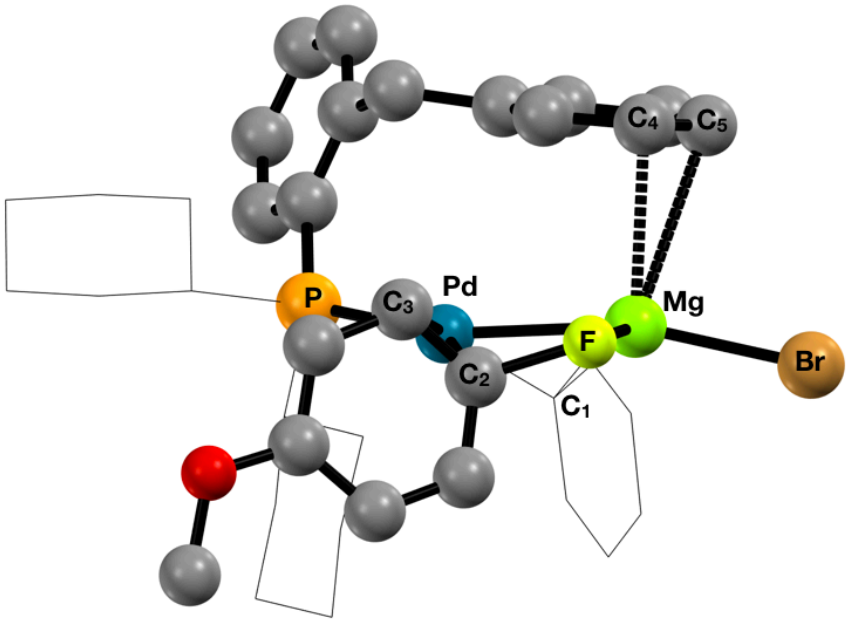

Figure 5.12 DFT optimized structure of **TS4F-OB**; all hydrogen atoms were removed for clarity. Important bond lengths (Å) and angles (deg): Pd-C1 2.158, Pd-C2 2.061, Pd-C3 2.405, Pd-Mg 2.662, Pd-P 2.386, F-C2 1.690, Mg-C1 2.294, Mg-C4 2.776, Mg-C5 3.062, F-Mg-Br 105.9, Pd-Mg-C1 51.1 C2-F-Mg 95.0.

Further modifications to the phosphine revealed the importance of both the cyclohexyl and pendant aryl moieties, as use of either $Ph_2P(o\text{-Bn-}C_6H_4)$ or $Cy_2P(o\text{-Me-}C_6H_4)$ resulted in comparable activity to the phosphine-free conditions (20% and 18% yield, respectively). We propose that the aliphatic cyclohexyl groups are necessary for creating an electron rich Pd center, as needed for binding Mg, and that the *o*-Bn group aids in retaining Mg in the coordination sphere of Pd. The diminished yield observed for $Cy_2P(o\text{-Bn-}C_6H_4)$ compared to

CyJohnPhos/DavePhos suggests, however, that the heterobimetallic activation of Ar–X is highly sensitive to the manner in which the Lewis acid is supported and positioned.

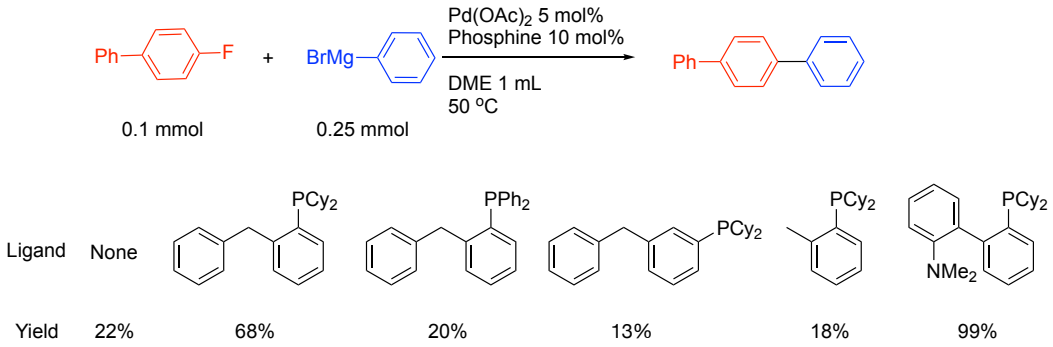

Figure 5.13 Reactions with modified phosphines.

5.3 Conclusion

In summary, a catalytic method for the cross coupling of unactivated aryl fluorides and aryl Grignard reagents has been developed. A wide array of substrates with different electronic and steric profiles lead to products in moderate to excellent yields when using conditions optimized with high throughput experimentation. A computational study was used to evaluate two possible reaction mechanisms. In stoichiometric Grignard:electrophile ratios, it is proposed that the electrophile outcompetes Grignard for binding to Pd(0). This leads to a traditional KTC pathway involving oxidative addition of the electrophile, followed by transmetallation from the Grignard. However, due to the Ar_P-assisted binding of Mg, coordination of Grignard competes for Pd(0) at elevated Grignard:electrophile ratios. The resulting heterobimetallic complex appears to be equally competent at

Ar–F and Ar–Cl activation, while providing a substantial decrease in the activation energy for each compared to the traditional oxidative addition pathway. The cooperativity of Mg and Pd was made possible by a cation-π interaction with a biphenyl group on the phosphine. This interaction supported the close proximity of Mg and Pd, which was shown to be integral to aryl halide bond activation. Further exploitation of this bimetallic cooperativity is underway.

5.4 References

(1) (a) Liu, X.; Echavarren, J.; Zarate, C.; Martin, R. *J. Am. Chem. Soc.* **2015**, 137, 39, 12470. (b) Ahrens, T.; Kohlmann, J.; Ahrens M.; Braun, T. *Chem. Rev.* **2015**, 115. (2), 931 (c) Amii, H.; Uneyama, K. *Chem. Rev.* **2009**, 109, 5, 2119. (d) Clot, E.; Eisenstein, O.; Jasim, N.; Macgregor, S. A.; McGrady, J. E.; Perutz, R. N. *Acc. Chem. Res.* **2011**, 44, 333. (e) O'Hagan, D. *Chem Soc Rev*. **2008**, 37, 308. (f) Reinhold, M.; McGrady, J. E.; Perutz, R. N. *J. Am. Chem. Soc.* **2004**, 126, 5268. (g) Bosque, R.; Clot, E.; Fantacci, S.; Maseras, F.; Eisenstein, O.; Perutz, R. N.; Renkema, K. B.; Caulton, K. G. *J. Am. Chem. Soc.* **1998**, 120, 12634..

(2) (a) Shen, Q.; Huang, Y.; Liu, C.; Xiao, J.; Chen, Q.; Guo, Y. *J. Fluor. Chem.* **2015**, 179, 14. (b) Utsumi, S.; Katagiri, T.; Uneyama, K. *J. Fluor. Chem.* **2013**, 152, 84. (c) Doster, M. E.; Johnson, S. A. *Angew. Chem. Int. Ed.* **2009**, 48, 2185. (d) Träff, A. M.; Janjetovic, M.; Ta, L.; Hilmersson, G. *Angew. Chem. Int. Ed.* **2013**, 52, 12073.

(3) (a) Dankwardt, J. W. *J. Organmet. Chem.* 2005, 690, 932. (b) Cargill, M. R.; Sandford, G.; Tadeusiak, A. J.; Yufit, D. S.; Howard, J. A. K.; Kilickiran, P.; Nelles, G.

J. Org. Chem. 2010, 75, 5860. (c) Bahmanyar, S.; Borer, B. C.; Kim, Y. M.; Kurtz, D. M.; Yu, S. *Org. Lett.* 2005, 7, 1011. (d) Ishikawa, S.; Manabe, K. *Synthesis-Stuttgart* 2008, 3180. (e) Widdowson, D. A.; Wilhelm, R. E. *Chem. Comm.*1999, 2211. (f) Widdowson, D. A.; Wilhelm, R. *Chem. Comm.* 2003, 578; (g) Yu, D. H.; Shen, Q. L.; Lu, L. *J. Org. Chem.* 2012, 77, 1798; (h) Kim, Y. M.; Yu, S. *J. Am. Chem. Soc.* 2003, 125, 1696.

(4) (a) Tasker, S. Z.; Standley, E. A.; Jamison, T. F. *Nature* **2014**, 509, 299. (b) Tobisu, M.; Xu, T.; Shimasaki, T.; Chatani, N. *J. Am. Chem. Soc.* **2011**, 133, 19505. (c) Littke, A. F.; Fu, G. C. *Angew. Chem., Int. Ed.* **2002**, 41, 4176.

(5) Yoshikai, N.; Matsuda, H.; Nakamura, E. *J. Am. Chem. Soc.* **2009**, 131, 9590.

(6) (a) Yoshikai, N.; Iida, R.; Nakamura, E. *Adv. Synth. Catal*. **2008**, 350, 1063. (b) Nakamura, E.; Mori, S. Angew. Chem., Int. Ed. 2000, 39, 3750–3771. (c) Yoshikai, N.; Nakamura, E. *J. Am. Chem. Soc.* **2004**, 126, 12264. (d) Rodriguez, M. M.; Bill, E.; Brennessel, W. W.; Holland, P. L. *Science* **2011**, 334, 780.

(7) (a) van der Veen, L. A.; Keeven, P. H.; Schoemaker, G. C.; Reek, J. N. H.; Kamer, P. C. J.; van Leeuwen, P. W. N. M.; Lutz, M.; Spek, A. L. *Organometallics* **2000**, 19, 872. (b) Zhang, J.; Bellomo, A.; Trongsiriwat, N.; Jia, T.; Carroll, P. J.; Dreher, S. D.; Tudge, M. T.; Yin, H.; Robinson, J. R.; Schelter, E. J.; Walsh, P. J. *J. Am. Chem. Soc.* **2014**, 136, 6276.

(8) (a) Schoenebeck, F.; Houk, K. N. *J. Am. Chem. Soc.* **2010**, 132, 2496; (b) Senn, H. M.; Ziegler, T. *Organometallics* **2004**, 23, 2980; (c) Kozuch, S.; Amatore, C.; Jutand, A.;

Shaik, S. *Organometallics* **2005**, 24, 2319; (d) Portnoy, M.; Milstein, D. *Organometallics* **1993**, 12, 1665.

(9) Zhang, J.; Sha, S.; Bellomo, A.; Trongsiriwat, N.; Gao, F.; Tomson, N. C.; Walsh, P. J.; *J. Am. Chem. Soc.* **2016**, 138, 4260.

(10) Sha, S.-C.; Tcyrulnikov, S.; Li, M.; Fu, Y.; Kozlowski, M. C.; Walsh, P. J.; Hu, B. *J. Am. Chem. Soc.* **2018**, 140, 12415. For an example with the (NIXANTPHOS)Ni catalyst see: Jiang, H.; Sha, S.-C.; Jeong, S. A.; Manor, B. C.; Walsh, P. J. *Org. Lett.* **2019**, 21, 1735.

(11) (a) Yoshikai, N.; Matsuda, H.; Nakamura, E. *J. Am. Chem. Soc.* **2008**, 130, 15258. (b) Martin, R.; Buchwald, S. L. *J. Am. Chem. Soc.* **2007**, 129, 3844.

(12) Popp, B. V.; Thorman, J. L.; Morales, C. M.; Landis, C. R.; Stahl, S. S. *J. Am. Chem. Soc.* **2004**, 126 (45), 14832.

(13) A. A. C. Braga, G. Ujaque, and F. Maseras, *Organometallics*, **2006**, 25 (15), 3647.

(14) R. Alvarez, M. Perez, O. N. Faza, and A. R. de Lera, *Organometallics*, **2008**, 27 (14), 3378.

(15) P. Ribagnac, M. Blig, J. Villa-Uribe, X. Le Goff, C. Gosmini, and N. Mezailles, *Chem. Eur. J.* **2011**, 17, 14389.

(16) A. B. Gozalez-Perez, R. Alvarez, O. N. Faza, A. R. de Lera, and J. M. Aurrecoechea, *Organometallics* **2012**, 31, 2053.

(17) (a) Tang, Y.; Zakharov, L. N.; Rheingold, A. L.; Kemp, R. A. *Organometallics* **2005** 24 (5), 836. (b) Kovbasyuk, L.; Hoppe, M.; Pritzkow, H.; Krämer, R. *Eur. J. Inorg. Chem.* **2001**, 1353. (c) Zuniga, M. F.; Kreutzer, J.; Teng, W.; Ruhlandt-Senge, K. *Inorg. Chem.* **2007**, 46 (24), 10400. (d) A.-F. Pécharman, M. S. Hill, C. L. McMullin, M. F. Mahon, *Angew. Chem. Int. Ed.* **2017**, 56, 16363.

(18) 4-(trifluoromethyl)fluorobenzene) did not react when using DavePhos as the ligand. 4-(trifluoromethyl)fluorobenzene) was re-optimized with a ligand screen were NIXANTPHOS was found to give the product in 78 % yield at 80 °C.

5.5 Experimental

General Methods. All reactions were performed under nitrogen using oven-dried glassware. Anhydrous CPME, 2-MeTHF, dioxane, DME, toluene and THF were purchased from Sigma-Aldrich and used as solvent without further purification. Unless otherwise stated, reagents were commercially available and used as purchased without further purification. Chemicals were obtained from Sigma-Aldrich, Acros, TCI America or Alfa Aesar, and solvents were purchased from Fisher Scientific. The progress of the reactions was monitored by thin layer chromatography using Whatman Partisil K6F 250 μm precoated 60 Å silica gel plates and visualized by short-wavelength ultraviolet light. Silica gel (230−400 mesh, Silicycle) was used for flash chromatography. The ^{1}H NMR and ^{13}C[16b] NMR spectra were obtained using a Bruker AM-500 Fourier transform NMR spectrometer at 500 and 125 MHz, respectively. Chemical shifts are reported in

units of parts per million (ppm) downfield from tetramethylsilane (TMS), and all coupling constants are reported in hertz.

Ligand Synthesis Procedure. A solution of *n*BuLi (1.6 M in hexanes, 1.1 mmol, 1.1 equiv) was added dropwise to a solution of bromoarenes (1 mmol, 1.0 equiv) in THF (5 mL) at –78 °C, and the mixture was stirred for 1.5 h at the same temperature. A solution of chlorodialkyl(or aryl)phosphine (1.2 mmol, 1.2 equiv) in THF (5 mL) was then added dropwise. The solution changed from orange to light yellow rapidly. The mixture was stirred overnight at room temperature. The reaction mixture was quenched with 10 mL saturated ammonium chloride solution, and then was extracted with Et_2O and dried with sodium sulfate. The volatiles were removed under vacuum and the residue was loaded onto a silica gel column and purified by flash chromatography.

General Procedure A. Pd-Catalyzed Kumada Cross-coupling of Aryl Fluorides with Phenyl Grignard Reagents. An oven-dried 10 mL reaction vial equipped with a stir bar was used under a nitrogen atmosphere. A solution (from a stock solution stirring for 30 min) of $Pd(OAc)_2$ (1.12 mg, 0.0050 mmol, 5 mol%) and DavePhos (3.93 mg, 0.0010 mmol, 10 mol%) in 1.0 mL of dry DME was taken up by syringe and added to the reaction vial. The corresponding aryl fluoride (0.1 mmol, 1 equiv) was added to the reaction mixture followed by 4-*tert*-butylphenyl magnesium bromide (0.125 mL, 0.25 mmol, 2.5 equiv) or 4-methoxyphenyl magnesium bromide (0.125 mL, 0.25 mmol, 2.5 equiv) at room temperature in the dry box and the solution turned slight yellow. The vial was then capped, taken out of the dry

box, stirred at 50 °C. After 4 h, the capped vial was opened to the air, quenched with three drops of H_2O, diluted with 3 mL of ethyl acetate, and filtered over a pad of silica. The pad was rinsed with additional 10 mL ethyl acetate and the solution was concentrated in vacuo. The crude material was loaded onto a silica gel column and purified by flash chromatography.

High Throughput Experimentation screenings

Ligand screening of aryl fluorides with aryl Grignard reagents: Experiments were set up inside a glovebox under a nitrogen atmosphere. Two 24-well aluminum blocks containing 1 mL glass vials were predosed with $Pd(OAc)_2$ (1 μmol) and 47 different phosphine ligands (2 μmol for monodentate phosphine ligands and 1 μmol for bidentate ligands) in THF. The volatile materials were removed to dryness using a J-Kem blow down block and a parylene stir bar was then added to each reaction vial. The 4-fluorobiphenyl (10 μmol/reaction) and 4-*tert*-butylphenyl magnesium bromide (25 μmol/reaction) were then dosed together into each reaction vial as a solution in THF (100 μL, 0.1 M) at room temperature. The 24-well plates were then sealed and stirred for 16 h at 80 ^{o}C. Work up: Upon opening the plate to air, 500 μL of acetonitrile was added into each vial. The plate was covered again and the vials stirred for 10 min to ensure good homogenization. Into a separate 96-well LC block was added 700 μL of acetonitrile, followed by 40 μL of the diluted reaction mixtures. The LC block was then sealed with a silicon-rubber storage mat and mounted on an automated HPLC instrument for analysis.

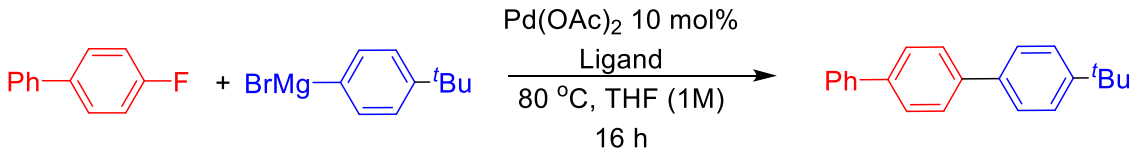

1 equiv. 2.5 equiv.

Entry	Ligand	Prod/IS
1	Benzyldi–1–adamantylphosphine (cataCXium ABn)	13.42
2	2-Dicyclohexylphosphino-2′-methylbiphenyl (MePhos)	13.37
3	N–phenyl–2–(dicyclohexylphosphino)pyrrole (cataCXium PCy)	12.06
4	2–Dicyclohexylphosphino–2'–(*N*,*N*–dimethylamino)biphenyl (DavePhos)	11.76
5	(2–Biphenyl)dicyclohexylphosphine (Cy-JohnPhos)	11.45
6	4,6–Bis(diphenylphosphino)phenoxazine (NIXANTPHOS)	6.00
7	5–(Di–t–butylphosphino)–1', 3', 5'–triphenyl–1'H–[1,4']bipyrazole (BippyPhos)	5.88
8	2-(Dicyclohexylphosphino)-1-(2,4,6-trimethyl-phenyl)-1H-imidazole (cataCXium PICy)	5.16
9	2–(Di–t–butylphosphino)–2'–methylbiphenyl (tBu–MePhos)	5.14
10	1,2,3,4,5–Pentaphenyl–1'–(di–t–butylphosphino)ferrocene (QPhos)	5.09

11	1–[2–[Bis(t–butyl)phosphino]phenyl]–3,5–diphenyl–1H–pyrazole (Trippyphos)	5.03
12	2–(Di–t–butylphosphino)biphenyl (JohnPhos)	5.02
13	Dicyclohexyl–[3,6–dimethoxy–2–(2,4,6–triisopropylphenyl)phenyl]phosphane (Brettphos)	5.02
14	Di(1-adamantyl)-2-morpholinophenylphosphine (MorDal Phos)	4.83
15	2-Di-tert-butylphosphino-2',4',6'-triisopropylbiphenyl (Di-tBu-XPhos)	4.82
16	2–Di–tert-butylphosphino-3,4,5,6-tetramethyl-2′,4′,6′-triisopropyl-1,1′-biphenyl (Me4–t–Bu XPhos)	4.77
17	(2R)-1-[(1R)-1-[Bis(1,1-dimethylethyl)phosphino]ethyl]-2-(dicyclohexylphosphino)ferrocene (Josiphos SL-J009-1)	4.74
18	Di–t–butyl–(1–phenylindol–2–yl)phosphane (cataCXium PIntB)	4.68
19	N–phenyl–2–(di–t–butylphosphino)pyrrole (CataXCium PtB)	4.50
20	9,9–Dimethyl–4,5–bis(diphenylphosphino)xanthene (Xantphos)	4.48
21	Dicyclohexyl(4-(*N*,*N*-dimethylamino)phenyl)phosphine (A-caPhos)	4.27
22	2–Di–tert–butylphosphino–3–Methoxy–6–Methyl–2'–4'–6'–	4.19

	triisopropylbiphenyl (RockPhos)	
23	*N*,*N*'-dicyclohexyl-1-diphenylphosphanyl-formamidine (DCyPF)	4.16
24	2-(Di-tert-butylphosphino)-2',4',6'- triisopropyl-3,6-dimeth+D25:E26oxy-1,1'-biphenyl (tBu-BrettPhos)	4.09
25	N-(dicyclohexylphosphino)-2-(2'-methylphenyl)-1H-indole	4.05
26	2–Dicyclohexylphosphino–2',6'–di–i–propoxy–1,1'–biphenyl (RuPhos)	4.05
27	2′–(Dicyclohexylphosphino)acetophenone ethylene ketal (SymPhos)	4.03
28	1,2-Bis(diphenylphosphino)ethane	3.93
29	Bis[(2-dicyclohexylphosphino)phenyl] ether (DCEPhos)	3.93
30	2–Dicyclohexylphosphino–2',6'–dimethoxy–1,1'–biphenyl (SPhos)	3.87
31	Tri(o–tolyl)phosphine	3.84
32	2–Dicyclohexylphosphino–2′,6′–bis(*N*,*N*–dimethylamino)biphenyl (CPhos)	3.81
33	Rac-2-(Di-tert-butylphosphino)-1,1′-binaphthyl (TrixiePhos)	3.78
34	Butyldi–1–adamantylphosphine (CataCXium A)	3.65

35	*N*,*N*-Dimethyl 4-(Di(tert-butyl)phosphino)aniline (A-taphos)	3.33
36	Di(1-adamantyl)-2-dimethylaminophenylphosphine (MeDal Phos)	3.31
37	Tris(2,4,6-trimethylphenyl)phosphine (PXy_3)	2.31
38	1,1'–Bis(diisopropylphosphino)ferrocene (dippf)	2.13
39	Tricyclohexylphosphine tetrafluoroborate (PCy_3 HBF_4)	1.99
40	Tri(furan-2-yl)phosphine	1.79
41	Triphenylphospine	1.77
42	1,1'–Bis(di–t–butylphosphino)ferrocene (dtbpf)	1.29
43	Tri-tert-butylphosphonium tetrafluoroborate ($PtBu_3$ HBF_4)	0.54
44	Di–tert–butyl(neopentyl)phosphine HBF4	0.54
45	[1,1′–Binaphthalene]–2,2′–diylbis[diphenylphosphine] (Binap)	0.45
46	2-(Dicyclohexylphosphino)-1-(2,4,6-trimethyl-phenyl)-1H-imidazole (cataCXium PICy)	0.13
47	1,3-Bis(diphenylphosphino)propane (dppp)	0.13

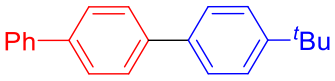

4-(*tert*-butyl)-1,1':4',1''-terphenyl 3a. The reaction was performed following the General Procedure A with 4-fluorobiphenyl (**1a**, 17.8 mg, 0.1 mmol) and 4-*tert*-butylphenyl magnesium bromide (0.125 mL, 0.25 mmol). The crude product was purified by flash chromatography on silica gel (eluted with hexanes) to give the product (28.5 mg, 99%) as a white solid. The spectroscopic data match the previously reported data.[1]

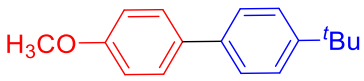

4-(*tert*-butyl)-4'-methoxy-1,1'-biphenyl 3b. The reaction was performed following the General Procedure A with 4-fluoroanisole (**1b**, 12.6 mg, 0.1 mmol) and 4-*tert*-butylphenyl magnesium bromide (0.125 mL, 0.25 mmol). The crude product was purified by flash chromatography on silica gel (eluted with hexanes) to give the product (22.8 mg, 95%) as a white solid. The spectroscopic data match the previously reported data.[2]

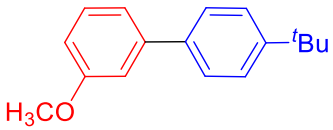

4'-(*tert*-butyl)-3-methoxy-1,1'-biphenyl 3c. The reaction was performed following the General Procedure A with 3-fluoroanisole (**1c**, 12.6 mg, 0.1 mmol) and 4-*tert*-butylphenyl magnesium bromide (0.125 mL, 0.25 mmol). The crude product was purified by flash chromatography on silica gel (eluted with hexanes) to give the product (23.7 mg, 99%) as a white solid. The spectroscopic data match the previously reported data.[3]

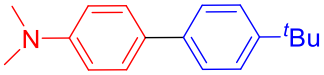

4'-(*tert*-butyl)-*N*,*N*-dimethyl-[1,1'-biphenyl]-4-amine 3d. The reaction was performed following the General Procedure A with 4-fluoroaniline (**1d**, 13.9 mg, 0.1 mmol) and 4-*tert*-butylphenyl magnesium bromide (0.125 mL, 0.25 mmol). The crude product was purified by flash chromatography on silica gel (eluted with hexanes to ethyl acetate=50:1) to give the product (23.0 mg, 91%) as a white solid. The spectroscopic data match the previously reported data.[4]

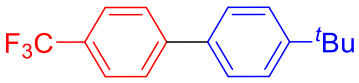

4-(*tert*-butyl)-4'-(trifluoromethyl)-1,1'-biphenyl 3e. The reaction was performed following the General Procedure A with 1-fluoro-4-(trifluoromethyl)benzene (**1e**, 16.4 mg, 0.1 mmol) and 4-*tert*-butylphenyl magnesium bromide (0.125 mL, 0.25 mmol). The crude product was purified by flash chromatography on silica gel (eluted with hexanes) to give the product (21.6 mg, 78%) as a white solid. The spectroscopic data match the previously reported data.[5]

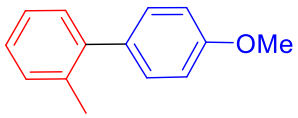

4'-methoxy-2-methyl-1,1'-biphenyl 3f. The reaction was performed following the General Procedure A with 2-fluorotoluene (**1f**, 11.0 mg, 0.1 mmol) and 4-methoxy-phenyl magnesium bromide (0.125 mL, 0.25 mmol). The crude product was purified by flash chromatography on silica gel (eluted with hexanes) to give the product (14.4 mg, 73%) as a white solid. The spectroscopic data match the previously reported data. [6]

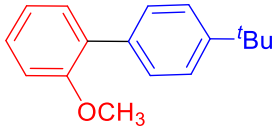

4'-(*tert*-butyl)-2-methoxy-1,1'-biphenyl 3g. The reaction was performed following the General Procedure A with 2-fluoroanisole (**1g**, 12.6 mg, 0.1 mmol) and 4-*tert*-butylphenyl magnesium bromide (0.125 mL, 0.25 mmol). The crude product was purified by flash chromatography on silica gel (eluted with hexanes) to give the product (18.9 mg, 79%) as a white solid. The spectroscopic data match the previously reported data.[7]

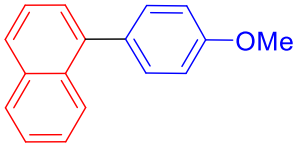

1-(4'-methoxy-[1,1'-biphenyl]-4-yl)naphthalene 3h. The reaction was performed following the General Procedure A with 1-fluoronaphthalene (**1h**, 14.6 mg, 0.1 mmol) and 4-methoxy-lphenyl magnesium bromide (0.125 mL, 0.25 mmol). The crude product was purified by flash chromatography on silica gel (eluted with hexanes) to give the product (22.4 mg, 96%) as a white solid. The spectroscopic data match the previously reported data.[8]

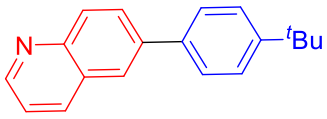

6-(4-(*tert*-butyl)phenyl)quinoline 3i. The reaction was performed following the General Procedure A with 6-fluoroquinoline (**1i**, 14.7 mg, 0.1 mmol) and 4-*tert*-butylphenyl magnesium bromide (0.125 mL, 0.25 mmol). The crude product was purified by flash chromatography on silica gel (eluted with hexanes to ethyl acetate=10:1, R_f=0.16) to give the product (15.4 mg, 59%) as a white solid. M.P.= 94.5-95.5 ^{o}C. ^{1}H NMR

(500 MHz, $CDCl_3$) δ 8.90 (dd, *J* = 4.2, 1.6 Hz, 1H), 8.25 – 8.12 (m, 2H), 8.02 – 7.96 (m, 2H), 7.67 (d, *J* = 8.4 Hz, 2H), 7.53 (d, *J* = 8.4 Hz, 2H), 7.42 (dd, *J* = 8.3, 4.2 Hz, 1H), 1.39 (s, 9 H) ppm. ^{13}C NMR (125 MHz, $CDCl_3$) δ 150.23, 136.20, 129.83, 129.21, 127.10, 125.95, 125.15, 121.41, 34.62, 31.36 ppm. IR (thin film) 2960, 2875, 1493, 1402, 1297, 826 cm^{-1}. HRMS (EI) m/z: [M]+ calcd for C19H19N 261.1517; Found 261.1488.

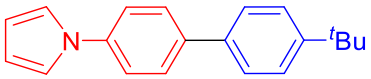

1-(4'-(*tert*-butyl)-[1,1'-biphenyl]-4-yl)-1*H*-pyrrole 3j. The reaction was performed following the General Procedure A with 1-(4-fluorophenyl)-1*H*-pyrrole (**1j**, 16.1 mg, 0.1 mmol) and 4-*tert*-butylphenyl magnesium bromide (0.125 mL, 0.25 mmol). The crude product was purified by flash chromatography on silica gel (eluted with hexanes, R_f=0.15) to give the product (25.1 mg, 91%) as a white solid. M.P. = 193-195 °C. ^1H NMR (500 MHz, $CDCl_3$) δ 7.64 (d, *J* = 8.5 Hz, 2H), 7.54 (d, *J* = 8.4 Hz, 2H), 7.46 (dd, *J* = 15.1, 8.5 Hz, 4H), 7.12 (t, *J* = 2.1 Hz, 2H), 6.36 (t, *J* = 2.1 Hz, 1H), 1.37 (s, 9H) ppm. ^{13}C NMR (125 MHz, $CDCl_3$) 150.64, 139.89, 138.58, 137.45, 128.17, 126.73, 126.01, 120.88, 119.46, 110.62, 34.73, 31.54 ppm. IR (thin film) 2961, 1506, 1396, 1330, 1250, 1076, 818, 723, 669 cm^{-1}. HRMS (EI) m/z: [M]+ calcd for C20H21N 275.1674; Found 275.1691.

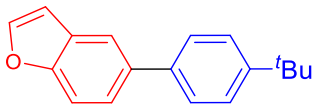

5-(4-(*tert*-butyl)phenyl)benzofuran 3k. The reaction was performed following the General Procedure A with 5-fluorobenzofuran (**1k**, 13.6 mg, 0.1 mmol) and 4-*tert*-butylphenyl magnesium

bromide (0.125 mL, 0.25 mmol). The crude product was purified by flash chromatography on silica gel (eluted with hexanes, R_f=0.35) to give the product (13.0 mg, 50%) as a white solid. M.P. = 96-97 °C. ^{1}H NMR (500 MHz, $CDCl_3$) δ 7.78 (d, *J* = 1.3 Hz, 1H), 7.64 (d, *J* = 2.2 Hz, 1H), 7.58 – 7.50 (m, 4H), 7.47 (d, *J* = 8.4 Hz, 2H), 6.80 (d, *J* = 2.0 Hz, 1H), 1.37 (s, 9H) ppm. ^{13}C NMR (125 MHz, $CDCl_3$) δ 154.66, 150.05, 145.67, 138.95, 136.53, 128.11, 127.28, 125.90, 124.11, 119.70, 111.63, 107.00, 34.71, 31.61 ppm. IR (thin film) 2960, 1460, 1131, 1030, 814, 766, 740 cm $^{-1}$. HRMS (EI) m/z: [M]+ calcd for C18H18O 250.1538; Found 250.1529.

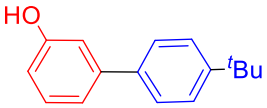

4'-(*tert*-butyl)-[1,1'-biphenyl]-3-ol 3l. The reaction was performed following the General Procedure A with 3-fluorophenol (**1l**, 11.2 mg, 0.1 mmol) and 4-*tert*-butylphenyl magnesium bromide (0.125 mL, 0.25 mmol). The crude product was purified by flash chromatography on silica gel (eluted with hexanes to ethyl acetate=10:1) to give the product (10.0 mg, 44%) as a white solid. The spectroscopic data match the previously reported data.[9]

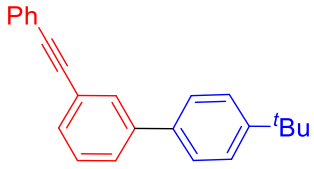

4'-(*tert*-butyl)-3-(phenylethynyl)-1,1'-biphenyl 3m. The reaction was performed following the General Procedure A with (3-fluorophenyl)phenylacetylene (**1m**, 19.6 mg, 0.1 mmol) and 4-tert-butylphenyl magnesium bromide (0.125 mL, 0.25 mmol). The crude product was purified by flash chromatography on silica gel

(eluted with hexanes, R_f=0.30) to give the product (17.0 mg, 55%) as a white solid. M.P. = 73-75 ^oC. ^1H NMR (500 MHz, $CDCl_3$) δ 7.76 (d, *J* = 1.5 Hz, 1H), 7.57 – 7.52 (m, 5H), 7.50 – 7.44 (m, 3H), 7.40 (t, *J* = 7.7 Hz, 1H), 7.35 (dd, *J* = 4.9, 2.1 Hz, 3H), 1.36 (s, 9H) ppm. $^{13}C\{^1H\}$ NMR (125 MHz, CDCl3) δ 150.69, 141.26, 137.44, 131.67, 130.20, 130.12, 128.76, 128.38, 128.30, 126.99, 126.76, 125.80, 123.66, 123.30, 89.40, 34.58, 31.37 ppm. IR (thin film) 2962, 1600, 1491, 1392, 1269, 836, 792, 754, 691 cm^{-1}. HRMS (EI) m/z: [M]+ calcd for C24H22 310.1722; Found 310.1722.

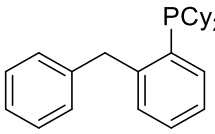

(2-benzylphenyl)dicyclohexylphosphane. The reaction was performed following the Ligand Synthesis Procedure with 1-benzyl-2-bromobenzene (247 mg, 1 mmol) and chlorodicyclohexylphosphine (280 mg, 1.2 mmol). The crude product was purified by flash chromatography on silica gel (eluted with hexanes) to give the product (145.6 mg, 40%) as a colorless oil. ^1H NMR (500 MHz, $CDCl_3$) δ 7.51 (d, *J* = 7.1 Hz, 1H), 7.34 – 7.24 (m, 4H), 7.19 (d, *J* = 7.3 Hz, 4H), 4.47 (s, 2H), 1.90 (dd, *J* = 16.4, 7.5 Hz, 4H), 1.85 – 1.51 (m, 8H), 1.37 – 1.13 (m,8H), 1.11 – 0.94 (m, 2H).$^{13}C\{^1H\}$ NMR (125 MHz, CDCl3) δ 190.71, 148.03, 147.74, 141.87, 134.37, 134.16, 132.85, 132.81, 130.37, 130.31, 129.17, 128.57, 128.17, 125.68, 125.53, 40.28, 40.01, 34.18, 34.04, 30.52, 30.33, 29.25, 29.15, 27.32, 27.18, 27.09, 26.41. $^{31}P\{^1H\}$ NMR (270 MHz, $CDCl_3$) *δ* 14.89 ppm. IR (thin film) 3058, 3025, 2923, 2849, 2360, 2341, 1602, 1589, 1447, 1176, 1122, 749 cm^{-1}. HRMS (ESI) m/z: [M+H]+ calcd for C25H34P 365.2398; Found 365.2413.

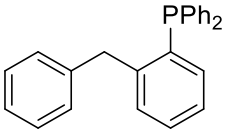

(2-benzylphenyl)diphenylphosphane. The reaction was performed following the Ligand Synthesis Procedure with 1-benzyl-2-bromobenzene (247 mg, 1 mmol) and chlorodiphenylphosphine (264 mg, 1.2 mmol). The crude product was purified by flash chromatography on silica gel (eluted with hexanes) to give the product (116.2 mg, 33%) as a colorless oil. ^{1}H NMR (500 MHz, $CDCl_3$) δ 7.34 – 7.28 (m, 6H), 7.26 – 7.20 (m, 5H), 7.17 (t, *J* = 7.3 Hz, 2H), 7.10 (dd, *J* = 17.4, 7.8 Hz, 4H), 6.92 – 6.87 (m, 1H), 4.23 (s, 2H) ppm. ^{13}C{^{1}H} NMR (125 MHz, CDCl3) δ 145.79, 145.59, 140.65, 136.77, 136.69, 136.06, 135.95, 134.06, 133.90, 133.67, 129.95, 129.91, 129.38, 129.04, 128.68, 128.61, 128.57, 128.51, 128.29, 126.50, 125.96, 40.10, 39.92 ppm. (More peaks than expected because of C-P coupling). ^{31}P{^{1}H} NMR (270 MHz, $CDCl_3$) *δ* 14.47 ppm. IR (thin film) 3054, 3028, 2980, 2956, 2855, 1740, 1589, 1447, 1239, 705 cm^{-1}. HRMS (ESI) m/z: [M+H]+ calcd for C25H22P 353.1459; Found 353.1447.

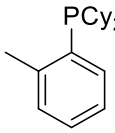

dicyclohexyl(o-tolyl)phosphane. The reaction was performed following the Ligand Synthesis Procedure with 2-bromotoluene (170 mg, 1 mmol) and chlorodicyclohexylphosphine (280 mg, 1.2 mmol). The crude product was purified by flash chromatography on silica gel (eluted with hexanes) to give the product (138.3mg, 48%) as a white solid. The spectroscopic data match the previously reported data.[10]

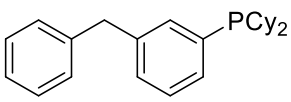

(3-benzylphenyl)dicyclohexylphosphane. The reaction was performed following the Ligand Synthesis Procedure with 1-benzyl-3-bromobenzene (247 mg, 1 mmol) and chlorodicyclohexylphosphine (280 mg, 1.2 mmol). The crude product was purified by flash chromatography on silica gel (eluted with hexanes) to give the product (138.5 mg, 38%) as a colorless oil. ^{1}H NMR (500 MHz, $CDCl_3$) δ 7.32 – 7.21 (m, 5H), 7.21 – 7.11 (m, 4H), 3.99 (s, 2H), 1.91 – 1.79 (m, 2H), 1.76 (dd, J = 12.9, 1.4 Hz, 2H), 1.64 (t, J = 10.2 Hz, 4H), 1.56 (d, J = 14.0 Hz, 2H), 1.37 – 1.04 (m, 8H), 1.02 – 0.88 (m, 2H). ^{13}C{^{1}H} NMR (125 MHz, CDCl3) δ 141.13, 140.47, 140.39, 135.51, 135.29, 134.77, 134.58, 132.44, 132.24, 129.34, 128.88, 128.43, 127.90, 127.83, 126.05, 41.89, 32.54, 32.41, 30.13, 29.95, 28.87, 28.79, 27.32, 27.19, 27.05, 26.97, 26.44 ppm (More peaks than expected because of C-P coupling). ^{31}P{^{1}H} NMR (270 MHz, $CDCl_3$) δ 2.99 ppm. IR (thin film) 3026, 2922, 2848, 2380, 2340, 1738, 1585, 1433, 1240, 1070, 1046, 743, 696 cm^{-1}. HRMS (ESI) m/z: [M+H]+ calcd for C25H34P 365.2398; Found 365.2392.

Computational Methods

Experimental

All density functional theory (DFT) calculations were performed with the ORCA program package, v3.0.3.[11] Geometry optimizations were carried out at the unrestricted B97 level of DFT with dispersion correction (B97-D3). The def2-TZVP basis sets and the def2-TZVP/J auxiliary basis sets (used to expand the electron density in the resolution-of-identity (RI) approach) were used for all atoms except hydrogen. All hydrogens were

described using the def2-SVP basis sets and def2-SV/J auxiliary basis sets.[12] The def2-SD effective core potential[13] and corresponding def2-TZVP/def2-TZVP/J basis sets (ibid.) were applied to Pd, and the Conductor-like Screening Model (COSMO; dipole moment corresponding to DME) was implemented as described in the results section.

The SCF calculations were tightly converged ($1x10^{-8}$ E_h in energy, $1x10^{-7}$ E_h in the density change, and $5x10^{-7}$ in the maximum element of the DIIS error vector). In all cases the geometries were considered converged after the energy change was less than $1x10^{-6}$ E_h, the gradient norm and maximum gradient element were smaller than $3x10^{-4}$ E_h-Bohr^{-1} and $1x10^{-4}$ E_h-Bohr^{-1}, respectively, and the root-mean square and maximum displacements of all atoms were smaller than $6x10^{-4}$ Bohr and $1x10^{-3}$ Bohr, respectively. Numerical frequency calculations were used to verify that the calculated structures represented either local minima (ground states) or saddle points (transition states) on the potential energy surface. The reported energies are Gibbs free energies, calculated for 298.15 K and 1.00 atm, as obtained from numerical frequency calculations on the optimized geometries.

Transition state searches were performed by educated and researched guesses of the transition state or by using relaxed coordinate/surface scans, involving successive geometry optimization calculations on species related by a regular change to fixed bond distances, bond angles, or torsion angles of interest, to provide suitable starting points for performing dedicated transition state optimization calculations.

References

1. Cho, C.-H.; Park, H.; Park, M.-A.; Ryoo, T.-Y.; Lee, Y.-S.; Park, K. *Eur. J. Org. Chem.* **2005**, 205, 3177.

2. Nguyen, M. H.; Smith, A. B. *Org. Lett.* **2014**, 16, 2070.

3. Yuen, O. Y.; So, C. M.; Man, H. W.; Kwong, F. Y. *Chem. Eur. J.* **2016**, 22, 6471.

4. Iglesias, M. J.; Prieto, A.; Nicasio, M. C. *Org. Lett.* **2012**, 14, 4318.

5. Shi, S.; Meng, G.; Szostak, M. *Angew. Chem. Int. Ed.* **2016**, 55, 6959.

6. Nakamura, Y.; Yoshikai, N.; Ilies, L.; Nakamura, E. *J. Am. Chem. Soc.* **2012**, 136, 646.

7. Shen, A.; Ni, C.; Cao, Y.-C.; Zhou, H.; Song, G.-H.; Ye, X.-F. *Tetrahedron Lett.* 2014, 55, 3278.

8. Li, X.-J.; Zhang, J.-L.; Geng, Y.; Jin, Z. *J. Org. Chem.* 2013, 78, 5078.

9. Izawa, Y.; Zheng, C.; Stahl, S. S.; *Angew. Chem. Int. Ed.* **2013**, 52, 3672.

10. Hirai, Y.; Uozumi, Y. *Synlett* **2017**, 28, 2966.

11. Neese, F. *WIREs Comput. Mol. Sci.* **2012**, 2, 73.

12. (a) Schaefer, A.; Horn, H.; Ahlrichs, R. *J. Chem. Phys.* **1992**, 97, 2571; (b) Schaefer, A.; Huber, C.; Ahlrichs, R. *J. Chem. Phys.* **1994**, 100, 5829; (c) Weigend, F.; Ahlrichs, R. *Phys. Chem. Chem. Phys.* **2005**, 7, 3297; (d) Weigend, F. *Phys. Chem. Chem. Phys.* **2006**, 8, 1057.